Bauhaus-Universität Weimar

Generalized Beam Theory for the analysis of thin-walled circular pipe members

Dissertation

as required for the conferral of the academic degree
Doktor-Ingenieur (Dr.-Ing.)

at the Faculty of Civil Engineering
of the
Bauhaus-Universität Weimar

Submitted by
Abinet Kifle Habtemariam
born in Addis Ababa, Ethiopia

Assessors: Prof. Dr.-Ing. habil. Carsten Könke
Prof. Dr. rer. nat. habil. Klaus Gürlebeck
Prof. Dr.-Ing. habil. Manfred Bischoff
Dr.-Ing. habil. Volkmar Zabel

Weimar, July 2021

to my grandfather

Acknowledgements

This dissertation was written during my time as researcher and teaching assistant at the Institute of Structural Mechanics at Bauhaus-Universität Weimar.

First, I would like to express my sincere gratitude to my advisors Prof. Dr.-Ing. habil. Carsten Könke and Dr.-Ing. habil. Volkmar Zabel for giving me the opportunity to work at the institute and be involved in various research projects. I want to thank them for their helpful guidance and for giving me the academic freedom to develop and realize new ideas and methods. Furthermore, I would like to thank Prof. Dr.-Ing. habil. Manfred Bischoff for his interest in my work and contribution as a reviewer of this thesis.

I am grateful for the Thüringer Graduiertenförderung scholarship program for the financial support during my study and Horizon 2020 EXCHANGE-Risk project for making my research stay in Vienna possible. I am also grateful to the anonymous reviewers from Thin-Walled Structures for giving me valuable comments and suggestions.

I also want to thank my coworkers at the institute for the friendly cooperation and the pleasant time that I had working with them. Especially, I am thankful to Marcelo Bianco and Fabiola Tartaglione for collaborating with me in my research and for the numerous inspiring discussions we had. Also a thanks goes to all wonderful people at the Chair of Computer Science in Architecture (InfAR) for including me in many of their activities and events.

Finally, I would like to thank my important friend Meret Arnold for proof reading my thesis, family Tatarin for making my life in Weimar joyful and to all my friends and family for their invaluable love and support.

Abinet Kifle Habtemariam
Weimar, July 2021

Abstract

The detailed structural analysis of thin-walled circular pipe members often requires the use of a shell or solid-based finite element method. Although these methods provide a very good approximation of the deformations, they require a higher degree of discretization which causes high computational costs. On the other hand, the analysis of thin-walled circular pipe members based on classical beam theories is easy to implement and needs much less computation time, however, they are limited in their ability to approximate the deformations as they cannot consider the deformation of the cross-section.

This dissertation focuses on the study of the Generalized Beam Theory (GBT) which is both accurate and efficient in analyzing thin-walled members. This theory is based on the separation of variables in which the displacement field is expressed as a combination of predetermined deformation modes related to the cross-section, and unknown amplitude functions defined on the beam's longitudinal axis. Although the GBT was initially developed for long straight members, through the consideration of complementary deformation modes, which amend the null transverse and shear membrane strain assumptions of the classical GBT, problems involving short members, pipe bends, and geometrical nonlinearity can also be analyzed using GBT. In this dissertation, the GBT formulation for the analysis of these problems is developed and the application and capabilities of the method are illustrated using several numerical examples. Furthermore, the displacement and stress field results of these examples are verified using an equivalent refined shell-based finite element model.

The developed static and dynamic GBT formulations for curved thin-walled circular pipes are based on the linear kinematic description of the curved shell theory. In these formulations, the complex problem in pipe bends due to the strong coupling effect of the longitudinal bending, warping and the cross-sectional ovalization is handled precisely through the derivation of the coupling tensors between the considered GBT deformation modes. Similarly, the geometrically nonlinear GBT analysis is formulated for thin-walled circular pipes based on the nonlinear membrane kinematic equations. Here, the initial linear and quadratic stress and displacement tangent stiffness matrices are built using the third and fourth-order GBT deformation mode coupling tensors.

Longitudinally, the formulation of the coupled GBT element stiffness and mass matrices are presented using a beam-based finite element formulation. Furthermore, the formulated GBT elements are tested for shear and membrane locking problems and the limitations of the formulations regarding the membrane locking problem are discussed.

Kurzfassung

Eine detaillierte Strukturanalyse dünnwandiger, kreisförmiger Rohrelemente erfordert oft die Verwendung von Schalenelementen in der Finite Elemente Methode. Diese Methode ermöglicht eine sehr gute Approximation des Verformungszustandes, erfordert jedoch einen hohen Grad der Diskretisierung, welcher wiederum einen hohen Rechenaufwand verursacht. Eine alternative Methode hierzu basiert auf klassischen Balkentheorien, welche eine einfache Modellierung ermöglichen und wesentlich geringeren Rechenaufwand erfordern. Diese weisen jedoch Einschränkungen bei der Approximation von Verformungen auf, da Querschnittsverformungen nicht berücksichtigt werden können.

Schwerpunkt dieser Dissertation ist eine Untersuchung der Verallgemeinerten Technischen Biegetheorie (VTB), die sowohl eine genaue als auch eine effiziente Analyse von dünnwandigen Tragwerkselementen ermöglicht. Diese Theorie basiert auf einer Trennung der Variablen, in der das Verschiebungsfeld als eine Kombination von vorbestimmten Verformungsmoden der Querschnitts und unbekannten Amplitudenfunktionen in Längsrichtung ausgedrückt wird. Obwohl die VTB ursprünglich für lange, gerade Elemente entwickelt wurde, können durch die Berücksichtigung komplementärer Verformungsmoden, welche die Null-Annahmen der klassischen VTB für Quer- und Schubmembrandehnung abändern, Probleme mit kurzen Elementen, Rohrbögen und geometrischer Nichtlinearität analysiert werden. In dieser Dissertation wird die VTB-Formulierung für die Analyse dieser Probleme entwickelt. Die Anwendung und Möglichkeiten der Methode werden anhand mehrerer numerischer Beispiele veranschaulicht, deren Verschiebungs- und Spannungsfeldanalysen anhand eines äquivalenten, verfeinerten, schalenbasierten Finite-Elemente-Modells verifiziert werden.

Die entwickelten statischen und dynamischen VTB-Formulierungen für Rohrbogenelemente basieren auf der linearen kinematischen Beschreibung der Theorie gekrümmter Schalen. In diesen Formulierungen wird das komplexe Problem in Rohrbögen aufgrund des starken Kopplungseffekts der Längsbiegung, der Verwölbung und der Querschnittsovalisierung durch die Herleitung der Kopplungstensoren zwischen den betrachteten VTB-Verformungsmoden präzise behandelt. In ähnlicher Weise wird die geometrisch nichtlineare VTB-Analyse für gerade Rohrelemente auf der Grundlage der nichtlinearen kinematischen Membrangleichungen formuliert. Die anfänglichen linearen und quadratischen Spannungs- und Verschiebungs-Tangentensteifigkeitsmatrizen werden dabei unter Verwendung der VTB-Kopplungstensoren dritter und vierter Ordnung aufgebaut.

In Längsrichtung wird die Formulierung der gekoppelten VTB-Element-Steifigkeits- und Massenmatrizen unter Verwendung einer balkenbasierten Finite-Elemente Formulierung dargestellt. Weiterhin werden die VTB-Elemente auf Schub- und Membran-Locking-Probleme getestet und die Einschränkungen der Formulierungen bezüglich des Membran-Locking-Problems diskutiert.

Contents

Abstract v

Kurzfassung vii

List of Figures xi

List of Tables xvi

Nomenclature xix

1 Introduction 1

1.1 Motivation . . . 2
1.2 Introduction to classical GBT . . . 4
1.3 Objective, methodology and contributions . . . 6
1.4 Structure of the dissertation . . . 7

2 Fundamentals of Generalized Beam Theory 9

2.1 State of the art . . . 9
2.1.1 Prismatic sections . . . 10
2.1.2 Circular pipe sections . . . 12
2.1.3 Numerical solution methods in GBT . . . 13
2.2 Linear formulation of GBT . . . 14
2.2.1 Assumptions in GBT . . . 14
2.2.2 Separation of variables . . . 15
2.2.3 Kinematic equations . . . 16
2.2.4 Variational formulation . . . 16
2.2.5 Deformation modes . . . 20
2.2.6 Finite element formulation . . . 22
2.2.7 Stress resultants . . . 25
2.3 Numerical example . . . 26
2.4 Locking problem . . . 37
2.4.1 Shear locking . . . 38
2.4.2 Membrane locking . . . 41

3 Formulation of GBT for pipe bends **45**
3.1 Linear GBT formulation for pipe bends . . . 46
3.1.1 Variation of internal energy . . . 48
3.1.2 Variation of the external energy . . . 50
3.2 Deformation modes . . . 51
3.2.1 Mode coupling . . . 52
3.3 Finite element formulation . . . 53
3.4 Stress resultants . . . 59
3.5 Numerical examples . . . 60
3.5.1 In-plane bending . . . 60
3.5.2 Out-of-plane bending . . . 67
3.5.3 Internal pressure loading . . . 69
3.6 Membrane locking . . . 72
3.7 Summary . . . 73

4 Vibration analysis of toroidal shells using GBT **75**
4.1 Hamilton's principle . . . 76
4.2 Deformation mode coupling . . . 78
4.3 Finite element formulation . . . 80
4.4 Numerical examples . . . 82
4.4.1 Cantilever arch pipe . . . 82
4.4.2 Toroidal shell . . . 87
4.5 Summary . . . 91

5 Geometrically nonlinear formulation of GBT for straight pipes **93**
5.1 Linearization . . . 95
5.2 Kinematic description . . . 96
5.3 Variation of the internal energy . . . 98
5.3.1 Variation of the longitudinal internal energy . . . 99
5.3.2 Variation of the transverse internal energy . . . 101
5.3.3 Variation of the shear internal energy . . . 104
5.4 Deformation modes coupling . . . 107
5.4.1 Third-order coupling tensor . . . 107
5.4.2 Fourth-order coupling tensor . . . 111
5.5 Finite element formulation . . . 114
5.6 Nonlinear stress resultants . . . 124
5.7 Numerical examples . . . 125
5.7.1 Transverse bending . . . 125
5.7.2 Longitudinal bending . . . 133

5.8 Summary 143

6 Conclusion and outlook **145**

6.1 Conclusion 145

6.2 Outlook 147

Bibliography **149**

Publications by the author **161**

List of Figures

1.1 Demolition of the 236 m high Wiederau J1 guyed antenna mast. . . . 3
1.2 TAPS at the fault crossing. . . . 4
1.3 Deformed configuration of a thin-walled circular pipe cross-section and its corresponding GBT modal decomposition. . . . 5

2.1 Geometry, displacements and stresses of a thin-walled circular pipe. . . . 14
2.2 External loading. . . . 18
2.3 Rigid-body modes warping $u(\theta)$ displacement. . . . 21
2.4 Rigid-body modes tangential $v(\theta)$ and radial $w(\theta)$ displacements. . . . 21
2.5 Axisymmetric mode a radial $w(\theta)$ displacement. . . . 21
2.6 Local shell-type modes. . . . 21
2.7 Stress resultants. . . . 26
2.8 Projected loading on a short cantilever circular pipe. . . . 27
2.9 Force and projected area in a local coordinate system. . . . 27
2.10 Radial displacement contribution of GBT deformation mode groups and comparison of final GBT solution with shell results. . . . 32
2.11 Deformation shape of a short cantilever pipe. . . . 33
2.12 GBT solution convergence. . . . 34
2.13 The sparsity patterns of the system stiffness matrices. . . . 35
2.14 GBT mode amplitude. . . . 35
2.15 Comparison of displacements at the mid span. . . . 36
2.16 Comparison of bending moments per unit length at the mid span. . . . 37
2.17 Comparison of normal forces per unit length at the mid span. . . . 37
2.18 Comparison of shear forces per unit length at the mid span. . . . 37
2.19 A simply supported thin-walled circular pipe under uniform bending moment. . . . 38
2.20 Displacement and normal force at the mid span. . . . 40
2.21 Pipe section under projected loading. . . . 42
2.22 The deformed shape of the pipe section (×3). . . . 44

3.1 Curved thin-walled circular cross-section with global and local coordinate systems. . . . 47
3.2 Radial displacement for deformation mode 5 or ovalization, ${}^{5}w(\theta)$. . . . 51
3.3 List of possible mode couplings for stiffness coefficients ${}^{ik}C_1$ and ${}^{ik}C_2$. . . . 52

3.4 List of possible mode couplings for stiffness coefficients ${}^{ik}B$ and the symbolic integral value of the coefficients. 53
3.5 List of possible mode couplings for stiffness coefficients ${}^{ik}C_4$ and ${}^{ik}D$. 53
3.6 List of possible mode couplings for stiffness coefficients ${}^{ik}D_{1\mu}$ and ${}^{ik}D_{3\mu}$. 54
3.7 In-plane loading of a circular section cantilever arch beam. 61
3.8 Distributed load in the local coordinate system. 61
3.9 GBT solution convergence. 63
3.10 In-plane deformation shape of a 90° cantilever pipe bend (×40). 63
3.11 The sparsity pattern of the system stiffness matrices 64
3.12 GBT deformation modes amplitude. 64
3.13 Comparison of displacements at the tip. 65
3.14 Comparison of displacements at the mid span. 66
3.15 Comparison of bending moment per unit length at the mid span. 66
3.16 Comparison of normal force per unit length at the mid span. 66
3.17 Comparison of shear force per unit length at the mid span. 66
3.18 Displacements and bending moment at the mid span when $\mu = 0$. 67
3.19 Out-of-plane loading of a circular section cantilever arch beam. 67
3.20 Out-of-plane deformation shape of a 90° cantilever pipe bend (×50). 68
3.21 Comparison of displacements at section A [mm]. 68
3.22 Comparison of bending moment per unit length at section A. 69
3.23 Comparison of normal force per unit length at section A. 69
3.24 Comparison of shear force per unit length at section A. 69
3.25 Internal pressure loading of an end restrained 45° pipe bend. 70
3.26 Internal pressure loading deformation shape of an end restrained 45° pipe bend. 70
3.27 Comparison of displacements at the mid span [mm]. 71
3.28 Comparison of bending moment per unit length at the mid span. 71
3.29 Comparison of normal force per unit length at the mid span. 71
3.30 Comparison of Q_θ at the mid span. 72
3.31 Displacement and stress resultants at the mid span when $\mu = 0$. 72

4.1 Curved thin-walled circular cross-section with global and local coordinate systems. . . . 76
4.2 List of possible mode couplings for inertia coefficient ${}^{ik}Q$. 78
4.3 List of possible mode couplings for inertia coefficient ${}^{ik}W$. 79
4.4 Free vibration analysis of a 90° cantilever arch pipe. 82
4.5 The first eight natural modes of a 90° cantilever pipe bend. 83
4.6 Participation of GBT modes to the vibration modes of a 90° cantilever pipe bend. 83
4.7 Participation of GBT modes to the vibration modes of a 90° cantilever pipe bend. 84

4.8 MAC value comparison of GBT and shell vibration mode shapes considering the warping displacement (u) of the cantilever arch pipe. 86
4.9 MAC value comparison of GBT and shell vibration mode shapes considering the tangential and radial displacements ($v + w$) of the cantilever arch pipe. 86
4.10 Closed toroidal shell. 87
4.11 The first eight natural modes of the toroidal shell. 88
4.12 Participation of GBT modes to the vibration modes of toroidal shell. 88
4.13 Participation of GBT modes (RB (rigid-body), LS (local shell-type), SV (Shear-v), SU (Shear-u)) to the vibration modes of toroidal shell. 89
4.14 MAC value comparison of GBT and shell mode shapes considering the warping displacements (u) of the toroidal shell. 90
4.15 MAC value comparison of GBT and shell mode shapes considering the tangential and radial displacements ($v + w$) of the toroidal shell. 91

5.1 Initial state and unknown neighboring state on the nonlinear response path 95
5.2 Thin-walled circular pipe section with global and local coordinate systems. 97
5.3 Third-order coupling tensor ${}^{jik}B_1$. 108
5.4 Third-order coupling tensor ${}^{jik}C_1$. 109
5.5 The projected view of the third-order coupling tensor ${}^{jik}D_1$. 110
5.6 Fourth-order coupling tensor ${}^{jlik}B_1$. 111
5.7 Fourth-order coupling tensor ${}^{jlik}C_1$. 112
5.8 Fourth-order coupling tensor ${}^{jlik}D_1$. 113
5.9 Pipe section under projected loading. 125
5.10 The third-order coupling tensor ${}^{jik}B_1$ considering only the selected modes. 127
5.11 The sparsity patterns of the element linear and tangent stiffness matrices. 128
5.12 The linear analysis (LA) and nonlinear analyses (NA) displacement response of the pipe under gradually increasing load q. 129
5.13 The nonlinear deformation shape of the pipe (×5). 130
5.14 Comparison of displacements at $q = 0.14 \frac{\mathrm{N}}{\mathrm{mm}^2}$. 130
5.15 Comparison of displacements at $q = 0.24 \frac{\mathrm{N}}{\mathrm{mm}^2}$. 131
5.16 GBT deformation modes amplitude at $q = 0.14 \frac{\mathrm{N}}{\mathrm{mm}^2}$. 131
5.17 Stress resultants of the linear analysis at $q = 0.14 \frac{\mathrm{N}}{\mathrm{mm}^2}$. 132
5.18 Stress resultants of the nonlinear analysis at $q = 0.14 \frac{\mathrm{N}}{\mathrm{mm}^2}$. 132
5.19 Stress resultants of the linear analysis at $q = 0.24 \frac{\mathrm{N}}{\mathrm{mm}^2}$. 132
5.20 Stress resultants of the nonlinear analysis at $q = 0.24 \frac{\mathrm{N}}{\mathrm{mm}^2}$. 133

5.21 Geometry, material property, loading and boundary condition of a cantilever circular pipe section. 133
5.22 The third-order coupling tensor ${}^{jik}C_1$ considering only the selected modes. Rows and columns related to shear-u modes are not shown since they have no coupling. 135
5.23 The sparsity patterns of the element initial linear stress and displacement stiffness matrices. 136
5.24 The sparsity patterns of the element initial quadratic stress and displacement stiffness matrices. 136
5.25 The sparsity patterns of the system tangent stiffness matrices. 137
5.26 GBT solution convergence. 138
5.27 The linear analysis (LA) and nonlinear analysis (NA) transverse or radial displacement response of the cantilever pipe under gradually increasing load q. 138
5.28 The linear analysis (LA) and nonlinear analysis (NA) longitudinal or warping displacement response of the cantilever pipe under gradually increasing load q. 139
5.29 The deformation shape of the cantilever pipe. 139
5.30 GBT deformation modes amplitude of the cantilever pipe at $q = 32.23 \frac{\text{N}}{\text{mm}}$. 140
5.31 Comparison of displacements in at the tip of the cantilever pipe. 141
5.32 Comparison of nonlinear analysis displacements at section A 141
5.33 Comparison of linear analysis displacements at section A 141
5.34 Comparison of nonlinear analysis bending moments at section A 142
5.35 Comparison of linear analysis bending moments at section A 142
5.36 Comparison of nonlinear analysis normal forces at section A 142
5.37 Comparison of linear analysis normal forces at section A 142
5.38 Comparison of nonlinear analysis shear forces at section A 143

List of Tables

2.1 Summary of orthogonal deformation modes of CHS according to classical GBT. 20
2.2 Summary of cross-sectional stiffness for classical GBT, axisymmetric and torsional modes. 22
2.3 Summary of the cross-sectional stiffness for non-conventional modes and their coupling. 23
2.4 External load modal decomposition. 28
2.5 Comparison of the GBT and shell transversal displacements results at the tip of the cantilever pipe. 32
2.6 Comparison of GBT and shell results without the cross-sectional deformation. 33
2.7 Comparison of GBT with different modes and shell results. 33
2.8 Computational speed comparison of GBT and shell. 34
2.9 Comparison of GBT and shell results. 36
2.10 The value of the amplitude function and its derivatives along x. 40
2.11 Comparison of the maximum displacements in shell and GBT model of the pipe section for different wall thicknesses t. 44

3.1 External load modal decomposition. 61
3.2 Comparison of GBT with different modes and shell results. 62
3.3 Computational speed comparison of GBT and shell. 63
3.4 Comparison of GBT and shell results at the mid span. 67
3.5 Comparison of shell and GBT with different modes. 68
3.6 Comparison of GBT and shell results at section A. 69
3.7 Comparison of shell and GBT with different modes. 70
3.8 Comparison of GBT and shell results at the mid span. 72
3.9 In-plane deformation results for a 90° cantilever pipe bend under tip load for different wall thicknesses t. 73

4.1 Comparison of GBT with different modes and shell results. 85
4.2 Comparison of GBT with different modes and shell results. 90

5.1 External load modal decomposition. 126
5.2 Comparison of nonlinear analyses results of GBT and shell at $q = 0.14\frac{\mathrm{N}}{\mathrm{mm}^2}$. 132
5.3 Comparison of nonlinear analyses results of GBT and shell at $q = 0.24\frac{\mathrm{N}}{\mathrm{mm}^2}$. 132
5.4 External load modal decomposition. 134
5.5 Comparison of nonlinear analysis results of GBT and shell model at section A. 143

Nomenclature

Abbreviations

CHS	Circular Hollow Sections
DoF	Degrees of Freedom
FEM	Finite Element Method
FSM	Finite Strip Method
GBT	Generalized Beam Theory
ISM	Institute of Structural Mechanics
MAC	Modal Assurance Criterion
MRD	Mean Relative Difference
TAPS	Trans-Alaska Pipeline System

Greek letters

α	toroidal to cross-sectional radius ratio
γ	shear strain
μ	Poisson's ratio
Π	total potential energy
ψ	longitudinal bend angle
ρ	density
σ	normal stress
τ	shear stress
$\theta,\ \varphi$	local coordinate system
ε	normal strain

Latin letters

B	section transverse stiffness
C	section longtudinal stiffness
D	section shear stiffness
E	Young's modulus
f	longitudinal load distribution function
G	shear modulus
K	plate bending stiffness
m	number of circumferential waves
$M_{x\theta}$	twisting moment
$M_x,\ M_\theta$	bending moments
$N_{x\theta}$	inplane shear force
$N_x,\ N_\theta$	normal forces
p	external load
Q	membrane extensional stiffness
q	distributed load
$Q_x,\ Q_\theta$	transverse shear forces
r	radius of a pipe
T	kinetic energy

t	thickness of a pipe wall
U_{ext}	external load potential energy
U_{int}	internal strain energy
V	longitudinal amplitude function
i, j, k, l	GBT defromation mode indices
L	element length
L_m	member length
m	external bending loding
R	longitudinal bend radius
u	longitudinal displacement
v	tangential displacement
w	radial displacement
$X,\ Y,\ Z$	global coordinate system
$x,\ z$	local coordinate system
LS	local shell-type deformation modes
RB	rigid-body deformation modes
SU	non-conventional shear-u modes
SV	non-conventional shear-v modes

General notations

$(),_{}$	indicates partial derivatives
$(\times\cdot)$	scaled by
$\delta(\cdot)$	variation notation
$\left[Sh_{(\cdot)}\right]$	completeness coefficient matrices
$[\cdot]$	matrix
$\left[\mathbb{V}_{(\cdot)}\right]$	component of stiffness or mass matrix
$[K]^e$	element stiffness matrix
$[M]^e$	element mass matrix
$\left\{\vartheta_{(\cdot)}\right\}$	vector of beam's nodal amplitude
$\{Tx\}$	the variable vector
$\{\cdot\}$	vector
$\{d\}$	element amplitude vector
$\sum_{i,j,k,\cdots}$	is the same as $\sum_i \sum_j \sum_k \cdots$
$\sum_k$	summation over the list of deformation indies in k
$\{\mathbb{V}_{(\cdot)}\}$	component of internal force vector
${}^{(\cdot)}[k]$	element stiffness sub-matrix
${}^{(\cdot)}[m]$	element mass sub-matrix
${}^{(\cdot)}\{f\}$	element force sub-vector
${}^{(\cdot)}\{F\}^e$	element force vector

Superscripts and subscripts

$\overset{\text{U}}{(\cdot)}$	non-conventional shear-u mode index
$\overset{\text{V}}{(\cdot)}$	non-conventional shear-v mode index
${}^{a}(\cdot)$	axis-symmetric deformation mode index
${}^{t}(\cdot)$	torsion deformation mode index
$(\cdot)^T$	transpose
$(\cdot)^{\text{B}}$	plate in bending
$(\cdot)^{\text{M}}$	membrane component
$(\cdot)_{\text{bending}}$	considering only bending defromation modes
$(\cdot)_{\text{H}}$	term based on cubic Hermite shape functions

$(\cdot)_{\text{local}}$	considering only local defromation modes
$(\cdot)_{\text{L}}$	term based on cubic Lagrange shape functions
$(\cdot)_{\text{total}}$	considering all defromation modes
$^{ijk\cdots}(\cdot)$	i, j, k, ... GBT deformation mode indices involved in a vector, matrix or tensor
$^{i}(\cdot)$	index of GBT mode

Chapter 1

Introduction

Thin-walled circular pipe members are widely applied in structures such as pipeline systems, air and space crafts, nuclear and fusion reactors, wind turbine towers and industrial plants. The preference of using circular pipes in these structures comes partly from the fact that they have a high strength-to-weight ratio and partly because they can be easily manufactured. For example, cold-formed steel circular pipes are produced by folding and welding a metal sheet. In structures, thin-walled circular pipe members can be subjected to axial and transverse loading, external and internal pressure, torsion, or a combination of these loads. Unlike solid section members, the load carrying capacity of thin-walled slender members is highly dependent on the change in shape of the cross-section. For instance, an increase in the cross-sectional ovalization of a thin-walled circular pipe member during bending will lead to a gradual loss of the bending stiffness. This complex structural behavior of thin-walled members requires the development of a more robust and accurate mathematical model.

The detailed analysis of thin-walled members by means of a numerical shell-based Finite Element Method (FEM) [17, 180] can approximate the displacement and stress fields in thin-walled members accurately. However, the large number of Degrees of Freedom (DoF) needed in this method results in high computational costs. Furthermore, the 3D shell finite element model generation process is usually tiresome and time consuming.

On the other hand, classical beam theories like Euler-Bernoulli and Timoshenko [164] are easy to implement and need much less computation time but cannot be used to analyze thin-walled members since they do not consider cross-sectional distortion and warping. The first beam theory to consider non-uniform out-of-plane warping of thin-walled beam cross-sections was introduced by Vlasov [169]. In this theory the warping displacement field and its corresponding stress field component named as Bi-moment are considered in addition to a uniform axial extension, major and minor axis bending. Although this theory is a major improvement compared to the classical beam theories, it still fails to provide a full mechanical description of thin-walled beams since it does not consider in-plane distortion.

So far, two numerical methods can be mentioned which can accurately and efficiently analyze thin-walled members. The first one, Finite Strip Method (FSM), can be considered as a special form of the

finite element procedure in which the unnecessary and extravagant analysis in FEM is simplified for structures having regular geometric plans and boundary conditions in order to reduce the computation effort [37, 140]. In this method, the member is discretized into rectangular strips which calls for the use of simple interpolation polynomials in one direction and continuously differentiable smooth series functions in the other direction, thus effectively reducing the dimension of the problem.

The second method, the Generalized Beam Theory (GBT), can be regarded as an extension of the Vlasov thin-walled beam theory to include cross-sectional distortions. This theory was first proposed by Richard Schardt in 1966 [128, 137] for the analysis of prismatic and circular thin-walled members. In GBT, the displacement fields are described using the separation of variables principle [86], which leads to two analysis steps involving the cross-section and the longitudinal direction of the thin-walled member. In the cross-sectional analysis, the cross-sectional deformation is decomposed into the basic beam, distortional, local, and other modes. For prismatic thin-walled members, the decomposition of the cross-sectional deformation is tedious since it requires solving a quadratic eigenvalue problem [8, 77], whereas the cross-sectional deformation modes for thin-walled circular pipes can be simply expressed in a Fourier-Series [131]. Once, the deformation modes are determined from the cross-sectional analysis, the longitudinal direction analysis is carried out by multiplying the modes with an approximated longitudinal amplitude shape function leading to a conventional beam finite element analysis. Further description of the theory is given later in section 1.2.

In this dissertation, the generalized beam theory is studied due to its outstanding computational efficiency and potential to comprehensively describe the displacement and stress fields of thin-walled members. Here, the linear GBT formulation for thin-walled circular pipes is extended concerning static and dynamic analyses of pipe bends and geometrically nonlinear analysis of straight pipes.

1.1 Motivation

The motivation to search and develop an efficient numerical method to analyze thin-walled circular pipes stems from two research projects carried out at the Institute of Structural Mechanics (ISM), Bauhaus-Universität Weimar.

In the first project, the demolition of guyed tubular masts was studied to ensure safe demolition. The demolition of guyed masts is usually carried out by cutting down some of the supporting guy cables using an explosive in such a way that the mast can fall into the desired direction. Without the cable supports, guyed tubular masts are extremely slender structures which are susceptible to local buckling due to a bending moment generated by inertia forces during the falling process. For example, in the demolition overlay Figure 1.1a the tubular mast buckled in an early phase of falling causing the upper part of the mast to fold back instead of falling like a tree straight into the originally planned direction.

The risk of undesirable demolition outcome due to the uncertainty in the failure mechanism can be mitigated by using numerical simulations [99, 100, 166] and optimization techniques to design a controlled

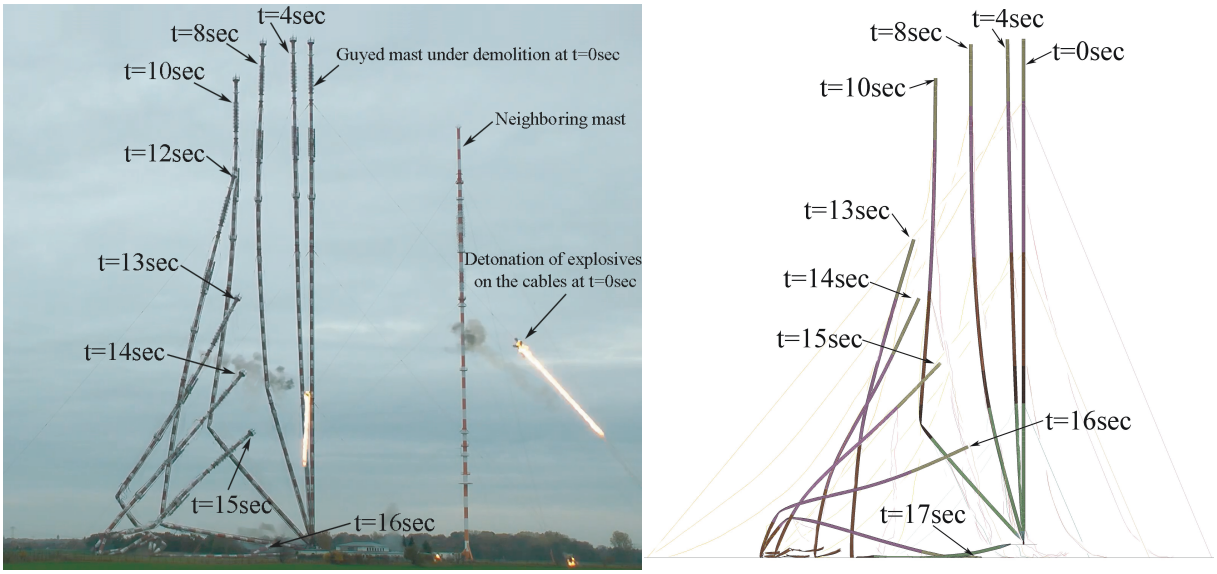

(a) Actual demolition in 2013

(b) FEM simulation using LS-DYNA

Figure 1.1: Demolition of the 236 m high Wiederau J1 guyed antenna mast.

detonation setup. Using shell-based explicit finite element analysis [175] implemented in LS-DYNA [72], this complex dynamic process involving large deformations and rotations can be simulated with reasonable accuracy as shown in Figure 1.1b. However, such a simulation has a high computational cost due to the very small time step requirement of the method in relation to the relatively longer duration of the falling. Additionally, this simulation needs to be computed multiple times with updated parameters for optimization of the detonation setup. Detailed findings of this research project can be found in [69].

In the second project, pipelines exposed to seismic risks were studied to mitigate possible damages. During an earthquake, pipelines crossing a fault may be deformed due to the relative movement of supports to both sides of the fault. For example, in the case of the Trans-Alaska Pipeline System (TAPS) the 2002 Denali earthquake caused a right lateral horizontal slip of about 5.50 m at the pipeline fault crossing putting the pipeline under compression [75, 157]. Figure 1.2 shows the lateral movement and bowing of the 579 m long pipeline segment with the sliding crossbeam supports in response to the fault slip, which acts to compress the pipeline. The simulation of such displacements, which can cause cross-sectional ovalization and local stress, requires a numerical method that appropriately describes the pipe, the support system, their interaction and failure modes characterized by local cross-sectional deformations. A structural analysis, which can fully evaluate these transversal and local effects, based on shell or solid finite-element models would require a significant amount of time to be modeled and solved, provided that it is even possible, considering the whole length of the pipeline at the fault crossing. Detail findings of this research project can be found in [70, 71].

As an alternative modeling technique, GBT can be used to easily model the structures in these projects using beam-finite elements considering all transversal and local effects. The motivation to study GBT is due to its remarkable computational efficiency, besides the scientific curiosity of understanding this

(a) Before fault slip

(b) After fault slip

Figure 1.2: TAPS at the fault crossing [75].

elegant and rather difficult theory.

Although the classical GBT formulation is not sufficient to model these complex engineering problems, the novel GBT formulations developed in this dissertation regarding the linear static and dynamic analyses of pipe bends and the geometrically nonlinear analysis of straight pipes in combination with recent studies at the ISM such as the formulation of GBT for semi-continued arbitrary support condition [29] and the coupled shell-GBT formulation [30] will make it possible to effectively analyze these and other structures involving thin-walled circular pipes.

1.2 Introduction to classical GBT

GBT is a beam theory specially formulated for thin-walled members with the capacity of determining the member cross-sectional deformation through the linear combination of a set of predetermined cross-sectional deformation modes which satisfy a number of orthogonality conditions. This modal nature of GBT has significant advantages in terms of its computational efficiency and the clear structure of the solution obtained [35]. In circular pipe members, once the cross-sectional deformation modes are defined by Fourier-Series [131], the amplitude of these orthogonal deformation modes along the length of the member is determined from the member equilibrium equations and boundary conditions. Figure 1.3 shows the linear combinations of the orthogonal deformation modes with their respective amplitude function ${}^{k}V$.

The credit to this innovative approach for solving structural problems involving thin-walled members goes to Richard Schardt and his co-workers at the Technical University of Darmstadt. The first publications by Schardt [128, 137] present already all basic aspects of GBT and discuss the first order analysis of

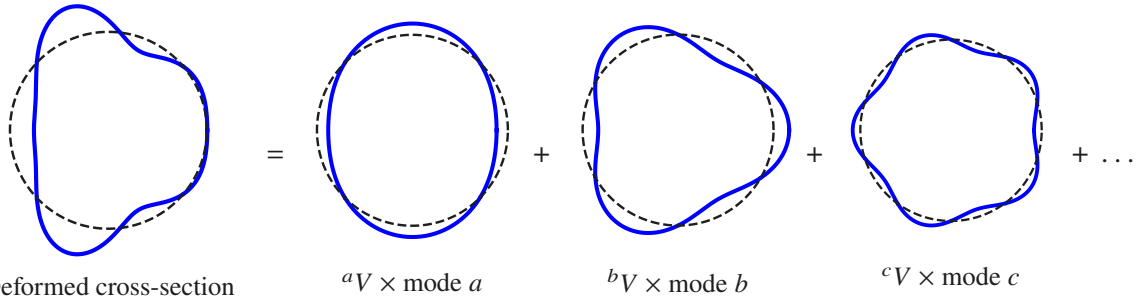

Figure 1.3: Deformed configuration of a thin-walled circular pipe cross-section and its corresponding GBT modal decomposition.

thin-walled members with open prismatic and cylindrical cross-sections. This initial work of Schardt follows Vlasov's [169] strategy of reducing complex two-dimensional problems of shell theory to one-dimensional problems through the definition of displacement fields as a sum of the product of pre-selected functions dependent only on the member's transversal perimeter to the unknown amplitude functions in the longitudinal direction. Furthermore, in the GBT formulation, Schardt adopted the Vlasov assumptions of negligible transverse elongation and in-plane shear distortions along the thin-walled member. However, the sum of four displacement components, which are the generalized longitudinal displacements, angles of rotation in major and minor axis and the generalized warping, used by Vlasov to define a displacement field of any point on the member is extended by Schardt in his generalized beam theory to include distortional, local and other cross-sectional deformations.

Since Schardt's first publications in the 1960s, for the next four decades, he and his co-workers published a number of papers and dissertations in German. These studies were mainly devoted to the development of GBT procedures used for the stability analysis of plates and open sections [135], the analysis of longitudinally curved thin-walled members with an open cross-section [167], the analysis of open cylindrical shells with arbitrary boundary conditions [123], the dynamic analysis of prismatic members [122, 134] and in relation to second-order analysis [102, 129, 138]. Based on these and several more studies, Schardt published his first book [131] titled *Verallgemeinerte Technische Biegetheorie*: *Lineare Probleme* in 1989, which is still the main reference in the GBT research community. A complete list of GBT publications by Schardt and his research group can be found on the website http://www.vtb.info/.

In 1983, Schard's first GBT related article [130] in English lead to the introduction of the theory to Davies, who then developed the exact finite element solution for the GBT's governing differential equation[38]. In the 1990s, more studies using GBT started to be published in English concerning the stability analysis of thin-walled members by Schardt [132, 133], Davies [39, 40] and Leach [87] which have played a major role in introducing GBT to the international research community.

In the last two decades, GBT has been studied by several research groups around the world making it one of the most evolved methods specialized in the analysis of thin-walled structures. Out of these groups, a Portuguese team lead by Camotim and Silvestre at the Technical University of Lisbon conducted the most

extensive studies focusing mainly on thin-walled prismatic cross-sections. In fact, out of the hundreds of research papers published by this group (http://www.civil.ist.utl.pt/gbt/) only five were devoted to thin-walled circular pipe sections. So far, the development of linear and nonlinear GBT formulations in circular pipe sections lags behind the development of prismatic sections, hence the need for this dissertation. A detailed literature review of recent GBT developments is given in section 2.1.

1.3 Objective, methodology and contributions

The main objective of this dissertation is the study and development of a GBT to analyze thin-walled circular pipes problems involving the coupling of GBT deformation modes. Such problems occur in pipes with a curved axis or when considering different types of nonlinearities.

In addition to the classical GBT deformation modes, shear deformations modes, which have recently been proposed by Muresa et al. [103], are considered in this study to eliminate Vlasov's assumptions of null transverse elongation and in-plane shear distortions. The resulting GBT differential equations, due to change in the kinematic equation or equilibrium conditions of each problem, are solved using a beam-based finite element method. Throughout this dissertation, several numerical examples are presented for the purpose of validation. These examples are compared with the solution of shell-based finite element models in both displacement and stress fields.

The main contributions of this dissertation based on the above objectives are listed as follows:

- Linear static formulation of GBT for pipe bends: based on the Sanders thin shell theory [125] the thin-walled circular pipe formulation of Schardt [131] is extended for the analyses of pipe bends. This formulation shows explicitly the complex coupling effect of longitudinal bending, warping, and cross-sectional ovalization through the GBT deformation modes coupled in the element stiffness matrix. Here, the formulated curved GBT element is investigated for the membrane locking problem.
- Dynamic analysis of pipe bends: continuing on the linear static formulation of GBT for pipe bends, the GBT dynamic formulation is developed for truncated and closed toroidal shells. Here, the coupled GBT element mass matrix is derived from the variation of the kinetic energy.
- Geometrically nonlinear GBT formulation of straight circular pipes: considering the nonlinear membrane kinematic equations based on Green-Lagrange strain definition the initial linear and quadratic stress and displacement tangent stiffness matrices are formulated using third and fourth-order GBT deformation mode coupling tensors. These tensors can predetermine the type of deformation modes needed for the nonlinear analysis based on the applied loading conditions. In the numerical examples, the complex nonlinear relationship between transverse loading and the cross-sectional ovalization is demonstrated for small to moderate displacements.

- Stress field: throughout the dissertation the stress resultants for the membrane forces, the shear forces, and the bending moment are derived and used to validate the numerical examples in addition to the displacement field.

Furthermore, in this study a Python-based [168] GBT-software is developed from the ground up since the currently available GBT-software, which are VtbGui (http://www.ib-haakh.de/vtb) and GBTUL [20], are exclusively created for prismatic sections. The numerical examples presented in this dissertation are computed using this software developed in Python.

1.4 Structure of the dissertation

The dissertation is structured in the following five chapters:

In Chapter 2, the recent studies and advancements of GBT are reviewed and the complete state-of-the-art linear GBT formulation for thin-walled circular pipe section is presented, which is the basis of all subsequent formulations in the next chapters. Here, the computational efficiency of GBT is shown in comparison to shell-based FEM.

Chapter 3 presents the linear GBT formulation for thin-walled pipes with circular axis. The formulation shows the variational formulations of internal and external energies, change in GBT deformation modes due to the effect of the toroidal to cross-sectional radius ratio, deformation modes couplings and the implementation of FEM. In this chapter, for the purpose of validation and to illustrate capabilities of the developed GBT formulation, a set of numerical examples with in-plane, out-of-plane, and pressure loading conditions involving a combination and coupling of bending, warping, torsional, axisymmetric, and local deformations are presented.

In Chapter 4, extending the static linear GBT formulations presented in Chapter 3 the dynamic analysis is developed for curved thin-walled pipes. Here, the variation of the kinetic energy is presented to determine the consistent element mass matrix of a curved GBT element which involves the coupling of certain types of GBT deformation modes resembling that of the element stiffness matrix in Chapter 3. Furthermore, numerical examples concerning the undamped free vibration analysis of truncated and closed toroidal shells with different support conditions are provided.

Chapter 5 develops the geometrically nonlinear formulation of GBT based on a linear incremental iterative procedure to approximate the nonlinear response of the thin-walled circular pipe members. Considering the nonlinear membrane kinematic relations the initial linear and quadratic stress and displacement tangent stiffness matrices are derived. At the end, two numerical examples are provided to analyze the nonlinear relationship between transversal loading and the cross-sectional ovalization for small to moderated displacements.

Finally, Chapter 6 summarizes the dissertation, discusses the limitations of the developed formulations, and provides an outlook for further studies.

Chapter 2

Fundamentals of Generalized Beam Theory

This chapter discusses the basic principles of GBT concerning the analysis of thin-walled circular pipe sections, which will be referred to in the next chapters. At first, a state-of-the-art review is given addressing the recent formulations and applications of GBT in prismatic and circular thin-walled sections separately.

Next, the chapter presents a comprehensive first-order GBT formulation of circular hollow sections (CHS) by improving the classical GBT formulation of Schardt [131] through the consideration of additional torsional, axis-symmetric [143], transverse and in-plane shear deformation modes [103]. This formulation starts from the general assumptions of GBT, followed by the derivation of the weak form of the differential equilibrium equations based on the principle of virtual work, which is then solved by means of the finite element method.

At the end, the formulated GBT element is verified and its computational efficiency is demonstrated by comparing the results of a numerical example with a refined shell finite element model. Furthermore, the GBT element is tested for a shear locking problem.

2.1 State of the art

Continuing on section 1.2, GBT studies in the past two decades are reviewed in this section.

One of the limitations of classical GBT is the null assumptions of transversal extension and in-plane shear strain energies of the membrane behavior. Although certain thin-walled beam problems can be addressed even with this limitation, a wide range of problems involving nonlinearities, short columns, and longitudinally curved members cannot be analyzed correctly without lifting this limitation. The need for additional deformation modes to amend the limitations related to null in-plane shear strain assumption was first proposed by Silvestre and Camotim [146, 148] by introducing shear deformation modes in addition to the conventional classical GBT deformation modes which were originally proposed by Schardt [131, 145].

This first attempt to incorporate shear deformation effects for a buckling analysis of composite lipped channel columns was later extended by Silva and Silvestre [141, 142, 150] to arbitrary branched cross-sections and composite thin-walled members. Here, the incorporation of shear deformation modes was done by defining additional Degrees of Freedom (DoF) associated with membrane shear arising solely from the axial displacements $u(x, \theta)$. Therefore, these additional DoF do not have cross-sectional in-plane displacements (${}^{j}v(\theta) = {}^{j}w(\theta) = 0$). In equation (2.1), the axial or longitudinal displacement is defined by the sum of the orthogonal classical GBT deformation modes ${}^{k}u(\theta)$ and shear deformation modes ${}^{j}u(\theta)$ with their corresponding amplitude functions ${}^{k}V(x)$ and ${}^{j}\tilde{V}(x)$.

$$u(x,\theta) = \underbrace{{}^{k}u(\theta)\ {}^{k}V_{,x}(x)}_{\text{classical GBT}} + \underbrace{{}^{j}u(\theta)\ {}^{j}\tilde{V}(x)}_{\text{shear component}} \tag{2.1}$$

Later, introducing the variability of the warping displacement along the wall thickness besides' that along the wall midline, de Miranda et al. [41] proposed a formulation based on new kinematics which preserves the general format of the original GBT for flexural modes recovering the classical shear strain components of the Timoshenko beam theory.

The introduction of transverse extension modes in addition to classical GBT modes (conventional modes) and shear modes to relax the limitations related to null transversal extension was proposed by Gonçalves et al. [55, 61, 64] considering members which are a combination of closed cells with open branches and complex multi-cell cross-sections undergoing torsion and distortion. These modes involve only in-plane displacements (i.e., $u(\theta) = 0$) and account for the cross-section deformation due to the wall membrane transverse extensions. Besides, they are also involved in membrane shear deformation. In general, transverse extension and shear deformation modes are commonly referred to as non-conventional modes.

Recently, the introduction of non-conventional modes was proposed in thin-walled circular cross-sections by Muresan et al. [103] to analyze the buckling of isotropic conical shells. The study presents the significance of considering both transverse and shear modes and explicitly shows their coupling with conventional modes and with each other. The non-conventional modes proposed in this publication are vital to the formulations presented in this dissertation. The only drawback of these non-conventional modes is the reduction of the computational efficiency of GBT due to the additional DoF associated with them. In the following subsections, further GBT studies are reviewed using three categories, i.e. studies concerning prismatic sections, circular pipe sections, and solution methods in GBT.

2.1.1 Prismatic sections

In the past two decades, most of the conducted studies published in GBT are focused on prismatic sections. The key step in a GBT analysis of prismatic thin-walled beams is the cross-section analysis. In this step, the GBT cross-sectional deformation modes and their corresponding modal mechanical properties are determined by means of specific discretization and orthogonalization procedures which are complicated and laborious processes based on the cross-section geometrical characteristics.

Schardt [131] initially proposed to formulate the cross-sectional analysis based on the GBT system of ordinary differential equations decoupled by applying a generic linear eigenvalue problem and neglecting the off-diagonal terms of the cross-sectional shear stiffness matrix. This procedure not only gives the orthogonal deformation modes but also simultaneously diagonalizes the cross-sectional stiffness matrices. Later, this initial attempt was elaborated by using a complex quadratic eigenvalue solution [9, 77], including non-conventional modes [64], considering an arbitrary flat-walled cross-section shape [24], using a dynamic approach which is formulated based on the planar and warping eigenvalue problem [115, 117, 160] and considering thin-walled cross-sections with circular rounded corners [46].

In the context of stability analysis [177], Schardt [132] formulated the basic equations of second-order GBT based on coupled differential equations. This paper presented the linear stability analysis of open sections subjected to longitudinally uniform normal stress distributions by introducing the concept of a third-order coupling tensor to define the interaction or coupling of the GBT deformation modes. Based on this concept, Simão [151, 152] later developed the nonlinear GBT analysis using a unified energy formulation focusing on buckling analysis of both open and closed thin-walled prismatic cross-sections and considering all modal interaction phenomena between local plate behavior, distortional behavior, and the more classical global responses.

The studies presented by Bebiano [25, 26] improved the existing studies which were restricted to members subjected to longitudinally uniform normal stress distributions by developing a GBT formulation to analyze the buckling behavior of thin-walled members under longitudinally varying stress distributions. Other important contributions which should be mentioned in this context are the development of buckling analysis of thin-walled steel members and frames under arbitrary loading [11, 12], with variable support condition in the cross-section [13, 36] and with variable cross-sections [106], the application of GBT in isotropic thin-walled members with arbitrarily branched open cross-sections[42, 43], and very recently Manta [95, 96] developed a coupled shell-GBT formulation based on Lagrange multipliers for buckling analysis. In the last decade, the contribution of these studies, which is mostly based on linear buckling analysis, led to the post-buckling analysis [14, 153] and the geometrically nonlinear analysis of prismatic thin-walled sections with large displacement and rotations. Literature reviews related to studies of geometrically nonlinear analysis are provided in Chapter 5.

In the context of physical nonlinearity, Gonçalves [56] is the first to address material nonlinearity in GBT to investigate the buckling behavior of aluminum and stainless steel thin-walled columns. In this paper, the plastic bifurcation of simply supported C-section and rectangular hollow section columns is analyzed using stress-strain laws of Ramberg-Osgood [116] under a uniform compression load which is then extended to include general loading conditions in [57]. The implementation of physical nonlinearity in GBT analysis is further developed by including non-conventional modes [1] and geometrically nonlinear effects [58], using a formulation based on B-Splines curves [48] and considering full material and geometrical nonlinear analysis for large displacement regime in [2, 3, 74]. Generally, in these studies, it can be observed that GBT is not very efficient in the analysis of physical nonlinearity since it requires

quite a large number of deformation modes to describe certain types of nonlinear material models. An additional literature review valid up to 2018 can be found on the PhD thesis of Ferrarotti [52].

2.1.2 Circular pipe sections

In comparison to prismatic members, the development of GBT for circular cross-sections has been given very little attention since Richard Schardt and Christof Schardt [127, 131] first formulated the first-order analysis of circular cylindrical sections in the 1980s. In fact, the publications discussed in this section are the only ones which have been produced in the past two decades. This resulted in a lack of GBT formulations related to pipe bends, fully geometrical and physical nonlinearities, explicit dynamic analysis, and nonlinear shell-GBT coupling which are already developed for prismatic cross-sections.

Unlike prismatic thin-walled members which require a tedious cross-sectional analysis step, in thin-walled circular pipes, this step is greatly simplified by using a Fourier-Series for the decomposition of the cross-sectional deformation. In the original Schardt [131] formulation, which is referred to as classical GBT in this dissertation, the transverse and in-plane shear membrane energies are neglected. Hence, this formulation is only suitable for relatively longer circular pipe members where the longitudinal membrane energy is dominant.

Following, the studies which have contributed to the development of this initial formulation are discussed:

- Silvestre [143]: was the first to investigate the buckling behavior of a simply supported CHS using GBT. In this study, he introduced the axisymmetric and the torsion deformation modes which are responsible for uniform transverse elongation and torsion, respectively. Later, he developed a GBT formulation to analyze the elastic buckling behavior of elliptical cylindrical shells and tubes under compression [144]. Here, the main contribution was the determination of deformation modes that account for the specific aspects related to elliptical cross-section geometry.

- Basaglia et al. [15]: developed the concepts and procedures involved in performing GBT buckling and vibration analyses of CHS which included the derivation of the mass tensors that account for the influence of the inertia forces. Additionally, they addressed in detail the constraint conditions required to simulate the displacement compatibility along the end section walls of the CHS members connected at a frame joint. In their more recent publication [16], they illustrated the application of a GBT formulation to analyze the buckling behavior of circular cylindrical steel shells subjected to combinations of axial compression and external pressure. In this study, shear deformation modes are considered and cubic polynomial functions are used for the FEM implementation. But since the study did not fully recover the null transverse elongation assumptions of classical GBT the Poisson's effects are neglected following the same approach as Schardt and Silvestre.

- Nedelcu [107]: developed the GBT formulation to analyze the elastic buckling behavior of isotropic conical shells with constant thickness under axial compression. Later, this was extended by Muresan et al.[103] who analyzed the buckling behavior of structural members with variable cross-sections under

various loading and boundary conditions. In this study, the non-conventional cross-section deformation modes are considered for the first time in the analysis of circular cross-sections.

- Bianco et al. [32]: here at Bauhaus-Universität Weimar, ISM, formulated the exact GBT stiffness matrices based on hyperbolic-trigonometric shape functions. In this study, the number of longitudinal discretizations required was reduced to just one element and the generalized internal shear was obtained without the typical discontinuity of Hermitian shape functions due to the higher-order continuous derivatives properties of hyperbolic-trigonometric shape functions. Later, in [30] he developed for the first time a coupled shell-GBT model for the analysis of warping and distortional transmissions based on the multi-freedom constraint techniques specifically using the Master-Slave method. More recently, he studied the coupling of the GBT's modes in linear analysis for semi-continued arbitrary support conditions in pipelines [29].

2.1.3 Numerical solution methods in GBT

Initially, Schardt [131, 136] used a finite difference method of analysis, which has a clear structure and can be directly applied on the strong form, to solve the underlying ordinary differential equations of GBT. Using the same method, Leach [87, 88] solved this equation for the first and second-order behavior of cold-formed members and compared the results using experimental tests. However, in the studies conducted in the past two decades, the solution method used to solve GBT's fundamental differential equation is substituted by the finite element method due to its versatility and increasing popularity among engineers.

The first attempt to formulate an exact finite element solution of GBT was carried out by Davies [38] using hyperbolic-trigonometric shape functions, which were originally studied by Schardt [131] to find the closed-form solution to the homogeneous part of GBT's differential equation. Here, the major drawback of this formulation is, since it is based on the homogeneous solution, it is not possible to consider any type of load function.

The most significant work in the formulation of the FEM solution in GBT was done by Silvestre [146, 147]. He developed a finite element based on Hermitian shape functions which have been used extensively in many GBT studies. Later, Gonçalves [60] proposed a cross-section node-based DoF approach for prismatic members to improve the computational efficiency of GBT finite elements, which generally decreases in the nonlinear analysis due to a large number of deformation modes required and the coupling between them resulting in a larger and denser stiffness matrix.

In the studies presented by Duan [47–49], cubic B-spline basis functions were employed to approximate the GBT amplitude functions which satisfy the higher-order continuity conditions. Whereas, Bebiano [22, 23] proposed an exact finite element solution in GBT based on the power series method which has the additional steps of determining the power series coefficients by means of a systematic recursive procedure.

More recently, Bianco [32] developed an exact finite element formulation using hyperbolic-trigonometric shape functions similar to that of Davies [38] but based on the inhomogeneous solution of GBT ordinary differential equations. In this approach, the shape functions are built based on the predefined stiffness values of GBT deformation modes. This leads to two restrictions: first, the hyperbolic and trigonometric amplification terms of the shape functions tend to infinity for higher GBT deformation modes depending on the geometry of the element, and second, in the nonlinear analysis the shape function expression is getting longer due to the third and fourth-order deformation modes coupling. However, the second limitation is claimed to be solved in the PhD thesis of Bianco [27] using the advantage of the mathematical properties of the shape functions in which the multiplication among the shape functions due to mode coupling is expressed by a simpler linear combination of the shape functions.

In this dissertation, the numerical solution of GBT is formulated based on the finite element method using the Hermitian shape functions which satisfy the convergence criteria and allow the easy implementation of the stiffness matrices.

2.2 Linear formulation of GBT

In this section, the complete linear (or first-order) GBT formulation of thin-walled circular pipe is presented considering the additional shear deformation modes, which are recently proposed in [103], to overcome null transverse extension and in-plane shear membrane strain assumptions of classical GBT formulations [131]. In this formulation, a CHS is considered with the local coordinate system ($x \in [-L/2, L/2]$, $\theta \in [0, 2\pi]$, $z \in [-t/2, t/2]$), the global cartesian coordinate system (X, Y, Z), a wall thickness t, radius r, and length L as shown in Figure 2.1a. The displacements of an arbitrary point of coordinates (x, θ) on the middle surface of the plate are denoted by u, v, and w in the axial (or longitudinal), circumferential (or tangential), and radial directions, respectively.

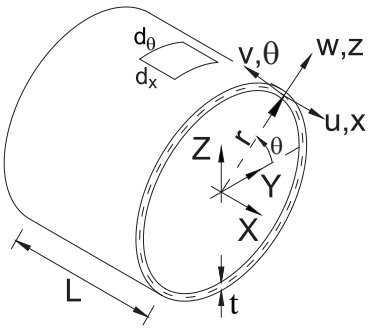

(a) Circular hallow section

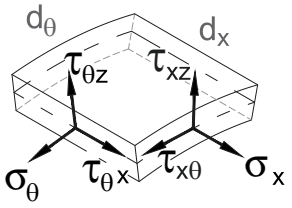

(b) Plate stresses

Figure 2.1: Geometry, displacements and stresses of a thin-walled circular pipe.

2.2.1 Assumptions in GBT

The CHS member is defined in GBT with a complete plate in bending behavior which satisfies the Love-Kirchhoff assumptions and membrane behavior which satisfies the Vlasov beam theory [169] assumptions.

The following are the general assumptions considered in this formulation:

(**A1**) The material follows Hooke's law for isotropic materials.

(**A2**) Kirchoff's plates assumptions are considered.

a. Thin plate $\frac{r}{t} > 20$.

b. The normal director remains straight and normal to the mid plane which means there is no shear deformation due to bending. The shear stress τ_{xz} and $\tau_{\theta z}$ are derived through equilibrium conditions independent of the deformations.

c. The stress in the direction normal to the plate middle surface is negligible, $\sigma_z = 0$.

(**A3**) Love's assumptions [94] $\frac{z}{r} << 1$, which means $\tau_{x\theta} = \tau_{\theta x}$ in Figure 2.1b.

(**A4**) The thickness remains constant during deformation.

(**A5**) The cross section is considered constant along the member's longitudinal axis.

(**A6**) In the case of classical GBT, Vlasov's kinematic assumptions are considered:

a. The in-plane membrane shear strain is negligible.

b. The transverse membrane strain is negligible.

Assumption (**A6**) is later amended through the consideration of the additional shear and transverse extension deformation modes [103].

2.2.2 Separation of variables

According to Schardt [131], in GBT, the displacements (u, v, w) in the local coordinate system (x, θ, z) are expressed in equations (2.2) to (2.4) based on the principle of separation of variables [86] for a straight CHS (Figure 2.1a). It contains the superposition of orthogonal modal cross-section displacement functions for the longitudinal ${}^k u(\theta)$, tangential ${}^k v(\theta)$, and radial ${}^k w(\theta)$ directions expressed as a function of the polar coordinate θ and an amplitude function ${}^k V(x)$ for each displacement function k along the beam length. The subscript index after a comma indicates the derivative of the respective function. For example, ${}^k V_{,x}(x)$ is the first derivative of the amplitude function ${}^k V(x)$ with respect to x.

$$u(x,\theta) = \sum_{k=1}^{\infty} {}^k u(\theta)\ {}^k V_{,x}(x) \tag{2.2}$$

$$v(x,\theta) = \sum_{k=1}^{\infty} {}^k v(\theta)\ {}^k V(x) \tag{2.3}$$

$$w(x,\theta) = \sum_{k=1}^{\infty} {}^k w(\theta)\ {}^k V(x) \tag{2.4}$$

2.2.3 Kinematic equations

Originally, the strain-displacement equations used by Schardt [131] to define the deformation of a CHS are similar to that of Vlasov's shell theory [170] in which up to the linear term of Taylor's series expansion is used to approximate the quotient $1/(1+z/r)$ in equations (2.5) to (2.7). The exact normal and shear strains are expressed as a sum of membrane ε^{M} and bending strains κ [89]:

$$\varepsilon_x = \varepsilon_x^{\mathrm{M}} + z\,\kappa_x \tag{2.5}$$

$$\varepsilon_\theta = \frac{1}{1+z/r}\left(\varepsilon_\theta^{\mathrm{M}} + z\,\kappa_\theta\right) \tag{2.6}$$

$$\gamma_{x\theta} = \frac{1}{1+z/r}\left(\gamma_{x\theta}^{\mathrm{M}} + z\left(1+\frac{z}{2r}\right)\kappa_{x\theta}\right) \tag{2.7}$$

In more recent studies of Silvestre and Basaglia et al. [16, 143], the Sanders-Koiter shell theory [81, 125] is used to describe the strain-displacement relationships, which adds a correction factor based on consistent rigid body motions under the assumption (**A3)**. These strain-displacement equations which were originally expressed in tensorial form are given in equation (2.8) to (2.13) [7, 176].

The membrane strains:

$$\varepsilon_x^{\mathrm{M}} = u_{,x} \tag{2.8}$$

$$\varepsilon_\theta^{\mathrm{M}} = \frac{v_{,\theta} + w}{r} \tag{2.9}$$

$$\gamma_{x\theta}^{\mathrm{M}} = \frac{u_{,\theta}}{r} + v_{,x} \tag{2.10}$$

The curvatures:

$$\kappa_x = -w_{,xx} \tag{2.11}$$

$$\kappa_\theta = \frac{-w_{,\theta\theta} + v_{,\theta}}{r^2} \tag{2.12}$$

$$\kappa_{x\theta} = \frac{-4rw_{,\theta x} + 3rv_{,x} - u_{,\theta}}{2r^2} \tag{2.13}$$

The only difference between these strain equations and the ones used by Schardt [131] is in the twisted curvature $\kappa_{x\theta}$ which is:

$$\kappa_{x\theta} = \frac{-2rw_{,\theta x} + rv_{,x} - u_{,\theta}}{r^2} \tag{2.14}$$

In the numerical examples developed in this dissertation, this difference did not show any significant change in the results of the displacement and stress fields. The detailed formulations of the strain equations used by Schardt can be found in the PhD thesis of Bianco [27]. Furthermore, a comprehensive review and comparison of various shell theories can be found in [89].

2.2.4 Variational formulation

The strong form of the coupled partial differential equations with initial and boundary conditions based on the kinematics, equilibrium and constitutive equations are in general difficult to solve analytically. Hence, the weak form of these equations is directly formulated by means of variational methods which is the basis of the finite element method used to solve these equations numerically. The main objective of the variational formulation is to find the displacement field that minimizes a preselected functional which

in this case is the total potential energy Π based on the virtual work principle. The total potential energy of the member is defined by the variation of internal U_{int} and external U_{ext} energies. The equilibrium is defined as a state of zero total potential energy. This gives:

$$\delta\Pi = \delta U_{int} + \delta U_{ext} = 0 \tag{2.15}$$

where δ is the variational operator.

The variation of internal energy is defined as the volume integral of the products of all stress components by the respective virtual strains:

$$\delta U_{int} = \int_V \left(\sigma_x \delta\varepsilon_x + \sigma_\theta \delta\varepsilon_\theta + \tau_{x\theta}\delta\varepsilon_{x\theta}\right) \mathrm{d}V \tag{2.16}$$

For an isotropic, linearly elastic material, the constitutive relations between stresses and strains are expressed by means of the Young's modulus E, the shear modulus G and the Poisson's ratio μ:

$$\sigma_x = \frac{E}{1-\mu^2}(\varepsilon_x + \mu\varepsilon_\theta), \quad \sigma_\theta = \frac{E}{1-\mu^2}(\varepsilon_\theta + \mu\varepsilon_x), \quad \tau_{x\theta} = G\gamma_{x\theta} \tag{2.17}$$

By substituting the GBT displacement functions in equations (2.2) to (2.4), the linear strain-displacement kinematic relation in equations (2.5) to (2.7) and constitutive relation in equation (2.17) into equation (2.16), it is possible to rewrite the variation of the internal energy as:

$$\begin{aligned}
\delta U_{int} = \sum_{k=1}^{\infty}\sum_{i=1}^{\infty}\int_{\frac{-L}{2}}^{\frac{+L}{2}} \oint \Bigg(& Q\, {}^{i}u(\theta)^{k}u(\theta)^{i}V_{,xx}(x)^{k}\delta V_{,xx}(x) \\
& + \mu Q\Big(\frac{{}^{i}v_{,\theta}(\theta) + {}^{i}w(\theta)}{r}\Big)^{k}u(\theta)^{i}V(x)^{k}\delta V_{,xx}(x) + K\,{}^{i}w(\theta)^{k}w(\theta)^{i}V_{,xx}(x)^{k}\delta V_{,xx}(x) \\
& + \mu K\Big(\frac{{}^{i}w_{,\theta\theta}(\theta) - {}^{i}v_{,\theta}(\theta)}{r^2}\Big)^{k}w(\theta)^{i}V(x)^{k}\delta V_{,xx}(x) \\
& + \mu Q\,{}^{i}u(\theta)\Big(\frac{{}^{k}v_{,\theta}(\theta) + {}^{k}w(\theta)}{r}\Big)^{i}V_{,xx}(x)^{k}\delta V(x) \\
& + Q\Big(\frac{{}^{i}v_{,\theta}(\theta) + {}^{i}w(\theta)}{r}\Big)\Big(\frac{{}^{k}v_{,\theta}(\theta) + {}^{k}w(\theta)}{r}\Big)^{i}V(x)^{k}\delta V(x) \\
& + \mu K\,{}^{i}w(\theta)\Big(\frac{{}^{k}w_{,\theta\theta}(\theta) - {}^{k}v_{,\theta}(\theta)}{r^2}\Big)^{i}V_{,xx}(x)^{k}\delta V(x) \\
& + K\Big(\frac{{}^{i}w_{,\theta\theta}(\theta) - {}^{i}v_{,\theta}(\theta)}{r^2}\Big)\Big(\frac{{}^{k}w_{,\theta\theta}(\theta) - {}^{k}v_{,\theta}(\theta)}{r^2}\Big)^{i}V(x)^{k}\delta V(x) \\
& + Gt\Big(\frac{{}^{i}u_{,\theta}(\theta)}{r} + {}^{i}v(\theta)\Big)\Big(\frac{{}^{k}u_{,\theta}(\theta)}{r} + {}^{k}v(\theta)\Big)^{i}V_{,x}(x)^{k}\delta V_{,x}(x) \\
& + \frac{Gt^3}{12}\Big(\frac{4r\,{}^{i}w_{,\theta}(\theta) - 3r\,{}^{i}v(\theta) + {}^{i}u_{,\theta}(\theta)}{2r^2}\Big) \\
& \times \Big(\frac{4r\,{}^{k}w_{,\theta}(\theta) - 3r\,{}^{k}v(\theta) + {}^{k}u_{,\theta}(\theta)}{2r^2}\Big)^{i}V_{,x}(x)^{k}\delta V_{,x}(x)\Bigg)\, r\, d\theta\, dx
\end{aligned} \tag{2.18}$$

In equation (2.18), the volume integral in equation (2.16) has been transferred into a surface integral by performing an integration over the wall thickness t. Separating the cross-sectional integration, equation (2.18) can be rewritten as:

$$\delta U_{int} = \sum_{k=1}^{\infty}\sum_{i=1}^{\infty}\int_{\frac{-L}{2}}^{\frac{+L}{2}} \Big({}^{ik}C\ {}^{i}V_{,xx}(x)^{k}\delta V_{,xx}(x) + {}^{ik}B\ {}^{i}V(x)^{k}\delta V(x) + {}^{ik}D\ {}^{i}V_{,x}(x)^{k}\delta V_{,x}(x) + {}^{ik}D_{\mu}\left({}^{i}V(x)^{k}\delta V_{,xx}(x) + {}^{i}V_{,xx}(x)^{k}\delta V(x)\right)\Big)\, dx \tag{2.19}$$

with the section properties:

$${}^{ik}C = Q\oint {}^{i}u(\theta)^{k}u(\theta)\ r\, d\theta + K\oint {}^{i}w(\theta)^{k}w(\theta)\ r\, d\theta \tag{2.20}$$

$${}^{ik}B = Q\oint \left(\frac{{}^{i}v_{,\theta}(\theta) + {}^{i}w(\theta)}{r}\right)\left(\frac{{}^{k}v_{,\theta}(\theta) + {}^{k}w(\theta)}{r}\right) r\, d\theta + K\oint \left(\frac{{}^{i}w_{,\theta\theta}(\theta) - {}^{i}v_{,\theta}(\theta)}{r^2}\right)\left(\frac{{}^{k}w_{,\theta\theta}(\theta) - {}^{k}v_{,\theta}(\theta)}{r^2}\right) r\, d\theta \tag{2.21}$$

$${}^{ik}D = Gt\oint \left(\frac{{}^{i}u_{,\theta}(\theta)}{r} + {}^{i}v(\theta)\right)\left(\frac{{}^{k}u_{,\theta}(\theta)}{r} + {}^{k}v(\theta)\right) r\, d\theta + \frac{Gt^3}{12}\oint \left(\frac{4r\ {}^{i}w_{,\theta}(\theta) - 3r\ {}^{i}v(\theta) + {}^{i}u_{,\theta}(\theta)}{2r^2}\right) \times \left(\frac{4r\ {}^{k}w_{,\theta}(\theta) - 3r\ {}^{k}v(\theta) + {}^{k}u_{,\theta}(\theta)}{2r^2}\right) r\, d\theta \tag{2.22}$$

$${}^{ik}D_{\mu} = \mu Q\oint \left(\frac{{}^{i}v_{,\theta}(\theta) + {}^{i}w(\theta)}{r}\right)^{k}u(\theta)\ r\, d\theta + \mu K\oint \left(\frac{{}^{i}w_{,\theta\theta}(\theta) - {}^{i}v_{,\theta}(\theta)}{r^2}\right)^{k}w(\theta)\ r\, d\theta \tag{2.23}$$

where:

$$K = \frac{Et^3}{12(1-\mu^2)} \tag{2.24}$$

$$Q = \frac{Et}{(1-\mu^2)} \tag{2.25}$$

The coefficients ${}^{ik}C$ and ${}^{ik}B$ represent the member's longitudinal and transversal directions extensional (terms related with Q) and bending (terms related with K) stiffnesses, respectively. Whereas the coefficients ${}^{ik}D$ and ${}^{ik}D_{\mu}$ represent the member's shear stiffness and additional shear stiffness due to the Poisson effect of coupling longitudinal and transversal strains, respectively.

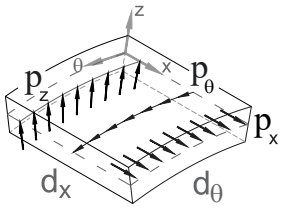

Figure 2.2: External loading.

Similarly, the variation of the external energy can be formulated by following the same principle of separation of variables [105] in the longitudinal and transversal directions as presented in [131].

A general external load $p(x,\theta)$ is applied acting at the mid-surface of a plate element as shown in Figure 2.2. The load consists of three components p_x, p_θ and p_z defined in the local coordinate system (x,θ,z). The expression of the variation of the external energy is defined as the load component times the corresponding virtual displacement as:

$$\delta U_{ext} = -\int_{\frac{-L}{2}}^{\frac{+L}{2}} \oint (p_x \delta u + p_\theta \delta v + p_z \delta w)\, r\, d\theta\, dx \tag{2.26}$$

Similar to the displacements, the external general loads functions $p_x(x,\theta)$, $p_\theta(x,\theta)$ and $p_z(x,\theta)$ are expressed as a product of two functions which define the cross-sectional $q(\theta)$ and longitudinal $f(x)$ load distribution:

$$p_x(x,\theta) = f_x(x) q_x(\theta) \tag{2.27}$$

$$p_\theta(x,\theta) = f_\theta(x) q_\theta(\theta) \tag{2.28}$$

$$p_z(x,\theta) = f_z(x) q_z(\theta) \tag{2.29}$$

Substituting equations (2.27) to (2.29) and the GBT displacement function equations (2.2) to (2.4) into equation (2.26), the δU_{ext} can be expressed as:

$$\begin{aligned}\delta U_{ext} = -\sum_{k=1}^{\infty} \int_{\frac{-L}{2}}^{\frac{+L}{2}} \oint \Big(& f_x(x) q_x(\theta)^k u(\theta)^k \delta V_{,x}(x) + f_\theta(x) q_\theta(\theta)^k v(\theta)^k \delta V(x) \\ & + f_z(x) q_z(\theta)^k w(\theta)^k \delta V(x) \Big)\, r\, d\theta\, dx\end{aligned} \tag{2.30}$$

Separating the cross-sectional integration and integrating by part, equation (2.30) can be rewritten as:

$$\delta U_{ext} = -\sum_{k=1}^{\infty} \Big[\int_{\frac{-L}{2}}^{\frac{+L}{2}} \Big(f_{x,x}(x)^k q_x + f_\theta(x)^k q_\theta + f_z(x)^k q_z \Big)^k \delta V(x)\, dx + f_x(x)^k \delta V(x) \Big] \tag{2.31}$$

Hence, the modal load decompositions ${}^k q_x$, ${}^k q_\theta$ and ${}^k q_z$ are achieved by the inner product of the deformation modes (Table 2.1), and the functions $q_x(\theta)$, $q_\theta(\theta)$ and $q_z(\theta)$ of the external load:

$${}^k q_x = -\oint q_x(\theta)^k u(\theta) r\, d\theta \tag{2.32}$$

$${}^k q_\theta = \oint q_\theta(\theta)^k v(\theta) r\, d\theta \tag{2.33}$$

$${}^k q_z = \oint q_z(\theta)^k w(\theta) r\, d\theta \tag{2.34}$$

2.2.5 Deformation modes

The shell-type deformation modes for a CHS are formulated by following the same procedure as described by Schardt [131]. The relationship between the longitudinal $u(\theta)$, tangential $v(\theta)$ and radial $w(\theta)$ displacement functions are derived from Vlasov's beam theory assumptions (**A6)** of (i) null membrane transverse strain $\varepsilon_\theta^{\mathrm{M}} = 0$ in equation (2.9) and (ii) null membrane in plane shear strain $\gamma_{x\theta}^{\mathrm{M}} = 0$ in equation (2.10). Which gives:

$$v(\theta) = -\frac{u_{,\theta}(\theta)}{r} \tag{2.35}$$

$$w(\theta) = -v_{,\theta}(\theta) = \frac{u_{,\theta\theta}(\theta)}{r} \tag{2.36}$$

Substituting equations (2.35) and (2.36) into equations (2.20) to (2.23) and imposing the orthogonality conditions on the deformation function ${}^{k}u(\theta)$ and its derivation until the fourth order leads to:

$$\oint {}^{i}u(\theta)\,{}^{k}u(\theta)\,d\theta = 0 \quad \text{for } i \neq k \tag{2.37}$$

$$\oint \left({}^{i}u_{,\theta\theta\theta\theta}(\theta) - {}^{i}u_{,\theta\theta}(\theta)\right)\left({}^{k}u_{,\theta\theta\theta\theta}(\theta) - {}^{k}u_{,\theta\theta}(\theta)\right) d\theta = 0 \quad \text{for } i \neq k \tag{2.38}$$

For thin-walled circular cross-sections, the solutions of equations (2.37) and (2.38) leads to two independent sets of trigonometric functions: $\sin(m\theta)$ and $\cos(m\theta)$, where m is a natural number. Hence, these deformation modes can be interpreted as the components of a Fourier-Series which approximate the total displacement field. Due to assumption (**A6)**, none of these deformation modes have a constant shear flow in the membrane component.

Table 2.1: Summary of orthogonal deformation modes of CHS according to classical GBT.

k	m	Deformation mode functions		
		${}^{k}u(\theta)$	${}^{k}v(\theta)$	${}^{k}w(\theta)$
1	0	1	0	0
2	1	$r\,\sin(\theta)$	$-\cos(\theta)$	$-\sin(\theta)$
3	1	$-r\,\cos(\theta)$	$-\sin(\theta)$	$\cos(\theta)$
4	2	$r\,\sin(2\theta)$	$-2\cos(2\theta)$	$-2^2\sin(2\theta)$
5	2	$-r\,\cos(2\theta)$	$-2\sin(2\theta)$	$2^2\cos(2\theta)$
⋮	⋮	⋮	⋮	⋮
2m	m	$r\,\sin(m\theta)$	$-m\cos(m\theta)$	$-m^2\sin(m\theta)$
2m+1	m	$-r\,\cos(m\theta)$	$-m\sin(m\theta)$	$m^2\cos(m\theta)$

Here, considering the axis-symmetric and torsion modes proposed by Silvestre [143] to include uniform torsion and transverse elongation and the non-conventional modes proposed by Muresan et al. [103] to overcome assumptions (**A6)**, the GBT shell-type deformation modes are classified and summarized as:

(i) Rigid-body (RB) modes (figures 2.3 and 2.4) which include:

a) $m = 0$ corresponding to the axial extension mode $k = 1$ $\left({}^{1}u(\theta) = 1, {}^{1}v(\theta) = 0 \text{ and } {}^{1}w(\theta) = 0\right)$

b) $m = 1$ corresponding to bending modes $k = 2$ and $k = 3$

c) Torsion (t) mode $\left({}^{t}u(\theta) = 0, {}^{t}v(\theta) = r \text{ and } {}^{t}w(\theta) = 0\right)$

(ii) Transverse extension or axis-symmetric (a) mode (Figure 2.5)
$\left({}^{a}u(\theta) = 0, {}^{a}v(\theta) = 0 \text{ and } {}^{a}w(\theta) = 1\right)$

(iii) Local shell-type (LS) modes (figure 2.6) for $m > 1$

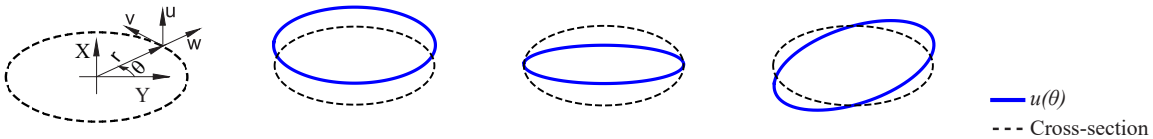

(a) Coordinate system (b) Axial mode 1 (c) Bending mode 2 (d) Bending mode 3

Figure 2.3: Rigid-body modes warping $u(\theta)$ displacement.

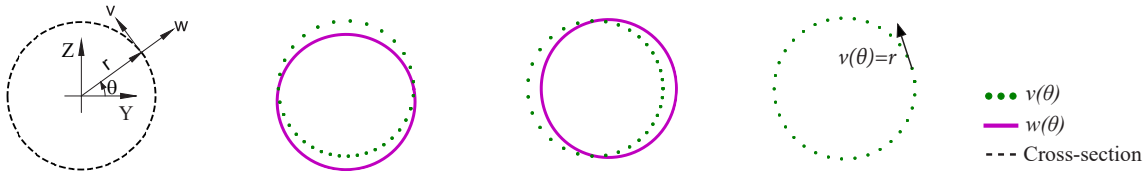

(a) Coordinate system (b) Bending mode 2 (c) Bending mode 3 (d) Torsion mode t

Figure 2.4: Rigid-body modes tangential $v(\theta)$ and radial $w(\theta)$ displacements.

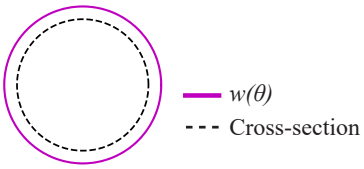

Figure 2.5: Axisymmetric mode a radial $w(\theta)$ displacement.

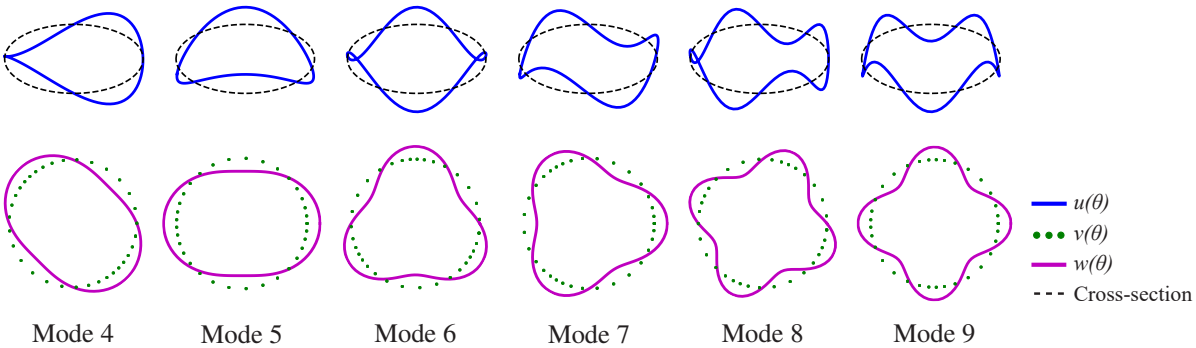

Figure 2.6: Local shell-type modes.

(iv) *Shear-u* modes (SU) are non-conventional shear deformation modes where the warping displacement ${}^{k}u(\theta)$ is identical to the one described for shell-type deformation modes (conventional mode), while the tangential and radial displacements are null, i.e., ${}^{k}v(\theta) = {}^{k}w(\theta) = 0$. To differentiate

these modes from the conventional modes k, an accent of U is added above the mode index $\overset{\text{U}}{k}$.

(v) *Shear-v* modes (SV) are non-conventional transverse extension modes where the tangential displacement ${}^{k}v(\theta)$ is identical with the one described for shell-type deformation modes (conventional mode), while warping and radial displacements are null, i.e., ${}^{k}u(\theta) = {}^{k}w(\theta) = 0$. These modes induce transverse membrane strains and a part of shear membrane strains. To differentiate these modes from the conventional modes k, an accent of V is added above the mode index $\overset{\text{V}}{k}$.

Once the deformation modes are determined, the matrices (second-order tensors) ${}^{ik}C$, ${}^{ik}B$, ${}^{ik}D$ and ${}^{ik}D_{\mu}$ describing the cross-sectional linear stiffness behaviour can be determined from equations (2.20) to (2.23). Due to the orthogonality conditions satisfied by $u(\theta)$, these cross-sectional stiffnesses related to conventional modes are greatly simplified to diagonal matrices.

Table 2.2: Summary of cross-sectional stiffness for classical GBT, axisymmetric and torsional modes.

Mode	Cross-sectional stiffness			
$i = k$	${}^{ik}C$	${}^{ik}B$	${}^{ik}D$	${}^{ik}D_{\mu}$
t	0	0	$G\pi tr(2r^2 + \frac{3}{8}t^2)$	0
a	$K2\pi r$	$Q\frac{2\pi}{r}$	0	0
1	$Q2\pi r$	0	0	0
2m 2m+1	$Q\pi r^3 + K\pi r m^4$	$K\frac{\pi m^4}{r^3}(m^2-1)^2$	$G\frac{\pi t^3 m^2}{3r}(m^2-1)^2$	$\mu K\frac{\pi m^4}{r}(1-m^2)$

However, for non-conventional modes, this is not true since they have a coupling with conventional modes and among themselves (Table 2.3). These couplings only exist for the same deformation mode index in all categories. These properties of conventional and non-conventional modes can be better understood by looking at the GBT element stiffness matrix (Equation (2.55)) derived in the next subsection.

2.2.6 Finite element formulation

In the longitudinal direction a finite element formulation is implemented with direct interpolation of the deformation mode amplitude functions [15, 32]. For the approximation of the modal amplitude, ${}^{k}V(x)$ corresponding to the axial extension mode $k = 1$, four node Lagrange cubic polynomials are used. Classic Hermite cubic polynomials are applied to the remaining conventional and non-conventional modes. The longitudinal modal amplitude function ${}^{k}V(x)$ and its variation ${}^{k}\delta V(x)$ can be defined as:

$${}^{k}V(x) = {}^{k}\{Tx\}\ {}^{k}[Sh]\ {}^{k}\{\vartheta\} \tag{2.39}$$

$${}^{k}\delta V(x) = {}^{k}\{Tx\}\ {}^{k}[Sh] \tag{2.40}$$

Table 2.3: Summary of the cross-sectional stiffness for non-conventional modes and their coupling.

Mode	Cross-sectional stiffness			
$i = k$	${}^{ik}C$	${}^{ik}B$	${}^{ik}D$	${}^{ik}D_{\mu}$
${}^{V\,V}_{i\,k}$	0	$\pi m^4 \left(\frac{Q}{r} + \frac{K}{r^3}\right)$	$G\pi t m^2 \left(r + \frac{3t^2}{16r}\right)$	0
${}^{U\,U}_{i\,k}$	$Q\pi r^3$	0	$G\pi t m^2 \left(r + \frac{t^2}{48r}\right)$	0
${}^{V\,U}_{i\,k}$	0	0	$G\pi t m^2 \left(\frac{t^2}{16r} - r\right)$	$\mu Q\pi r m^2$
${}^{U\,V}_{i\,k}$				0
${}^{V}_{i\,k}$	0	$\frac{K\pi m^4}{r^3}(1-m^2)$	$\frac{G\pi t^3 m^2}{4r}(1-m^2)$	$\mu\pi m^2 \left(Q r + \frac{Km^2}{r}\right)$
${}_{i\,k}^{V}$				0
${}^{U}_{i\,k}$	$Q\pi r^3$	0	$\frac{G\pi t^3 m^2}{12r}(1-m^2)$	0
${}_{i\,k}^{U}$				

where $\{Tx\}$ is the variable vector, $[Sh]$ is the completeness coefficient matrix of either the cubic Hermite $[Sh_H]$ or Lagrange $[Sh_L]$ shape functions, and $\{\vartheta\}$ is the vector of the beam's nodal amplitude.

$$\{Tx\} = \begin{Bmatrix} x^3 & x^2 & x & 1 \end{Bmatrix} \tag{2.41}$$

$$[Sh_H] = \begin{bmatrix} \frac{2}{L^3} & \frac{1}{L^2} & -\frac{2}{L^3} & \frac{1}{L^2} \\ 0 & -\frac{1}{2L} & 0 & \frac{1}{2L} \\ -\frac{3}{2L} & -\frac{1}{4} & \frac{3}{2L} & -\frac{1}{4} \\ \frac{1}{2} & \frac{L}{8} & \frac{1}{2} & -\frac{L}{8} \end{bmatrix} \quad \text{and} \quad [Sh_L] = \begin{bmatrix} -\frac{9}{2L^3} & \frac{27}{2\,L^3} & -\frac{27}{2\,L^3} & \frac{9}{2L^3} \\ \frac{9}{4L^2} & -\frac{9}{4L^2} & -\frac{9}{4L^2} & \frac{9}{4L^2} \\ \frac{1}{8L} & -\frac{27}{8\,L} & \frac{27}{8\,L} & -\frac{1}{8L} \\ -\frac{1}{16} & \frac{9}{16} & \frac{9}{16} & -\frac{1}{16} \end{bmatrix} \tag{2.42}$$

$$\{\vartheta_H\}^T = \left\{ \begin{array}{cccc} V(\frac{-L}{2}) & V_{,x}(\frac{-L}{2}) & V(\frac{L}{2}) & V_{,x}(\frac{L}{2}) \end{array} \right\} \text{ and}$$

$$\{\vartheta_L\}^T = \left\{ \begin{array}{cccc} V(\frac{-L}{2}) & V(\frac{-L}{6}) & V(\frac{L}{6}) & V(\frac{L}{2}) \end{array} \right\} \tag{2.43}$$

The GBT element stiffness matrix is derived by substituting equations (2.39) and (2.40) into the variation of the internal energy equation (2.19). This gives:

$$\delta U_{int} = \sum_i \sum_k \left({}^{ik}C \; {}^{ik}[\mathbb{V}_1] + {}^{ik}B \; {}^{ik}[\mathbb{V}_2] + {}^{ik}D \; {}^{ik}[\mathbb{V}_3] + {}^{ik}D_\mu \left({}^{ik}[\mathbb{V}_4] + {}^{ik}[\mathbb{V}_4]^T \right) \right) {}^{i}\{\vartheta\} \quad (2.44)$$

where:

$${}^{ik}[\mathbb{V}_1] = {}^{k}[Sh]^T \int_{\frac{-L}{2}}^{\frac{+L}{2}} {}^{k}\{Tx\}_{,xx}^T \; {}^{i}\{Tx\}_{,xx} \; dx \; {}^{i}[Sh] \quad (2.45)$$

$${}^{ik}[\mathbb{V}_2] = {}^{k}[Sh]^T \int_{\frac{-L}{2}}^{\frac{+L}{2}} {}^{k}\{Tx\}^T \; {}^{i}\{Tx\} \; dx \; {}^{i}[Sh] \quad (2.46)$$

$${}^{ik}[\mathbb{V}_3] = {}^{k}[Sh]^T \int_{\frac{-L}{2}}^{\frac{+L}{2}} {}^{k}\{Tx\}_{,x}^T \; {}^{i}\{Tx\}_{,x} \; dx \; {}^{i}[Sh] \quad (2.47)$$

$${}^{ik}[\mathbb{V}_4] = {}^{k}[Sh]^T \int_{\frac{-L}{2}}^{\frac{+L}{2}} {}^{k}\{Tx\}_{,xx}^T \; {}^{i}\{Tx\} \; dx \; {}^{i}[Sh] \quad (2.48)$$

Analytical integration of equations (2.45) to (2.48) using the Hermite shape functions (i.e. if $i \neq 1$ and $k \neq 1$) gives:

$${}^{ik}[\mathbb{V}_1] = \frac{1}{L^3} \begin{bmatrix} 12 & 6L & -12 & 6L \\ & 4L^2 & -6L & 2L^2 \\ & & 12 & -6L \\ \text{sym.} & & & 4L^2 \end{bmatrix} \text{ and } {}^{ik}[\mathbb{V}_2] = \frac{1}{420} \begin{bmatrix} 156L & 22L^2 & 54L & -13L^2 \\ & 4L^3 & 13L^2 & -3L^3 \\ & & 156L & -22L^2 \\ \text{sym.} & & & 4L^3 \end{bmatrix} \quad (2.49)$$

$${}^{ik}[\mathbb{V}_3] = \frac{1}{30L} \begin{bmatrix} 36 & 3L & -36 & 3L \\ & 4L^2 & -3L & -L^2 \\ & & 36 & -3L \\ \text{sym.} & & & 4L^2 \end{bmatrix} \text{ and } {}^{ik}[\mathbb{V}_4] = \frac{1}{30L} \begin{bmatrix} -36 & -3L & 36 & -3L \\ -33L & -4L^2 & 3L & L^2 \\ 36 & 3L & -36 & 3L \\ -3L & L^2 & 33L & -4L^2 \end{bmatrix} \quad (2.50)$$

The sub-matrix components ${}^{ik}[k]$ of the element stiffness matrix are extracted from equation (2.44) as:

$${}^{ik}[k] = {}^{ik}C \; {}^{ik}[\mathbb{V}_1] + {}^{ik}B \; {}^{ik}[\mathbb{V}_2] + {}^{ik}D \; {}^{ik}[\mathbb{V}_3] + {}^{ik}D_\mu \left({}^{ik}[\mathbb{V}_4] + {}^{ik}[\mathbb{V}_4]^T \right) \quad (2.51)$$

In case of the axial extension mode $i = k = 1$, the sub-matrix component ${}^{11}[k]$ is derived from the Lagrange shape functions and is only dependent on the longitudinal extensional stiffness as shown in Table 2.2. This gives:

$${}^{11}[k] = {}^{11}C \; {}^{11}[\mathbb{V}_1] \quad (2.52)$$

where:

$$ {}^{11}[\mathbb{V}_1] = \frac{1}{40L}\begin{bmatrix} 148 & -189 & 54 & -13 \\ & 432 & -297 & 54 \\ & & 432 & -189 \\ \text{sym.} & & & 148 \end{bmatrix} \tag{2.53} $$

In assembling the element stiffness matrix, the order of the deformation modes is chosen based on the one which results in minimum bandwidth of the stiffness matrix. That is:

$$ k \in [t,\ a,\ 1,\ 2,\ \overset{\text{V}}{2},\ \overset{\text{U}}{2},\ 3,\ \overset{\text{V}}{3},\ \overset{\text{U}}{3},\ 4,\ \overset{\text{V}}{4},\ \overset{\text{U}}{4},\ 5,\ \overset{\text{V}}{5},\ \overset{\text{U}}{5},\ \dots] \tag{2.54} $$

In equation (2.55), the element stiffness matrix $[K]^e$ which is built based on the sub-matrix in equation (2.51) and the generalized modal amplitude vector $\{d\}$ are shown.

$$ [K]^e = \begin{bmatrix} {}^{tt}[k] & 0 & 0 & 0 & 0 & 0 & 0 & 0 & \dots \\ & {}^{aa}[k] & 0 & 0 & 0 & 0 & 0 & 0 & \dots \\ & & {}^{11}[k] & 0 & 0 & 0 & 0 & 0 & \dots \\ & & & {}^{22}[k] & {}^{2\overset{\text{V}}{2}}[k] & {}^{2\overset{\text{U}}{2}}[k] & 0 & 0 & \dots \\ & & & & {}^{\overset{\text{V}}{2}\overset{\text{V}}{2}}[k] & {}^{\overset{\text{V}}{2}\overset{\text{U}}{2}}[k] & 0 & 0 & \dots \\ & & & & & {}^{\overset{\text{U}}{2}\overset{\text{U}}{2}}[k] & 0 & 0 & \dots \\ & & & & & & {}^{33}[k] & {}^{3\overset{\text{V}}{3}}[k] & \dots \\ & & & & & & & {}^{\overset{\text{V}}{3}\overset{\text{V}}{3}}[k] & \dots \\ \text{sym.} & & & & & & & & \ddots \end{bmatrix} \tag{2.55} $$

The zeros in equation (2.55) represent a 4×4 zero sub-matrix ($0 \rightarrow [0]$).

$$ \{d\}^T = \left\{ {}^{t}\{\vartheta\} \quad {}^{a}\{\vartheta\} \quad {}^{1}\{\vartheta\} \quad {}^{2}\{\vartheta\} \quad {}^{\overset{\text{V}}{2}}\{\vartheta\} \quad {}^{\overset{\text{U}}{2}}\{\vartheta\} \quad {}^{3}\{\vartheta\} \quad {}^{\overset{\text{V}}{3}}\{\vartheta\} \quad \dots \right\} \tag{2.56} $$

The GBT linear element stiffness matrix is decoupled for the same deformation mode index. Unfortunately, the additional non-conventional modes increase the size of the stiffness matrix by almost three fold in comparison to the classical GBT formulation reducing the computational efficiency.

2.2.7 Stress resultants

The stress resultants for membrane forces, shear forces, and bending moment are formulated for a curved GBT member. In the original Schardt formulation [131], the stress resultants $N_{\theta\theta}$ and $N_{\varphi\theta}$, which are forces per unit length, were derived using equilibrium conditions because of the null transverse and in-plane shear membrane strain assumptions. Taking the additional non-conventional modes into account, these stress resultants are directly derived from the membrane stresses. The complete stress resultants,

which are forces per unit length, and the stress moments, which are moments per unit length, shown in Figure 2.7 are derived as:

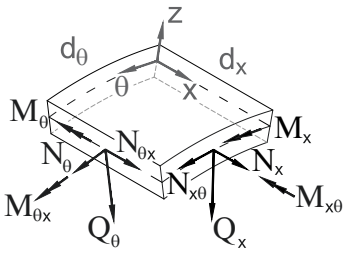

Figure 2.7: Stress resultants.

$$N_x = \int_{\frac{-t}{2}}^{\frac{+t}{2}} \sigma_x \, dz = Q \sum_{k=1}^{\infty} \left({}^k u(\theta) \; {}^k V_{,xx}(x) + \mu \frac{{}^k v_{,\theta}(\theta) + {}^k w(\theta)}{r} \; {}^k V(x) \right) \tag{2.57}$$

$$N_\theta = \int_{\frac{-t}{2}}^{\frac{+t}{2}} \sigma_\theta \, dz = Q \sum_{k=1}^{\infty} \left(\frac{{}^k v_{,\theta}(\theta) + {}^k w(\theta)}{r} \; {}^k V(x) + \mu {}^k u(\theta) \; {}^k V_{,xx}(x) \right) \tag{2.58}$$

$$N_{x\theta} = \int_{\frac{-t}{2}}^{\frac{+t}{2}} \tau_{x\theta} \, dz = Gt \sum_{k=1}^{\infty} \left(\frac{{}^k u_{,\theta}(\theta)}{r} + {}^k v(\theta) \right) {}^k V_{,x}(x) \tag{2.59}$$

$$M_x = \int_{\frac{-t}{2}}^{\frac{+t}{2}} \sigma_x \, z \, dz = K \sum_{k=1}^{\infty} \left(- {}^k w(\theta) \; {}^k V_{,xx}(x) + \mu \frac{{}^k v_{,\theta}(\theta) - {}^k w_{,\theta\theta}(\theta)}{r^2} \; {}^k V(x) \right) \tag{2.60}$$

$$M_\theta = \int_{\frac{-t}{2}}^{\frac{+t}{2}} \sigma_\theta \, z \, dz = K \sum_{k=1}^{\infty} \left(\frac{{}^k v_{,\theta}(\theta) - {}^k w_{,\theta\theta}(\theta)}{r^2} \; {}^k V(x) - \mu {}^k w(\theta) \; {}^k V_{,xx}(x) \right) \tag{2.61}$$

$$M_{x\theta} = \int_{\frac{-t}{2}}^{\frac{+t}{2}} \tau_{x\theta} z \; dz = -\frac{Gt^3}{12} \sum_{k=1}^{\infty} \left(\frac{4r {}^k w_{,\theta}(\theta) - 3r {}^k v(\theta) + {}^k u_{,\theta}(\theta)}{2r^2} \right) {}^k V_{,x}(x) \tag{2.62}$$

Due to the Love-Kirchhoff assumption, the shear stress resultants Q_x and Q_θ are obtained from equilibrium conditions and are given by:

$$Q_x = M_{x,x} + \frac{M_{x\theta,\theta}}{r} \tag{2.63}$$

$$Q_\theta = M_{x\theta,x} + \frac{M_{\theta,\theta}}{r} \tag{2.64}$$

2.3 Numerical example

In this section, a numerical example is developed in Python [168] to validate and illustrate the application and capabilities of the linear GBT formulation and its numerical implementation. Here, a short cantilever

pipe is considered as a numerical example with the physical properties and boundary conditions shown in Figure 2.8. This specific example is chosen to show the significance of the non-conventional modes since the energy related to the transverse and the in-plane shear membrane cannot be ignored.

The GBT analysis results of this example are compared with an equivalent shell finite element model using ANSYS [10] software. The shell element model has been developed using quadrilateral elements with 6 DoF per node which are based on Reissner-Mindlin's kinematic assumption with linear interpolation functions as implemented in the software ANSYS under the name SHELL 181. The element sizes used for the shell element models are approximately 40×40 mm.

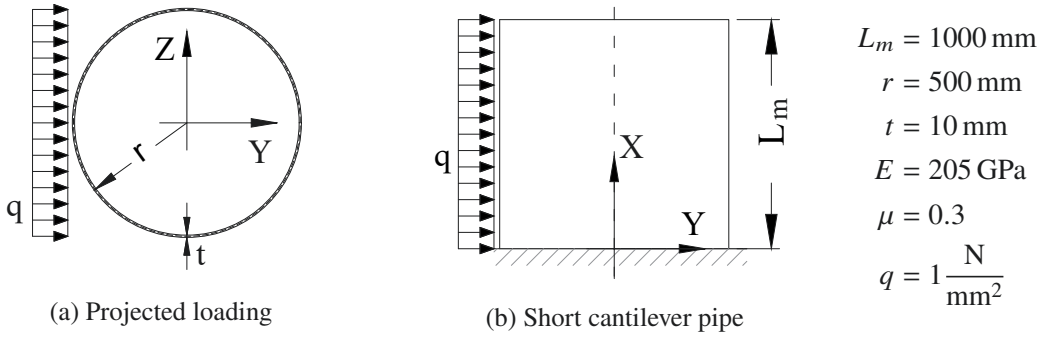

(a) Projected loading

(b) Short cantilever pipe

Figure 2.8: Projected loading on a short cantilever circular pipe.

As the first step in the GBT analysis, the projected load q has to be transformed into the local coordinates, x, θ, z, whereas the longitudinal component in the x direction is zero in this case.

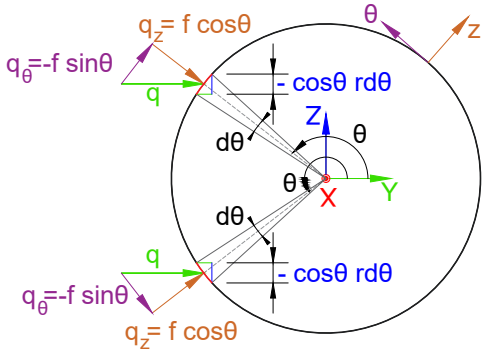

Figure 2.9: Force and projected area $\left(f = -q\cos(\theta)\right)$ in a local coordinate system.

The external load q in Figure 2.9 is expressed in the local coordinate system in $\left[\frac{\text{N}}{\text{mm}^2}\right]$:

$$q_x(\theta) = 0 \tag{2.65}$$

$$q_\theta(\theta) = q\sin(\theta)\cos(\theta) \tag{2.66}$$

$$q_z(\theta) = -q\cos(\theta)^2 \tag{2.67}$$

The external force participation in each mode is determined by integrating the modal decomposition which is the inner product of the forces in equations (2.65) to (2.67) with the respective deformation modes in Table 2.4. In this example, there is no participation from torsion, axial and even modes since the respective integrals are zero.

The selection of deformation modes to consider for the analysis depends on if the deformation mode

has an external load participation or not. All modes with no external load participation can be ignored since the stiffness matrix is decoupled for the same deformation mode index as shown in equation (2.55). However, this criteria cannot be applied in longitudinally curved pipes and in nonlinear analyses since the deformation modes in the stiffness matrices are coupled. In these cases, different approaches must be considered which are explained in Chapter 3 and 5.

Table 2.4: External load modal decomposition.

Mode k	${}^{k}q_{\theta}\left[\frac{\mathrm{N}}{\mathrm{mm}}\right]$	${}^{k}q_{z}\left[\frac{\mathrm{N}}{\mathrm{mm}}\right]$
a	0	−785.39
3	333.33	666.67
$\overset{\mathrm{V}}{3}$	333.33	0
$\overset{\mathrm{U}}{3}$	0	0
5	−785.40	−1570.79
$\overset{\mathrm{V}}{5}$	−785.40	0
$\overset{\mathrm{U}}{5}$	0	0
7	600.00	1200.00
$\overset{\mathrm{V}}{7}$	600.00	0
$\overset{\mathrm{U}}{7}$	0	0
⋮	⋮	⋮

Substituting equations (2.66) and (2.67) into equations (2.33) and (2.34) the modal decomposition of the external load can be determined in $\left[\frac{\mathrm{N}}{\mathrm{mm}}\right]$ as:

$$ {}^{k}q_{\theta} = \int_{\frac{\pi}{2}}^{\frac{3\pi}{2}} q \sin(\theta) \cos(\theta)\, {}^{k}v(\theta)\, r d\theta \tag{2.68} $$

$$ {}^{k}q_{z} = \int_{\frac{\pi}{2}}^{\frac{3\pi}{2}} -q \cos(\theta)^2\, {}^{k}w(\theta)\, r d\theta \tag{2.69} $$

The number of deformation modes need to be considered depends on the magnitude of the external load participation on the deformation mode and the cross-sectional stiffness. For example, in Table 2.4 the magnitude of the external load decreases while the transverse and shear stiffnesses shown in Table 2.2 increase by m^4 going to higher local shell-type modes $(5, 7, 11, 15, 19, 23, \dots)$ which results in a decreasing displacement contribution of higher modes.

Currently, the number of deformation modes needed for the analysis is decided by performing a convergence analysis. Unfortunately, there is no systematic or efficient way to decide this. In this example, the consideration of deformation modes up to 15 is enough to approximate the displacement field with reasonable accuracy.

The second step in the GBT analysis is to build the element stiffness matrix $[K]^e$ and force vector $\{F\}^e$ in order to calculate the generalized modal amplitude vector $\{d\}^e$. In equations (2.72) and (2.71) the element stiffness matrix and force vector is organized considering only the deformation mode with external load participation.

$$ \{d\}^T = \left\{ {}^{a}\{\vartheta\} \quad {}^{3}\{\vartheta\} \quad {}^{\mathrm{V}}_{3}\{\vartheta\} \quad {}^{\mathrm{U}}_{3}\{\vartheta\} \quad {}^{5}\{\vartheta\} \quad {}^{\mathrm{V}}_{5}\{\vartheta\} \quad {}^{\mathrm{U}}_{5}\{\vartheta\} \quad {}^{7}\{\vartheta\} \quad \dots \right\} \tag{2.70} $$

$$\{F\}^T = \left\{ \begin{array}{cccccccc} {}^{a}\{f\} & {}^{3}\{f\} & {}^{\overset{V}{3}}\{f\} & {}^{\overset{U}{3}}\{f\} & {}^{5}\{f\} & {}^{\overset{V}{5}}\{f\} & {}^{\overset{U}{5}}\{f\} & {}^{7}\{f\} \quad \dots \end{array} \right\} \tag{2.71}$$

$$[K]^e = \begin{bmatrix} {}^{aa}[k] & 0 & 0 & 0 & 0 & 0 & 0 & 0 & \dots \\ & {}^{33}[k] & {}^{\overset{V}{3}\overset{V}{3}}[k] & {}^{\overset{U}{3}\overset{U}{3}}[k] & 0 & 0 & 0 & 0 & \dots \\ & & {}^{\overset{V}{3}\overset{V}{3}}[k] & {}^{\overset{V}{3}\overset{U}{3}}[k] & 0 & 0 & 0 & 0 & \dots \\ & & & {}^{\overset{U}{3}\overset{U}{3}}[k] & 0 & 0 & 0 & 0 & \dots \\ & & & & {}^{55}[k] & {}^{\overset{V}{5}\overset{V}{5}}[k] & {}^{\overset{U}{5}\overset{U}{5}}[k] & 0 & \dots \\ & & & & & {}^{\overset{V}{5}\overset{V}{5}}[k] & {}^{\overset{V}{5}\overset{U}{5}}[k] & 0 & \dots \\ & & & & & & {}^{\overset{U}{5}\overset{U}{5}}[k] & 0 & \dots \\ & & & & & & & {}^{77}[k] & \dots \\ \text{sym.} & & & & & & & & \ddots \end{bmatrix} \tag{2.72}$$

The calculations of the sub-matrices and sub-vectors for the first three types of deformation modes are presented below based on the equations provided in subsections 2.2.5 and 2.2.6. The GBT element length is $L = 40$mm following the convergence analysis presented in Figure 2.12.

The sub-matrix ${}^{aa}[k]$ can be calculated as follows:

$${}^{aa}[k] = {}^{aa}C\ [\mathbb{V}_1] + {}^{aa}B\ [\mathbb{V}_2] \tag{2.73}$$

$${}^{aa}[k] = \frac{K\,2\pi r}{L^3} \begin{bmatrix} 12 & 6\,L & -12 & 6\,L \\ & 4\,L^2 & -6\,L & 2\,L^2 \\ & & 12 & -6\,L \\ \text{sym.} & & & 4\,L^2 \end{bmatrix} + \frac{Q\,2\pi}{420r} \begin{bmatrix} 156\,L & 22\,L^2 & 54\,L & -13\,L^2 \\ & 4\,L^3 & 13\,L^2 & -3\,L^3 \\ & & 156\,L & -22\,L^2 \\ \text{sym.} & & & 4\,L^3 \end{bmatrix} \tag{2.74}$$

$${}^{aa}[k] = 10^7 \begin{bmatrix} 1.15 & 22.35 & -1.09 & 21.98 \\ & 591.49 & -21.98 & 293.59 \\ & & 1.15 & -22.35 \\ sym. & & & 591.49 \end{bmatrix} \text{ and } {}^{a}\{f\} = \frac{{}^{a}q_z}{12} \begin{Bmatrix} 6L \\ L^2 \\ 6L \\ -L^2 \end{Bmatrix} = 10^3 \begin{Bmatrix} -15.71 \\ -104.72 \\ -15.71 \\ 104.72 \end{Bmatrix} \tag{2.75}$$

In equations (2.76) to (2.79) the sub-matrices and sub-vectors for deformation mode index 3 are presented which gives similar results as a Timoshenko's beam [163].

$$ {}^{33}[k] = 10^{11} \begin{bmatrix} 1.66 & 33.18 & -1.66 & 33.18 \\ & 884.68 & -33.18 & 442.34 \\ & & 1.66 & -33.18 \\ sym. & & & 884.68 \end{bmatrix} \simeq {}^{\mathrm{U}\,\mathrm{U}}_{33}[k] \simeq {}^{\mathrm{U}}_{33}[k] \tag{2.76} $$

$$ {}^{\mathrm{V}\,\mathrm{V}}_{33}[k] = 10^{8} \begin{bmatrix} 0.37 & 1.25 & -0.37 & 1.23 \\ & 66.15 & -1.23 & -16.58 \\ & & 0.37 & -1.25 \\ sym. & & & 66.15 \end{bmatrix} \text{ and } {}^{\mathrm{V}}_{3}\{f\} = 10^{3} \begin{Bmatrix} 6.67 \\ 44.44 \\ 6.67 \\ -44.44 \end{Bmatrix} \tag{2.77} $$

$$ {}^{\mathrm{V}}_{33}[k] = 10^{8} \begin{bmatrix} -0.32 & -1.06 & 0.32 & -1.06 \\ -11.67 & -56.62 & 1.06 & 14.15 \\ 0.32 & 1.06 & -0.32 & 1.06 \\ -1.06 & 14.15 & 11.67 & -56.62 \end{bmatrix} \text{ and } {}^{3}\{f\} = 10^{3} \begin{Bmatrix} 20.00 \\ 133.33 \\ 20.00 \\ -133.33 \end{Bmatrix} \tag{2.78} $$

$$ {}^{\mathrm{V}\,\mathrm{U}}_{33}[k] = 10^{8} \begin{bmatrix} -0.69 & -12.92 & 0.69 & -2.30 \\ -2.30 & -122.67 & 2.30 & 30.67 \\ 0.69 & 2.30 & -0.69 & 12.92 \\ -2.30 & 30.67 & 2.30 & -122.67 \end{bmatrix} \text{ and } {}^{\mathrm{U}}_{3}\{f\} = \begin{Bmatrix} 0.00 \\ 0.00 \\ 0.00 \\ 0.00 \end{Bmatrix} \tag{2.79} $$

In equations (2.80) to (2.83) the sub-matrices and sub-vectors for deformation mode index 5 are presented. This mode represents ovalization deformation which is similar to the ones used by von Kármá [171] and to the elbow element formulated by Bathe [18].

$$ {}^{55}[k] = 10^{11} \begin{bmatrix} 1.66 & 33.19 & -1.66 & 33.19 \\ & 885.12 & -33.19 & 442.56 \\ & & 1.66 & -33.19 \\ sym. & & & 885.12 \end{bmatrix} \simeq {}^{\mathrm{U}\,\mathrm{U}}_{55}[k] \simeq {}^{\mathrm{U}}_{55}[k] \tag{2.80} $$

$$ {}^{\text{V}\,\text{V}}_{5\,5}[k] = 10^8 \begin{bmatrix} 1.52 & 5.14 & -1.47 & 4.84 \\ & 265.62 & -4.84 & -67.09 \\ & & 1.52 & -5.14 \\ sym. & & & 265.62 \end{bmatrix} \text{ and } {}^{\text{V}}_{5}\{f\} = 10^3 \begin{Bmatrix} -15.71 \\ -104.72 \\ -15.71 \\ 104.72 \end{Bmatrix} \tag{2.81} $$

$$ {}^{\text{V}}_{5\,5}[k] = 10^8 \begin{bmatrix} -1.27 & -4.25 & 1.27 & -4.25 \\ -46.71 & -226.58 & 4.25 & 56.65 \\ 1.27 & 4.25 & -1.27 & 4.25 \\ -4.25 & 56.65 & 46.71 & -226.58 \end{bmatrix} \text{ and } {}^{5}\{f\} = 10^3 \begin{Bmatrix} -47.12 \\ -314.16 \\ -47.12 \\ 314.16 \end{Bmatrix} \tag{2.82} $$

$$ {}^{\text{V}\,\text{U}}_{5\,5}[k] = 10^8 \begin{bmatrix} -2.76 & -51.66 & 2.76 & -9.20 \\ -9.20 & -490.68 & 9.20 & 122.67 \\ 2.76 & 9.20 & -2.76 & 51.66 \\ -9.20 & 122.67 & 9.20 & -490.68 \end{bmatrix} \text{ and } {}^{\text{U}}_{5}\{f\} = 10^3 \begin{Bmatrix} 0.00 \\ 0.00 \\ 0.00 \\ 0.00 \end{Bmatrix} \tag{2.83} $$

Once all the sub-matrices and sub-vectors are determined, the system stiffness matrix and the force vector are assembled using the LM connectivity matrix described in [17] after having to modify it based on the GBT's requirements. Finally, the generalized modal amplitude vector $\{d\}$ in equation (2.84) is solved after applying fixed boundary conditions using pythons NumPy linear equation solver which is based on LU decomposition with partial pivoting.

$$ \{F\} = [K]\{d\} \tag{2.84} $$

The third step in the GBT analysis is to determine the local displacements u, v and w (equations (2.85) to (2.87)) by summing up the modal amplitude of the deformations modes considered in the analysis, equation (2.88), after multiplying them by their respective deformation function (Table 2.1) .

$$ u(x,\theta) = \sum_i {}^i u(\theta)\, {}^i V_{,x}(x) \tag{2.85} $$

$$ v(x,\theta) = \sum_i {}^i v(\theta)\, {}^i V(x) \tag{2.86} $$

$$ w(x,\theta) = \sum_i {}^i w(\theta)\, {}^i V(x) \tag{2.87} $$

where

$$ i \in [a, 3, \overset{\text{V}}{3}, \overset{\text{U}}{3}, 5, \overset{\text{V}}{5}, \overset{\text{U}}{5}, 7, \overset{\text{V}}{7}, \overset{\text{U}}{7}, 11, \overset{\text{V}}{11}, \overset{\text{U}}{11}, 15, \overset{\text{V}}{15}, \overset{\text{U}}{15}] \tag{2.88} $$

As a sample, in Table 2.5 the solution of the GBT at the tip of the cylinder $X = 1000\,\text{mm}$ is presented by substituting the value of the modal amplitude value $V(\frac{x}{L_m} = 1)$ (Figure 2.14) into equations (2.86) and (2.87). Here, only the transversal displacements v and w are presented since the longitudinal displacement u is small in comparison.

Table 2.5: Comparison of the GBT and shell transversal displacements results at the tip of the cantilever pipe.

	GBT[mm]		Shell[mm]		Difference[%]	
θ	v	w	v	w	v	w
0.00	0.000	0.408	0.000	0.402	0.00	1.55
0.2π	0.060	−0.869	0.061	−0.874	−1.63	−0.46
0.4π	0.605	0.098	0.599	0.100	0.95	−1.80
0.6π	−0.796	3.769	−0.802	3.763	−0.80	0.14
0.8π	−2.206	−0.684	−2.205	−0.688	0.05	−0.65
1.0π	0.000	−5.301	0.000	−5.320	0.00	−0.17
1.2π	2.206	−0.684	2.205	−0.688	0.05	−0.65
1.4π	0.796	3.769	0.802	3.763	−0.80	0.14
1.6π	−0.605	0.098	−0.599	0.100	0.95	−1.80
1.8π	−0.060	−0.869	−0.061	−0.874	−1.63	−0.46

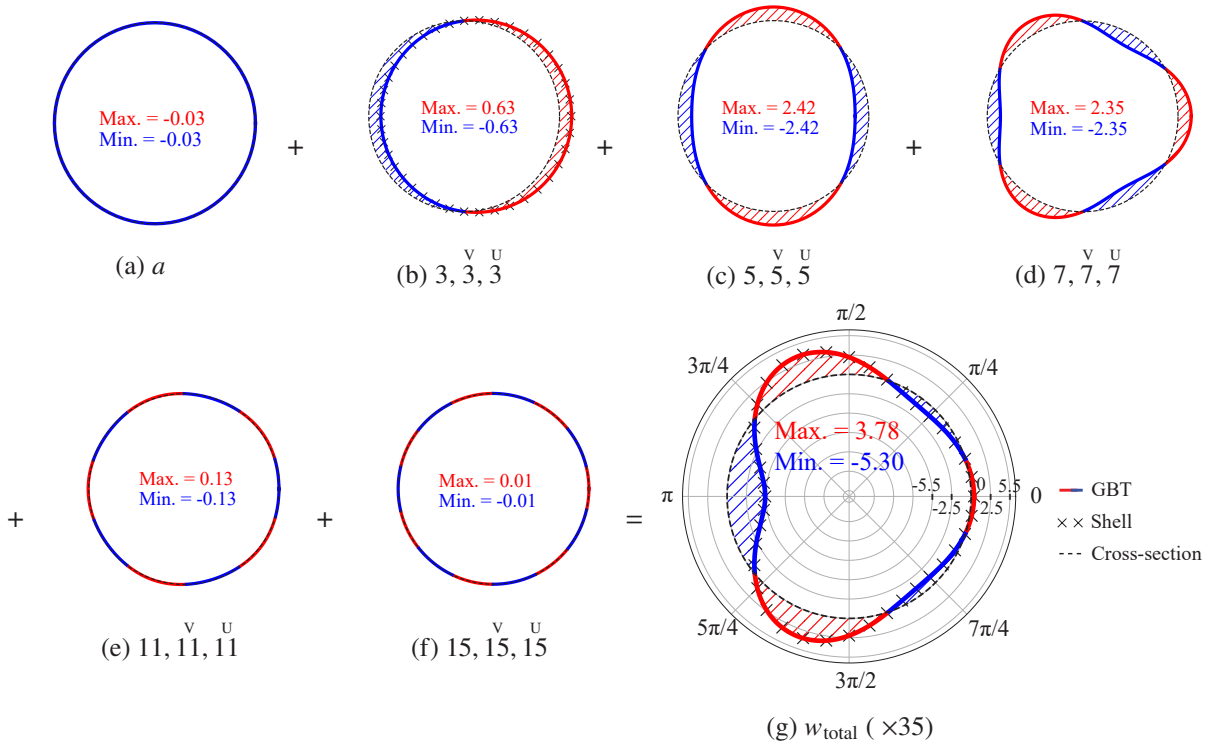

(a) a (b) $3, \overset{V}{3}, \overset{U}{3}$ (c) $5, \overset{V}{5}, \overset{U}{5}$ (d) $7, \overset{V}{7}, \overset{U}{7}$

(e) $11, \overset{V}{11}, \overset{U}{11}$ (f) $15, \overset{V}{15}, \overset{U}{15}$ (g) w_{total} ($\times 35$)

Figure 2.10: Displacement contribution of GBT deformation mode groups and comparison of final GBT solution with shell results [mm].

In Figure 2.10, the same results as in Table 2.5 are presented graphically showing the GBT modal decomposition. The coordinate system shown in Figure 2.10g applies to all cross-sectional plots in this example. The modes which contribute most to the final deformation shape of the cantilever pipe are those

of groups 5 and 7. Deformation mode groups above 15 have a contribution of displacement which is less than 10^{-2}. The comparison shown in Figure 2.10b is between the center line displacement of the shell model and the GBT model involving only bending modes $(3, \overset{V}{3}, \overset{U}{3})$.

The deformed configuration in Figure 2.11 shows a perfect agreement between the GBT and shell model.

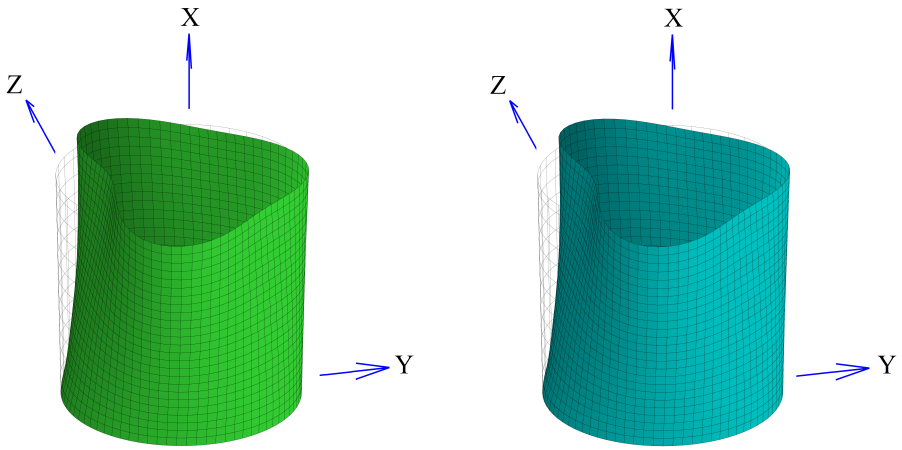

(a) GBT (b) Shell

Figure 2.11: Deformation shape of a short cantilever pipe (×40).

Table 2.6: Comparison of GBT and shell results without the cross-sectional deformation.

Type of analysis	Tip displacement in [mm]	Mean relative difference [%]
Shell (considering the center line displacement)	0.61	-
GBT, RB(3) ⇒ Euler-Bernoulli beam	0.14	77.78
GBT, RB(3) + SU + SV modes ⇒ Timoshenko beam	0.63	3.27

Table 2.7: Comparison of GBT with different modes and shell results.

Type of analysis	Tip displacement in [mm] at $\theta = \pi$	Mean relative difference [%]
Shell	5.32	-
GBT, RB(3) + LS(5,7,11) modes ⇒ Classical GBT	3.14	43.23
GBT, RB(3) + LS(5,7,11,15) + a+ SU + SV modes	5.30	0.35
GBT, RB(3) + LS(5,7,11,15,19,23)+ a + SU + SV modes	5.31	0.21

The mean relative difference (MRD) is calculated by comparing all cross-sectional nodal displacements of the shell finite element model with the GBT model.

$$\text{Mean relative difference} = \frac{1}{m}\sum_{i=1}^{m}\left|\frac{\text{GBT}_i - \text{Shell}_i}{\text{Shell}_i}\right| \times 100\% \tag{2.89}$$

where:

m is the total number of points at the cross-section. This value is governed by the number of cross-sectional nodes on the shell element model since GBT has a continuous solution at the cross-section.

Shell_i is the solution of the shell analysis at the i^{th} node.

GBT_i is the solution of the GBT analysis at the location of the i^{th} shell node.

In Tables 2.6 and 2.7, the convergence of the GBT solution while considering different combinations of deformation modes is presented. In Table 2.6, the interpretation of GBT deformation modes in terms of classical beam theories is presented and the results of GBT are compared with the center line displacement of the shell model. The comparisons in Table 2.7 show that in this example the non-conventional modes are crucial for the analysis. A classical GBT alone cannot solve this problem.

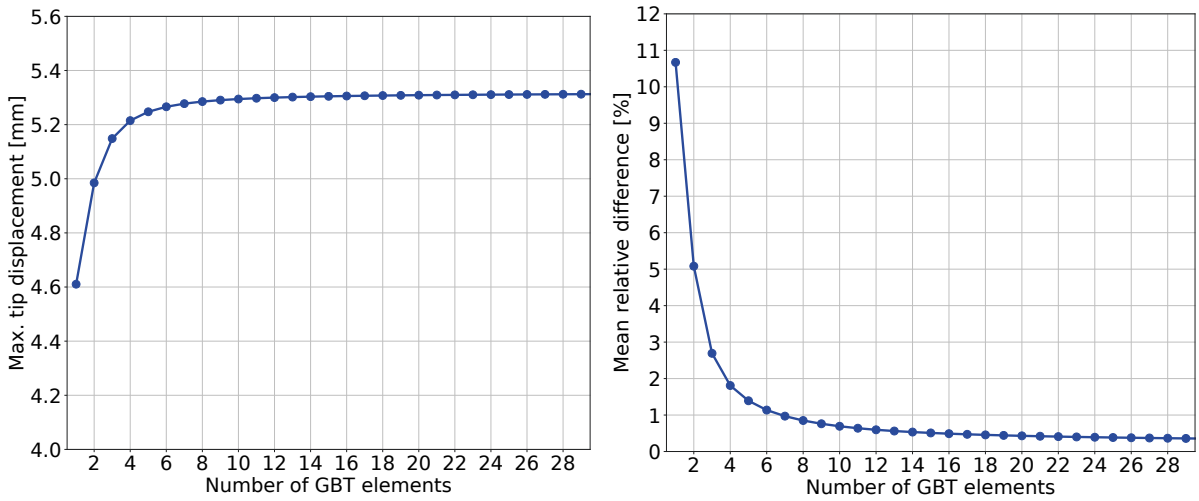

Figure 2.12: GBT solution convergence.

Figure 2.12 shows the finite element solution convergence with respect to the number of GBT elements. Longitudinally, the GBT model is discretized by 25 elements, which is enough to reach a displacement convergence of above 99.50 %. In fact in this example, with just two GBT elements the solution can be approximated with an accuracy of above 94 %.

Considering the number of modes and elements used, the total degrees of freedom (DoF) for the GBT model is 800 which is below 7.0 % of the equivalent shell element model which has 12, 000 DoF. Although the GBT has a denser stiffness matrix than the shell element model as shown in Figure 2.13, the GBT stiffness matrix would still require significantly less storage and computational steps due to its very small size.

Here, to have a fair comparison between GBT and shell computation speed the stiffness matrix of the shell element model is extracted from ANSYS and solved using the same linear equation solver and computer processor as the GBT model. Table 2.8 shows that the GBT model needs less than 1.0 % of the time needed by the shell element model.

Table 2.8: Computational speed comparison of GBT and shell.

	GBT	Shell
System stiffness matrix size	800×800	12000×12000
Computation speed: using the same linear equation solver and processor	0.0005 s	0.0660 s

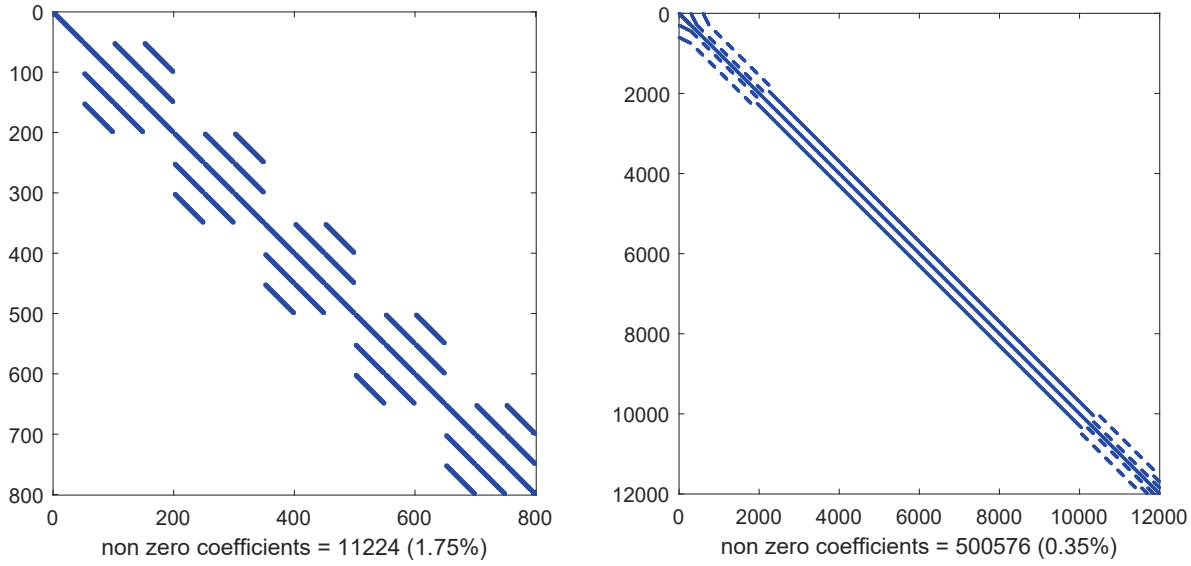

(a) GBT (b) Shell

Figure 2.13: The sparsity pattern of the system stiffness matrices.

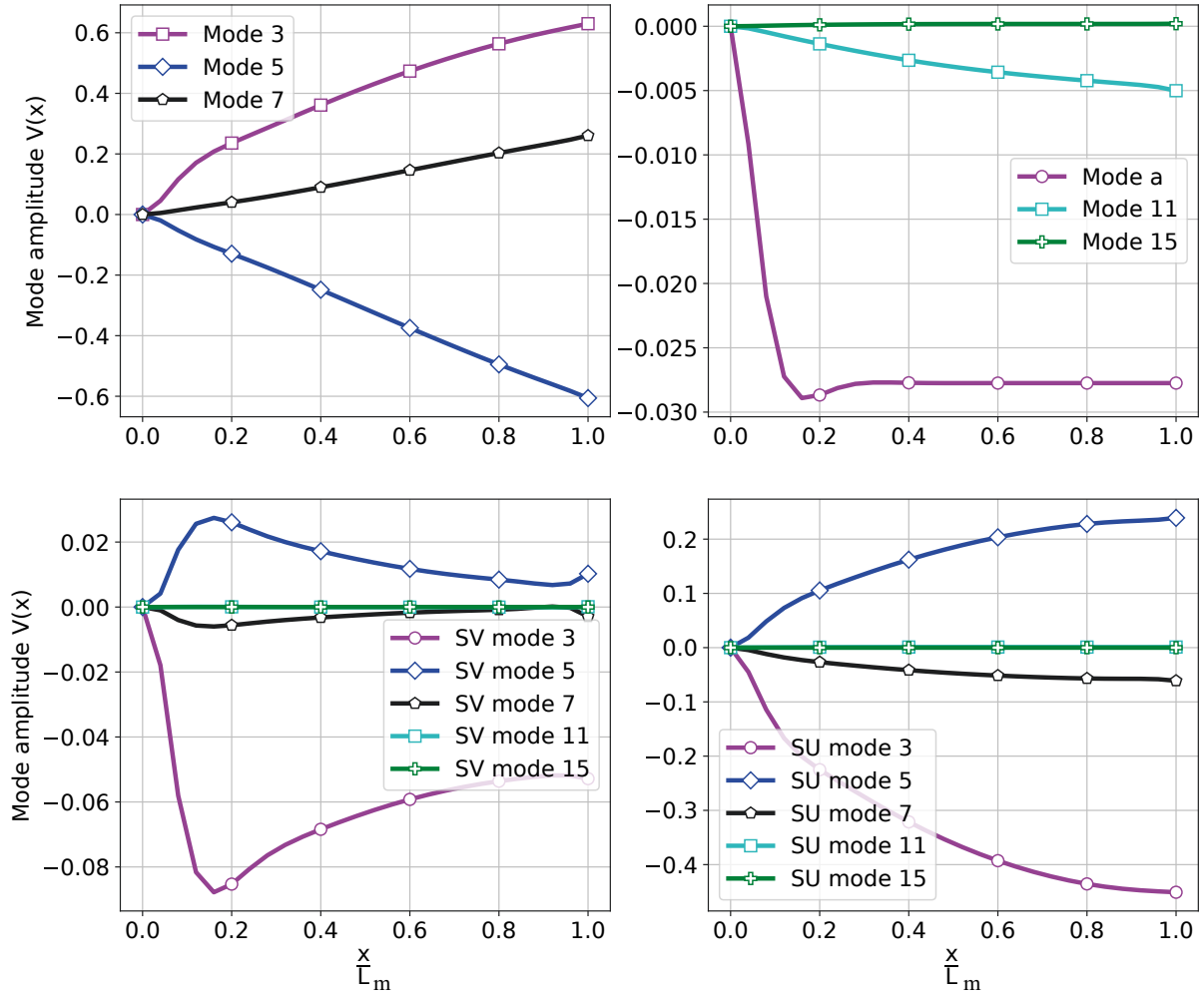

Figure 2.14: GBT mode amplitude.

In Figure 2.14, the modal decomposition of GBT is presented for the longitudinal solution $V(x)$. This important feature of GBT shows explicitly the behavior and contribution of each deformation mode along the member length. For example, for the deformation mode a, which represents a uniform radial extension, it can be clearly seen that how the local effect of bending at clamped support $\frac{x}{L_m} = 0$ fade away into the membrane behavior. This decay length [4] is about $0.2L_m$ which is directly dependent on the wall-thickness and support condition. The same effect can be observed for the SV modes which also involve pure transversal displacement. In these figures, it can be observed that deformation modes $3, 5, 7$ have the highest contribution to the total deformation. From the non-conventional modes, SU have generally larger contribution in comparison to SV modes.

The last step in the GBT analysis is to determine the stress resultants based on the equations (2.57) to (2.64). Unfortunately, this step is very often overlooked in many GBT studies by being solely dependent on the displacement field results to validate various GBT formulations. In this dissertation, the formulations presented in the next three chapters are validated not only using displacement field results but also stress field results.

In Figures 2.15 to 2.18, detailed cross-sectional comparisons of displacement and stress resultants of GBT and shell are presented at the mid span of the cantilever pipe. The radial and angular coordinates of the polar plots in these figures are similar to that of Figure 2.10g and represent the magnitude of the displacement or the stress resultant and the angle θ, respectively. The dashed line (or the undeformed cross-section) represents zero magnitude. The local displacement w is shown as w_{total} for all modes, w_{bending} for bending modes and w_{local} for all LS modes.

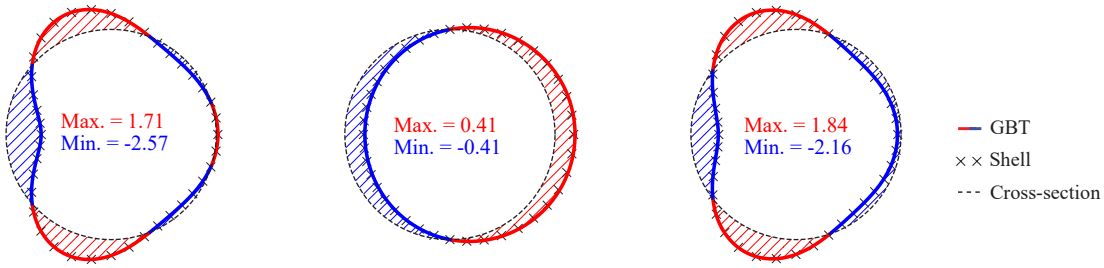

(a) w_{total} (×80) (b) w_{bending} (×260) (c) w_{local} (×80)

Figure 2.15: Comparison of displacements at the mid span [mm].

Table 2.9 summarizes the quantitative deviations between the GBT and shell model analyses at a cross-section using the mean relative difference (equation (2.89)) and the standard deviation of the relative differences. Here, the maximum differences between GBT and shell for the significant stress resultants are below 6%.

Table 2.9: Comparison of GBT and shell results.

	M_x	M_θ	$M_{x\theta}$	N_x	N_θ	$N_{x\theta}$	Q_x	Q_θ	w_{local}	w_{bending}	w_{total}
Relative mean difference (%)	5.24	4.15	1.59	4.29	0.19	2.68	9.22	4.39	0.31	1.32	0.34
Standard deviation (%)	1.85	1.39	0.35	2.25	0.11	0.06	4.00	3.13	0.65	–	0.7

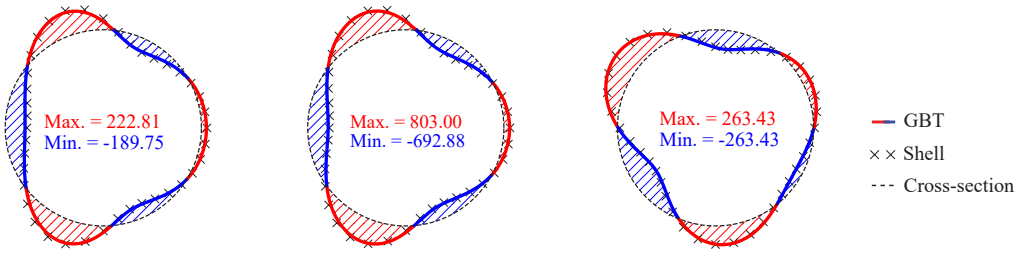

(a) M_x (b) M_θ (c) $M_{x\theta}$

Figure 2.16: Comparison of bending moment per unit length at the mid span $\left[\frac{\text{Nmm}}{\text{mm}}\right]$.

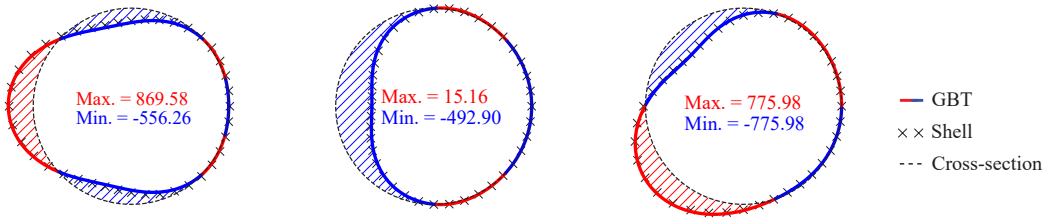

(a) N_x (b) N_θ (c) $N_{x\theta}$

Figure 2.17: Comparison of normal force per unit length at the mid span $\left[\frac{\text{N}}{\text{mm}}\right]$.

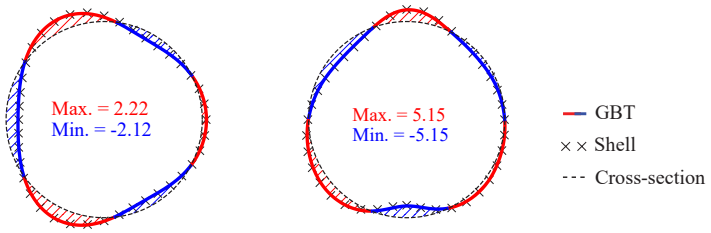

(a) Q_x (b) Q_θ

Figure 2.18: Comparison of shear force per unit length at the mid span $\left[\frac{\text{N}}{\text{mm}}\right]$.

The maximum relative difference is observed for the shear force in the longitudinal direction. This is probably be caused by the difference in plate theory assumption which is the shell model considers shear deformations through the thickness.

2.4 Locking problem

Locking is an effect that is due to the inability of a finite element formulation to represent certain deformation modes without unwanted, parasitic strains and/or stresses [34].

2.4.1 Shear locking

In this subsection, the developed GBT formulation is tested using a single element for a possible in-plane shear locking problem. In-plane shear locking is caused by incompatible shape functions which leads to artificial in-plane shear forces.

Using a simply supported thin-walled circular pipe beam under a constant moment load as shown in Figure 2.19, it is possible to study the ability of the GBT element to describe a constant curvature and shear strain.

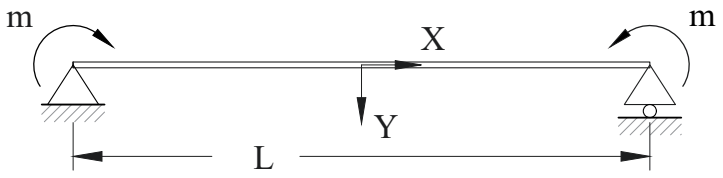

$L = 1000\,\text{mm}$
$r = 5\,\text{mm}$
$t = 0.005\,\text{mm}$
$E = 205\,\text{GPa}$
$\mu = 0.3$
$m = 1\,\text{kN mm}$

Figure 2.19: A simply supported thin-walled circular pipe under uniform bending moment.

Here, a very thin-walled pipe $\frac{r}{t} = 1000$ is considered to reduce the plate energy in bending and to focus on the membrane behavior. The moment load is applied in the GBT model using a longitudinally distributed force based on the deformation function ${}^{3}u(\theta)$, which generates pure bending in the deformation mode index group 3 and zero force in all the other deformation modes.

$$[K] = \begin{bmatrix} {}^{33}[k] & {}^{\text{V}}_{33}[k] & {}^{\text{U}}_{33}[k] \\ & {}^{\text{V V}}_{33}[k] & {}^{\text{V U}}_{33}[k] \\ sym. & & {}^{\text{U U}}_{33}[k] \end{bmatrix}, \{d\} = \begin{Bmatrix} {}^{3}\{\vartheta\} \\ {}^{\text{V}}_{3}\{\vartheta\} \\ {}^{\text{U}}_{3}\{\vartheta\} \end{Bmatrix} \text{ and } \{F\} = \begin{Bmatrix} {}^{3}\{f\} \\ {}^{\text{V}}_{3}\{f\} \\ {}^{\text{U}}_{3}\{f\} \end{Bmatrix} \tag{2.90}$$

Hence, in equation (2.90) the stiffness matrix $[K]$ and force vector $\{F\}$ used to calculate the generalized modal amplitude vector $\{d\}$ are only dependent on deformation mode 3. In equations (2.91) to (2.95) the sub-matrices and sub-vectors for deformation mode index 3 are presented.

$${}^{33}[k] = {}^{\text{U}}_{33}[k] = \begin{bmatrix} 0.01 & 2.65 & -0.01 & 2.65 \\ & 1769.30 & -2.65 & 884.65 \\ & & 0.01 & -2.65 \\ sym. & & & 1769.30 \end{bmatrix} \text{ and } {}^{3}\{f\} = \begin{Bmatrix} 0.00 \\ 1000.00 \\ 0.00 \\ -1000.00 \end{Bmatrix} \tag{2.91}$$

$$ {}^{\overset{v}{3}\overset{v}{3}}[k] = 10^5 \begin{bmatrix} 0.26 & 37.07 & 0.09 & -21.91 \\ & 6741.03 & 21.91 & -5055.36 \\ & & 0.26 & -37.07 \\ sym. & & & 6741.03 \end{bmatrix} \text{ and } {}^{\overset{v}{3}}\{f\} = \begin{Bmatrix} 0.00 \\ 0.00 \\ 0.00 \\ 0.00 \end{Bmatrix} \tag{2.92} $$

$$ {}^{\overset{u}{3}\overset{u}{3}}[k] = \begin{bmatrix} 7.44 & 621.91 & -7.44 & 621.91 \\ & 827444.31 & -621.91 & -205534.10 \\ & & 7.44 & -621.91 \\ sym. & & & 827444.31 \end{bmatrix} \text{ and } {}^{\overset{u}{3}}\{f\} = \begin{Bmatrix} 0.00 \\ 1000.00 \\ 0.00 \\ -1000.00 \end{Bmatrix} \tag{2.93} $$

$$ {}^{3\overset{v}{3}}[k] = \begin{bmatrix} -6.37 & -530.79 & 6.37 & -530.79 \\ -5838.70 & -707721.48 & 530.79 & 176930.37 \\ 6.37 & 530.79 & -6.37 & 530.79 \\ -530.79 & 176930.37 & 5838.70 & -707721.48 \end{bmatrix} \tag{2.94} $$

$$ {}^{\overset{v}{3}\overset{u}{3}}[k] = \begin{bmatrix} -13.80 & -6457.96 & 13.80 & -1150.05 \\ -1150.05 & -1533396.36 & 1150.05 & 383349.09 \\ 13.80 & 1150.05 & -13.80 & 6457.96 \\ -1150.05 & 383349.09 & 1150.05 & -1533396.36 \end{bmatrix} \tag{2.95} $$

The generalized modal amplitude vector $\{d\}$ in equation (2.84) is solved after applying the boundary conditions, which are:

a) pin-pin for the ${}^{33}[k]$ matrix which has two singularities.

b) pin-free for the ${}^{\overset{u}{3}\overset{u}{3}}[k]$ matrix which has one singularity.

c) free-free for the ${}^{\overset{v}{3}\overset{v}{3}}[k]$ matrix which has no singularities.

The results of the generalized modal amplitude vector $\{d\}$ as presented in equation (2.96) shows the rotations at the support in ${}^{3}\{\vartheta\}$ and a uniform transverse v displacement due to the Poisson effect in ${}^{\overset{v}{3}}\{\vartheta\}$

$$ \{d\} = \begin{Bmatrix} {}^{3}\{\vartheta\} \\ {}^{3}\{\vartheta\} \\ {}^{\overset{u}{3}}\{\vartheta\} \end{Bmatrix} \text{ where } {}^{3}\{\vartheta\} = \begin{Bmatrix} 0.00 \\ 1.24 \\ 0.00 \\ -1.24 \end{Bmatrix}, {}^{\overset{v}{3}}\{\vartheta\} = \begin{Bmatrix} 0.02 \\ 0.00 \\ 0.02 \\ 0.00 \end{Bmatrix} \text{ and } {}^{\overset{u}{3}}\{\vartheta\} = \begin{Bmatrix} 0.00 \\ 0.00 \\ 0.00 \\ 0.00 \end{Bmatrix} \tag{2.96} $$

In Figure 2.20, the cross-sectional w displacement and the membrane longitudinal force at the mid span are shown based on the interpolation of the nodal results. All the rest of the stress resultants are negligible in this example.

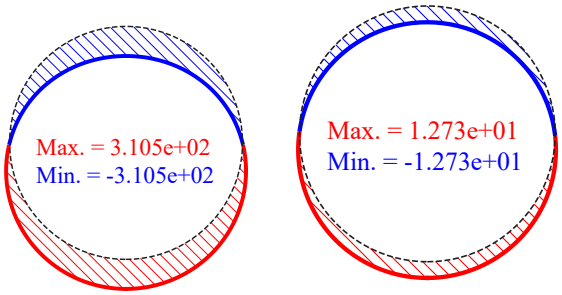

(a) w in [mm] (b) N_x in $\left[\frac{\text{N}}{\text{mm}}\right]$

Figure 2.20: Displacement and normal force at the mid span.

Table 2.10: The value of the amplitude function and its derivatives along x.

	$V(x)$			$V_{,x}(x)$			$V_{,xx}(x)$		
x	3	$\overset{\text{V}}{3}$	$\overset{\text{U}}{3}$	3	$\overset{\text{V}}{3}$	$\overset{\text{U}}{3}$	3	$\overset{\text{V}}{3}$	$\overset{\text{U}}{3}$
$\frac{-L}{2}$	0.00	0.02	0.00	1.24	0.00	0.00	-2.48×10^{-3}	0.00	0.00
0	310.55	0.02	0.00	0.00	0.00	0.00	-2.48×10^{-3}	0.00	0.00
$\frac{L}{2}$	0.00	0.02	0.00	−1.24	0.00	0.00	-2.48×10^{-3}	0.00	0.00

In order to check if the element produces a constant bending moment and zero shear force throughout the span, the cross-sectional bending moment and shear force are calculated based on the GBT modal amplitude function and its derivatives presented in Table 2.10.

The cross-sectional bending moment is determined as:

$$M_Z(x) = \int_A \sigma_x \; y \, dA = \int_A \sigma_x \; r \; \cos(\theta) \, dA = r^2 t \oint \cos(\theta)\sigma_x \, d\theta \tag{2.97}$$

Substituting the GBT displacement functions in equations (2.2) to (2.4), the constitutive relation in equation (2.17), and the amplitude function values in Table 2.10 into equation (2.97) gives:

$$\begin{aligned} M_Z(x) &= Qr^2 \oint \cos(\theta) \sum_k \left({}^k u(\theta) \; {}^k V_{,xx}(x) + \mu \frac{{}^k v_{,\theta}(\theta) + {}^k w(\theta)}{r} \; {}^k V(x) \right) d\theta \quad \text{for } k \in [3, \overset{\text{V}}{3}, \overset{\text{U}}{3}] \\ &= Qr^2 \oint \cos(\theta) \left({}^3 u(\theta) \; {}^3 V_{,xx}(x) + \mu \frac{\overset{\text{V}}{3} v_{,\theta}(\theta)}{r} \; \overset{\text{V}}{3} V(x) + \overset{\text{U}}{3} u(\theta) \; \overset{\text{U}}{3} V_{,xx}(x) \right) d\theta \\ &= 1000 \, \text{N mm} \qquad \text{for } \forall x \text{ and } x \in \left[\frac{-L}{2}, \frac{L}{2} \right] \end{aligned} \tag{2.98}$$

Following the same procedure the cross-sectional shear force can be calculated as:

$$\begin{aligned} Q_Y(x) &= \int_A \tau_{x\theta}\, dA = Gt \oint \sum_k \left(\frac{{}^k u_{,\theta}(\theta)}{r} + {}^k v(\theta) \right) {}^k V_{,x}(x)\, r\, d\theta \quad \text{for } k \in [3, \overset{\text{V}}{3}, \overset{\text{U}}{3}] \\ &= \int_A \tau_{x\theta}\, dA = Gt \oint \left(\frac{{}^{\overset{\text{U}}{3}} u_{,\theta}(\theta)}{r} {}^{\overset{\text{U}}{3}} V_{,x}(x) + {}^{\overset{\text{V}}{3}} v(\theta) {}^{\overset{\text{V}}{3}} V_{,x}(x) \right) r\, d\theta \\ &= 0 \qquad \text{for } \forall x \text{ and } x \in \left[\frac{-L}{2}, \frac{L}{2} \right] \end{aligned} \tag{2.99}$$

The results in equations (2.98) and (2.99) show that the formulated GBT element can produce a constant bending moment and zero shear force, proving that the element is shear lock free.

For further validation, the simply supported beam in Figure 2.19 is analyzed using the lock free mixed Timoshenko element stiffness matrix in equation (2.100) as presented by Bathe [17] in Chapter 4, which is based on the Hellinger-Reissner variational principle [73, 118].

$$[K]_{\text{mixed}} = \begin{bmatrix} \frac{GA_s}{L} & \frac{GA_s}{2} & \frac{-GA_s}{L} & \frac{GA_s}{2} \\ & \frac{GA_s L}{4} + \frac{EI}{L} & \frac{-GA_s}{2} & \frac{GA_s L}{4} - \frac{EI}{L} \\ & & \frac{GA_s}{L} & \frac{-GA_s}{2} \\ sym. & & & \frac{GA_s L}{4} + \frac{EI}{L} \end{bmatrix} \text{ and } \{F\} = \begin{Bmatrix} 0 \\ m \\ 0 \\ -m \end{Bmatrix} \tag{2.100}$$

$$\{d\} = \begin{Bmatrix} 0.00 \\ \frac{m\,L}{2EI} \\ 0.00 \\ \frac{-m\,L}{2EI} \end{Bmatrix} = \begin{Bmatrix} 0.00 \\ 1.24 \\ 0.00 \\ -1.24 \end{Bmatrix} \tag{2.101}$$

After applying the material, geometry and boundary conditions, the displacement fields which are obtained from equation (2.100) are the same as the results of GBT in equation (2.96).

2.4.2 Membrane locking

In this subsection, the linear GBT element is tested using an example involving a single GBT element which could show a possible membrane locking problem related to the transverse curvature of the pipe. Membrane locking is a problem which results from the inability of an element to represent inextensional bending deformations without additional parasitic membrane contributions [33, 34]. This type of locking only occurs in curved elements since the bending and membrane actions are coupled together.

Here, the critical parameter is the wall thickness of the member since the ratio of the bending stiffness

in equation (2.24) to that of membrane stiffness in equation (2.25) is proportional to the square of the thickness t. Hence, a decrease in the wall thickness or an increase in the slenderness $\frac{r}{t}$ will cause the large parts of the internal energy to be influenced by the parasitic membrane action [51, 124].

To test the formulated GBT element for a possible membrane locking problem during transverse bending, a short strip of a pipe is analyzed using a single GBT element under a projected symmetric loading as shown in Figure 2.21. Since this pipe has a free boundary condition, no axial loading, and no Poisson effect, the problem will only involve pure transverse deformation.

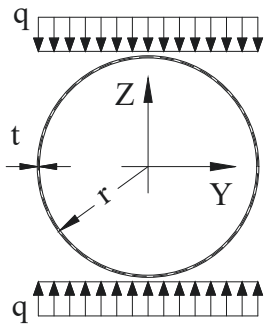

(a) Cross-section

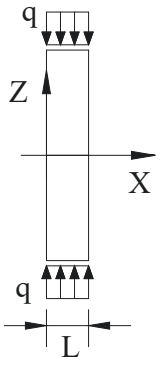

(b) Longitudinal section

$L = 100\,\text{mm}$
$r = 500\,\text{mm}$
$E = 205\,\text{GPa}$
$\mu = 0.0$
$q = 0.0002\,\frac{\text{N}}{\text{mm}^2}$
$t \rightarrow$ variable

Figure 2.21: Pipe section under projected loading.

Due to the symmetric nature of the load q, the GBT load decomposition in equations (2.68) and (2.69) will result in load contributions only in modes a, 5, and $\overset{\text{v}}{5}$. Hence, for this pipe section the stiffness matrix $[K]$, the external force vector $\{F\}$ and the generalized modal amplitude vector $\{d\}$ can be formulated as:

$$[K] = \begin{bmatrix} {}^{aa}[k] & [0] & [0] \\ & {}^{55}[k] & {}^{5\overset{\text{v}}{5}}[k] \\ sym. & & {}^{\overset{\text{v}}{5}\overset{\text{v}}{5}}[k] \end{bmatrix}, \{d\} = \begin{Bmatrix} {}^{a}\{\vartheta\} \\ {}^{5}\{\vartheta\} \\ {}^{\overset{\text{v}}{5}}\{\vartheta\} \end{Bmatrix} \text{ and } \{F\} = \begin{Bmatrix} {}^{a}\{f\} \\ {}^{5}\{f\} \\ {}^{\overset{\text{v}}{5}}\{f\} \end{Bmatrix} \tag{2.102}$$

In equations (2.104) and (2.105), the values of the stiffness matrix $[K]$, the external force vector $\{F\}$, and the generalized modal amplitude vector $\{d\}$ are calculated for $t = 1.0\,\text{mm}$. Using equation (2.4), Table 2.1 and vector $\{d\}$ in equation (2.105), the maximum cross-sectional displacement at $\theta = \frac{\pi}{2}$ (referring to the coordinate system shown in Figure 2.1) can be calculated as:

$$\begin{aligned} w(x, \tfrac{\pi}{2}) = \sum_k {}^{k}w(\tfrac{\pi}{2})\,{}^{k}V(x) &= {}^{a}w(\tfrac{\pi}{2})\,{}^{a}\{\vartheta\} + {}^{5}w(\tfrac{\pi}{2})\,{}^{5}\{\vartheta\} + {}^{\overset{\text{v}}{5}}w(\tfrac{\pi}{2})\,{}^{\overset{\text{v}}{5}}\{\vartheta\} \\ &= -1.22 \times 10^{-4} + 2^2 \cos(\pi)\,(-1.52 \times 10^{1}) = -60.8\,\text{mm} \end{aligned} \tag{2.103}$$

In Figure 2.22, the deformed configuration of the pipe is shown for $t = 1.0\,\text{mm}$. Here, the mean relative difference between the GBT and shell model is below 0.25 % in the displacement field.

$$[K] = \left[\begin{array}{cccccccccccc}
9.6\times 10^{4} & 1.4\times 10^{6} & 3.2\times 10^{4} & -7.7\times 10^{5} & 0.0 & 0.0 & 0.0 & 0.0 & 0.0 & 0.0 & 0.0 & 0.0 \\
 & 2.7\times 10^{7} & 7.7\times 10^{5} & -1.7\times 10^{7} & 0.0 & 0.0 & 0.0 & 0.0 & 0.0 & 0.0 & 0.0 & 0.0 \\
 & & 9.6\times 10^{4} & -1.4\times 10^{6} & 0.0 & 0.0 & 0.0 & 0.0 & 0.0 & 0.0 & 0.0 & 0.0 \\
 & & & 2.7\times 10^{7} & 0.0 & 0.0 & 0.0 & 0.0 & 0.0 & 0.0 & 0.0 & 0.0 \\
 & & & & 9.7\times 10^{8} & 4.8\times 10^{10} & -9.7\times 10^{8} & 4.8\times 10^{10} & -2.4\times 10^{1} & -2.0\times 10^{2} & 2.3\times 10^{1} & -1.9\times 10^{2} \\
 & & & & & 3.2\times 10^{12} & -4.8\times 10^{10} & 1.6\times 10^{12} & -2.0\times 10^{2} & -2.6\times 10^{4} & 1.9\times 10^{2} & 6.6\times 10^{3} \\
 & & & & & & 9.7\times 10^{8} & -4.8\times 10^{10} & 2.3\times 10^{1} & 1.9\times 10^{2} & -2.4\times 10^{1} & 2.0\times 10^{2} \\
 & & & & & & & 3.2\times 10^{12} & -1.9\times 10^{2} & 6.6\times 10^{3} & 2.0\times 10^{2} & -2.6\times 10^{4} \\
 & & & & & & & & 8.5\times 10^{6} & 7.5\times 10^{7} & -7.5\times 10^{6} & 5.8\times 10^{7} \\
 & & & & & & & & & 8.8\times 10^{9} & -5.8\times 10^{7} & -2.3\times 10^{9} \\
 & & & & & & & & & & 8.5\times 10^{6} & -7.5\times 10^{7} \\
sym. & & & & & & & & & & & 8.8\times 10^{9}
\end{array}\right] \tag{2.104}$$

$$\{F\} = \left\{\begin{array}{c}
-15.71 \\ -261.80 \\ -15.71 \\ 261.80 \\ -47.12 \\ -785.40 \\ -47.12 \\ 785.40 \\ -15.71 \\ -261.80 \\ -15.71 \\ 261.80
\end{array}\right\} \text{ and } \{d\} = \left\{\begin{array}{c}
-1.22\times 10^{-4} \\ 2.25\times 10^{-21} \\ -1.22\times 10^{-4} \\ 5.28\times 10^{-21} \\ -1.52\times 10^{1} \\ -2.10\times 10^{-10} \\ -1.52\times 10^{1} \\ -2.10\times 10^{-10} \\ -3.05\times 10^{-5} \\ -6.31\times 10^{-16} \\ -3.05\times 10^{-5} \\ -6.31\times 10^{-16}
\end{array}\right\} \tag{2.105}$$

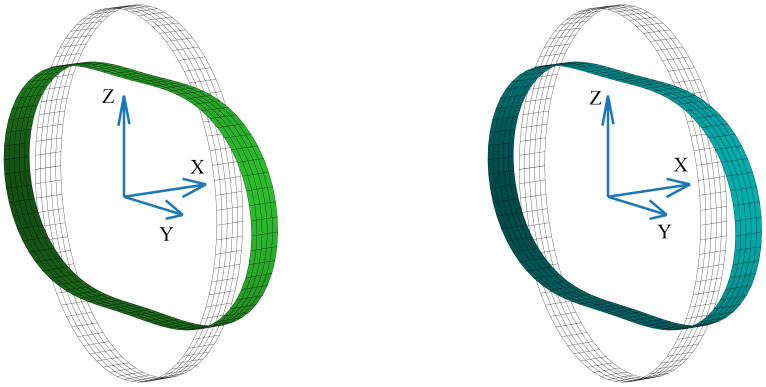

(a) GBT (b) Shell

Figure 2.22: The deformed shape of the pipe section (×3).

Table 2.11: Comparison of the maximum displacements in shell and GBT model of the pipe section for different wall thicknesses t.

	Change in thickness t [mm]			
	4	2	1	0.5
Slenderness $\frac{r}{t}$	125	250	500	1000
Shell model [mm]	0.95	7.58	60.67	485.42
GBT model [mm]	0.95	7.62	60.80	487.81
Difference [%]	0.21	0.53	0.21	0.49

In Table 2.11, the maximum displacement of the shell (4 nodes, locking-free) and GBT models are compared while changing the wall thickness t gradually. Since the displacement response of the GBT model remains accurate during the change in the wall thickness of the pipe, the formulated GBT element does not exhibit a membrane locking problem. The reason for this is because the cross-sectional deformations are approximated exactly through the GBT deformation modes. In other words, the solution calculated with the GBT element is exact in this test.

Chapter 3

Formulation of GBT for pipe bends

Pipe bends are essential to engineering structures such as pipeline systems, bridges, and industrial plants. In comparison to the stress and deformation analyses of straight pipes, the analysis of pipe bends is a complex problem due to the strong coupling effect of the longitudinal bending, warping, and cross-sectional ovalization.

In this chapter, the linear Generalized Beam Theory (GBT) is formulated for the stress and deformation analysis of curved thin-walled circular pipes. The decoupled GBT stiffness matrix formulated for the straight circular pipes in the previous chapter is not applicable for the circular pipe bends since the reformulated GBT deformation modes based on the kinematics of pipe bends will have a strong coupling effect with each other. This nature of pipe bends is explicitly presented in this chapter through the identification of the possible couplings between the considered GBT deformation modes and the formulation of the corresponding coupled curved GBT stiffness matrix.

Since the early study of von Karman [171] on the behavior of circular pipe bends numerous studies have been conducted on this topic. In his study, von Karman used flexibility and stress intensification factors to scale the stiffness constants and stress results of a simple curved beam analysis assuming constant ovalization throughout the pipe bend. This formulation was later extended by Bathe [18] considering variable ovalization along the pipe bend or elbow. Due to the limitations of beam analysis, other studies focused on shell finite element methods [156] which require a higher degree of discretization. Here, to overcome the high computational costs of the shell finite element method, alternative formulations have been proposed in [54] and [91]. A more detailed review of pipe bends mechanical behavior can be found in [80] based on previous analytical [109], numerical [110], and experimental studies.

In the context of GBT, the study of curved members was first conducted by Peres et al. [111] for arbitrary prismatic open cross-sections. Later, Peres extended this study in [112] by developing a systematic procedure to obtain the cross-section deformation modes for arbitrary flat-walled cross-sections which are open, closed, or mixed. In these studies, illustrative examples were presented involving complex local-distortional-global deformations, which have a perfect agreement with shell finite element analysis in displacement field comparison. In a more recent study [113], he addressed the problem of membrane

locking, which was observed in his previous studies, by developing a mixed finite element formation.

However, the studies conducted on curved prismatic thin-walled sections cannot be applied to circular pipe bends since the formulations used there cannot consider membrane transverse and shear coupling behavior. Therefore, the main objectives of this chapter are the following:

- to develop a linear GBT formulation for circular pipe bends considering any type of loading and boundary conditions.
- to show the effect of the toroidal to cross-sectional radius ratio α, i.e., $\alpha = \frac{r}{R}$, using the GBT deformation modes.
- to present the effect of the Poisson ratio in stress and displacement fields, which is often ignored in the studies of circular pipe sections since non-conventional modes are often not considered.
- to identify the limitations of the developed displacement-based formulation due to the membrane locking problem.

In this chapter, the step-by-step formulation of a curved GBT element is presented starting from the kinematic descriptions leading to the internal and external energy variational formulations which give the coupled stiffness coefficients and describe the modal load decomposition, respectively. Next, in Sections 3.2 to 3.4, the procedure for determining the GBT deformation modes, the finite element formulation of the stiffness matrix based on the possible mode couplings, and the derivation of the stress resultants following the fundamental principles of GBT are presented. Finally, to illustrate the application and capabilities of the developed GBT formulation, a set of numerical examples with in-plane, out-of-plane, and pressure loading conditions involving a combination and coupling of bending, warping, torsional, axisymmetric, and local deformations is presented. For the purpose of validation, these examples are compared with refined shell finite element models in both displacement and stress fields. Furthermore, the developed displacement-based GBT element is tested for membrane locking problem to identify the limitations of the formulated GBT element.

3.1 Linear GBT formulation for pipe bends

In GBT, the displacements (u, v, w) in the local coordinate system (φ, θ, z) are expressed in equations (3.1) to (3.3) based on the principle of separation of variables for a curved CHS as shown in Figure 3.1, with a bend angle ψ and radius R. It contains the superposition of orthogonal modal cross-section displacement functions for the longitudinal ${}^k u(\theta)$, tangential ${}^k v(\theta)$, and radial ${}^k w(\theta)$ directions expressed as a function of the polar coordinate θ and an amplitude function ${}^k V(\varphi)$ for each displacement function k along the beam length. The subscript index after a comma indicates the derivative of the respective function. For

example, ${}^{k}V_{,\varphi}(\varphi)$ is the first derivative of the amplitude function ${}^{k}V(\varphi)$ with respect to φ.

$$u(\varphi,\theta) = \sum_{k=1}^{\infty} {}^{k}u(\theta)\,{}^{k}V_{,\varphi}(\varphi) \tag{3.1}$$

$$v(\varphi,\theta) = \sum_{k=1}^{\infty} {}^{k}v(\theta)\,{}^{k}V(\varphi) \tag{3.2}$$

$$w(\varphi,\theta) = \sum_{k=1}^{\infty} {}^{k}w(\theta)\,{}^{k}V(\varphi) \tag{3.3}$$

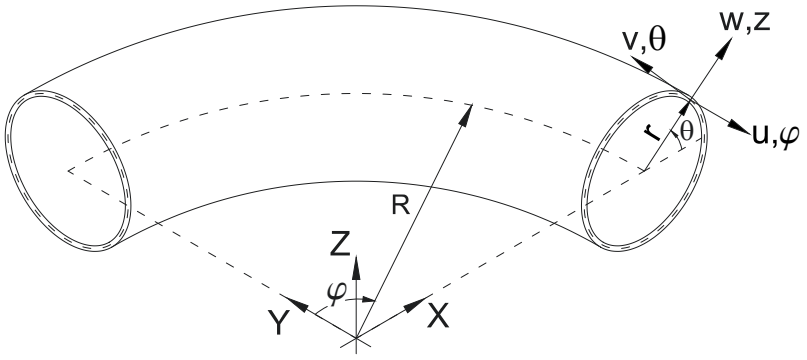

Figure 3.1: Curved thin-walled circular cross-section with global (X, Y, Z) and local ($\varphi \in [-\psi/2, \psi/2]$, $\theta \in [0, 2\pi]$, $z \in [-t/2, t/2]$) coordinate systems.

The linear kinematic relations that satisfy the Love-Kirchhoff assumption are given by equations (3.4) to (3.9) for membrane and plate in bending strains following the governing equations of the linear Sanders thin shell theory [125], expressed in a toroidal coordinate system [101, 179].

Membrane strains:

$$\varepsilon_{\varphi}^{\mathrm{M}} = \frac{1}{\xi}\left(\frac{u_{,\varphi}}{R} - \frac{v\sin(\theta)}{R} + \frac{w\cos(\theta)}{R}\right) \tag{3.4}$$

$$\varepsilon_{\theta}^{\mathrm{M}} = \frac{v_{,\theta} + w}{r} \tag{3.5}$$

$$\gamma_{\varphi\theta}^{\mathrm{M}} = \frac{u_{,\theta}}{r} + \frac{1}{\xi}\left(\frac{v_{,\varphi}}{R} + \frac{u\sin(\theta)}{R}\right) \tag{3.6}$$

and bending strains:

$$\varepsilon_{\varphi}^{\mathrm{B}} = -\,z\left(\frac{\sin(\theta)\left(v - w_{,\theta}\right)}{Rr\xi} + \frac{w_{,\varphi\varphi} - u_{,\varphi}\cos(\theta)}{(R\xi)^2}\right) \tag{3.7}$$

$$\varepsilon_{\theta}^{\mathrm{B}} = -\,z\left(\frac{w_{,\theta\theta} - v_{,\theta}}{r^2}\right) \tag{3.8}$$

$$\gamma^{\mathrm{B}}_{\varphi\theta} = -z\left(\frac{2w_{,\theta\varphi}}{Rr\xi} + \frac{2w_{,\varphi}\sin(\theta)}{(R\xi)^2} - \frac{v_{,\varphi}(1+2\xi)}{2Rr\xi^2} - \left(\frac{\cos(\theta)}{Rr\xi} - \frac{1}{2r^2\xi}\right)u_{,\theta} - \frac{2r^2\sin(2\theta) + (1-2\xi)Rr\sin(\theta)}{2(Rr\xi)^2}u\right) \tag{3.9}$$

where:

$$\xi = 1 + \alpha\,\cos(\theta) \tag{3.10}$$

$$\alpha = \frac{r}{R} \tag{3.11}$$

3.1.1 Variation of internal energy

The variation of internal energy is defined as the volume integral of the products of all stress components by the respective virtual strains:

$$\delta U_{\mathrm{int}} = \int_V (\sigma_\varphi \delta\varepsilon_\varphi + \sigma_\theta \delta\varepsilon_\theta + \tau_{\varphi\theta}\delta\gamma_{\varphi\theta})\mathrm{d}V \tag{3.12}$$

For an isotropic, linearly elastic material, the constitutive relations between stresses and strains are expressed by means of the Young's modulus E, the shear modulus G and the Poisson's ratio μ:

$$\sigma_\varphi = \frac{E}{1-\mu^2}(\varepsilon_\varphi + \mu\varepsilon_\theta), \quad \sigma_\theta = \frac{E}{1-\mu^2}(\varepsilon_\theta + \mu\varepsilon_\varphi), \quad \tau_{\varphi\theta} = G\gamma_{\varphi\theta} \tag{3.13}$$

Substituting the GBT displacement functions in equations (3.1) to (3.3), the linear strain-displacement kinematic relations in equations (3.4) to (3.9), and the constitutive relations in equation (3.13) into equation (3.12), it is possible to rewrite the variation of the internal energy as:

$$\begin{aligned}\delta U_{\mathrm{int}} = \sum_{k=1}^{\infty}\sum_{i=1}^{\infty}\int_{-\frac{\psi}{2}}^{+\frac{\psi}{2}} \Big(&{}^{ik}C_1\,{}^{i}V_{,\varphi\varphi}(\varphi)^{k}\delta V_{,\varphi\varphi}(\varphi) + {}^{ik}C_2\,{}^{i}V(\varphi)^{k}\delta V_{,\varphi\varphi}(\varphi) + {}^{ik}C_3\,{}^{i}V_{,\varphi\varphi}(\varphi)^{k}\delta V(\varphi) \\ &+ {}^{ik}C_4\,{}^{i}V(\varphi)^{k}\delta V(\varphi) + {}^{ik}B\,{}^{i}V(\varphi)^{k}\delta V(\varphi) + {}^{ik}D\,{}^{i}V_{,\varphi}(\varphi)^{k}\delta V_{,\varphi}(\varphi) + {}^{ik}D_{1\mu}{}^{i}V(\varphi)^{k}\delta V_{,\varphi\varphi}(\varphi) \\ &+ {}^{ik}D_{2\mu}{}^{i}V_{,\varphi\varphi}(\varphi)^{k}\delta V(\varphi) + {}^{ik}D_{3\mu}{}^{i}V(\varphi)^{k}\delta V(\varphi) + {}^{ik}D_{4\mu}{}^{i}V(\varphi)^{k}\delta V(\varphi)\Big)\,R\,d\varphi\end{aligned} \tag{3.14}$$

with the section properties

$${}^{ik}C_1 = Q\oint \frac{{}^{i}u(\theta)}{R\xi}\,\frac{{}^{k}u(\theta)}{R}r\,d\theta + K\oint \frac{{}^{i}u(\theta)\cos(\theta) - {}^{i}w(\theta)}{(R\xi)^2}\,\frac{{}^{k}u(\theta)\cos(\theta) - {}^{k}w(\theta)}{R^2\xi}r\,d\theta \tag{3.15}$$

$$\begin{aligned}{}^{ik}C_2 = {}&Q\oint \frac{{}^{i}w(\theta)\cos(\theta) - {}^{i}v(\theta)\sin(\theta)}{R\xi}\,\frac{{}^{k}u(\theta)}{R}r\,d\theta \\ &+ K\oint \frac{\sin(\theta)\left({}^{i}w_{,\theta}(\theta) - {}^{i}v(\theta)\right)}{Rr\xi}\,\frac{{}^{k}u(\theta)\cos(\theta) - {}^{k}w(\theta)}{R^2\xi}r\,d\theta\end{aligned} \tag{3.16}$$

$${}^{ik}C_3 = {}^{ki}C_2 \tag{3.17}$$

$$
\begin{aligned}
{}^{ik}C_4 &= Q \oint \frac{{}^{i}w(\theta)\cos(\theta) - {}^{i}v(\theta)\sin(\theta)}{R\xi} \, \frac{{}^{k}w(\theta)\cos(\theta) - {}^{k}v(\theta)\sin(\theta)}{R} r \, d\theta \\
&+ K \oint \frac{\sin(\theta)\left({}^{i}w_{,\theta}(\theta) - {}^{i}v(\theta)\right)}{Rr\xi} \, \frac{\sin(\theta)\left({}^{k}w_{,\theta}(\theta) - {}^{k}v(\theta)\right)}{Rr} r \, d\theta
\end{aligned} \tag{3.18}
$$

$$
\begin{aligned}
{}^{ik}B &= Q \oint \frac{{}^{i}v_{,\theta}(\theta) + {}^{i}w(\theta)}{r} \, \frac{{}^{k}v_{,\theta}(\theta) + {}^{k}w(\theta)}{r} \xi r \, d\theta \\
&+ K \oint \frac{{}^{i}v_{,\theta}(\theta) - {}^{i}w_{,\theta\theta}(\theta)}{r^2} \, \frac{{}^{k}v_{,\theta}(\theta) - {}^{k}w_{,\theta\theta}(\theta)}{r^2} \xi r \, d\theta
\end{aligned} \tag{3.19}
$$

$$
\begin{aligned}
{}^{ik}D &= Gt \oint \left(\frac{{}^{i}u_{,\theta}(\theta)}{r} + \frac{{}^{i}v(\theta)}{R\xi} + \frac{{}^{i}u(\theta)\sin(\theta)}{R\xi}\right)\left(\frac{{}^{k}u_{,\theta}(\theta)}{r} + \frac{{}^{k}v(\theta)}{R\xi} + \frac{{}^{k}u(\theta)\sin(\theta)}{R\xi}\right)\xi r \, d\theta \\
&+ \frac{Gt^3}{12} \oint \left(-\frac{2\,{}^{i}w_{,\theta}(\theta)}{Rr\xi} - \frac{2\,{}^{i}w(\theta)\sin(\theta)}{(R\xi)^2} + \frac{{}^{i}v(\theta)(1+2\xi)}{2Rr\xi^2} + F_1\,{}^{i}u_{,\theta}(\theta) + F_2\,{}^{i}u(\theta)\right) \\
&\times \left(-\frac{2\,{}^{k}w_{,\theta}(\theta)}{Rr\xi} - \frac{2\,{}^{k}w(\theta)\sin(\theta)}{(R\xi)^2} + \frac{{}^{k}v(\theta)(1+2\xi)}{2Rr\xi^2} + F_1\,{}^{k}u_{,\theta}(\theta) + F_2\,{}^{k}u(\theta)\right)\xi r \, d\theta
\end{aligned} \tag{3.20}
$$

$$
\begin{aligned}
{}^{ik}D_{1\mu} &= \mu Q \oint \frac{{}^{i}v_{,\theta}(\theta) + {}^{i}w(\theta)}{r} \, \frac{{}^{k}u(\theta)}{R} r \, d\theta \\
&+ \mu K \oint \frac{{}^{i}v_{,\theta}(\theta) - {}^{i}w_{,\theta\theta}(\theta)}{r^2} \, \frac{{}^{k}u(\theta)\cos(\theta) - {}^{k}w(\theta)}{R^2\xi} r \, d\theta
\end{aligned} \tag{3.21}
$$

$$
{}^{ik}D_{2\mu} = {}^{ki}D_{1\mu} \tag{3.22}
$$

$$
\begin{aligned}
{}^{ik}D_{3\mu} &= \mu Q \oint \frac{{}^{i}v_{,\theta}(\theta) + {}^{i}w(\theta)}{r} \, \frac{{}^{k}w(\theta)\cos(\theta) - {}^{k}v(\theta)\sin(\theta)}{R} r \, d\theta \\
&+ \mu K \oint \frac{{}^{i}v_{,\theta}(\theta) - {}^{i}w_{,\theta\theta}(\theta)}{r^2} \, \frac{\sin(\theta)\left({}^{k}w_{,\theta}(\theta) - {}^{k}v(\theta)\right)}{Rr} r \, d\theta
\end{aligned} \tag{3.23}
$$

$$
{}^{ik}D_{4\mu} = {}^{ki}D_{3\mu} \tag{3.24}
$$

where:

$$
F_1 = \frac{\cos(\theta)}{Rr\xi} - \frac{1}{2r^2\xi} \tag{3.25}
$$

$$
F_2 = \frac{2r^2\sin(2\theta) + (1-2\xi)Rr\sin(\theta)}{2(Rr\xi)^2} \tag{3.26}
$$

$$
K = \frac{Et^3}{12(1-\mu^2)} \tag{3.27}
$$

$$
Q = \frac{Et}{(1-\mu^2)} \tag{3.28}
$$

The coefficients ${}^{ik}C_1$, ${}^{ik}B$ and ${}^{ik}D$ represent the section's warping, transverse bending, and shear stiffnesses, respectively. The additional stiffness coefficients ${}^{ik}C_2$, ${}^{ik}C_3$ and ${}^{ik}C_4$ are the results of additional coupling between warping and transverse deformations due to the effect of the toroidal to cross-sectional radius ratio α in equation (3.11) i.e., the larger the radius ratio the higher the contribution of these stiffness coefficients. The coefficients ${}^{ik}D_{1\mu}$, ${}^{ik}D_{2\mu}$, ${}^{ik}D_{3\mu}$ and ${}^{ik}D_{4\mu}$ are an additional shear stiffness due to the Poisson effect and the radius ratio.

3.1.2 Variation of the external energy

The virtual work of external forces can be formulated by following the principle of separation of variables in the longitudinal and transverse directions. For a general external load $p(\varphi, \theta)$, applied at the mid-surface of a plate element consisting of three components p_φ, p_θ and p_z in the local coordinate system (φ, θ, z), the external virtual work can be defined as the load component times the corresponding virtual displacement as:

$$\delta U_{\text{ext}} = -\int_{\frac{-\psi}{2}}^{\frac{+\psi}{2}} \oint \left(p_\varphi \delta u + p_\theta \delta v + p_z \delta w\right) \xi R r \, d\theta \, d\varphi \tag{3.29}$$

Similar to the displacements, the external general load functions $p_\varphi(\varphi, \theta)$, $p_\theta(\varphi, \theta)$ and $p_z(\varphi, \theta)$ can be expressed as a product of two functions which defines the cross-sectional $q(\theta)$ and longitudinal $f(\varphi)$ load distribution:

$$p_\varphi(\varphi, \theta) = f_\varphi(\varphi) q_\varphi(\theta), \quad p_\theta(\varphi, \theta) = f_\theta(\varphi) q_\theta(\theta), \quad p_z(\varphi, \theta) = f_z(\varphi) q_z(\theta) \tag{3.30}$$

Substituting equation (3.30) and the GBT displacement functions in equations (3.1) to (3.3) into equation (3.29) the δU_{ext} can be expressed as:

$$\begin{aligned}\delta U_{\text{ext}} = -\sum_{k=1}^{\infty} \int_{\frac{-\psi}{2}}^{\frac{+\psi}{2}} \oint \Big(& f_\varphi(\varphi) q_\varphi(\theta)^k u(\theta)^k \delta V_{,\varphi}(\varphi) + f_\theta(\varphi) q_\theta(\theta)^k v(\theta)^k \delta V(\varphi) + \\ & f_z(\varphi) q_z(\theta)^k w(\theta)^k \delta V(\varphi) \Big) \xi R r \, d\theta \, d\varphi \end{aligned} \tag{3.31}$$

Separating the cross-sectional integration and integrating by parts, equation (3.31) can be rewritten as:

$$\delta U_{\text{ext}} = -\sum_{k=1}^{\infty} \left(\int_{\frac{-\psi}{2}}^{\frac{+\psi}{2}} \left(f_{\varphi,\varphi}(\varphi)^k q_\varphi + f_\theta(\varphi)^k q_\theta + f_z(\varphi)^k q_z\right)^k \delta V(\varphi) \, d\varphi + f_\varphi(\varphi)^k {q_\varphi}^k \delta V(\varphi) \Big|_{\frac{-\varphi}{2}}^{\frac{+\varphi}{2}} \right) \tag{3.32}$$

Hence, the modal load decompositions ${}^k q_\varphi$, ${}^k q_\theta$ and ${}^k q_z$ are achieved by the inner product of the deformation modes and the functions $q_\varphi(\theta)$, $q_\theta(\theta)$ and $q_z(\theta)$ of the external load:

$${}^k q_\varphi = -\oint q_\varphi(\theta)^k u(\theta) \, \xi R r \, d\theta \tag{3.33}$$

$${}^k q_\theta = \oint q_\theta(\theta)^k v(\theta) \, \xi R r \, d\theta \tag{3.34}$$

$${}^k q_z = \oint q_z(\theta)^k w(\theta) \, \xi R r \, d\theta \tag{3.35}$$

3.2 Deformation modes

In this section, the shell-type deformation modes for a thin-walled curved CHS are formulated. The relationship between the longitudinal $u(\theta)$, tangential $v(\theta)$ and radial $w(\theta)$ displacement functions are derived from Vlasov's beam theory assumptions (**A6)** of (i) null membrane transverse strain $\varepsilon_{\theta}^{\mathrm{M}} = 0$ in equation (3.5) and (ii) null membrane in-plane shear strain $\gamma_{\varphi\theta}^{\mathrm{M}} = 0$ in equation (3.6). This gives:

$$v(\theta) = -\frac{u_{,\theta}(\theta)}{\alpha}\xi - u(\theta)\sin(\theta) \tag{3.36}$$

$$w(\theta) = -v_{,\theta}(\theta) \tag{3.37}$$

Here, two independent sets of orthogonal trigonometric functions, which are assumed by Schardt [131] for a straight CHS member, are adopted to approximate the longitudinal displacement $u(\theta)$ after dividing it by R to account for the first derivative of the amplitude function in equation (3.1). After determining tangential $v(\theta)$ and radial $w(\theta)$ displacements from equations (3.36) and (3.37) the shell-type displacement modes k are defined by:

$m \geq 1$, $k = 2m$:

$$^{k}u(\theta) = \alpha\sin(m\theta) \tag{3.38}$$

$$^{k}v(\theta) = -m\cos(m\theta) - \alpha\cos(\theta)\, m\cos(m\theta) - \alpha\sin(m\theta)\sin(\theta) \tag{3.39}$$

$$^{k}w(\theta) = -m^2\sin(m\theta) - \alpha\cos(\theta)\, m^2\sin(m\theta) + \alpha\sin(m\theta)\cos(\theta) \tag{3.40}$$

$m \geq 1$, $k = 2m + 1$:

$$^{k}u(\theta) = -\alpha\cos(m\theta) \tag{3.41}$$

$$^{k}v(\theta) = -m\sin(m\theta) - \alpha\cos(\theta)\, m\sin(m\theta) + \alpha\cos(m\theta)\sin(\theta) \tag{3.42}$$

$$^{k}w(\theta) = -m^2\sin(m\theta) - \alpha\cos(\theta)\, m^2\sin(m\theta) + \alpha\sin(m\theta)\cos(\theta) \tag{3.43}$$

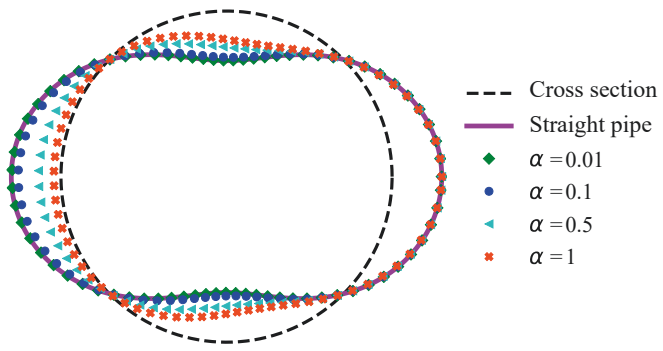

Figure 3.2: Radial displacement for deformation mode 5 or ovalization, $^{5}w(\theta)$.

The last two summations in the transverse displacements are dependent on the radius ratio α. For example, in Figure 3.2 for a smaller value of the radius ratio, the contribution of these summations becomes less significant, and the deformation modes become more similar to a straight pipe. Here, the classification and type of the deformation modes considered are the same as the ones used in Section 2.2.5.

3.2.1 Mode coupling

The curved GBT coefficient matrices have off-diagonal terms which arise from deformation mode coupling in addition to the conventional to non-conventional deformation modes coupling within the same mode index as presented in Section 2.2.5. Substituting equations (3.38) to (3.43) into equations (3.15) to (3.24) and performing a numerical integration, the possible mode couplings are identified for each section property. Figures 3.3 to 3.6 show the mode couplings between t, a and the first six conventional GBT deformation modes as a sample in a tabular form (matrix). In these figures, the non-conventional modes are not shown since their coupling behavior is the same as the conventional ones. The empty cells in the tables make evident that the coupling between modes i and k is zero.

	t	a	1	2	3	4	5	6
t								
a		${}^{aa}C_1$	${}^{a1}C_1$		${}^{a3}C_1$		${}^{a5}C_1$	
1		${}^{1a}C_1$	${}^{11}C_1$		${}^{13}C_1$		${}^{15}C_1$	
2				${}^{22}C_1$		${}^{24}C_1$		${}^{26}C_1$
3		${}^{3a}C_1$	${}^{31}C_1$		${}^{33}C_1$		${}^{35}C_1$	
4				${}^{42}C_1$		${}^{44}C_1$		${}^{46}C_1$
5		${}^{5a}C_1$	${}^{51}C_1$		${}^{53}C_1$		${}^{55}C_1$	
6				${}^{62}C_1$		${}^{64}C_1$		${}^{66}C_1$

	t	a	1	2	3	4	5	6
t				${}^{t2}C_2$		${}^{t4}C_2$		${}^{t6}C_2$
a			${}^{a1}C_2$		${}^{a3}C_2$		${}^{a5}C_2$	
1								
2				${}^{22}C_2$		${}^{24}C_2$		${}^{26}C_2$
3			${}^{31}C_2$		${}^{33}C_2$		${}^{35}C_2$	
4				${}^{42}C_2$		${}^{44}C_2$		${}^{46}C_2$
5		${}^{5a}C_2$	${}^{51}C_2$		${}^{53}C_2$		${}^{55}C_2$	
6				${}^{62}C_2$		${}^{64}C_2$		${}^{66}C_2$

Figure 3.3: List of possible mode couplings for stiffness coefficients ${}^{ik}C_1$ and ${}^{ik}C_2$.

The i and k indexes of the stiffness coefficients define the relationship between two deformation modes. For example, if ${}^{ik}C_1$ exists then the indexes can be interpreted as the forces in mode k will cause a displacement in mode i.

In all section properties, it can be observed that mode a is only coupled with odd modes, and mode t is only coupled with even modes while no coupling exists between even and odd modes. Section property coefficients ${}^{ik}C_3$, ${}^{ik}D_{2\mu}$ and ${}^{ik}D_{4\mu}$ are not shown here since they are the transpose of ${}^{ik}C_2$, ${}^{ik}D_{1\mu}$ and ${}^{ik}D_{3\mu}$, respectively. In the case of stiffness coefficient ${}^{ik}B$, the integral value of the coefficients are shown symbolically since it was easy enough to perform analytical (symbolic) integration.

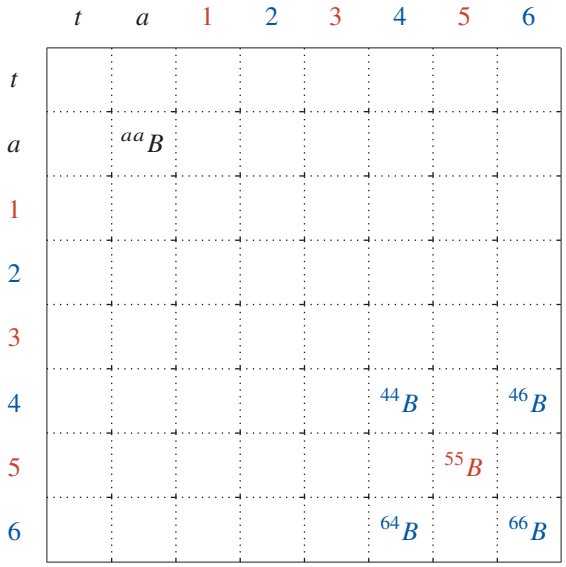

$$^{aa}B = \frac{2\pi\, Q}{r} \tag{3.44}$$

$$^{44}B = {}^{55}B = \frac{144\pi\,\left(R^2 + 2\,r^2\right) K}{R^2 r^3} \tag{3.45}$$

$$^{46}B = {}^{64}B = \frac{144\pi\,\left(10\,R^2 + 3\,r^2\right) K}{R^3 r^2} \tag{3.46}$$

$$^{66}B = \frac{288\pi\,\left(18\,R^2 + 31\,r^2\right) K}{R^2 r^3} \tag{3.47}$$

Figure 3.4: List of possible mode couplings for stiffness coefficients ^{ik}B and the symbolic integral value of the coefficients.

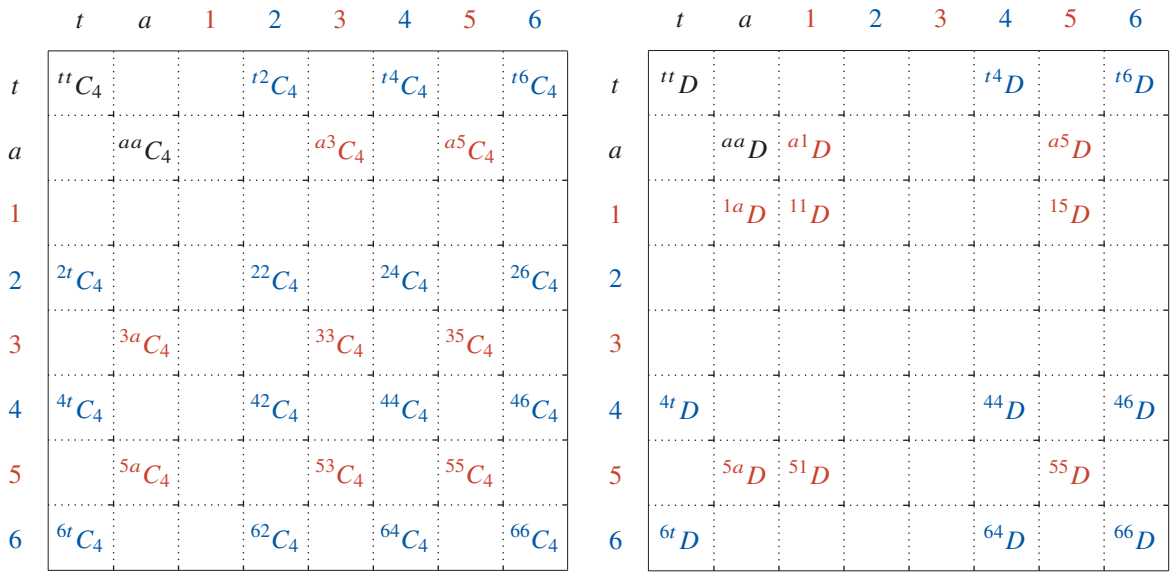

Figure 3.5: List of possible mode couplings for stiffness coefficients $^{ik}C_4$ and ^{ik}D.

3.3 Finite element formulation

In the longitudinal direction, a finite element method is implemented with direct interpolation of the deformation mode amplitude functions. For the approximation of the modal amplitude, $^{k}V(\varphi)$ corresponding to the axial extension mode $k = 1$, four node Lagrange cubic polynomials are used. Classic

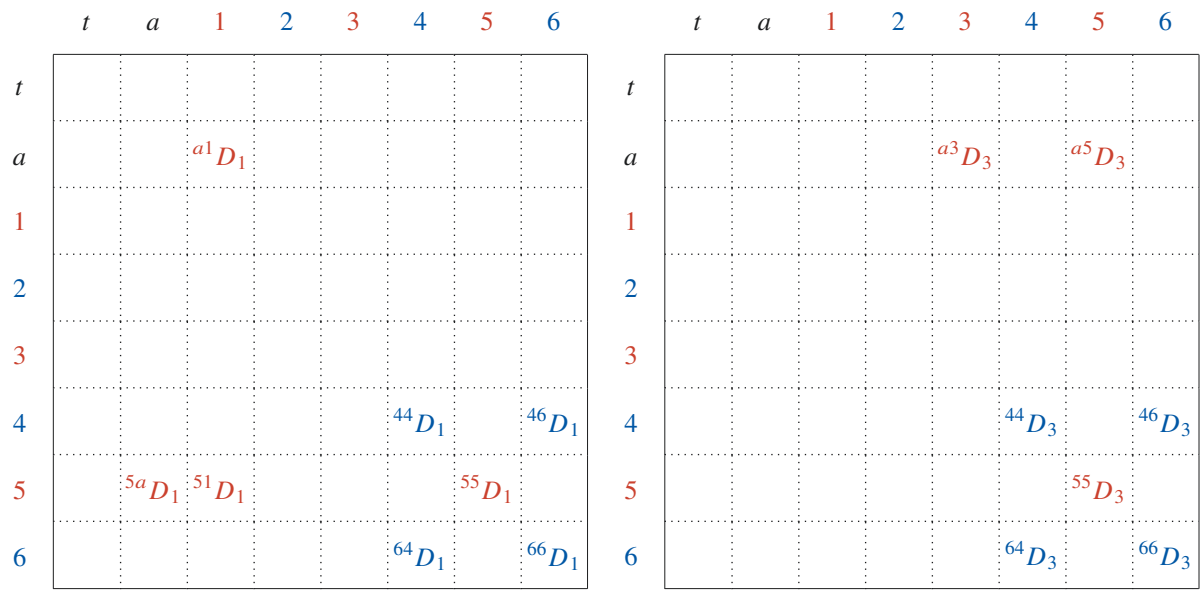

Figure 3.6: List of possible mode couplings for stiffness coefficients $^{ik}D_{1\mu}$ and $^{ik}D_{3\mu}$.

Hermite cubic polynomials are applied to the remaining shell-type and the non-conventional deformation modes. The longitudinal modal amplitude function $^{k}V(\varphi)$ and it's variation $^{k}\delta V(\varphi)$ can be defined as:

$$^{k}V(\varphi) = {}^{k}\{T\varphi\}\,{}^{k}[Sh]\,{}^{k}\{\vartheta\} \tag{3.48}$$

$$^{k}\delta V(\varphi) = {}^{k}\{T\varphi\}\,{}^{k}[Sh] \tag{3.49}$$

where $\{T\varphi\}$ is the variable vector, $[Sh]$ is the completeness coefficient matrices of either the cubic Hermite $[Sh_H]$ or Lagrange $[Sh_L]$ shape functions, and $\{\vartheta\}$ is the vector of the beam's nodal amplitude.

$$\{T\varphi\} = \left\{\varphi^3 \quad \varphi^2 \quad \varphi \quad 1\right\} \tag{3.50}$$

$$[Sh_H] = \begin{bmatrix} \frac{2}{\psi^3} & \frac{1}{\psi^2} & -\frac{2}{\psi^3} & \frac{1}{\psi^2} \\ 0 & -\frac{1}{2\psi} & 0 & \frac{1}{2\psi} \\ -\frac{3}{2\psi} & -\frac{1}{4} & \frac{3}{2\psi} & -\frac{1}{4} \\ \frac{1}{2} & \frac{\psi}{8} & \frac{1}{2} & -\frac{\psi}{8} \end{bmatrix} \quad \text{and} \quad [Sh_L] = \begin{bmatrix} -\frac{9}{2\psi^3} & \frac{27}{2\psi^3} & -\frac{27}{2\psi^3} & \frac{9}{2\psi^3} \\ \frac{9}{4\psi^2} & -\frac{9}{4\psi^2} & -\frac{9}{4\psi^2} & \frac{9}{4\psi^2} \\ \frac{1}{8\psi} & -\frac{27}{8\psi} & \frac{27}{8\psi} & -\frac{1}{8\psi} \\ -\frac{1}{16} & \frac{9}{16} & \frac{9}{16} & -\frac{1}{16} \end{bmatrix} \tag{3.51}$$

$$\{\vartheta_H\}^T = \left\{ V(\tfrac{-\psi}{2}) \quad V_{,\varphi}(\tfrac{-\psi}{2}) \quad V(\tfrac{\psi}{2}) \quad V_{,\varphi}(\tfrac{\psi}{2}) \right\} \text{ and}$$

$$\{\vartheta_L\}^T = \left\{ V(\tfrac{-\psi}{2}) \quad V(\tfrac{-\psi}{6}) \quad V(\tfrac{\psi}{6}) \quad V(\tfrac{\psi}{2}) \right\} \tag{3.52}$$

The GBT curved element stiffness matrix is derived by substituting equations (3.48) and (3.49) into the variation of the strain energy in equation(3.14). This gives:

$$\delta U_{\text{int}} = \sum_{k=1}^{\infty}\sum_{i=1}^{\infty}\Big({}^{ik}C_1\,{}^{ik}[\mathbb{V}_5] + \left({}^{ik}C_2 + {}^{ik}D_{1\mu}\right){}^{ik}[\mathbb{V}_6] + \left({}^{ik}C_3 + {}^{ik}D_{2\mu}\right){}^{ik}[\mathbb{V}_6]^T + \left({}^{ik}C_4 + {}^{ik}B + {}^{ik}D_{3\mu} + {}^{ik}D_{4\mu}\right){}^{ik}[\mathbb{V}_7] + {}^{ik}D\,{}^{ik}[\mathbb{V}_8]\Big)\,{}^{i}\{\vartheta\} \tag{3.53}$$

where:

$${}^{ik}[\mathbb{V}_5] = {}^{k}[Sh]^T \int_{\frac{-\psi}{2}}^{\frac{+\psi}{2}} {}^{k}\{T\varphi\}_{,\varphi\varphi}^T\,{}^{i}\{T\varphi\}_{,\varphi\varphi}\; R\,d\varphi\,{}^{i}[Sh] \tag{3.54}$$

$${}^{ik}[\mathbb{V}_6] = {}^{k}[Sh]^T \int_{\frac{-\psi}{2}}^{\frac{+\psi}{2}} {}^{k}\{T\varphi\}_{,\varphi\varphi}^T\,{}^{i}\{T\varphi\}\; R\,d\varphi\,{}^{i}[Sh] \tag{3.55}$$

$${}^{ik}[\mathbb{V}_7] = {}^{k}[Sh]^T \int_{\frac{-\psi}{2}}^{\frac{+\psi}{2}} {}^{k}\{T\varphi\}^T\,{}^{i}\{T\varphi\}\; R\,d\varphi\,{}^{i}[Sh] \tag{3.56}$$

$${}^{ik}[\mathbb{V}_8] = {}^{k}[Sh]^T \int_{\frac{-\psi}{2}}^{\frac{+\psi}{2}} {}^{k}\{T\varphi\}_{,\varphi}^T\,{}^{i}\{T\varphi\}_{,\varphi}\; R\,d\varphi\,{}^{i}[Sh] \tag{3.57}$$

Due to the coupling between deformation mode i and k, there are three possible outcomes for the equations (3.54) to (3.57).

Case 1: if $i \neq 1$ and $k \neq 1$ the integration in equations (3.54) to (3.57) will be based on the Hermite shape function. This gives:

$${}^{ik}[\mathbb{V}_5] = \frac{R}{\psi^3}\begin{bmatrix} 12 & 6\psi & -12 & 6\psi \\ & 4\psi^2 & -6\psi & 2\psi^2 \\ & & 12 & -6\psi \\ \text{sym.} & & & 4\psi^2 \end{bmatrix} \text{ and } {}^{ik}[\mathbb{V}_6] = \frac{R}{30\psi}\begin{bmatrix} -36 & -3\psi & 36 & -3\psi \\ -33\psi & -4\psi^2 & 3\psi & \psi^2 \\ 36 & 3\psi & -36 & 3\psi \\ -3\psi & \psi^2 & 33\psi & -4\psi^2 \end{bmatrix} \tag{3.58}$$

$${}^{ik}[\mathbb{V}_7] = \frac{R}{420}\begin{bmatrix} 156\psi & 22\psi^2 & 54\psi & -13\psi^2 \\ & 4\psi^3 & 13\psi^2 & -3\psi^3 \\ & & 156\psi & -22\psi^2 \\ \text{sym.} & & & 4\psi^3 \end{bmatrix} \text{ and } {}^{ik}[\mathbb{V}_8] = \frac{R}{30\psi}\begin{bmatrix} 36 & 3\psi & -36 & 3\psi \\ & 4\psi^2 & -3\psi & -\psi^2 \\ & & 36 & -3\psi \\ \text{sym.} & & & 4\psi^2 \end{bmatrix} \tag{3.59}$$

Case 2: if $i = 1$ and $k = 1$ the integration in equations (3.54) and (3.57) will be based on the Lagrange shape function. Here, $[\mathbb{V}_6]$ and $[\mathbb{V}_7]$ are ignored since the corresponding section stiffnesses are zero. Whereas the matrices $[\mathbb{V}_5]$ and $[\mathbb{V}_8]$ are computed as:

$$ {}^{11}[\mathbb{V}_5] = \frac{R}{40\psi}\begin{bmatrix} 148 & -189 & 54 & -13 \\ & 423 & -297 & 54 \\ & & 432 & -189 \\ \text{sym.} & & & 148 \end{bmatrix} \text{ and } {}^{11}[\mathbb{V}_8] = \frac{R\psi}{1680}\begin{bmatrix} 128 & 99 & -36 & 19 \\ & 648 & -81 & -36 \\ & & 648 & 99 \\ -3\,\text{sym.} & & & 128 \end{bmatrix} \tag{3.60} $$

Case 3: if $i = 1$ and $k \neq 1$ the integration in equations (3.54) and (3.57) will be based on the Hermite shape function for mode k and the Lagrange shape function for mode i. This gives:

$$ {}^{1k}[\mathbb{V}_5] = \frac{R}{4\psi^2}\begin{bmatrix} 18 & -18 & -18 & 18 \\ 13\psi & -9\psi & -9\psi & 5\psi \\ -18 & 18 & 18 & -18 \\ 5\psi & -9\psi & -9\psi & 13\psi \end{bmatrix} \text{ and } {}^{1k}[\mathbb{V}_6] = \frac{R}{20\psi}\begin{bmatrix} -11 & -27 & 27 & 11 \\ -8\psi & -21\psi & 6\psi & 3\psi \\ 11 & 27 & -27 & -11 \\ -3\psi & -6\psi & 21\psi & 8\psi \end{bmatrix} \tag{3.61} $$

$$ {}^{1k}[\mathbb{V}_7] = \frac{R\psi}{840}\begin{bmatrix} 96 & 279 & 36 & 9 \\ 6\psi & 45\psi & 18\psi & \psi \\ 9 & 36 & 279 & 96 \\ -\psi & -18\psi & -45\psi & -6\psi \end{bmatrix} \text{ and } {}^{1k}[\mathbb{V}_8] = \frac{R}{120}\begin{bmatrix} -6 & -54 & -54 & -6 \\ 10\psi & 9\psi & -18\psi & -\psi \\ 6 & 54 & 54 & 6 \\ -\psi & -18\psi & 9\psi & 10\psi \end{bmatrix} \tag{3.62} $$

In this case, the order of i and k is important for ${}^{ik}[\mathbb{V}_6]$. If $i \neq 1$ and $k = 1$ then ${}^{i1}[\mathbb{V}_6]$ will not be the transpose of the above expression. Instead it becomes:

$$ {}^{i1}[\mathbb{V}_6] = \frac{R}{120}\begin{bmatrix} -114 & -10\psi & -6 & \psi \\ 54 & -9\psi & -54 & 18\psi \\ 54 & 18\psi & -54 & -9\psi \\ 6 & \psi & 114 & -10\psi \end{bmatrix} \tag{3.63} $$

The sub-matrix components ${}^{ik}[k]$ of the element stiffness matrix are extracted from equation (3.53) as:

$$ \begin{aligned} {}^{ik}[k] = {}& {}^{ik}C_1\,{}^{ik}[\mathbb{V}_5] + \left({}^{ik}C_2 + {}^{ik}D_{1\mu}\right){}^{ik}[\mathbb{V}_6] + \left({}^{ik}C_3 + {}^{ik}D_{2\mu}\right){}^{ik}[\mathbb{V}_6]^T \\ & + \left({}^{ik}C_4 + {}^{ik}B + {}^{ik}D_{3\mu} + {}^{ik}D_{4\mu}\right){}^{ik}[\mathbb{V}_7] + {}^{ik}D\,{}^{ik}[\mathbb{V}_8] \end{aligned} \tag{3.64} $$

In equation (3.66), the element mass matrix $[K]^e$ which is built based on the sub-matrix in equation (3.64) is shown following the natural order of GBT deformation modes in equation (3.65).

$$ \{d\}^T = \left\{ {}^{t}\{\vartheta\}, {}^{a}\{\vartheta\}, {}^{1}\{\vartheta\}, {}^{2}\{\vartheta\}, {}^{\overset{v}{2}}\{\vartheta\}, {}^{\overset{u}{2}}\{\vartheta\}, {}^{3}\{\vartheta\}, {}^{\overset{v}{3}}\{\vartheta\}, {}^{\overset{u}{3}}\{\vartheta\}, {}^{4}\{\vartheta\}, \ldots \right\} \tag{3.65} $$

$$[K]^e = \begin{bmatrix}
{}_{tt}[k] & [0] & [0] & {}_{t2}[k] & {}^{\vee}_{t2}[k] & {}^{\cup}_{t2}[k] & [0] & [0] & [0] & {}_{t4}[k] & {}^{\vee}_{t4}[k] & {}^{\cup}_{t4}[k] & [0] & [0] & [0] & \cdots \\
 & {}_{aa}[k] & {}_{a1}[k] & [0] & [0] & [0] & {}_{a3}[k] & {}^{\vee}_{a3}[k] & {}^{\cup}_{a3}[k] & [0] & [0] & [0] & {}_{a5}[k] & {}^{\vee}_{a5}[k] & {}^{\cup}_{a5}[k] & \cdots \\
 & & {}_{11}[k] & [0] & [0] & [0] & {}_{13}[k] & {}^{\vee}_{13}[k] & {}^{\cup}_{13}[k] & [0] & [0] & [0] & {}_{15}[k] & {}^{\vee}_{15}[k] & {}^{\cup}_{15}[k] & \cdots \\
 & & & {}_{22}[k] & {}^{\vee}_{22}[k] & {}^{\cup}_{22}[k] & [0] & [0] & [0] & {}_{24}[k] & {}^{\vee}_{24}[k] & {}^{\cup}_{24}[k] & [0] & [0] & [0] & \cdots \\
 & & & & {}^{\vee\vee}_{22}[k] & {}^{\vee\cup}_{22}[k] & [0] & [0] & [0] & {}^{\vee}_{24}[k] & {}^{\vee\vee}_{24}[k] & {}^{\vee\cup}_{24}[k] & [0] & [0] & [0] & \cdots \\
 & & & & & {}^{\cup\cup}_{22}[k] & [0] & [0] & [0] & {}^{\cup}_{24}[k] & {}^{\cup\vee}_{24}[k] & {}^{\cup\cup}_{24}[k] & [0] & [0] & [0] & \cdots \\
 & & & & & & {}_{33}[k] & {}^{\vee}_{33}[k] & {}^{\cup}_{33}[k] & [0] & [0] & [0] & {}_{35}[k] & {}^{\vee}_{35}[k] & {}^{\cup}_{35}[k] & \cdots \\
 & & & & & & & {}^{\vee\vee}_{33}[k] & {}^{\vee\cup}_{33}[k] & [0] & [0] & [0] & {}^{\vee}_{35}[k] & {}^{\vee\vee}_{35}[k] & {}^{\vee\cup}_{35}[k] & \cdots \\
 & & & & & & & & {}^{\cup\cup}_{33}[k] & [0] & [0] & [0] & {}^{\cup}_{35}[k] & {}^{\cup\vee}_{35}[k] & {}^{\cup\cup}_{35}[k] & \cdots \\
 & & & & & & & & & {}_{44}[k] & {}^{\vee}_{44}[k] & {}^{\cup}_{44}[k] & [0] & [0] & [0] & \cdots \\
 & & & & & & & & & & {}^{\vee\vee}_{44}[k] & {}^{\vee\cup}_{44}[k] & [0] & [0] & [0] & \cdots \\
 & & & & & & & & & & & {}^{\cup\cup}_{44}[k] & [0] & [0] & [0] & \cdots \\
 & & & & & & & & & & & & {}_{55}[k] & {}^{\vee}_{55}[k] & {}^{\cup}_{55}[k] & \cdots \\
 & & & & & & & & & & & & & {}^{\vee\vee}_{55}[k] & {}^{\vee\cup}_{55}[k] & \cdots \\
 & & & & & & & & & & & & & & {}^{\cup\cup}_{55}[k] & \cdots \\
sym. & & & & & & & & & & & & & & & \ddots
\end{bmatrix} \tag{3.66}$$

$$
[K]^e = \begin{bmatrix}
{}^{aa}[k] & {}^{a1}[k] & {}^{a3}[k] & {}^{\overset{v}{a}3}[k] & {}^{\overset{u}{a}3}[k] & {}^{a5}[k] & {}^{\overset{v}{a}5}[k] & {}^{\overset{u}{a}5}[k] & \dots & [0] & [0] & [0] & [0] & [0] & [0] & \dots \\
 & {}^{11}[k] & {}^{13}[k] & {}^{\overset{v}{1}3}[k] & {}^{\overset{u}{1}3}[k] & {}^{15}[k] & {}^{\overset{v}{1}5}[k] & {}^{\overset{u}{1}5}[k] & \dots & [0] & [0] & [0] & [0] & [0] & [0] & \dots \\
 & & {}^{33}[k] & {}^{\overset{v}{3}3}[k] & {}^{\overset{u}{3}3}[k] & {}^{35}[k] & {}^{\overset{v}{3}5}[k] & {}^{\overset{u}{3}5}[k] & \dots & [0] & [0] & [0] & [0] & [0] & [0] & \dots \\
 & & & {}^{\overset{v}{3}\overset{v}{3}}[k] & {}^{\overset{v}{3}\overset{u}{3}}[k] & {}^{\overset{v}{3}5}[k] & {}^{\overset{v}{3}\overset{v}{5}}[k] & {}^{\overset{v}{3}\overset{u}{5}}[k] & \dots & [0] & [0] & [0] & [0] & [0] & [0] & \dots \\
 & & & & {}^{\overset{u}{3}\overset{u}{3}}[k] & {}^{\overset{u}{3}5}[k] & {}^{\overset{u}{3}\overset{v}{5}}[k] & {}^{\overset{u}{3}\overset{u}{5}}[k] & \dots & [0] & [0] & [0] & [0] & [0] & [0] & \dots \\
 & & & & & {}^{55}[k] & {}^{\overset{v}{5}5}[k] & {}^{\overset{u}{5}5}[k] & \dots & [0] & [0] & [0] & [0] & [0] & [0] & \dots \\
 & & & & & & {}^{\overset{v}{5}\overset{v}{5}}[k] & {}^{\overset{v}{5}\overset{u}{5}}[k] & \dots & [0] & [0] & [0] & [0] & [0] & [0] & \dots \\
 & & & & & & & {}^{\overset{u}{5}\overset{u}{5}}[k] & \dots & [0] & [0] & [0] & [0] & [0] & [0] & \dots \\
 & & & & & & & & \ddots & [0] & [0] & [0] & [0] & [0] & [0] & \dots \\
 & & & & & & & & & {}^{t\,t}[k] & {}^{t\,2}[k] & {}^{t\overset{v}{2}}[k] & {}^{t\overset{u}{2}}[k] & {}^{t\,4}[k] & {}^{t\overset{v}{4}}[k] & \dots \\
 & & & & & & & & & & {}^{22}[k] & {}^{\overset{v}{2}2}[k] & {}^{\overset{u}{2}2}[k] & {}^{2\,4}[k] & {}^{\overset{v}{2}4}[k] & \dots \\
 & & & & & & & & & & & {}^{\overset{v}{2}\overset{v}{2}}[k] & {}^{\overset{v}{2}\overset{u}{2}}[k] & {}^{\overset{v}{2}4}[k] & {}^{\overset{v}{2}\overset{v}{4}}[k] & \dots \\
 & & & & & & & & & & & & {}^{\overset{u}{2}\overset{u}{2}}[k] & {}^{\overset{u}{2}4}[k] & {}^{\overset{u}{2}\overset{v}{4}}[k] & \dots \\
 & & & & & & & & & & & & & {}^{44}[k] & {}^{\overset{v}{4}4}[k] & \dots \\
 & & & & & & & & & & & & & & {}^{\overset{v}{4}\overset{v}{4}}[k] & \dots \\
sym. & & & & & & & & & & & & & & & \ddots
\end{bmatrix} \tag{3.67}
$$

In equation (3.67), the bandwidth of the element stiffness matrix is reduced by half by optimizing the order of the deformation modes in such a way that the modes which have coupling are arranged together. This order of deformation modes can be clearly seen on the corresponding generalized modal amplitude vector $\{d\}$ in equation (3.68).

$$\{d\}^T = \left\{ {}^{a}\{\vartheta\}, {}^{1}\{\vartheta\}, {}^{3}\{\vartheta\}, {}^{\overset{v}{3}}\{\vartheta\}, {}^{\overset{u}{3}}\{\vartheta\}, \dots, {}^{t}\{\vartheta\}, {}^{2}\{\vartheta\}, {}^{\overset{v}{2}}\{\vartheta\}, {}^{\overset{u}{2}}\{\vartheta\}, {}^{4}\{\vartheta\}, \dots \right\} \tag{3.68}$$

3.4 Stress resultants

The stress resultants for membrane forces, shear forces, and bending moment are formulated for a curved GBT member. Here, since the non-conventional deformation modes are considered, the stress resultants N_θ and $N_{\varphi\theta}$ are directly derived from the membrane stresses. The complete stress resultants, which are forces per unit length, and the stress moments, which are moments per unit length, are derived as:

$$\begin{aligned} N_\varphi &= \int_{\frac{-t}{2}}^{\frac{+t}{2}} \sigma_{\varphi\varphi}\ dz \\ &= Q \sum_{k=1}^{\infty} \Big(\frac{{}^{k}u(\theta)}{R\xi} V_{,\varphi\varphi}(\varphi) + \Big(\frac{{}^{k}w(\theta)\cos(\theta) - {}^{k}v(\theta)\sin(\theta)}{R\xi} + \mu \frac{{}^{k}v_{,\theta}(\theta) + {}^{k}w(\theta)}{r} \Big) V(\varphi) \Big) \end{aligned} \tag{3.69}$$

$$\begin{aligned} N_\theta &= \int_{\frac{-t}{2}}^{\frac{+t}{2}} \sigma_{\theta\theta}\ dz \\ &= Q \sum_{k=1}^{\infty} \Big(\Big(\frac{{}^{k}v_{,\theta}(\theta) + {}^{k}w(\theta)}{r} + \mu \frac{{}^{k}w(\theta)\cos(\theta) - {}^{k}v(\theta)\sin(\theta)}{R\xi} \Big) V(\varphi) + \mu \frac{{}^{k}u(\theta)}{R\xi} V_{,\varphi\varphi}(\varphi) \Big) \end{aligned} \tag{3.70}$$

$$N_{\varphi\theta} = \int_{\frac{-t}{2}}^{\frac{+t}{2}} \tau_{\varphi\theta}\ dz = Gt \sum_{k=1}^{\infty} \Big(\frac{{}^{k}u_{,\theta}(\theta)}{r} + \frac{{}^{k}v(\theta) + {}^{k}u(\theta)\sin(\theta)}{R\xi} \Big) V_{,\varphi}(\varphi) \tag{3.71}$$

$$\begin{aligned} M_\varphi = \int_{\frac{-t}{2}}^{\frac{+t}{2}} \sigma_{\varphi\varphi} z\ dz = K \sum_{k=1}^{\infty} \Big(& \frac{{}^{k}u(\theta)\cos(\theta) - {}^{k}w(\theta)}{(R\xi)^2} V_{,\varphi\varphi}(\varphi) \\ & + \Big(\frac{\sin(\theta)\big({}^{k}w_{,\theta}(\theta) - {}^{k}v(\theta)\big)}{Rr\xi} + \mu \frac{{}^{k}v_{,\theta}(\theta) - {}^{k}w_{,\theta\theta}(\theta)}{r^2} \Big) V(\varphi) \Big) \end{aligned} \tag{3.72}$$

$$\begin{aligned} M_\theta = \int_{\frac{-t}{2}}^{\frac{+t}{2}} \sigma_{\theta\theta} z\ dz = K \sum_{k=1}^{\infty} \Big(& \Big(\frac{{}^{k}v_{,\theta}(\theta) - {}^{k}w_{,\theta\theta}(\theta)}{r^2} + \mu\ \frac{\sin(\theta)\big({}^{k}w_{,\theta}(\theta) - {}^{k}v(\theta)\big)}{Rr\xi} \Big) V(\varphi) \\ & + \mu \frac{{}^{k}u(\theta)\cos(\theta) - {}^{k}w(\theta)}{(R\xi)^2} V_{,\varphi\varphi}(\varphi) \Big) \end{aligned} \tag{3.73}$$

$$M_{\varphi\theta} = \int_{\frac{-t}{2}}^{\frac{+t}{2}} \tau_{\varphi\theta} z \; dz$$
$$= \frac{Gt^3}{12} \sum_{k=1}^{\infty} \Big(- \frac{2^k w_{,\theta}(\theta)}{Rr\xi} - \frac{2^k w(\theta) \sin(\theta)}{(R\xi)^2} + \frac{^k v(\theta)(1+2\xi)}{2Rr\xi^2} + F_1 \, ^k u_{,\theta}(\theta) + F_2 \, ^k u(\theta) \Big) V_{,\varphi}(\varphi) \tag{3.74}$$

Due to the Love-Kirchhoff assumption the shear stress resultants Q_φ and Q_θ are obtained from equilibrium conditions and are given by [179].

$$Q_\varphi = \frac{M_{\varphi\theta,\theta}}{r} + \frac{M_{\varphi\varphi,\varphi} - 2\sin(\theta) M_{\varphi\theta}}{R\xi} \tag{3.75}$$

$$Q_\theta = \frac{M_{\theta\theta,\theta}}{r} + \frac{M_{\varphi\theta,\varphi} + \sin(\theta)\big(M_{\varphi\varphi} - M_{\theta\theta}\big)}{R\xi} \tag{3.76}$$

3.5 Numerical examples

In this section, numerical examples are presented for curved thin-walled circular pipes with various bend angles, boundary conditions, and load cases. All examples are compared with equivalent shell finite element models using ANSYS software [10]. These models have been developed using quadrilateral elements with 6 DoF per node which are based on Reissner-Mindlin's kinematic assumption with linear interpolation functions as implemented in the software ANSYS under the name SHELL 181. The element sizes used for the shell element models are approximately 40×40 mm for the first two examples and 20×20 mm for the last one.

3.5.1 In-plane bending

In this example, a cantilever pipe bend is considered with a radius ratio of $\alpha = \dfrac{1}{12}$ and a bend angle of $\psi = \dfrac{\pi}{2}$. As shown in Figure 3.7, the free end of the pipe is loaded with a uniform line load q distributed around the perimeter of the pipe. Here, the steps involved in the GBT analysis are the same as the ones presented in the previous chapter.

Therefore, as a first step, the line load q was transformed into local coordinates, $^k q_\varphi$, $^k q_\theta$, $^k q_z$, whereas the longitudinal component $^k q_\varphi$ is zero in this case (equations (3.77) to (3.79)). The load contribution in each mode k is then determined by using equations (3.80) and (3.81) as shown in Table 3.1. Only the in-plane bending mode 3, the ovalization mode 5, and their respective shear-v modes are associated with the external load. The longitudinal integration in equation (3.32) is not necessary in this case since the load is applied only at the tip of the cantilever.

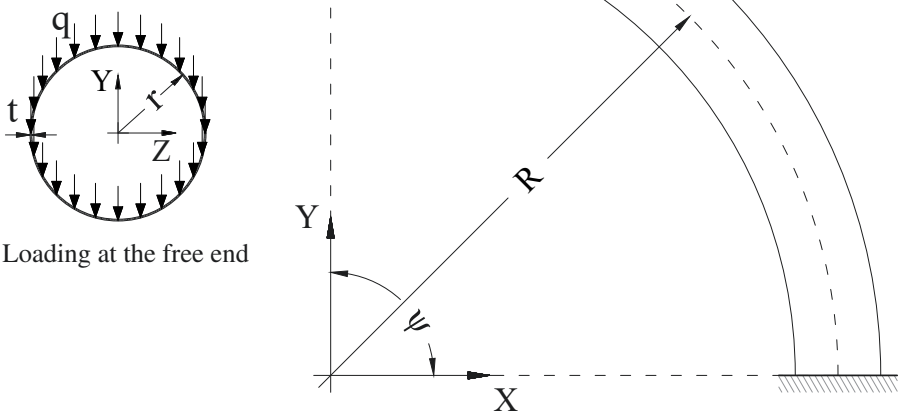

(a) Loading at the free end

(b) Cantilever arch pipe

$R = 6000\,\text{mm}$
$r = 500\,\text{mm}$
$t = 10\,\text{mm}$
$\psi = 90°$
$E = 205\,\text{GPa}$
$\mu = 0.3$
$q = \frac{50}{2\pi r}\,\frac{\text{kN}}{\text{mm}}$

Figure 3.7: In-plane loading of a circular section cantilever arch beam.

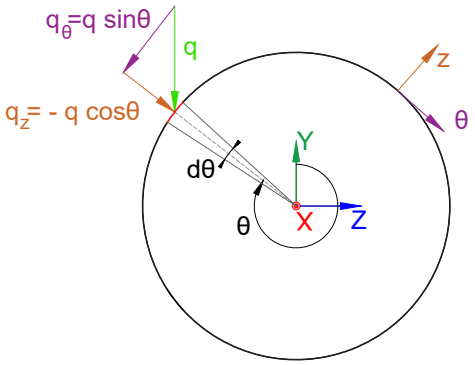

Figure 3.8: Distributed load in the local coordinate system.

The external load q in Figure 3.8 is expressed in the local coordinate system in $\left[\frac{\text{N}}{\text{mm}}\right]$:

$$q_\varphi(\theta) = 0 \tag{3.77}$$

$$q_\theta(\theta) = q\sin(\theta) \tag{3.78}$$

$$q_z(\theta) = -q\cos(\theta) \tag{3.79}$$

Mode k	${}^k q_\theta$[N]	${}^k q_z$[N]
3	$-r\pi q$	$-r\pi q$
$\overset{v}{3}$	$-r\pi q$	0
5	$-\frac{3r^2\pi q}{2R}$	$-\frac{3r^2\pi q}{2R}$
$\overset{v}{5}$	$-\frac{3r^2\pi q}{2R}$	0

Table 3.1: External load modal decomposition.

Substituting equations (3.78) and (3.79) into equations (3.34) and (3.35) the modal decomposition of the external load can be calculated as:

$${}^k q_\theta = \int_0^{2\pi} q\sin(\theta)\,{}^k v(\theta)\,r d\theta \tag{3.80}$$

$${}^k q_z = \int_0^{2\pi} -q\cos(\theta)\,{}^k w(\theta)\,r d\theta \tag{3.81}$$

Here, only the odd deformation modes are selected for the GBT analysis since the even modes neither have any applied force nor are they coupled with the odd modes as explained in section 3.2.1. The number of odd modes to be used is decided by performing a convergence test.

In the next step of the GBT analysis, the element stiffness matrix $[K]^e$ and external force vector $\{F\}^e$, used to calculate the generalized modal amplitude vector $\{d\}^e$, are built based on the finite element formulation presented in Section 3.3 for the selected number and types of GBT deformation modes.

In Table 3.2, the solution convergence of the GBT analysis is presented starting from consideration of only RB modes which is equivalent to an Euler-Bernoulli beam to shear deformable GBT model with LS modes. In the table, the maximum tip displacement refers to the local radial displacement w. Here, the significance of the shear-u modes can be seen as it improves the classical GBT displacement results from about 80 % to less than 6 %. This observation has also been reported for square hollow arch sections in [111]. In this example, modes up to 11 are considered for the analysis since the changes in displacement and stress fields are insignificant for the additional number of modes. Although the axisymmetric mode a has a coupling effect with the odd modes, its contribution is negligible as shown in the last row of Table 3.2.

Table 3.2: Comparison of GBT with different modes and shell results.

Type of analysis	Max. tip displacement [mm]	Mean relative difference [%]
Shell	47.26	-
GBT, RB(1,3) ⇒ Euler-Bernoulli beam	3.82	91.99
GBT, RB(1,3) + SV modes	4.44	90.67
GBT, RB(1,3) + SU modes	9.76	79.55
GBT, RB(1,3) + SU + SV modes ⇒ Timoshenko beam	10.70	77.57
GBT, RB(1,3) + LS(5,7,9,11) modes ⇒ Classical GBT	9.83	81.14
GBT, RB(1,3) + LS(5,7,9,11) + SV modes	11.82	77.09
GBT, RB(1,3) + LS(5,7,9,11) + SU modes	44.70	5.39
GBT, RB(1,3) + LS(5,7,9,11)+ SU + SV modes	47.20	0.12
GBT, RB(1,3) + LS(5,7,9,11,15,17,19,21)+ a + SU + SV modes	47.22	0.08

Longitudinally, the GBT model is discretized by 40 elements, which is enough to reach a displacement convergence of above 99.50 % as shown in Figure 3.9. Considering the number of modes and elements used, the total degrees of freedom (DoF) for the GBT model is $1,351$ which is below 1.20 % of the equivalent shell element model which has $115,680$ DoF. Figure 3.9 shows the finite element solution convergence with respect to the number of GBT elements. In this example, with just two GBT elements the solution can be approximated with an accuracy of above 85 %.

The deformed configuration in Figure 3.10 shows a perfect agreement between the GBT and the shell model. In Figure 3.10, the ovalization of the pipe bend due to the in-plane bending can be clearly observed near the mid span. In the GBT model, the coupled warping stiffness matrix ${}^{53}C$ is mainly responsible for this effect. This stiffness matrix relates the forces in mode 3 to the displacement in mode 5.

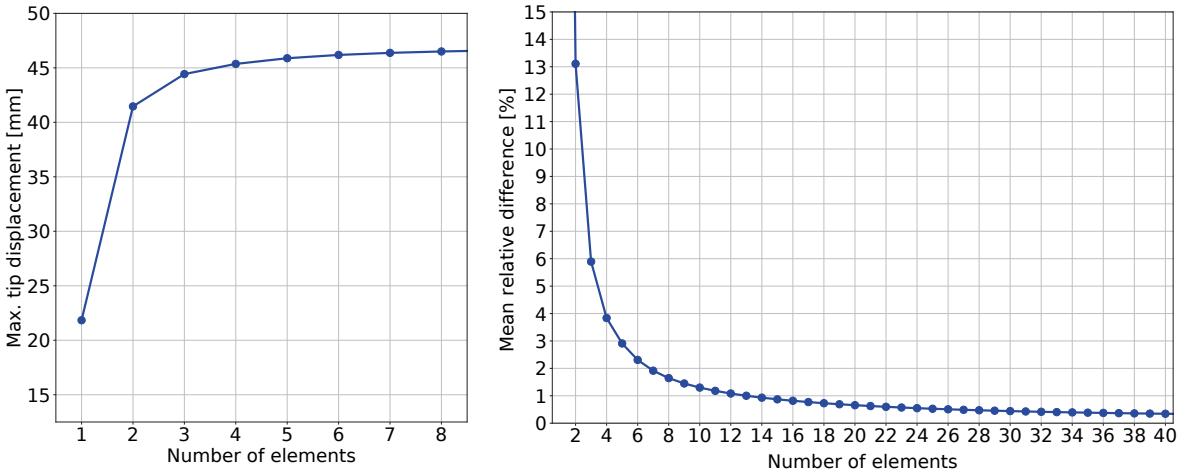

Figure 3.9: GBT solution convergence.

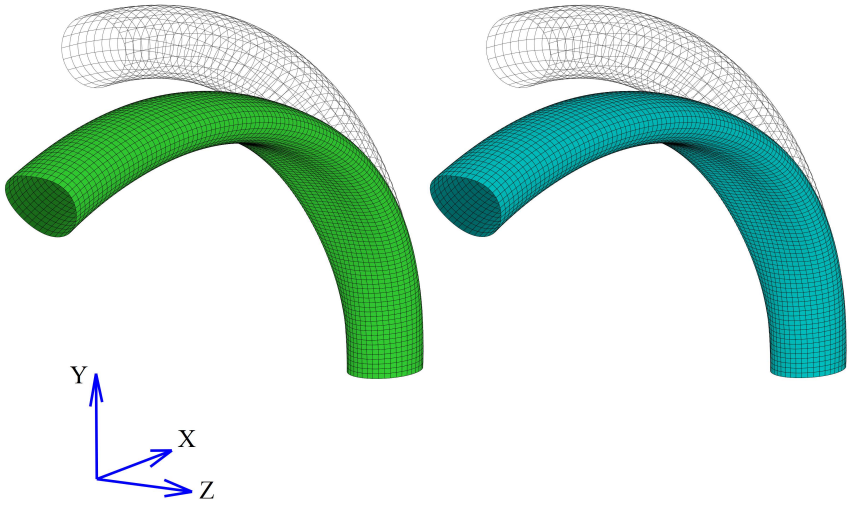

(a) GBT (b) Shell

Figure 3.10: In-plane deformation shape of a 90° cantilever pipe bend (×40).

Here, to have a fair comparison between GBT and shell computation speed the stiffness matrix of the shell element model is extracted from ANSYS and solved using the same linear equation solver and computer processor as the GBT model. In Table 3.3, it is shown that the GBT model needs less than 1.5 % of the time needed by the shell element model.

Table 3.3: Computational speed comparison of GBT and shell.

	GBT	Shell
System stiffness matrix size	1320×1320	115200×115200
Computation speed: using the same linear equation solver and processor	0.0096 s	0.8175 s

In Figure 3.11, the sparsity pattern of the system stiffness matrices of GBT and shell shows that the GBT model has a much denser stiffness matrix than the shell element model.

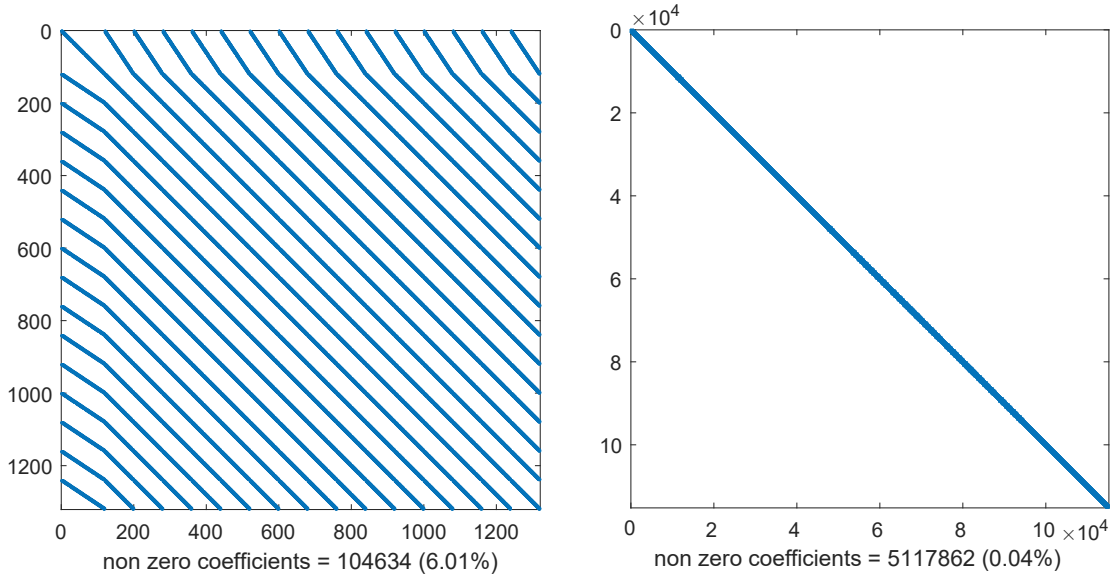

(a) GBT (b) Shell

Figure 3.11: The sparsity pattern of the system stiffness matrices.

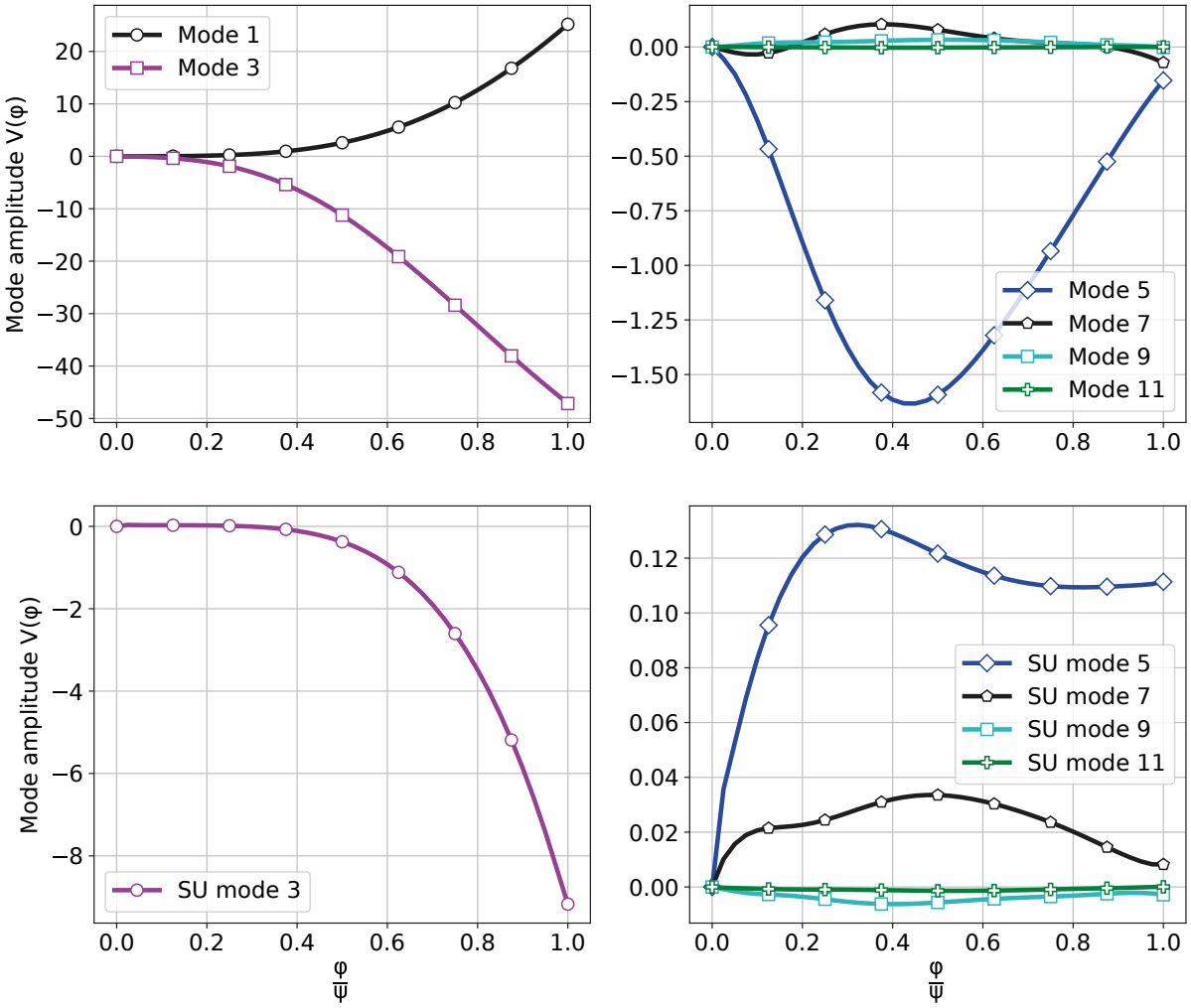

Figure 3.12: GBT deformation modes amplitude.

The relatively high density of the GBT stiffness matrix is insignificant in the computational speed presented in Table 3.3 since the shell element model has a considerably larger number of DoF. However, it can be summarized that the increase in the density of the GBT stiffness matrix in problems involving deformation mode coupling will reduce the computational efficiency of GBT.

In Figure 3.12, the modal decomposition of GBT is presented for the longitudinal solution $V(\varphi)$ considering modes with a significant contribution. In these figures, it can be observed that deformation modes 1, 3, and 5 have the highest contribution in the total displacement and stress fields. Although, the direct contribution of SU (shear-u) modes does not appear significant in the figures, without their coupling effect with classical GBT modes the amplitude of RB (rigid-body) and LS (local shell-type) modes would have been very inaccurate. From the amplitude of deformation mode 5, the maximum ovalization on the pipe bend occurs at around $\frac{\varphi}{\psi} = 0.40$.

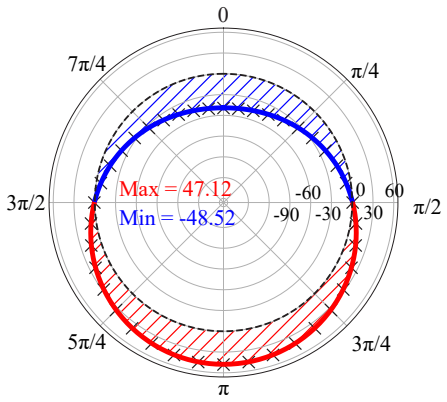

(a) w_{total} (×10)

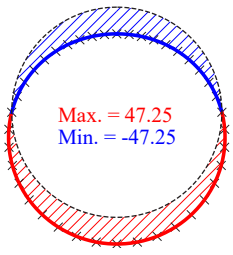

(b) w_{bending} (×10)

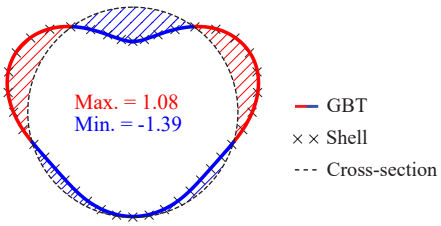

(c) w_{local} (×370)

Figure 3.13: Comparison of displacements at the tip [mm].

In Figures 3.13 to 3.17, detailed cross-sectional comparisons of displacement and stress resultants of GBT and shell are presented at the free end (tip) and the mid span of the cantilever curved pipe. The radial and angular coordinates of the polar plots in these figures represent the magnitude of the displacement or the stress resultant and the angle θ, respectively. The dashed line (undeformed cross-section) represents a magnitude of zero. In Figure 3.13a, the polar coordinates are shown on the plot as a sample. The local displacement w is shown as w_{total} for all modes, w_{bending} for bending modes, and w_{local} for all LS modes. Table 3.4 summarizes the quantitative deviations between the GBT and shell model analyses at a cross-section using the mean relative difference (Equation (2.89)) and the standard deviation of the

relative differences. Here, the maximum differences between GBT and shell for the significant stress resultants are below 3%.

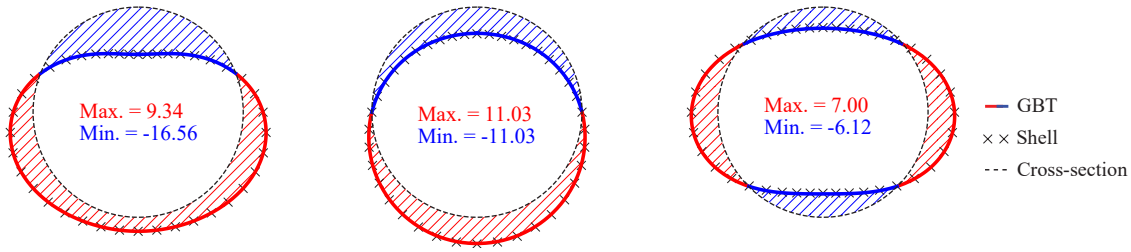

(a) w_{total} (×40) (b) w_{bending} (×35) (c) w_{local} (×60)

Figure 3.14: Comparison of displacements at the mid span [mm].

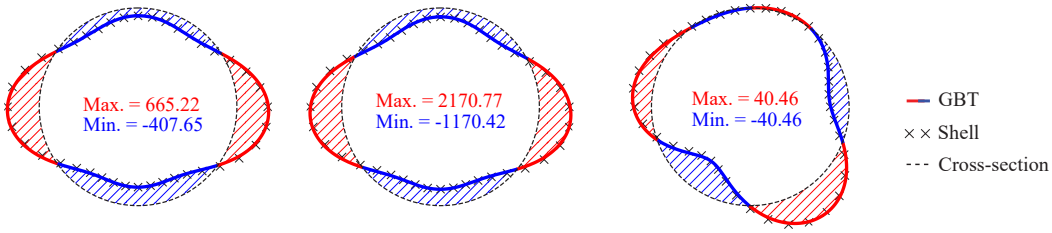

(a) M_φ (b) M_θ (c) $M_{\varphi\theta}$

Figure 3.15: Comparison of bending moment per unit length at the mid span $\left[\frac{\text{Nmm}}{\text{mm}}\right]$.

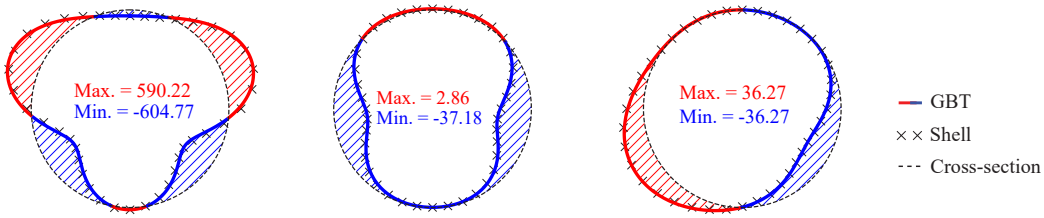

(a) N_φ (b) N_θ (c) $N_{\varphi\theta}$

Figure 3.16: Comparison of normal force per unit length at the mid span $\left[\frac{\text{N}}{\text{mm}}\right]$.

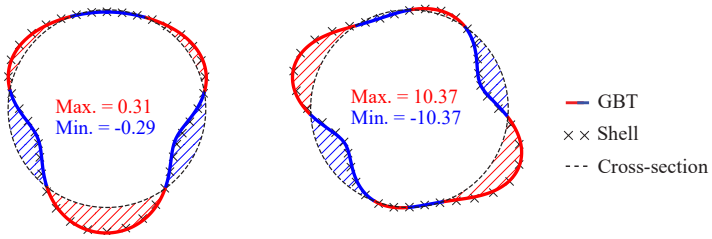

(a) Q_φ (b) Q_θ

Figure 3.17: Comparison of shear force per unit length at the mid span $\left[\frac{\text{N}}{\text{mm}}\right]$.

Table 3.4: Comparison of GBT and shell results at the mid span.

	M_φ	M_θ	$M_{\varphi\theta}$	N_φ	N_θ	$N_{\varphi\theta}$	Q_φ	Q_θ	w_{local}	w_{bending}	w_{total}
Relative mean difference [%]	0.57	0.67	2.64	0.47	0.56	1.12	5.12	0.56	0.32	0.02	0.19
Standard deviation [%]	0.59	0.79	3.19	0.53	0.39	0.82	4.72	0.64	0.35	0.00	0.26

For this example, the effect of the Poisson ratio is investigated by comparing the displacement and stress field results calculated with $\mu = 0.3$ to $\mu = 0.0$. As shown in Figure 3.18, the Poisson value has a negligible effect in the displacement field but has a significant effect in the longitudinal bending moment's stress resultant.

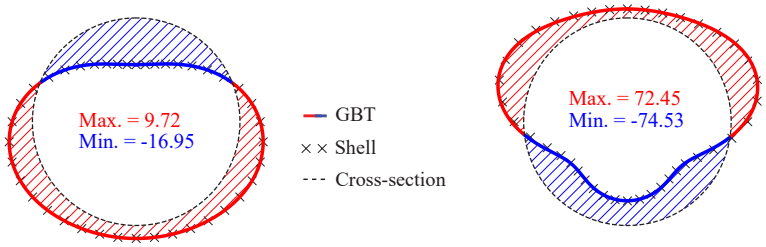

(a) w_{total} (×40) (b) M_φ

Figure 3.18: Displacements and bending moment at the mid span when $\mu = 0$.

3.5.2 Out-of-plane bending

In this example, the radius ratio of the curved pipe is increased to $\alpha = \frac{1}{6}$ and the direction of the distributed uniform line load q is changed, such that it will cause an out-of-plane bending as shown in Figure 3.19. The rest of the parameters are kept the same as those used in the previous example.

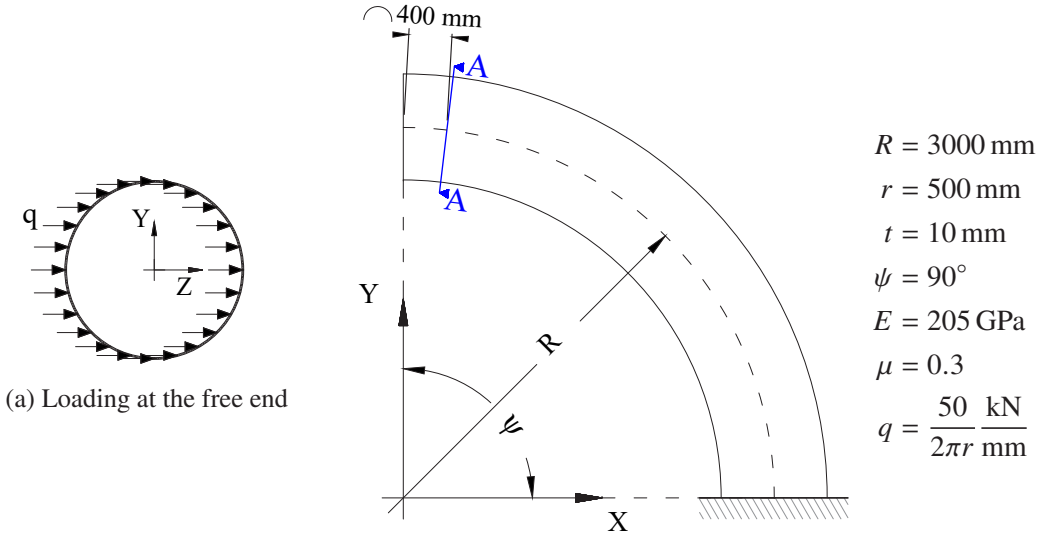

(a) Loading at the free end

(b) Cantilever arch pipe

Figure 3.19: Out-of-plane loading of a circular section cantilever arch beam.

Due to the change in the direction of the loading, the modes which have an external load contribution are mode 2 and 4 and their respective shear-v modes. Therefore, the even modes are chosen for the GBT analysis. The torsion mode is also included in the analysis since it has a coupling effect with even modes.

Table 3.5: Comparison of shell and GBT with different modes.

Type of analysis	Max. displacement at section A [mm]	Mean relative difference [%]
Shell	9.18	-
GBT, RB(t,2) + LS(4,6,8,10) + SU + SV modes	9.10	0.69
GBT, RB(t,2) + LS(4,6,8,10,12,14,16) + SU + SV modes	9.17	0.13

Although the even modes up to 10 would have been enough to reach a displacement field convergence, even modes up to 16 are considered in the analysis to also achieve a reasonable convergence in the stress field (Table 3.5). In total 20 GBT elements are used.

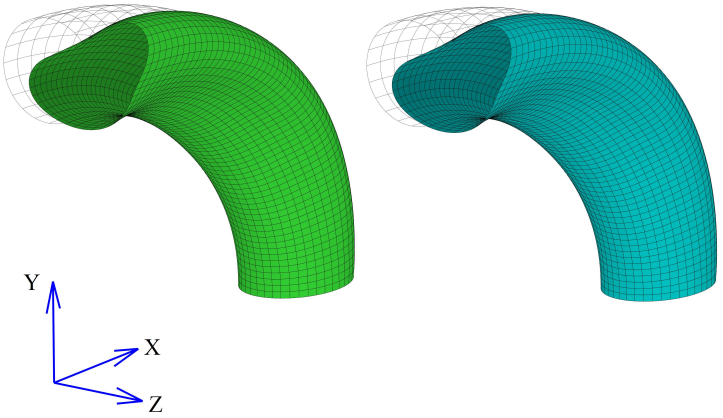

(a) GBT (b) Shell

Figure 3.20: Out-of-plane deformation shape of a 90° cantilever pipe bend (×50).

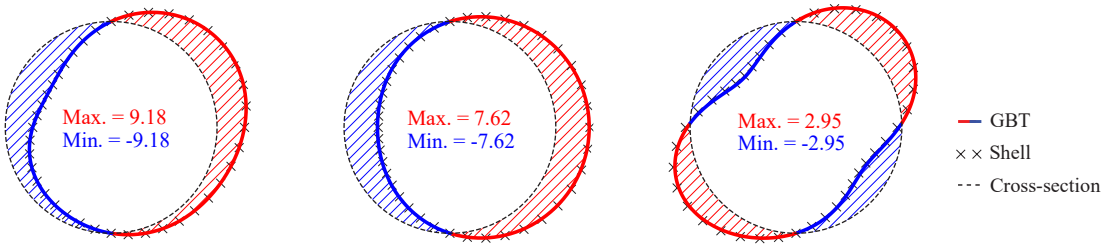

(a) w_{total} (×55) (b) w_{bending} (×65) (c) w_{local} (×170)

Figure 3.21: Comparison of displacements at section A [mm].

In this example, the maximum differences between GBT and shell for the stress resultants are below 6% (Table 3.6). Here, the relatively high difference in stress resultants is visible due to the proximity of section A to the free end.

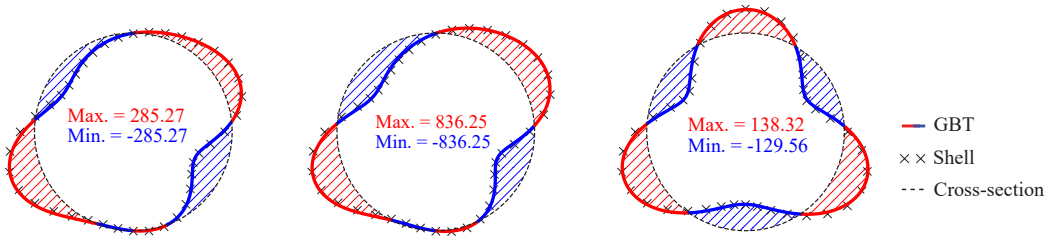

(a) M_φ (b) M_θ (c) $M_{\varphi\theta}$

Figure 3.22: Comparison of bending moment per unit length at section A $\left[\frac{\text{Nmm}}{\text{mm}}\right]$.

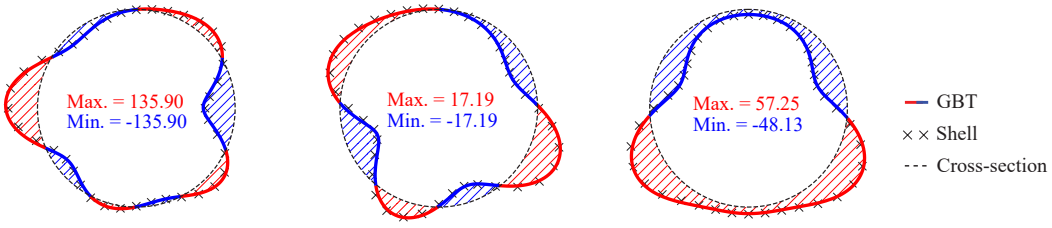

(a) N_φ (b) N_θ (c) $N_{\varphi\theta}$

Figure 3.23: Comparison of normal force per unit length at section A $\left[\frac{\text{N}}{\text{mm}}\right]$.

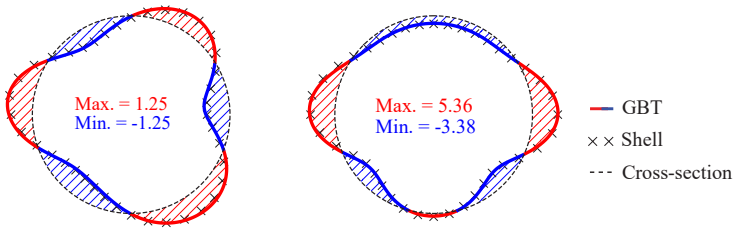

(a) Q_φ (b) Q_θ

Figure 3.24: Comparison of shear force per unit length at section A $\left[\frac{\text{N}}{\text{mm}}\right]$.

Table 3.6: Comparison of GBT and shell results at section A.

	M_φ	M_θ	$M_{\varphi\theta}$	N_φ	N_θ	$N_{\varphi\theta}$	Q_φ	Q_θ	w_{local}	w_{bending}	w_{total}
Mean relative difference [%]	4.01	3.49	2.11	5.54	5.00	1.80	5.65	3.27	0.17	0.12	0.13
Standard deviation [%]	3.14	2.39	1.22	2.23	4.69	3.41	3.12	2.79	0.42	0.00	0.04

3.5.3 Internal pressure loading

The longitudinal bending deformation of circular pipe bends due to an internal pressure is a common problem in pipeline systems. To analyze this problem using the developed GBT formulation, an example of a 45° pipe bend with a radius ratio of $\alpha = \frac{1}{10}$ is considered. As shown in Figure 3.25, both ends of the pipe are clamped and the pipe is loaded with an internal pressure load throughout the span. Based on the

loading condition and bend radius ratio α, the only modes which have an external load contribution are axisymmetric mode a, bending mode 3, and ovalization mode 5. Here, considering odd modes up to 13 with their respective SU and SV modes is enough to reach convergence (Table 3.7). In this example, the model consisted of 18 GBT elements.

Table 3.7: Comparison of shell and GBT with different modes.

Type of analysis	Max. displacement at the mid span [mm]	Mean relative difference [%]
Shell	0.5103	-
GBT, RB(1,3) + a + LS(5,7,9)+ SU + SV modes	0.5112	0.298
GBT, RB(1,3) + a + LS(5,7,9,11,13)+ SU + SV modes	0.5109	0.087
GBT, RB(1,3) + a + LS(5,7,9,11,13,15,17)+ SU + SV modes	0.5109	0.087

$R = 3000\,\text{mm}$
$r = 300\,\text{mm}$
$t = 15\,\text{mm}$
$\psi = 45°$
$E = 205\,\text{GPa}$
$\mu = 0.3$
$q = 10\frac{\text{N}}{\text{mm}^2}$

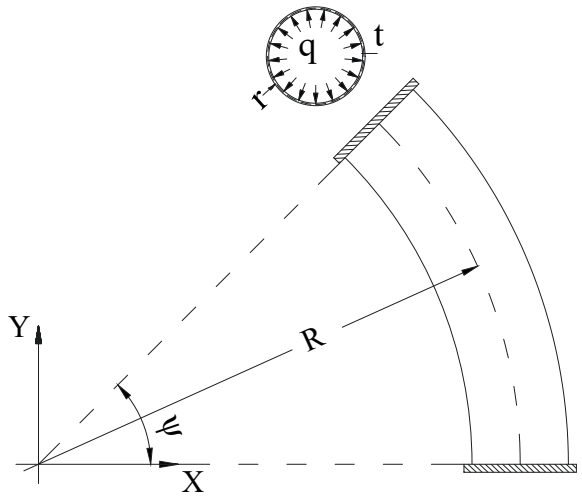

Figure 3.25: Internal pressure loading of an end restrained 45° pipe bend.

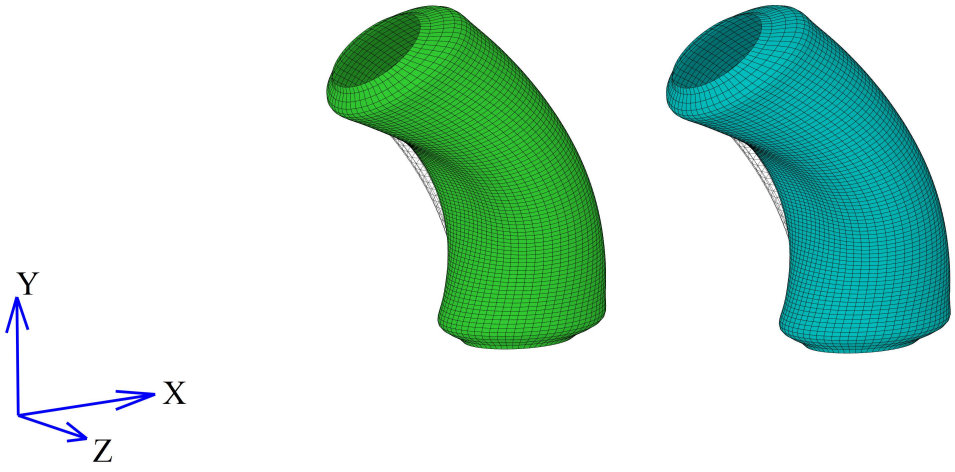

(a) GBT (b) Shell

Figure 3.26: Internal pressure loading deformation shape of an end restrained 45° pipe bend (×600).

In Figures 3.27 to 3.30, detailed cross-sectional comparisons of displacement and stress resultants of GBT and shell are presented at the mid span of the pipe bend.

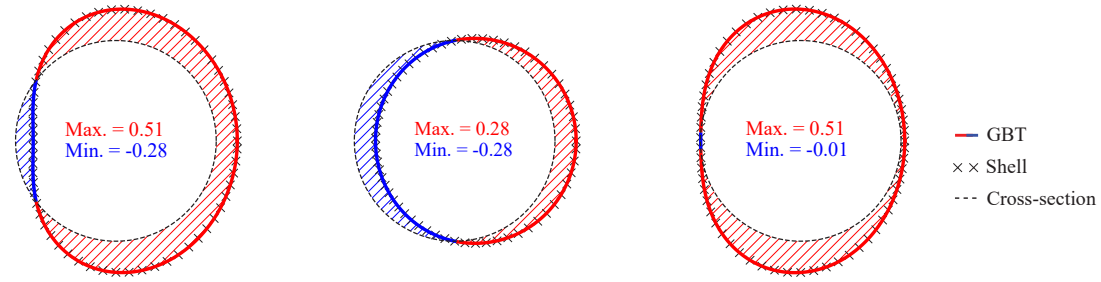

(a) w_{total} (×580) (b) w_{bending} (×715) (c) w_{local} (×580)

Figure 3.27: Comparison of displacements at the mid span [mm].

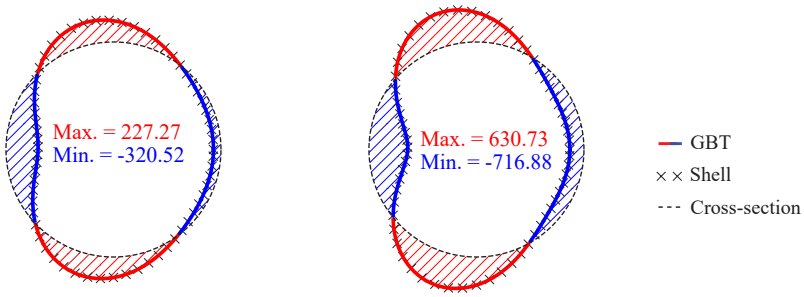

(a) M_φ (b) M_θ

Figure 3.28: Comparison of bending moment per unit length at the mid span $\left[\frac{\text{Nmm}}{\text{mm}}\right]$.

Stress resultants such as the twist bending moment $M_{\varphi\theta}$, shear membrane force $N_{\varphi\theta}$ and the longitudinal plate's shear Q_φ are zero at the mid span. In Table 3.8, the quantitative differences between GBT and shell displacement and stress resultants are presented which in this case are below 3%.

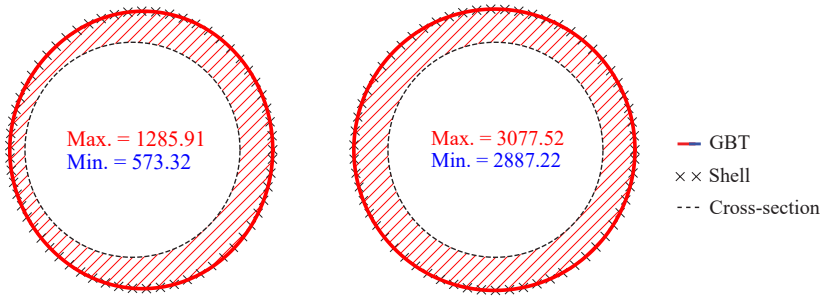

(a) N_φ (b) N_θ

Figure 3.29: Comparison of normal force per unit length at the mid span $\left[\frac{\text{N}}{\text{mm}}\right]$.

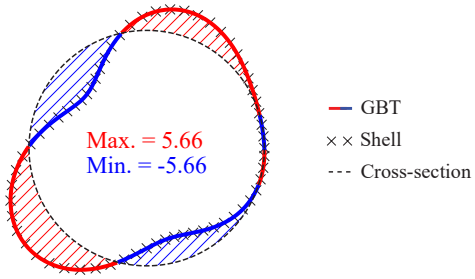

Figure 3.30: Comparison of Q_θ at the mid span $\left[\frac{\text{N}}{\text{mm}}\right]$.

Table 3.8: Comparison of GBT and shell results at the mid span.

	M_φ	M_θ	N_φ	N_θ	Q_θ	w_{local}	w_{bending}	w_{total}
Mean relative difference [%]	0.56	0.14	0.01	0.02	2.90	0.51	0.03	0.08
Standard deviation [%]	1.62	0.03	0.00	0.01	15.88	1.77	0.00	0.05

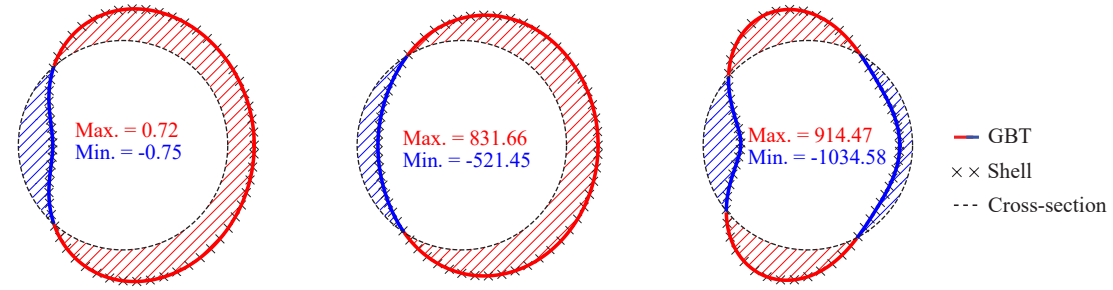

(a) w_{total} (×415) (b) N_φ (c) M_θ

Figure 3.31: Displacement and stress resultants at the mid span when $\mu = 0$.

In this example, due to the boundary condition, the effect of the Poisson ratio is large in both displacement and stress fields. As shown in Figure 3.31, neglecting the Poisson value ($\mu = 0.0$) will result in a significant change of displacement and stress resultants.

3.6 Membrane locking

The membrane locking problem was first identified and analyzed by Stolarski and Belytschko [158, 159] for curved C^1 beam elements with linear axial and cubic transverse displacement fields. This problem results from the inability of an element to represent inextensional bending deformations without additional parasitic membrane contributions [33, 34]. This type of locking only occurs in curved elements since the bending and membrane actions are coupled together.

Here, the critical parameter is the wall thickness of the member since the ratio of bending stiffness in equation (3.27) to membrane stiffness in equation (3.28) is proportional to the square of the thickness t. Hence, the decrease in the wall thickness or increase in the slenderness $\frac{R}{t}$ will cause the large parts of

the internal energy to be from the parasitic membrane action [51, 124].

For the curved GBT formulation presented in this chapter, the membrane locking effect is tested using the in-plane bending numerical example in Section 3.5.1. In this example, all parameters are kept the same except for the wall thickness which is decreased gradually, and Poisson's ratio which is considered to be zero to avoid any possible material-based locking effects.

Table 3.9: In-plane deformation results for a 90° cantilever pipe bend under tip load for different wall thicknesses t.

	Change in thickness t [mm]						
	10	8	6	4	2	1	0.5
Slenderness $\frac{R}{t}$	600	750	1000	1500	3000	6000	12000
Shell model [mm]	48.81	72.94	122.25	253.60	887.45	3137.56	11322.70
GBT model [mm]	48.75	72.81	121.56	246.34	728.56	1749.87	3693.98
Difference [%]	−0.11	−0.18	−0.57	−2.87	−17.90	−44.23	−67.38

In Table 3.9, the maximum tip displacement of the shell (locking-free) and GBT models are compared through the gradual change in thickness of the wall. Unfortunately, the GBT element fails the membrane locking test since the displacement response of the GBT model becomes too stiff and the difference compared to the shell model becomes larger for a higher slenderness ratio. Therefore, the formulated GBT element should not be used for a slenderness ratio higher than 1500 without additional treatment such as reformulation of the GBT element based on a mixed-finite element formulation [73, 118]. Furthermore, in curved pipe members, since their slenderness can also be affected by the radius r, it is important to pay attention to the relationship between R, r, and t.

3.7 Summary

This chapter presents the linear GBT formulation for the analysis of curved thin-walled circular pipes. In this formulation, the virtual work of internal and external forces are derived using Sander's linear kinematic description of doubly curved shells with the displacement functions of GBT. These functions are separated into cross-sectional displacements which are approximated by predefined GBT deformation modes and longitudinal displacement which is approximated by a standard beam finite element method. Here, the coupling between GBT modes due to the radius ratio of the pipe bend is precisely and explicitly determined by including membrane energy contributions of transverse and shear membrane stains.

Several numerical examples are presented to demonstrate the potential of GBT. The GBT solutions are shown to converge in terms of the displacement field components with an increasing number of modes taken into account. In all examples, the mean relative difference between GBT and shell models in

displacement fields is below 0.2%. In some cases, it is observed that the number of GBT modes needed for the convergences of the stress field can be higher than that of the displacement field. In the examples studied, the stress field components of the GBT solutions in regions distant from the boundaries converge faster than those close to the boundaries. Here, depending on the location of the cross-section the mean relative difference between GBT and shell models in the stress fields can be up to 6%.

Furthermore, the numerical examples show that GBT uses a much fewer number of DoF than the shell finite element analysis to achieve an accurate solution in both stress and displacement fields. Particularly in the first example, the GBT model has only 1.20 % of the DoF needed in the shell model.

However, the formulated displacement-based GBT element show limitations due to the membrane locking problem, therefore it should not be applied for the analysis of members with a higher slenderness ratio.

Chapter 4

Vibration analysis of toroidal shells using GBT

The dynamic analysis of pipe bends or toroidal shells is an important part of the design process in applications such as particle accelerators, fusion reactors, spacecrafts, and in many other practical engineering structures. This chapter presents the dynamic analysis extension of the Generalized Beam Theory (GBT) formulation developed in the previous chapter for curved thin-walled pipes.

The dynamic behavior of truncated or closed toroidal shells has been studied extensively based on the linear thin shell theories since the earlier studies of Liepins [92, 93] on free vibrations of prestressed toroidal shells using the finite difference method. Later, studies were conducted to improve the accuracy and computational efficiency of determining the vibration behavior of toroidal shells under different initial conditions by approximating the displacement field using power series expansion [84], Fourier series expansions [90, 139] or series of trigonometric functions [101] and solving the resulting system of partial differential equations using various types of solution approaches, such as Galerkin's method [90, 101], differential quadrature method [173, 174], and Rayleigh-Ritz method [79, 139].

In the context of GBT, the first dynamic formulation of GBT was developed by Schardt [134] to perform a free vibration analysis of thin-walled prismatic sections. Since then, several studies have been conducted on thin-walled prismatic sections, such as a study on the free vibration behavior of loaded cold-formed steel members under axial compression [149] and non-uniform bending [26], the application of GBT for the dynamic analysis of high-speed railway bridge decks [19], the dynamic response analysis of a cold-formed steel lipped channel beam considering damping and various loading conditions [21], the vibration analysis of single-cell regular polygons [59] and multi-cell rectangular tubes [62], and the formulation of exact element shape functions using power series to improve the computational efficiency of the vibration eigenvalue problem [23]. However, for the vibration analysis of thin-walled cylindrical hollow sections (CHS), the only study was conducted by Basaglia [15], who formulated a GBT-based stiffness and mass matrices incorporating the effect of the frame joints.

So far, the GBT studies conducted on curved thin-walled members are limited to static analysis. Hence, the main objective of this chapter is to develop a dynamic GBT formulation for truncated or closed toroidal shells to determine their vibration behavior. The application of the developed GBT formulation is demonstrated by using two numerical examples with different boundary conditions involving a combination and coupling of bending, warping, torsional, axisymmetric, and local GBT deformation modes. For validation purposes, these examples are compared to refined shell finite element models based on the natural vibration frequencies and the associated vibration mode shapes. Here, the similarity of the mode shapes between the GBT and the shell finite element models are quantitatively determined using the Modal Assurance Criterion (MAC) [6] analysis value.

This chapter is organized as follows. First, the variation of the kinetic energy is presented based on Hamilton's principle. Then the possible deformation mode couplings are identified for the out-of-plane and in-plane inertia of the cross-section. This leads to the formulation of the element mass matrix based on the finite element method. Finally, a selection of numerical examples is presented, where the undamped free vibration behavior of the pipes is determined by solving an eigenvalue problem. The validation of the proposed approach is carried out by comparing the results obtained with refined shell finite element models.

4.1 Hamilton's principle

The formulation of the equations of motion describing the dynamic behavior of thin-walled pipes involves the application of Hamilton's Principle, which is given by:

$$\int_{t_1}^{t_2} \delta\left(U_{\text{int}} + U_{\text{ext}} - T\right) dt = 0 \tag{4.1}$$

where δ is the variational operator, U_{int} is the strain energy, U_{ext} is the potential of the applied loads, T is the kinetic energy and t denotes the time.

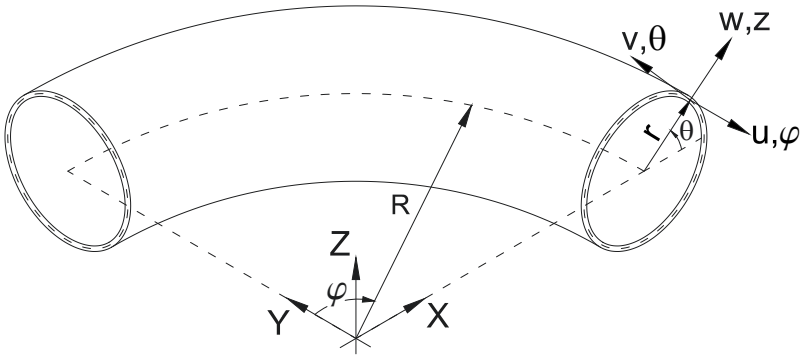

Figure 4.1: Curved thin-walled circular cross-section with global (X, Y, Z) and local ($\varphi \in [-\psi/2, \psi/2]$, $\theta \in [0, 2\pi]$, $z \in [-t/2, t/2]$) coordinate systems.

The variation of the kinetic energy is defined as the volume integral of the products of the material mass density ρ, the velocity components ($u^p_{,t}$, $v^p_{,t}$, $w^p_{,t}$) of an arbitrary wall point p, and its respective virtual velocity:

$$\delta T = \int_V \rho(u^p_{,t}\delta u^p_{,t} + v^p_{,t}\delta v^p_{,t} + w^p_{,t}\delta w^p_{,t})\,\mathrm{d}V \tag{4.2}$$

The orthogonal displacements of the pipe bend at a point p with coordinates (φ, θ, $r + z$) are denoted by u^{p}, v^p, w^p, in the longitudinal, tangential and radial directions, respectively. These displacements can be expressed by u, v and w, which are displacements of points located on the middle surface of the pipe.

$$u^p = \left(1 + z\frac{\cos(\theta)}{R\xi}\right)u - z\frac{w_{,\varphi}}{R\xi} \tag{4.3}$$

$$v^p = \left(1 + z\frac{1}{r}\right)v - z\frac{w_{,\theta}}{r} \tag{4.4}$$

$$w^p = w \tag{4.5}$$

where:

$$\xi = 1 + \alpha\,\cos(\theta)$$
$$\alpha = \frac{r}{R} \tag{4.6}$$

Substituting equations (4.3) to (4.5) into equation (4.2), the δT can be expressed as:

$$\begin{aligned}\delta T = \rho \int_{\frac{-\psi}{2}}^{\frac{+\psi}{2}} \oint \int_{\frac{-t}{2}}^{\frac{+t}{2}} \Bigg(& u_{,t}\delta u_{,t} - z\left(u_{,t}\delta\left(\frac{w_{,\varphi t} - u_{,t}\cos(\theta)}{R\xi}\right) + \delta u_{,t}\,\frac{w_{,\varphi t} - u_{,t}\cos(\theta)}{R\xi}\right) \\ & + z^2\frac{w_{,\varphi t} - u_{,t}\cos(\theta)}{R\xi}\delta\left(\frac{w_{,\varphi t} - u_{,t}\cos(\theta)}{R\xi}\right) + v_{,t}\delta v_{,t} - z\left(v_{,t}\delta\left(\frac{w_{,\theta t} - v_{,t}}{r}\right) - \delta v_{,t}\,\frac{w_{,\theta t} - v_{,t}}{r}\right) \\ & + z^2\frac{w_{,\theta t} - v_{,t}}{r}\delta\left(\frac{w_{,\theta t} - v_{,t}}{r}\right) + w_{,t}\delta w_{,t}\Bigg)\,\xi R\, r\, dz\, d\theta\, d\varphi\end{aligned} \tag{4.7}$$

Then, inserting equations (3.1) to (3.3) into equation (4.7), the variation of the kinetic energy can be rewritten as:

$$\delta T = \sum_{k=1}^{\infty}\sum_{i=1}^{\infty}\int_{\frac{-\psi}{2}}^{\frac{+\psi}{2}} \left({}^{ik}Q\;{}^{i}V_{,\varphi t}(\varphi)^{k}\delta V_{,\varphi t}(\varphi) + {}^{ik}W\;{}^{i}V_{,t}(\varphi)^{k}\delta V_{,t}(\varphi)\right) R\,d\varphi \tag{4.8}$$

with the section properties

$${}^{ik}Q = \rho t \oint {}^{i}u(\theta)^{k}u(\theta)\,\xi\, r\, d\theta + \frac{\rho t^3}{12R^2}\oint \left({}^{i}w(\theta) - {}^{i}u(\theta)\cos(\theta)\right)\left({}^{k}w(\theta) - {}^{k}u(\theta)\cos(\theta)\right)\frac{r}{\xi}\,d\theta \tag{4.9}$$

$$\begin{aligned}{}^{ik}W = \rho t \oint & \left({}^{i}v(\theta)^{k}v(\theta) + {}^{i}w(\theta)^{k}w(\theta)\right)\xi\, r\, d\theta \\ & + \frac{\rho t^3}{12r^2}\oint \left({}^{i}w_{,\theta}(\theta) - {}^{i}v(\theta)\right)\left({}^{k}w_{,\theta}(\theta) - {}^{k}v(\theta)\right)\xi\, r\, d\theta\end{aligned} \tag{4.10}$$

where the first and the second integral terms of the coefficients ${}^{ik}Q$ represent the out-of-plane translational and rotational inertia of cross-section, respectively, whereas for the coefficients ${}^{ik}W$ these terms represent an in-plane translational and rotational inertia of the cross-section.

4.2 Deformation mode coupling

The GBT deformation modes used in this section are the same as the ones derived for circular pipe bends in the previous chapter. The inertia coefficient matrices of the GBT element has off-diagonal terms due to the deformation mode coupling, which is dependent on the radius ratio α of the pipe. Using equations (4.9) and (4.10), the possible mode couplings are identified for out-of-plane ${}^{ik}Q$ and in-plane ${}^{ik}W$ inertia coefficients. Figures 4.2 and 4.3 show the mode coupling between t, a and the first five conventional and non-conventional modes as a sample in a table (matrix).

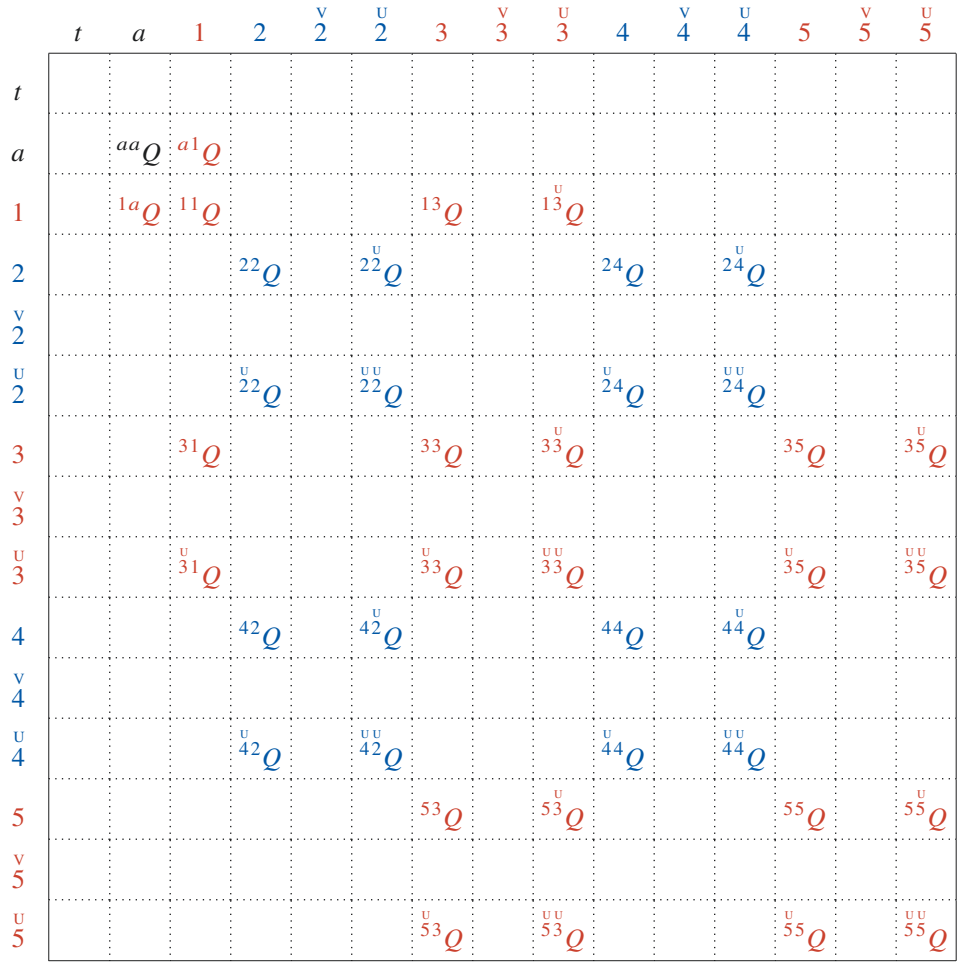

Figure 4.2: List of possible mode couplings for inertia coefficient ${}^{ik}Q$.

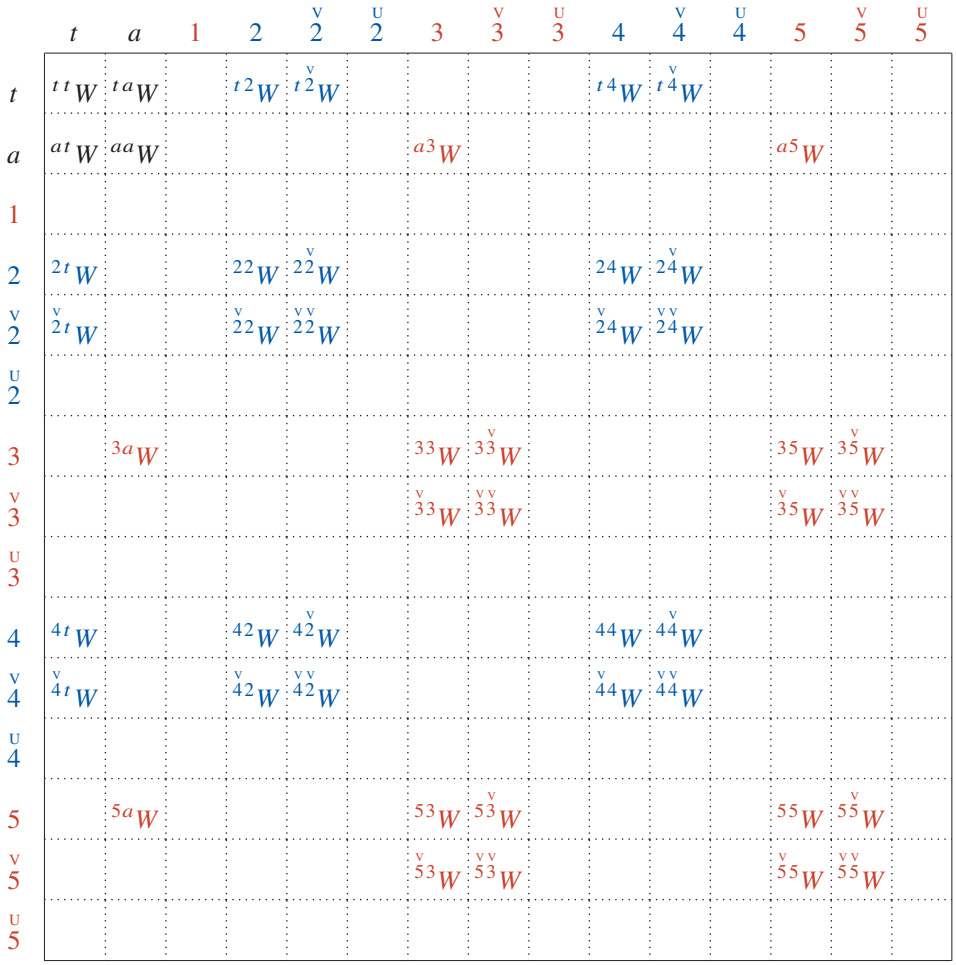

Figure 4.3: List of possible mode couplings for inertia coefficient ${}^{ik}W$.

The empty cells in these tables make evident that the coupling between modes i and k is zero. Here, the contribution of the out-of-plane ${}^{ik}Q$ coefficient is insignificant for all modes besides mode 1. On the other hand, the in-plane ${}^{ik}W$ coefficient has no contribution in mode 1 but is significant for all the other modes.

4.3 Finite element formulation

Following the same procedure used to formulate the element stiffness matrix of curved pipes in the previous chapter, the GBT curved consistent element mass matrix is derived by substituting equations (3.48) and (3.49) into the variation of the kinetic energy equation (4.8). This gives:

$$\delta T = \sum_{k=1}^{\infty} \sum_{i=1}^{\infty} \left({}^{ik}Q \, {}^{ik}\left[\mathbb{V}_8\right] + {}^{ik}W \, {}^{ik}\left[\mathbb{V}_7\right] \right) {}^{i}\{\vartheta\}_{,t} \tag{4.11}$$

where:

$${}^{ik}\left[\mathbb{V}_7\right] = {}^{k}[Sh]^T \int_{\frac{-\psi}{2}}^{\frac{+\psi}{2}} {}^{k}\{T\varphi\}^T \, {}^{i}\{T\varphi\} \; R \, d\varphi \; {}^{i}[Sh] \tag{4.12}$$

$${}^{ik}\left[\mathbb{V}_8\right] = {}^{k}[Sh]^T \int_{\frac{-\psi}{2}}^{\frac{+\psi}{2}} {}^{k}\{T\varphi\}_{,\varphi}^T \, {}^{i}\{T\varphi\}_{,\varphi} \; R \, d\varphi \; {}^{i}[Sh] \tag{4.13}$$

Equations (4.12) and (4.13) are the same as equations (3.56) and (3.57), respectively.

The sub-matrix component ${}^{ik}[m]$ of the element mass matrix is extracted from equation (4.11) as:

$${}^{ik}[m] = {}^{ik}Q \, {}^{ik}\left[\mathbb{V}_8\right] + {}^{ik}W \, {}^{ik}\left[\mathbb{V}_7\right] \tag{4.14}$$

The element mass matrix $[M]^e$ in equation (4.16) is built based on the sub-matrix in equation (4.14). The existence of the matrix ${}^{ik}[m]$ depends on the possible mode coupling between modes i and k as explained in Section 4.2.

The order of deformation modes used in the element mass matrix is given on the corresponding generalized modal amplitude vector $\{d\}$ in equation (4.15).

$$\{d\}^T = \left\{ {}^{a}\{\vartheta\}, {}^{1}\{\vartheta\}, {}^{3}\{\vartheta\}, {}^{\overset{v}{3}}\{\vartheta\}, {}^{\overset{u}{3}}\{\vartheta\}, \ldots, {}^{t}\{\vartheta\}, {}^{2}\{\vartheta\}, {}^{\overset{v}{2}}\{\vartheta\}, {}^{\overset{u}{2}}\{\vartheta\}, {}^{4}\{\vartheta\}, \ldots \right\} \tag{4.15}$$

- Mass lumping or diagonalization: the densely populated consistent element mass matrix in equation (4.16) has a drawback for the future implementation of an explicit finite element method [175], which is a useful tool in solving the large deformation transient dynamics problem. The diagonalization of the mass matrix will avoid the need for inverting the mass matrix and decouple the system of equations, which makes the explicit method efficient and practical. Simpler mass lumping schemes such as the row sum method and diagonal scaling [50, 180] cannot be applied in this case since they would lead to wrong results. Here, the application of a more advanced mass lumping technique for GBT's consistent element mass matrix needs to be studied, which is beyond the scope of this dissertation.

$$
[M]^e = \begin{bmatrix}
{}^{aa}[m] & {}^{a1}[m] & [0] & [0] & [0] & [0] & [0] & [0] & \dots & {}^{at}[m] & [0] & [0] & [0] & [0] & [0] & \dots \\
 & {}^{11}[m] & {}^{13}[m] & [0] & {}^{1\overset{\cup}{3}}[m] & [0] & [0] & [0] & \dots & [0] & [0] & [0] & [0] & [0] & [0] & \dots \\
 & & {}^{33}[m] & {}^{3\overset{\vee}{3}}[m] & {}^{3\overset{\cup}{3}}[m] & {}^{35}[m] & {}^{3\overset{\vee}{5}}[m] & {}^{3\overset{\cup}{5}}[m] & \dots & [0] & [0] & [0] & [0] & [0] & [0] & \dots \\
 & & & {}^{\overset{\vee}{3}\overset{\vee}{3}}[m] & [0] & {}^{\overset{\vee}{3}5}[m] & {}^{\overset{\vee}{3}\overset{\vee}{5}}[m] & [0] & \dots & [0] & [0] & [0] & [0] & [0] & [0] & \dots \\
 & & & & {}^{\overset{\cup}{3}\overset{\cup}{3}}[m] & {}^{\overset{\cup}{3}5}[m] & [0] & {}^{\overset{\cup}{3}\overset{\cup}{5}}[m] & \dots & [0] & [0] & [0] & [0] & [0] & [0] & \dots \\
 & & & & & {}^{55}[m] & {}^{5\overset{\vee}{5}}[m] & {}^{5\overset{\cup}{5}}[m] & \dots & [0] & [0] & [0] & [0] & [0] & [0] & \dots \\
 & & & & & & {}^{\overset{\vee}{5}\overset{\vee}{5}}[m] & [0] & \dots & [0] & [0] & [0] & [0] & [0] & [0] & \dots \\
 & & & & & & & {}^{\overset{\cup}{5}\overset{\cup}{5}}[m] & \dots & [0] & [0] & [0] & [0] & [0] & [0] & \dots \\
 & & & & & & & & \ddots & [0] & [0] & [0] & [0] & [0] & [0] & \dots \\
 & & & & & & & & & {}^{tt}[m] & {}^{t2}[m] & {}^{t\overset{\vee}{2}}[m] & [0] & {}^{t4}[m] & {}^{t\overset{\vee}{4}}[m] & \dots \\
 & & & & & & & & & & {}^{22}[m] & {}^{2\overset{\vee}{2}}[m] & {}^{2\overset{\cup}{2}}[m] & {}^{24}[m] & {}^{2\overset{\vee}{4}}[m] & \dots \\
 & & & & & & & & & & & {}^{\overset{\vee}{2}\overset{\vee}{2}}[m] & [0] & {}^{\overset{\vee}{2}4}[m] & {}^{\overset{\vee}{2}\overset{\vee}{4}}[m] & \dots \\
 & & & & & & & & & & & & {}^{\overset{\cup}{2}\overset{\cup}{2}}[m] & {}^{\overset{\cup}{2}4}[m] & [0] & \dots \\
 & & & & & & & & & & & & & {}^{44}[m] & {}^{4\overset{\vee}{4}}[m] & \dots \\
 & & & & & & & & & & & & & & {}^{\overset{\vee}{4}\overset{\vee}{4}}[m] & \dots \\
sym. & & & & & & & & & & & & & & & \ddots
\end{bmatrix}
\tag{4.16}
$$

4.4 Numerical examples

In this section, two examples of truncated and closed toroidal shells with fixed and free boundary conditions are presented. Here, the undamped free vibration behavior of the pipes is determined by solving an eigenvalue problem

$$\big([K] - \omega^2[M]\big)\{d\} = \{0\} \tag{4.17}$$

where $[K]$ is the member stiffness matrix, $[M]$ is the member mass matrix, $\{d\}$ is the generalized modal amplitude vector and ω is the circular natural frequency. Both examples are compared to equivalent shell finite element models using ANSYS [10] software. These models have been developed using quadrilateral elements with 6 DoF per node which are based on Reissner-Mindlin's kinematic assumption with linear interpolation functions as implemented in the ANSYS software under the name SHELL 181. The element sizes used for the shell element models are approximately 30×30 mm.

4.4.1 Cantilever arch pipe

In this example, a cantilever pipe bend with a radius ratio of $\alpha = \dfrac{1}{6}$ and a bend angle of $\psi = \dfrac{\pi}{2}$ is considered. The cross-section dimensions and material parameters are provided in Figure 4.4. The GBT analysis is performed considering several combinations of the deformation mode classes RB, a, LS, SU, and SV which have previously been described in Sections 2.2.5 and 3.2. In the case of LS deformation modes and their respective SU and SV modes, the analyses are carried out considering modes up to 10, 15, and 20 in order to check the convergence of the solution.

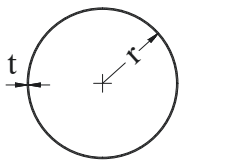

(a) Cross-section

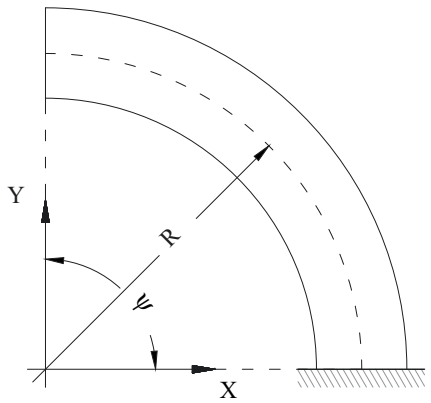

$R = 3000\,\text{mm}$
$r = 500\,\text{mm}$
$t = 10\,\text{mm}$
$\psi = 90°$
$E = 205\,\text{GPa}$
$\rho = 7850\,\dfrac{\text{kg}}{\text{m}^3}$
$\mu = 0.3$

(b) Cantilever arch pipe

Figure 4.4: Free vibration analysis of a 90° cantilever arch pipe.

Here, for the selected number and types of GBT deformation modes the element mass and stiffness matrices are built using equations (4.16) and (3.67), respectively.

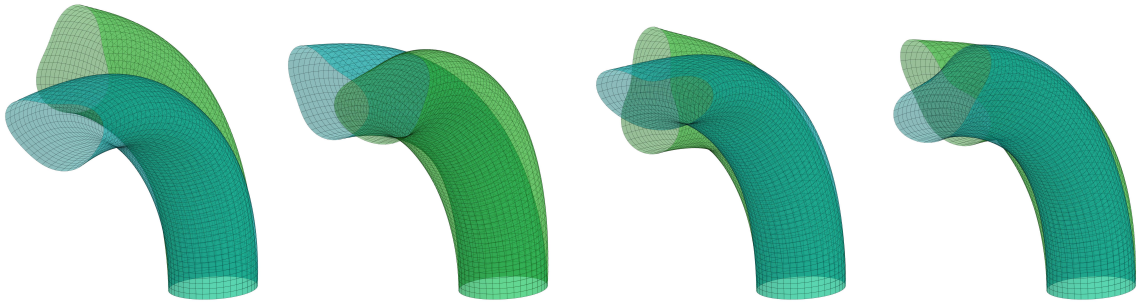

(a) Mode 1, $n = 1$, $m = 1$ (b) Mode 2, $n = 1$, $m = 1$ (c) Mode 3, $n = 2$, $m = 1$ (d) Mode 4, $n = 2$, $m = 1$

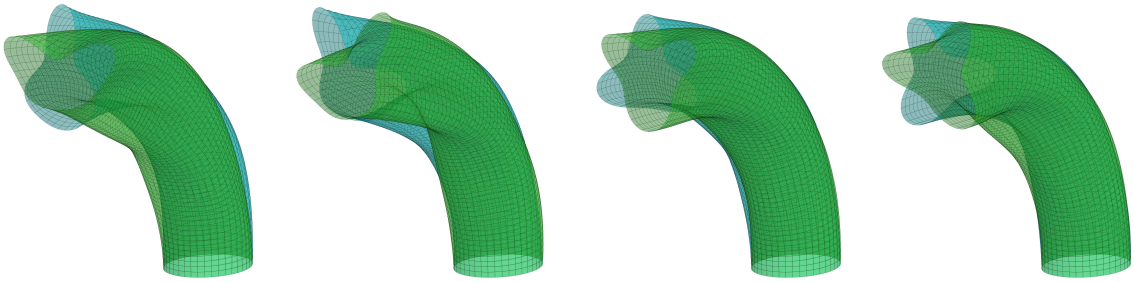

(e) Mode 5, $n = 3$, $m = 1$ (f) Mode 6, $n = 3$, $m = 1$ (g) Mode 7, $n = 3$, $m = 2$ (h) Mode 8, $n = 3$, $m = 2$

Figure 4.5: The first eight natural modes of a 90° cantilever pipe bend.

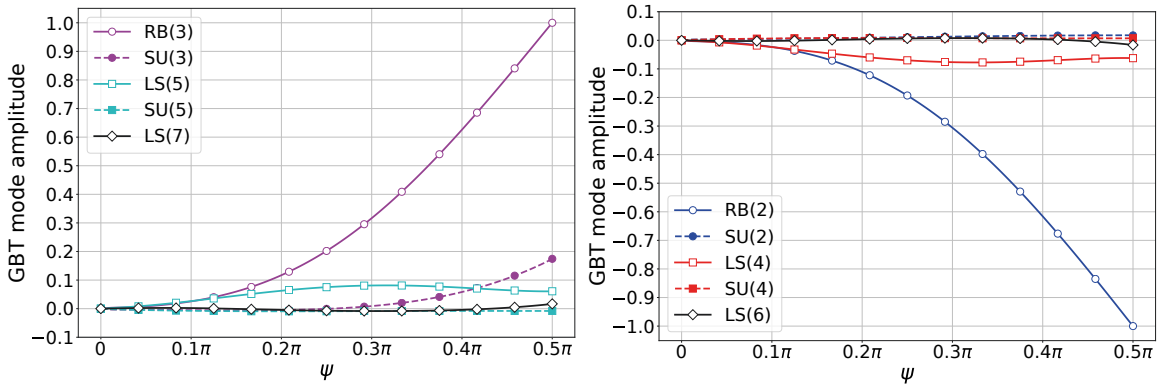

(a) Vibration mode 1

(b) Vibration mode 2

(c) Vibration mode 3

(d) Vibration mode 4

Figure 4.6: Participation of GBT modes (RB(rigid-body), LS(local shell-type), SU(Shear-u)) to the vibration modes of a 90° cantilever pipe bend.

Longitudinally, the GBT model is discretized into 20 elements. Considering the number of GBT deformation modes and elements used, the total Dof for the GBT model is 1, 909 which is below 3.40 % of the equivalent shell element model which has 56, 880 DoF.

In Figure 4.5, the mode shapes of the GBT model are illustrated as an overlay for the two extreme ranges of vibration. The parameters m and n represent the longitudinal and circumferential (cross-sectional) wave number, respectively.

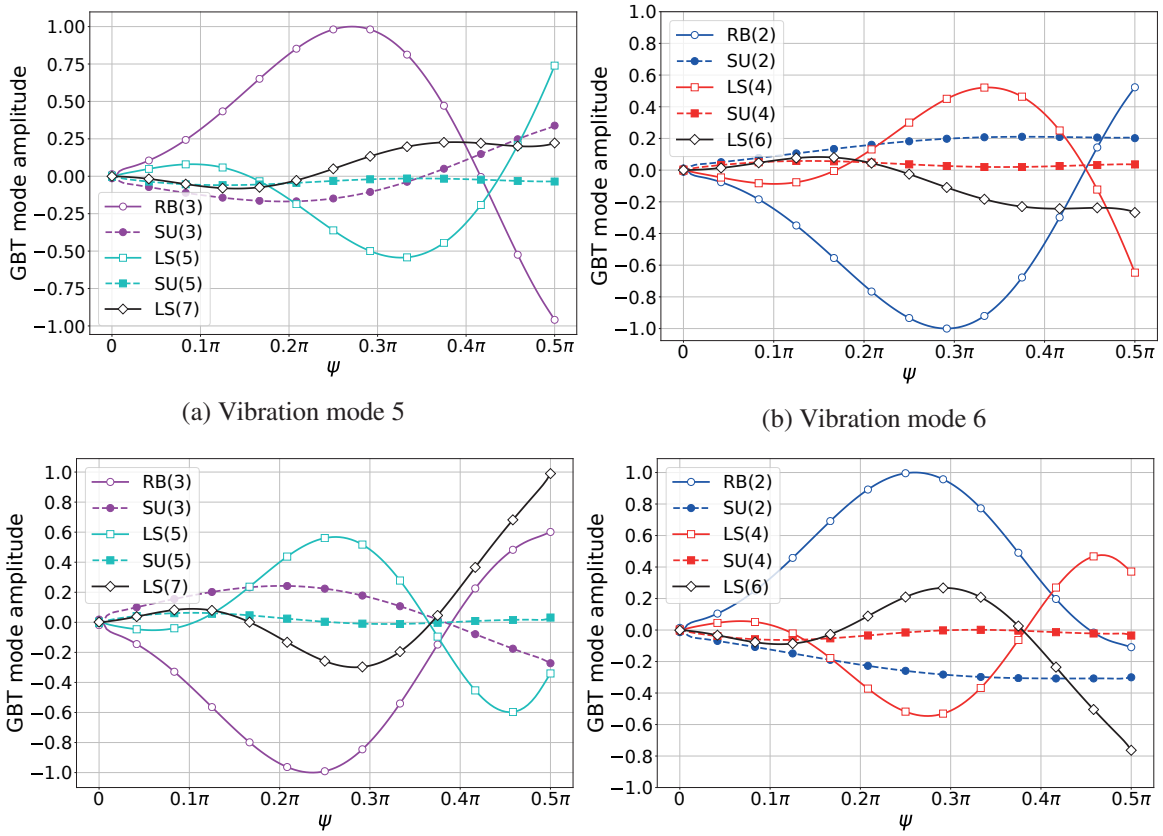

(a) Vibration mode 5

(b) Vibration mode 6

(c) Vibration mode 7

(d) Vibration mode 8

Figure 4.7: Participation of GBT modes to the vibration modes of a 90° cantilever pipe bend.

In Figures 4.6 and 4.7, the modal decomposition of GBT is presented for each of the first eight vibration modes of the cantilever arch pipe. In these figures, only the participation of the GBT modes with a significant contribution is shown after normalizing the generalized modal amplitude vectors. The first and second vibration modes, which are in-plane and out-of-plane bending modes, are mainly from the GBT RB modes 3 and 2, respectively.

In general, vibration modes involving in-plane vibrations (odd vibration modes) are only dependent on the odd GBT modes. Similarly, vibration modes involving out-of-plane vibrations (even vibration modes) are only dependent on the even GBT modes. This characteristic is associated with the GBT element stiffness and mass matrices, in which the coupling of GBT modes only exists within even or odd modes, while no coupling exists between even and odd modes. The contribution of LS modes becomes more

significant for higher vibration modes. The SU modes in general have a higher contribution than the SV modes. The effect of the SU modes can be observed more significantly in odd vibration modes.

In Table 4.1, the associated natural frequencies of the GBT model mode shapes are compared to the shell model. Here, it is evident that the GBT model converges rapidly to the shell model solution when more GBT deformation modes are considered in the analysis. However, Table 4.1 also shows that the change in the natural frequencies is insignificant for the increment of modes above 15. The maximum relative difference (equation (4.18)) of the natural frequencies between the GBT model (15 modes) and the shell model is below 0.80 %.

$$\text{Relative difference} = \frac{f_{\text{GBT}} - f_{\text{Shell}}}{f_{\text{Shell}}} \times 100\% \tag{4.18}$$

where f_{GBT} and f_{Shell} are the natural frequencies of the GBT and shell model, respectively.

Table 4.1: Comparison of GBT with different modes and shell results.

Mode No.	n	m	Natural frequency (Hz)				Relative difference [%]
			GBT (10 modes)	GBT (15 modes)	GBT (20 modes)	Shell	
1	1	1	21.48	21.13	21.13	21.13	0.02
2	1	1	21.66	21.60	21.60	21.60	0.03
3	2	1	40.39	39.80	39.80	39.85	−0.12
4	2	1	40.48	40.37	40.37	40.42	−0.12
5	3	1	82.02	79.53	79.53	79.67	−0.18
6	3	1	82.55	81.75	81.75	81.94	−0.22
7	3	2	94.29	92.84	92.84	93.16	−0.34
8	3	2	95.15	94.00	94.00	94.30	−0.32
9	3	3	131.84	128.92	128.92	129.30	−0.29
10	3	3	133.85	132.91	132.91	133.34	−0.32
11	4	3	144.26	144.18	144.18	144.09	0.06
12	4	3	157.84	155.29	155.29	156.41	−0.72

In addition to the comparison of the natural frequencies, the similarity of the GBT and shell model vibration mode shapes are quantitatively compared to each other using the Modal Assurance Criterion (MAC) [6]. The MAC value is calculated as the normalized scalar product of the two sets of vectors $\{\phi_A\}$ and $\{\phi_X\}$. The resulting scalars are arranged into the MAC matrix.

$$\text{MAC}(A, X) = \frac{|\{\phi_A\}^T \{\phi_X\}|^2}{(\{\phi_A\}^T \{\phi_A\})(\{\phi_X\}^T \{\phi_X\})} \tag{4.19}$$

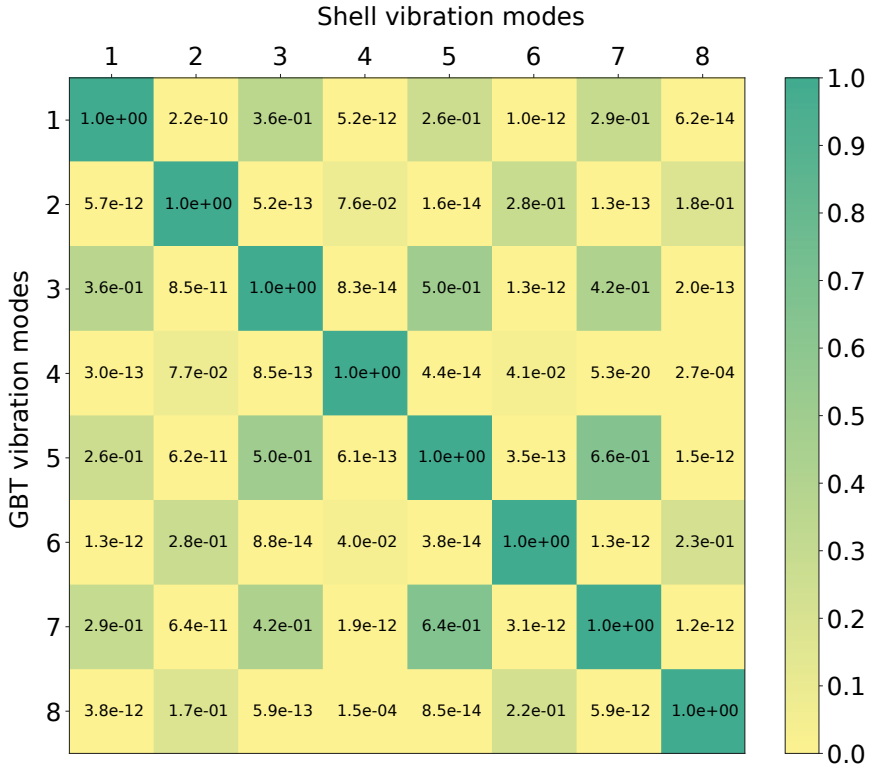

Figure 4.8: MAC value comparison of GBT and shell vibration mode shapes considering the warping displacement (u) of the cantilever arch pipe.

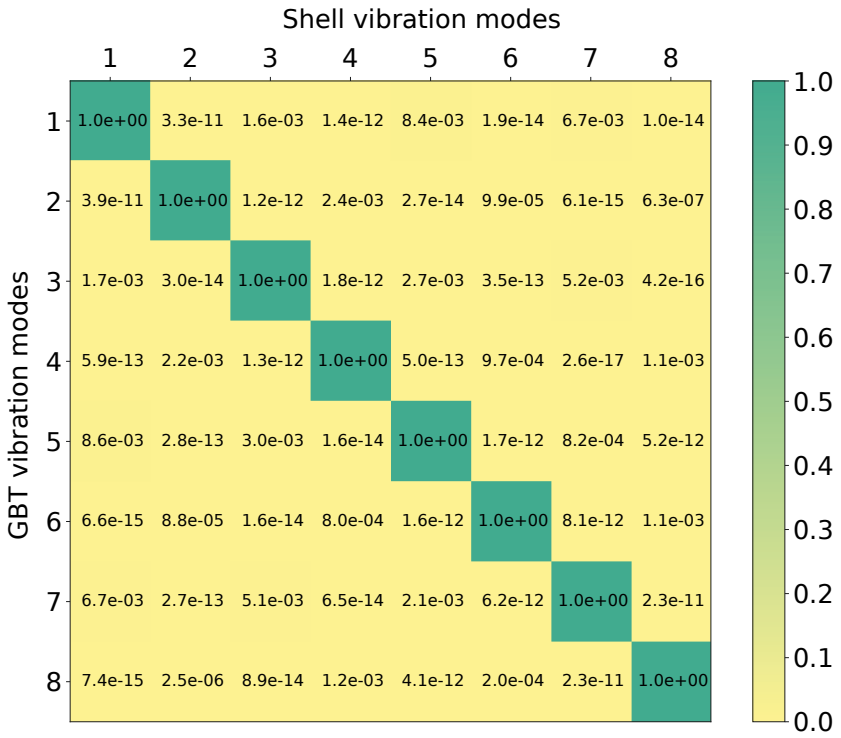

Figure 4.9: MAC value comparison of GBT and shell vibration mode shapes considering the tangential and radial displacements ($v + w$) of the cantilever arch pipe.

In equation (4.19), the vectors $\{\phi_A\}$ and $\{\phi_X\}$ are built for the GBT and shell mode shapes, respectively, by using the local u, v, and w displacements. If the result of the MAC value is closer to one, the two mode shapes are identical or fully correlated, whereas if the MAC value is closer to zero, the mode shapes are different or have no correlation. In this example, since the longitudinal displacements u are much smaller than the transverse displacements $v + w$, the MAC values are quantified treating both directions separately. In Figure 4.8, the MAC values are presented for the longitudinal displacement u, while in Figure 4.9 the MAC values are computed by stacking the transverse displacements v and w together. Here, both MAC matrices show a strong correlation for all modes, which is in complete agreement with the previous assessment regarding the natural frequencies.

4.4.2 Toroidal shell

In this example, a closed toroidal shell with a radius ratio of $\alpha = \frac{2}{5}$ and a free support condition is considered. The geometric and physical properties shown in Figure 4.10 are taken from the example in [139], where the authors used a semi-analytical method to determine the vibration behavior. Following the same procedure as in the previous example, the number of GBT deformation modes needed to reach convergence is determined. Here, the total DoF of the GBT model considering 15 deformation modes and 80 elements longitudinally is 7, 280 which is below 7.0 % of the equivalent shell element model with 104, 280 DoF.

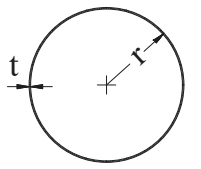

(a) Cross-section

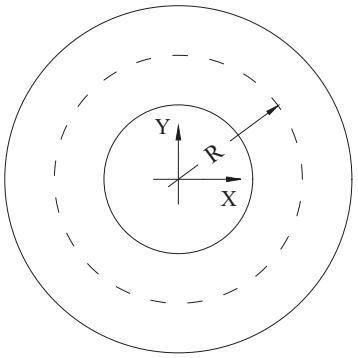

$R = 1000\,\text{mm}$
$r = 400\,\text{mm}$
$t = 10\,\text{mm}$
$E = 210\,\text{GPa}$
$\rho = 7850\frac{\text{kg}}{\text{m}^3}$
$\mu = 0.3$

(b) Toroidal shell

Figure 4.10: Closed toroidal shell.

In Figure 4.11, the first eight mode shapes of the GBT model are shown. Except for the first mode, all the other modes shown in the figure appear twice due to the spatial symmetry of the model. The detailed cross-sectional profiles showing the classification of mode types (symmetric or asymmetric) can be referred in [139]. In Figures 4.12 and 4.13, the modal decomposition of GBT is presented for each of the first eight vibration modes of the toroidal shell. For the first vibration mode, the longitudinal wave number $m = 0$ since the contributing even GBT mode amplitudes are constant (Figure 4.12a). In general, the longitudinal wave number of the vibration modes corresponds with the periodic wave number of the GBT mode's amplitude.

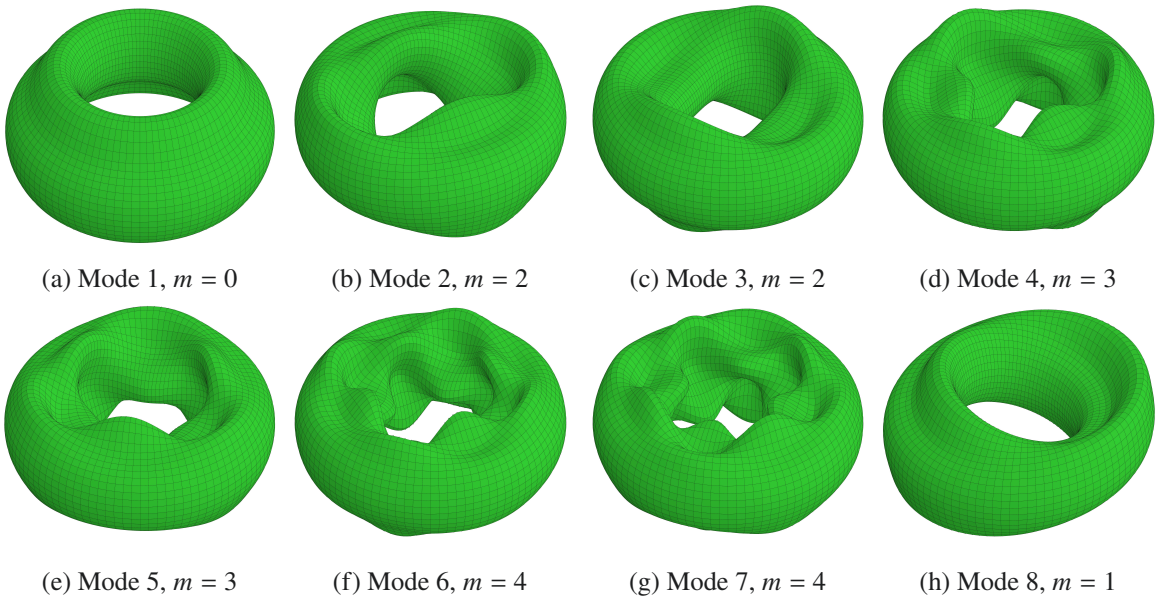

(a) Mode 1, $m = 0$ (b) Mode 2, $m = 2$ (c) Mode 3, $m = 2$ (d) Mode 4, $m = 3$

(e) Mode 5, $m = 3$ (f) Mode 6, $m = 4$ (g) Mode 7, $m = 4$ (h) Mode 8, $m = 1$

Figure 4.11: The first eight natural modes of the toroidal shell.

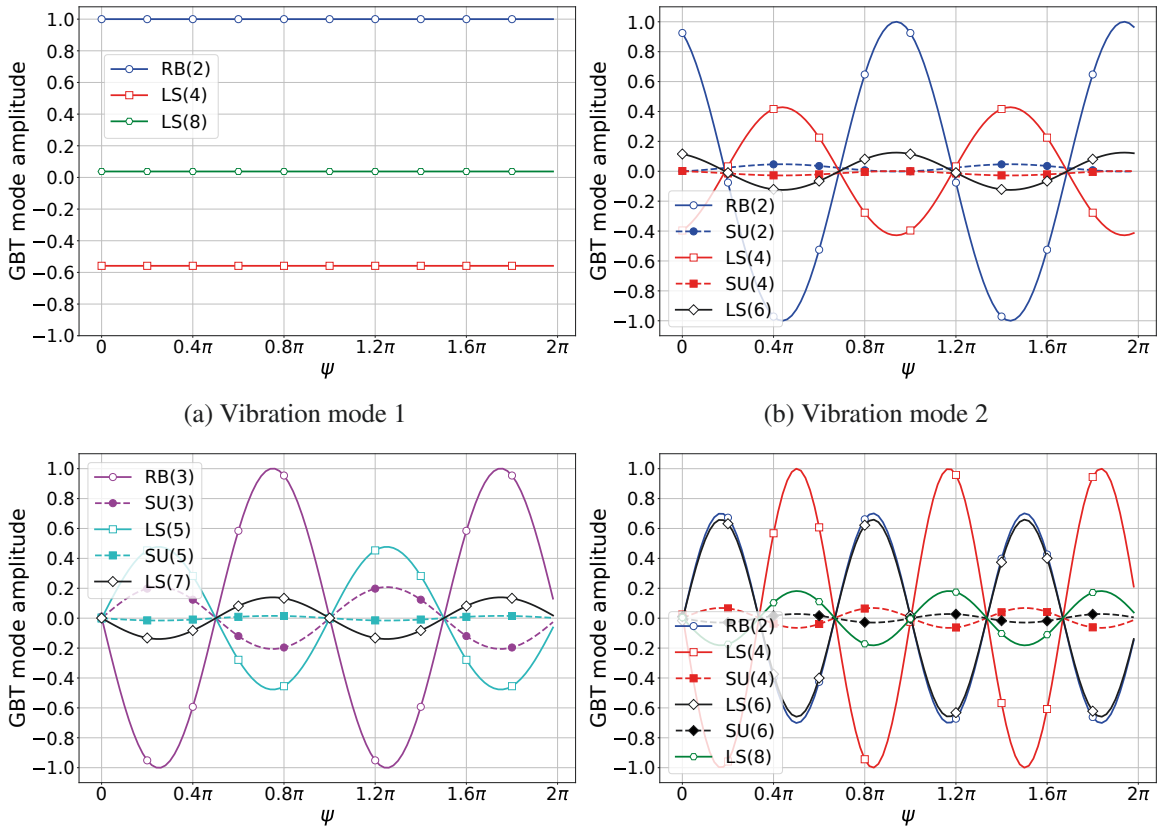

(a) Vibration mode 1 (b) Vibration mode 2

(c) Vibration mode 3 (d) Vibration mode 4

Figure 4.12: Participation of GBT modes (RB (rigid-body), LS (local shell-type), SU (Shear-u)) to the vibration modes of toroidal shell.

From vibration modes 2 till 7, the contribution of LS modes increases gradually since the cross-sectional wave number of the vibration modes are directly related to that of the LS modes. The vibration mode 8 is dependent on even GBT modes with a significant participation of SV and SU modes.

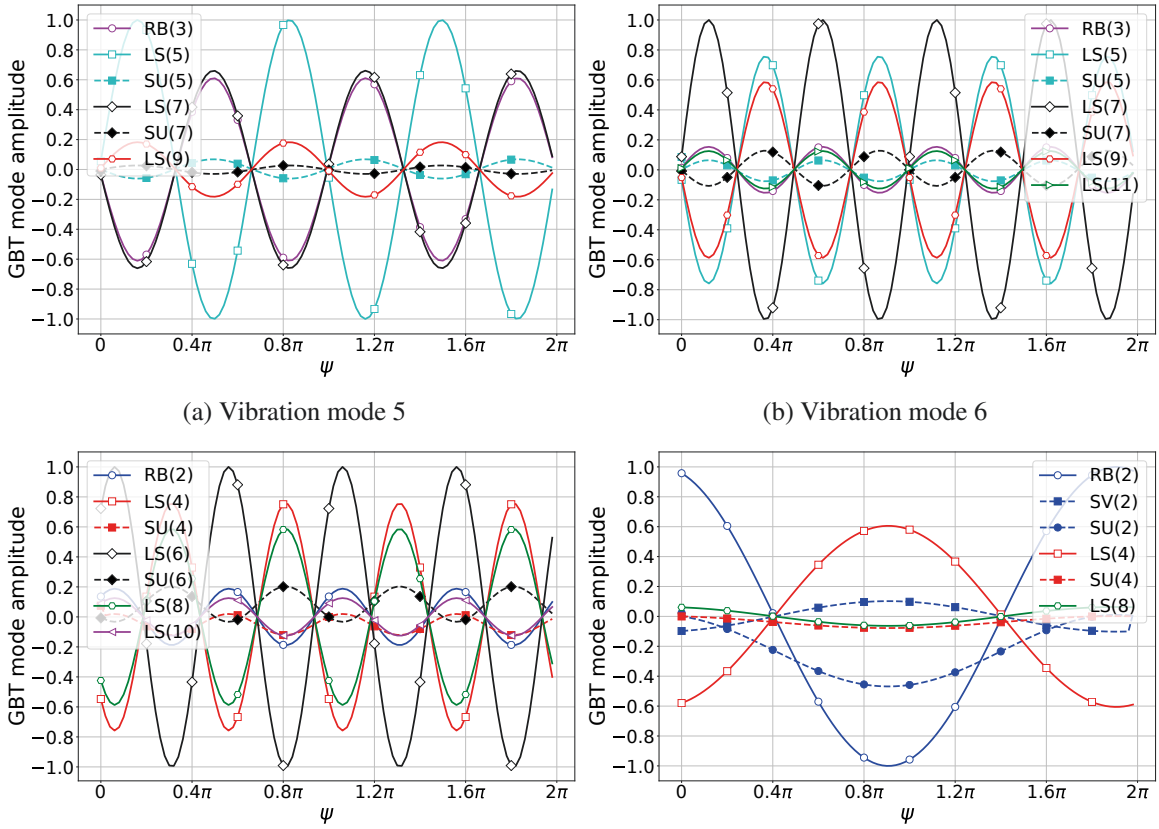

(a) Vibration mode 5

(b) Vibration mode 6

(c) Vibration mode 7

(d) Vibration mode 8

Figure 4.13: Participation of GBT modes (RB (rigid-body), LS (local shell-type), SV (Shear-v), SU (Shear-u)) to the vibration modes of toroidal shell.

In Table 4.2, the first 11 natural frequencies are presented for the GBT model using 15 and 20 deformation modes, the results of reference [139] using 15 Fourier terms, and the shell model. The last column in Table 4.2 shows the relative difference between the GBT model with 15 deformation modes and the shell model. Here, the maximum relative difference is below 0.30%.

In Figure 4.14, the comparison of mode shapes between the GBT model and the shell model is performed by computing the MAC values for the longitudinal displacements u, while in Figure 4.15, the MAC values are computed by stacking the transverse displacements v and w together. Here, the corresponding GBT and shell mode shapes were chosen from their subspaces such that a proper alignment (spatial rotation) could be achieved before the computation of the MAC values. The results show the total correlation between the vibration modes of the GBT and shell analyses. In Figure 4.14, the MAC value for the vibration mode 1 is zero since the mode does not have any warping displacements u.

Table 4.2: Comparison of GBT with different modes and shell results.

Mode No.	Mode type	m	Natural frequency (Hz)				Relative difference [%]
			GBT (15 modes)	GBT (20 modes)	Ref. [139]	Shell	
1	Asym.	0	80.85	80.78	80.73	80.74	0.138
2	Asym.	2	110.53	110.30	111.11	110.32	0.191
3	Sym.	2	122.44	122.17	123.05	122.20	0.193
4	Asym.	3	205.77	205.68	207.40	205.76	0.003
5	Sym.	3	206.22	206.33	207.85	206.22	0.001
6	Sym.	4	307.08	307.22	309.74	307.90	−0.265
7	Asym.	4	307.23	307.74	309.89	308.05	−0.265
8	Asym.	1	351.23	351.24	351.06	351.27	−0.012
9	Asym.	2	398.76	398.46	398.61	398.87	−0.027
10	Sym.	2	401.49	401.50	401.28	401.56	−0.018
11	Sym.	1	415.69	415.68	415.22	415.74	−0.013

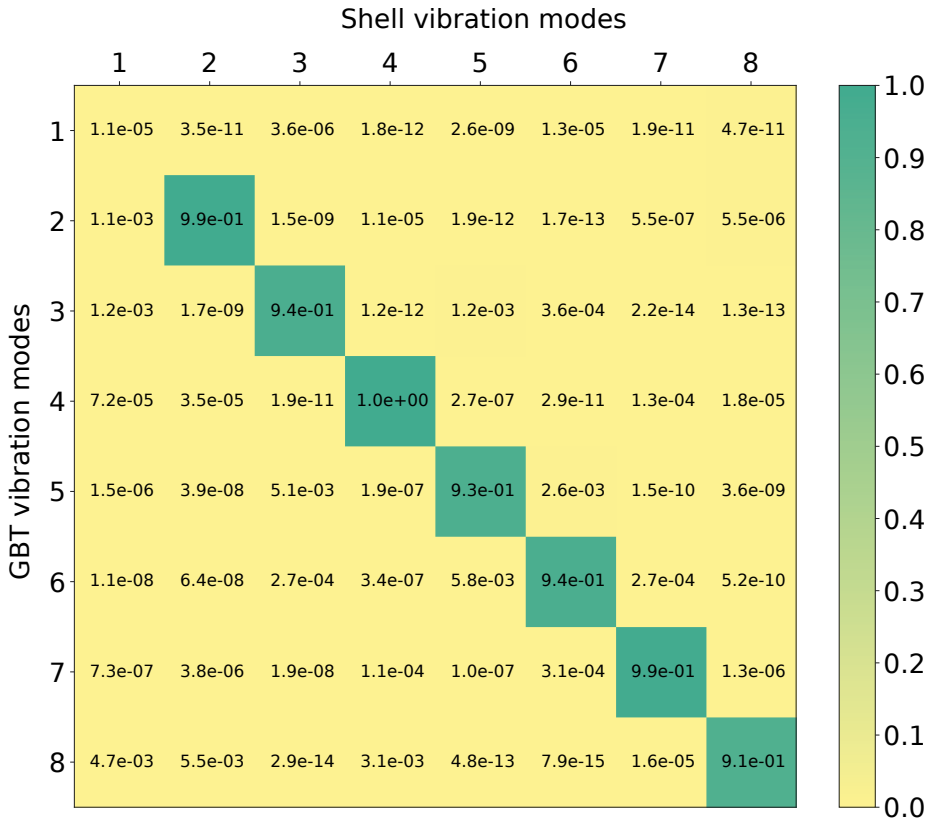

Figure 4.14: MAC value comparison of GBT and shell mode shapes considering the warping displacements (u) of the toroidal shell.

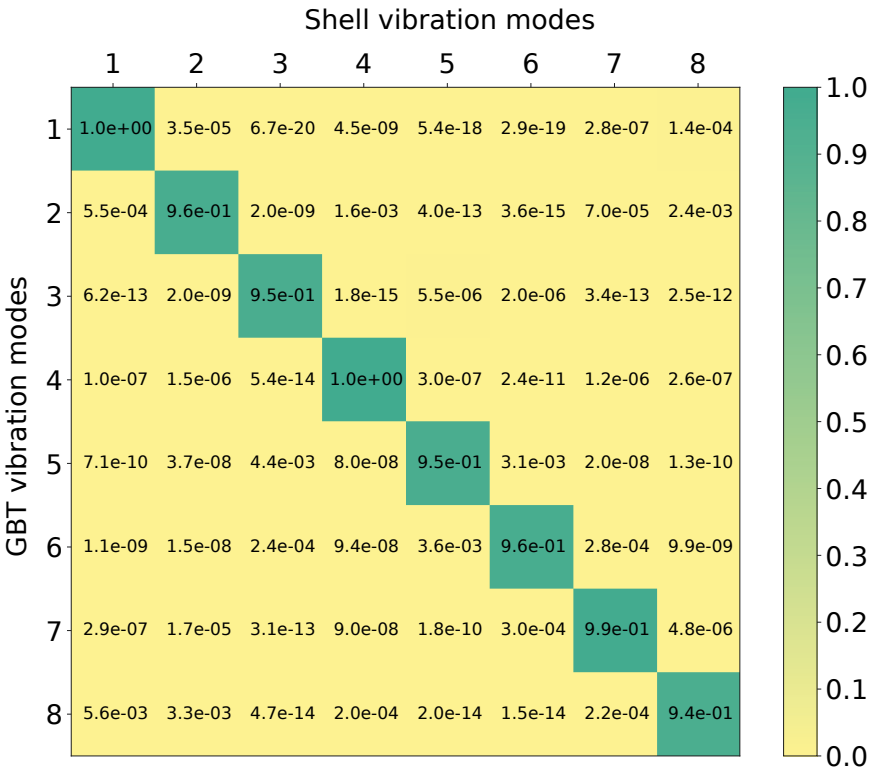

Figure 4.15: MAC value comparison of GBT and shell mode shapes considering the tangential and radial displacements ($v + w$) of the toroidal shell.

4.5 Summary

A dynamic GBT formulation for the analysis of curved thin-walled pipes has been presented in this chapter. Here, the inertia of the GBT element is formulated from the variation of the kinetic energy. Due to the radius ratio α, the consistent mass matrix derived from this formulation has off-diagonal terms as a result of the deformation mode coupling within even modes and odd modes in both in-plane and out-of-plane inertia components. Longitudinally, the GBT solution is approximated using a standard beam finite element method.

Two numerical examples have been presented to exhibit the potential of the dynamic GBT formulation, specifically by conducting the analysis of the undamped free vibration of arch pipes and toroidal shells involving a combination and coupling of several GBT deformation modes. The eigenvalues of the GBT modal solution converge with an increasing number of deformation modes taken into account. Based on the modal decomposition of GBT, the shear modes have a significant contribution to the vibration modes. In both examples, the relative difference between the GBT and shell models regarding the natural frequencies did not exceed 0.80 %. In addition, the MAC values have demonstrated the full correlation of the mode shapes between the GBT and the shell models. Hence, the few number of GBT deformation modes and elements used in the GBT modal analysis provide a comprehensive insight into the structural behavior of curved members with significantly fewer DoF than the shell element models.

Based on recent studies which have developed a coupling scheme between the GBT and the shell finite element analysis [30, 95], it is possible to incorporate GBT into standard commercial FEM software packages and utilize the exceptional computational efficiency of GBT in prismatic and circular thin-walled cross-sections. However, further studies are required to develop a lumped GBT mass matrix which is vital for the application of an explicit dynamic analysis.

Chapter 5

Geometrically nonlinear formulation of GBT for straight pipes

One of the main aspects in the design of pipe members is to minimize the thickness as much as possible to save material and reduce weight. Since the load carrying capacity of pipe members is mainly influenced by their curvature, the buckling of these members is usually caused by the change in geometry rather than failure of the material strength. For example, an increase in the cross-sectional ovalization of a thin-walled circular pipe member during bending will lead to a gradual loss of the bending stiffness. In this chapter, the analysis of this complex structural behavior of thin-walled circular pipe members is carried out through the formulation of a geometrically nonlinear GBT analysis.

The nonlinear circular cylindrical shell theories were established early on based on the shallow-shell assumption [44, 104, 170]. They were mainly applicable for deformations dominated by the radial displacement w. In the study conducted by von Kármán and Tsien [172], the stability of axially loaded circular cylindrical shells was correctly analyzed based on this assumption. However, in theories developed by Flügge [53] for moderately thick shells, and by Novozhilov [108] concerning large deflections of thin shells the shallow-shell assumption was eliminated.

The nonlinear thin shell theory developed by Sanders [126] and Koiter [82] was emphasized on the simplification of the kinematic equations and was suitable for finite deformations with small strains and moderately small rotations. There are several more nonlinear shell theories developed in the past based on the available solution method and the requirement of the structural problem. In general, classical shell theories emphasized on simplicity and omitted relatively small terms, since most of these theories were developed in the pre-computer era for analytical studies [161]. However, with the development of the finite element method, more advanced nonlinear shell theories were formulated considering large displacements, rotations, and strains [5, 34, 76, 155]. These formulations have pushed forward the shell based finite element method to be one of the most reliable and robust tool in the analysis of thin-walled structures.

In the context of GBT, the development of geometrically nonlinear formulations of thin-walled members was mainly focused on prismatic sections. The first geometrically nonlinear GBT formulation was proposed by Silvestre [147] for the elastic post-buckling analysis of uniformly compressed thin-walled members with open cross-sections based on simplified nonlinear kinematic equations. Later, the studies conducted by Gonçalves [63, 65] extended this initial formulation considering large displacements and rotations based on Reissner-Simo's beam theory [119, 154]. This theory is geometrically exact regardless of the magnitude of the displacements and rotations involved. Furthermore, in [58] he included the physical nonlinearity to analyze elastoplastic thin-walled members while keeping the geometrical nonlinearity restricted to the total Lagrangian description. Other studies in this area developed nonlinear formulations based on the implicit corotational method [121], the nonlinear Galerkin method [114], and the nonlinear bending strain terms [97]. However, the most complete nonlinear GBT formulation, which is geometrically exact and considers physical nonlinearity, is presented by Duan [47]. Additionally, he developed a nonlinear explicit dynamic finite element formulation in GBT [45] to simulate the dynamic response of prismatic thin-walled members under transverse impulsive loading.

Unfortunately, in the case of thin-walled circular pipe sections, the nonlinear analysis in GBT is currently limited to the buckling analysis for members subjected to combinations of axial compression and external pressure [15, 16, 143]. So far, no fully geometrical nonlinear GBT formulations are available for the analysis of thin-walled circular pipe sections under arbitrary loading.

Hence, the main objective of this chapter is the development of fully geometrical nonlinear GBT formulations for the analysis of thin-walled circular pipe sections under arbitrary loading. This formulation is based on the nonlinear shell theory proposed by Rotter and Jumikis [78, 120, 161, 162] which retains all terms of the nonlinear Green-Lagrange membrane strains while keeping bending strains linear. Here, non-conventional GBT deformation modes are considered in the formulation which are necessary to recover the transverse and shear membrane energies. Generally, this formulation is restricted to the range of small-to-moderate rotations since it is based on the total Lagrangian description [17] for the reason of simplicity.

In this chapter, the step-by-step formulation of a geometrical nonlinear GBT element is presented. Starting from the approximation of the nonlinear response using a linear incremental procedure, the derivation of the tangent stiffness matrices and the internal forces are presented based on the variation of the internal energy which considers the nonlinear kinematic description of membrane strains. Here, the finite element formulation of the linear and quadratic tangent stiffness matrix based on the third and fourth order coupling tensors, and the derivation of the nonlinear membrane stress resultant following the fundamental principles of GBT are presented. Finally, to illustrate the application and capabilities of the developed GBT formulation, two numerical examples involving transverse and longitudinal bending are presented to show the nonlinear relationship between bending and cross-sectional ovalization. For the purpose of validation, these examples are compared with refined shell finite element models within the permissible displacement range of the GBT formulation in both displacement and stress fields.

5.1 Linearization

In this chapter, the nonlinear response of the thin-walled circular pipe members is approximated using a linear incremental iterative procedure. Here, the explanation of this procedure is presented based on the lecture materials of Krätzig [85] and Könke [83]. The nonlinear equilibrium equation between the internal forces $\mathbf{F}$ which are the nonlinear functions of the displacements $\mathbf{V}$ and the external applied loads $\mathbf{P}$ can be defined as:

$$\mathbf{F}(\mathbf{V}) = \mathbf{P} \tag{5.1}$$

In Figure 5.1, the function $\mathbf{F}(\mathbf{V})$ can be approximated at the neighboring state $\bar{\mathbf{V}} + \overset{+}{\mathbf{V}}$ using a Taylor series expansion in equation (5.2).

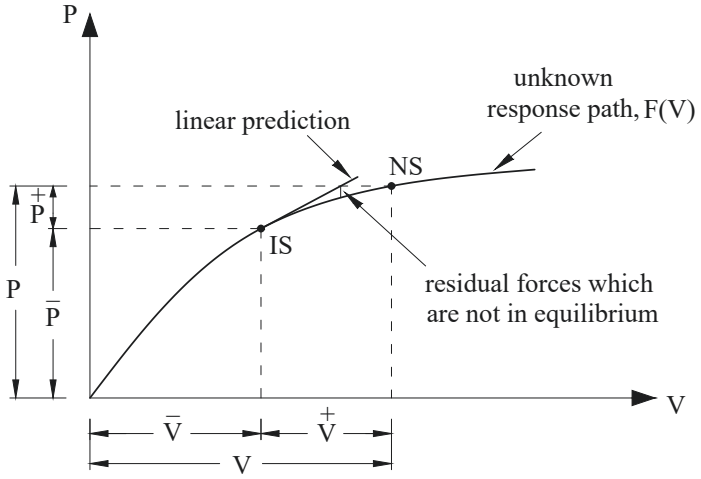

Figure 5.1: Initial State (IS) and unknown Neighboring State (NS) on the nonlinear response path [83].

$$\mathbf{F}(\bar{\mathbf{V}} + \overset{+}{\mathbf{V}}) = \mathbf{F}(\bar{\mathbf{V}}) + \mathbf{F}_{,\bar{\mathbf{V}}}(\bar{\mathbf{V}})\overset{+}{\mathbf{V}} + \mathbf{F}_{,\bar{\mathbf{V}}\bar{\mathbf{V}}}(\bar{\mathbf{V}})\frac{1}{2!}\overset{+}{\mathbf{V}}^2 + \ldots \tag{5.2}$$

Considering the first two terms of the Taylor series expansion in equation (5.2), the function $\mathbf{F}(\mathbf{V})$ is approximated at the increment $\overset{+}{\mathbf{V}}$ using a linear function which is the slope of the function $\mathbf{F}(\mathbf{V})$ at $\bar{\mathbf{V}}$. However, since this linear prediction of the neighboring state is not in equilibrium, an iteration is required until the equilibrium between the internal forces and external loads is obtained. In this study, the Newton-Raphson solver is used for the iteration.

Substituting the first two terms of equation (5.2) into equation (5.1), the linearized stiffness relation is expressed at the neighboring state as:

$$\mathbf{F}(\bar{\mathbf{V}}) + \mathbf{F}_{,\bar{\mathbf{V}}}(\bar{\mathbf{V}})\overset{+}{\mathbf{V}} = \bar{\mathbf{P}} + \overset{+}{\mathbf{P}} \tag{5.3}$$

In equation (5.3) , the function $\mathbf{F}_{,\bar{\mathbf{V}}}(\bar{\mathbf{V}})$ is called tangential stiffness and represented as $\mathbf{K}_{\mathrm{T}}$ and the

function $\mathbf{F}(\bar{\mathbf{V}})$ is called internal forces and represented as $\mathbf{F}_{\text{int}}$. Two steps are involved in solving for the load increment $\overset{+}{\mathbf{P}}$. In the first step, since the system is already in equilibrium at the initial state $\mathbf{F}_{\text{int}} = \bar{\mathbf{P}}$, the new incremental displacement is calculated for the load increment $\mathbf{K}_{\text{T}}\overset{+}{\mathbf{V}} = \overset{+}{\mathbf{P}}$. In the second step, since the new neighboring state is not in equilibrium, the incremental displacement $\overset{+}{\mathbf{V}}$ is iterated $\mathbf{K}_{\text{T}}\overset{+}{\mathbf{V}} = (\bar{\mathbf{P}} + \overset{+}{\mathbf{P}}) - \mathbf{F}_{\text{int}}$ without the additional load increment until the equilibrium is achieved.

Here, the tangential stiffness matrix $\mathbf{K}_{\text{T}}$ is derived from the principle of virtual works. Applying the same incremental procedure, the nonlinear kinematic relation at the neighboring state can be defined as:

$$\boldsymbol{\varepsilon}(\mathbf{V}) = \boldsymbol{\varepsilon}(\bar{\mathbf{V}} + \overset{+}{\mathbf{V}}) \tag{5.4}$$

Using the first three terms of the Taylor series expansion the strain at the incremental displacement $\overset{+}{\mathbf{V}}$ can be approximated as:

$$\boldsymbol{\varepsilon}(\bar{\mathbf{V}} + \overset{+}{\mathbf{V}}) = \boldsymbol{\varepsilon}(\bar{\mathbf{V}}) + \boldsymbol{\varepsilon}_{,\bar{\mathbf{V}}}(\bar{\mathbf{V}})\overset{+}{\mathbf{V}} + \boldsymbol{\varepsilon}_{,\bar{\mathbf{V}}\bar{\mathbf{V}}}(\bar{\mathbf{V}})\frac{1}{2!}\overset{+}{\mathbf{V}}^2 \tag{5.5}$$

$$\boldsymbol{\varepsilon}(\mathbf{V}) = \bar{\boldsymbol{\varepsilon}} + \overset{+}{\boldsymbol{\varepsilon}} + \overset{++}{\boldsymbol{\varepsilon}} \tag{5.6}$$

where $\bar{\boldsymbol{\varepsilon}}$ is arbitrarily dependent on $\bar{\mathbf{V}}$ and independent of $\overset{+}{\mathbf{V}}$, $\overset{+}{\boldsymbol{\varepsilon}}$ is arbitrarily dependent on $\bar{\mathbf{V}}$ and linearly dependent on $\overset{+}{\mathbf{V}}$ and $\overset{++}{\boldsymbol{\varepsilon}}$ is arbitrarily dependent on $\bar{\mathbf{V}}$ and quadratically dependent on $\overset{+}{\mathbf{V}}$.

In equation (5.5), taking the third term of the Taylor series guaranties a quadratic convergence of the Newton-Raphson solver. The detailed formulation of the GBT tangent stiffness matrix based on the nonlinear kinematic relations and the principle of virtual works is presented in the next sections.

5.2 Kinematic description

The nonlinear strain-displacement relation for the thin-walled circular pipe shown in Figure 5.2 is based on the thin shell nonlinear kinematic description proposed by Rotter and Jumikis [78, 120] which retains all nonlinear terms, large and small. Here, the nonlinear membrane strains in equations (5.7) to (5.9) are defined using the Green-Lagrange strain measurement which is applicable for moderate rotations. Since in thin-walled sections the membrane energy is dominant compared to the plate in bending energy, the bending strains are assumed to be linear and the same as the ones defined in equations (2.11) to (2.13).

Nonlinear membrane strains:

$$\varepsilon_x^{\text{M}} = u_{,x} + \frac{1}{2}\left(u_{,x}^2 + v_{,x}^2 + w_{,x}^2\right) \tag{5.7}$$

$$\varepsilon_\theta^{\text{M}} = \frac{v_{,\theta} + w}{r} + \frac{1}{2r^2}\left(u_{,\theta}^2 + (v_{,\theta} + w)^2 + (w_{,\theta} - v)^2\right) \tag{5.8}$$

$$\gamma_{x\theta}^{\text{M}} = \frac{u_{,\theta}}{r} + v_{,x} + \frac{1}{r}\left(u_{,x}u_{,\theta} + v_{,x}(v_{,\theta} + w) + w_{,x}(w_{,\theta} - v)\right) \tag{5.9}$$

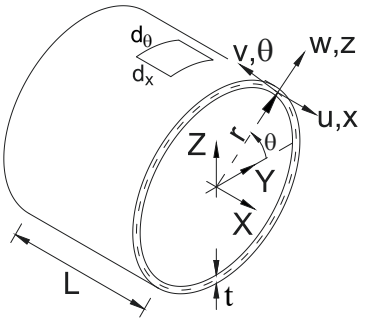

Figure 5.2: Thin-walled circular pipe section with global (X, Y, Z) and local ($x \in [-L/2, L/2]$, $\theta \in [0, 2\pi]$, $z \in [-t/2, t/2]$) coordinate systems.

Based on the linearization procedure explained in the previous section, each displacement is divided into two states: $\bar{u}, \bar{v}$ and $\bar{w}$ which are concerning the initial displacement state; and $\overset{+}{u}, \overset{+}{v}$ and $\overset{+}{w}$ which are concerning the incremental displacement state.

$$\varepsilon_x^{\mathrm{M}} = \bar{u}_{,x} + \overset{+}{u}_{,x} + \frac{1}{2}\Big((\bar{u}_{,x} + \overset{+}{u}_{,x})^2 + (\bar{v}_{,x} + \overset{+}{v}_{,x})^2 + (\bar{w}_{,x} + \overset{+}{w}_{,x})^2\Big) = \bar{\varepsilon}_x + \overset{+}{\varepsilon}_x + \overset{++}{\varepsilon}_x \tag{5.10}$$

$$\begin{aligned}\varepsilon_\theta^{\mathrm{M}} &= \frac{(\bar{v}_{,\theta} + \overset{+}{v}_{,\theta}) + (\bar{w} + \overset{+}{w})}{r} \\ &+ \frac{1}{2r^2}\Big((\bar{u}_{,\theta} + \overset{+}{u}_{,\theta})^2 + (\bar{v}_{,\theta} + \overset{+}{v}_{,\theta} + \bar{w} + \overset{+}{w})^2 + (\bar{w}_{,\theta} + \overset{+}{w}_{,\theta} - \bar{v} - \overset{+}{v})^2\Big) = \bar{\varepsilon}_\theta + \overset{+}{\varepsilon}_\theta + \overset{++}{\varepsilon}_\theta\end{aligned} \tag{5.11}$$

$$\begin{aligned}\gamma_{x\theta}^{\mathrm{M}} &= \frac{(\bar{u}_{,\theta} + \overset{+}{u}_{,\theta})}{r} + (\bar{v}_{,x} + \overset{+}{v}_{,x}) \\ &+ \frac{1}{r}\Big((\bar{u}_{,x} + \overset{+}{u}_{,x})(\bar{u}_{,\theta} + \overset{+}{u}_{,\theta}) + (\bar{v}_{,x} + \overset{+}{v}_{,x})\big(\bar{v}_{,\theta} + \overset{+}{v}_{,\theta} + \bar{w} + \overset{+}{w}\big) + (\bar{w}_{,x} + \overset{+}{w}_{,x})\big(\bar{w}_{,\theta} + \overset{+}{w}_{,\theta} - \bar{v} - \overset{+}{v}\big)\Big) \\ &= \bar{\gamma}_{x\theta} + \overset{+}{\gamma}_{x\theta} + \overset{++}{\gamma}_{x\theta}\end{aligned} \tag{5.12}$$

where:

$$\bar{\varepsilon}_x = \bar{u}_{,x} + \frac{\bar{u}_{,x}\bar{u}_{,x}}{2} + \frac{\bar{v}_{,x}\bar{v}_{,x}}{2} + \frac{\bar{w}_{,x}\bar{w}_{,x}}{2} \tag{5.13}$$

$$\overset{+}{\varepsilon}_x = \overset{+}{u}_{,x} + \bar{u}_{,x}\overset{+}{u}_{,x} + \bar{v}_{,x}\overset{+}{v}_{,x} + \bar{w}_{,x}\overset{+}{w}_{,x} \tag{5.14}$$

$$\overset{++}{\varepsilon}_x = \frac{\overset{+}{u}_{,x}\overset{+}{u}_{,x}}{2} + \frac{\overset{+}{v}_{,x}\overset{+}{v}_{,x}}{2} + \frac{\overset{+}{w}_{,x}\overset{+}{w}_{,x}}{2} \tag{5.15}$$

$$\bar{\varepsilon}_\theta = \frac{\bar{v}_{,\theta} + \bar{w}}{r} + \frac{\bar{u}_{,\theta}\bar{u}_{,\theta}}{2r^2} + \frac{\bar{v}_{,\theta}\bar{v}_{,\theta} + 2\bar{v}_{,\theta}\bar{w} + \bar{w}\bar{w}}{2r^2} + \frac{\bar{w}_{,\theta}\bar{w}_{,\theta} - 2\bar{w}_{,\theta}\bar{v} + \bar{v}\bar{v}}{2r^2} \tag{5.16}$$

$$\overset{+}{\varepsilon}_\theta = \frac{\overset{+}{v}_{,\theta} + \overset{+}{w}}{r} + \frac{\bar{u}_{,\theta}\overset{+}{u}_{,\theta}}{r^2} + \frac{\bar{v}_{,\theta}\overset{+}{v}_{,\theta} + \bar{v}_{,\theta}\overset{+}{w} + \bar{w}\overset{+}{v}_{,\theta} + \bar{w}\overset{+}{w}}{r^2} + \frac{\bar{w}_{,\theta}\overset{+}{w}_{,\theta} - \bar{w}_{,\theta}\overset{+}{v} - \bar{v}\overset{+}{w}_{,\theta} + \bar{v}\overset{+}{v}}{r^2} \tag{5.17}$$

$$\overset{++}{\varepsilon}_\theta = \frac{\overset{+}{u}_{,\theta}\overset{+}{u}_{,\theta}}{2r^2} + \frac{\overset{+}{v}_{,\theta}\overset{+}{v}_{,\theta} + 2\overset{+}{v}_{,\theta}\overset{+}{w} + \overset{+}{w}\overset{+}{w}}{2r^2} + \frac{\overset{+}{w}_{,\theta}\overset{+}{w}_{,\theta} - 2\overset{+}{w}_{,\theta}\overset{+}{v} + \overset{+}{v}\overset{+}{v}}{2r^2} \tag{5.18}$$

$$\bar{\gamma}_{x\theta} = \frac{\bar{u}_{,\theta}}{r} + \bar{v}_{,x} + \frac{\bar{u}_{,x}\bar{u}_{,\theta}}{r} + \frac{\bar{v}_{,x}\bar{v}_{,\theta} + \bar{v}_{,x}\bar{w} + \bar{w}_{,x}\bar{w}_{,\theta} - \bar{w}_{,x}\bar{v}}{r} \tag{5.19}$$

$$\overset{+}{\gamma}_{x\theta} = \frac{\overset{+}{u}_{,\theta}}{r} + \overset{+}{v}_{,x} + \frac{\bar{u}_{,x}\overset{+}{u}_{,\theta} + \overset{+}{u}_{,x}\bar{u}_{,\theta}}{r} + \frac{\bar{v}_{,x}\overset{+}{v}_{,\theta} + \bar{v}_{,x}\overset{+}{w} + \bar{w}_{,x}\overset{+}{w}_{,\theta} - \bar{w}_{,x}\overset{+}{v}}{r} + \frac{\overset{+}{v}_{,x}\bar{v}_{,\theta} + \overset{+}{v}_{,x}\bar{w} + \overset{+}{w}_{,x}\bar{w}_{,\theta} - \overset{+}{w}_{,x}\bar{v}}{r} \tag{5.20}$$

$$\overset{++}{\gamma}_{x\theta} = \frac{\overset{+}{u}_{,x}\overset{+}{u}_{,\theta}}{r} + \frac{\overset{+}{v}_{,x}\overset{+}{v}_{,\theta} + \overset{+}{v}_{,x}\overset{+}{w} + \overset{+}{w}_{,x}\overset{+}{w}_{,\theta} - \overset{+}{w}_{,x}\overset{+}{v}}{r} \tag{5.21}$$

Strain terms with $\bar{\cdot}$ are only dependent on the initial displacement and have no variation,whereas strain terms with $\overset{+}{\cdot}$ and $\overset{++}{\cdot}$ are linearly and quadratically dependent on the incremental displacement, respectively, and have variation in their incremental components, which gives:

$$\delta\overset{+}{\varepsilon}_x = \delta\overset{+}{u}_{,x} + \bar{u}_{,x}\delta\overset{+}{u}_{,x} + \bar{v}_{,x}\delta\overset{+}{v}_{,x} + \bar{w}_{,x}\delta\overset{+}{w}_{,x} \tag{5.22}$$

$$\delta\overset{++}{\varepsilon}_x = \overset{+}{u}_{,x}\delta\overset{+}{u}_{,x} + \overset{+}{v}_{,x}\delta\overset{+}{v}_{,x} + \overset{+}{w}_{,x}\delta\overset{+}{w}_{,x} \tag{5.23}$$

$$\delta\overset{+}{\varepsilon}_\theta = \frac{\delta\overset{+}{v}_{,\theta} + \delta\overset{+}{w}}{r} + \frac{\bar{u}_{,\theta}\delta\overset{+}{u}_{,\theta}}{r^2} + \frac{\bar{v}_{,\theta}\delta\overset{+}{v}_{,\theta} + \bar{v}_{,\theta}\delta\overset{+}{w} + \bar{w}\delta\overset{+}{v}_{,\theta} + \bar{w}\delta\overset{+}{w}}{r^2} + \frac{\bar{w}_{,\theta}\delta\overset{+}{w}_{,\theta} - \bar{w}_{,\theta}\delta\overset{+}{v} - \bar{v}\delta\overset{+}{w}_{,\theta} + \bar{v}\delta\overset{+}{v}}{r^2} \tag{5.24}$$

$$\delta\overset{++}{\varepsilon}_\theta = \frac{\overset{+}{u}_{,\theta}\delta\overset{+}{u}_{,\theta}}{r^2} + \frac{\overset{+}{v}_{,\theta}\delta\overset{+}{v}_{,\theta} + \overset{+}{v}_{,\theta}\delta\overset{+}{w} + \overset{+}{w}\delta\overset{+}{v}_{,\theta} + \overset{+}{w}\delta\overset{+}{w}}{r^2} + \frac{\overset{+}{w}_{,\theta}\delta\overset{+}{w}_{,\theta} - \overset{+}{w}_{,\theta}\delta\overset{+}{v} - \overset{+}{v}\delta\overset{+}{w}_{,\theta} + \overset{+}{v}\delta\overset{+}{v}}{r^2} \tag{5.25}$$

$$\delta\overset{+}{\gamma}_{x\theta} = \frac{\delta\overset{+}{u}_{,\theta}}{r} + \delta\overset{+}{v}_{,x} + \frac{\bar{u}_{,x}\delta\overset{+}{u}_{,\theta} + \delta\overset{+}{u}_{,x}\bar{u}_{,\theta}}{r} + \frac{\bar{v}_{,x}\delta\overset{+}{v}_{,\theta} + \bar{v}_{,x}\delta\overset{+}{w} + \bar{w}_{,x}\delta\overset{+}{w}_{,\theta} - \bar{w}_{,x}\delta\overset{+}{v}}{r} + \frac{\delta\overset{+}{v}_{,x}\bar{v}_{,\theta} + \delta\overset{+}{v}_{,x}\bar{w} + \delta\overset{+}{w}_{,x}\bar{w}_{,\theta} - \delta\overset{+}{w}_{,x}\bar{v}}{r} \tag{5.26}$$

$$\delta\overset{++}{\gamma}_{x\theta} = \frac{\delta\overset{+}{u}_{,x}\overset{+}{u}_{,\theta} + \overset{+}{u}_{,x}\delta\overset{+}{u}_{,\theta}}{r} + \frac{\overset{+}{v}_{,x}\delta\overset{+}{v}_{,\theta} + \overset{+}{v}_{,x}\delta\overset{+}{w} + \overset{+}{w}_{,x}\delta\overset{+}{w}_{,\theta} - \overset{+}{w}_{,x}\delta\overset{+}{v}}{r} + \frac{\delta\overset{+}{v}_{,x}\overset{+}{v}_{,\theta} + \delta\overset{+}{v}_{,x}\overset{+}{w} + \delta\overset{+}{w}_{,x}\overset{+}{w}_{,\theta} - \delta\overset{+}{w}_{,x}\overset{+}{v}}{r} \tag{5.27}$$

5.3 Variation of the internal energy

The virtual work due to internal forces is defined as the volume integral of the products of all stress components by the respective virtual strains:

$$\delta U_{\text{int}} = \int_V \left(\sigma_x\delta\varepsilon_x + \sigma_\theta\delta\varepsilon_\theta + \tau_{x\theta}\delta\gamma_{x\theta}\right)\mathrm{d}V \tag{5.28}$$

For an isotropic, linearly elastic material, the constitutive relations between stresses and strains are expressed by means of the Young's modulus E, the shear modulus G, and the Poisson's ratio μ:

$$\sigma_x = \frac{E}{1-\mu^2}(\varepsilon_x + \mu\varepsilon_\theta) \tag{5.29}$$

$$\sigma_\theta = \frac{E}{1-\mu^2}(\varepsilon_\theta + \mu\varepsilon_x) \tag{5.30}$$

$$\tau_{x\theta} = G\gamma_{x\theta} \tag{5.31}$$

In the next subsections, the variation of the internal energy is formulated based on the fundamental principles of GBT considering the longitudinal, transversal and shear internal energies separately.

$$\delta U_{\text{int}} = \int_V \sigma_x \delta\varepsilon_x \mathrm{d}V + \int_V \sigma_\theta \delta\varepsilon_\theta \mathrm{d}V + \int_V \tau_{x\theta} \delta\gamma_{x\theta} \mathrm{d}V = \delta U_x + \delta U_\theta + \delta U_{x\theta} \tag{5.32}$$

5.3.1 Variation of the longitudinal internal energy

Considering the constitutive relation in equation (5.29) and the incremental longitudinal strain in equation (5.10) the variation of longitudinal internal energy extracted from equation (5.32) can be expressed as:

$$\begin{aligned}\delta U_x &= \int_V \sigma_x \delta\varepsilon_x \mathrm{d}V = \int_V \frac{E}{1-\mu^2}\Big(\overset{-}{\varepsilon}_x + \overset{+}{\varepsilon}_x + \overset{++}{\varepsilon}_x + \mu(\overset{-}{\varepsilon}_\theta + \overset{+}{\varepsilon}_\theta + \overset{++}{\varepsilon}_\theta)\Big)\Big(\overset{+}{\delta\varepsilon}_x + \overset{++}{\delta\varepsilon}_x\Big)\mathrm{d}V \\ &= \frac{E}{1-\mu^2}\int_V \Big(\overset{-}{\varepsilon}_x\overset{+}{\delta\varepsilon}_x + \overset{+}{\varepsilon}_x\overset{+}{\delta\varepsilon}_x + \overset{-}{\varepsilon}_x\overset{++}{\delta\varepsilon}_x + \mu\big(\overset{-}{\varepsilon}_\theta\overset{+}{\delta\varepsilon}_x + \overset{+}{\varepsilon}_\theta\overset{+}{\delta\varepsilon}_x + \overset{-}{\varepsilon}_\theta\overset{++}{\delta\varepsilon}_x\big)\Big)\mathrm{d}V\end{aligned} \tag{5.33}$$

In equation (5.33), the first term $\overset{-}{\varepsilon}_x\overset{+}{\delta\varepsilon}_x$ corresponds to the virtual work of the initial stress at the initial state. This term gives the internal forces F_{int} which should be in equilibrium with the external forces F_{ext} through the iteration procedure. The second term $\overset{+}{\varepsilon}_x\overset{+}{\delta\varepsilon}_x$ is the virtual work of the initial displacement and can be split up into the linear stiffness matrix $[K_{\text{L}}]$ (independent of the displacement), the linear initial displacement matrices $[K_{\text{uL}}]$ (linearly dependent on the initial displacement), and quadratic initial displacement matrices $[K_{\text{uN}}]$ (quadratically dependent on the initial displacement). The third term $\overset{-}{\varepsilon}_x\overset{++}{\delta\varepsilon}_x$ represents the virtual work of the initial stress linearly and quadratically dependent on the incremental displacement, which leads to the linear $[K_{\sigma\text{L}}]$ and quadratic $[K_{\sigma\text{N}}]$ initial stress stiffness matrices. The rest of the higher order terms such as $\overset{+}{\varepsilon}_x\overset{++}{\delta\varepsilon}_x$, $\overset{++}{\varepsilon}_x\overset{+}{\delta\varepsilon}_x$, and $\overset{++}{\varepsilon}_x\overset{++}{\delta\varepsilon}_x$ are neglected since they are much smaller than the first three terms. Here, the tangent stiffness matrix $[K_{\text{T}}]$ can be expressed as a summation of the stiffness matrices.

$$[K_{\text{T}}] = [K_{\text{L}}] + [K_{\text{uL}}] + [K_{\text{uN}}] + [K_{\sigma\text{L}}] + [K_{\sigma\text{N}}] \tag{5.34}$$

Substituting the strain-displacement kinematic relations in equations (5.13), (5.14), (5.22) and (5.23) into equation (5.33) and neglecting the terms related to Poisson effect for the reason of simplicity, the variation of the longitudinal internal energy can be expressed as:

$$\begin{aligned}\delta U_x = \frac{E}{1-\mu^2}\Bigg(&\int_V \Big(\bar{u}_{,x} + \frac{\bar{u}_{,x}\bar{u}_{,x}}{2} + \frac{\bar{v}_{,x}\bar{v}_{,x}}{2} + \frac{\bar{w}_{,x}\bar{w}_{,x}}{2}\Big)\Big(\overset{+}{\delta u}_{,x} + \bar{u}_{,x}\overset{+}{\delta u}_{,x} + \bar{v}_{,x}\overset{+}{\delta v}_{,x} + \bar{w}_{,x}\overset{+}{\delta w}_{,x}\Big)\mathrm{d}V \\ &+ \int_V \Big(\overset{+}{u}_{,x} + \bar{u}_{,x}\overset{+}{u}_{,x} + \bar{v}_{,x}\overset{+}{v}_{,x} + \bar{w}_{,x}\overset{+}{w}_{,x}\Big)\Big(\overset{+}{\delta u}_{,x} + \bar{u}_{,x}\overset{+}{\delta u}_{,x} + \bar{v}_{,x}\overset{+}{\delta v}_{,x} + \bar{w}_{,x}\overset{+}{\delta w}_{,x}\Big)\mathrm{d}V \\ &+ \int_V \Big(\bar{u}_{,x} + \frac{\bar{u}_{,x}\bar{u}_{,x}}{2} + \frac{\bar{v}_{,x}\bar{v}_{,x}}{2} + \frac{\bar{w}_{,x}\bar{w}_{,x}}{2}\Big)\Big(\overset{+}{u}_{,x}\overset{+}{\delta u}_{,x} + \overset{+}{v}_{,x}\overset{+}{\delta v}_{,x} + \overset{+}{w}_{,x}\overset{+}{\delta w}_{,x}\Big)\mathrm{d}V\Bigg)\end{aligned} \tag{5.35}$$

Introducing the GBT's separation of variable assumptions and the modes superposition concept, given in equations (2.2), (2.3) and (2.4), the domain of integration in equation (5.35) can be split into longitudinal and transversal directions, x and θ, respectively. This gives:

$$
\begin{aligned}
\delta U_x \;=\; & \left.\sum_{i,k}\int_L {}^{ik}C\;{}^{i}\overset{+}{V}_{,xx}\,\delta^{k}\overset{+}{V}_{,xx}\,\mathrm{d}x\;\right\} K_{\mathrm{L}} \\
& \left.\begin{aligned}
&+\sum_{j,i,k}\int_L {}^{ijk}C_1\;{}^{j}\bar{V}_{,x}\,{}^{i}\overset{+}{V}_{,xx}\,\delta^{k}\overset{+}{V}_{,x}\,\mathrm{d}x+\sum_{j,i,k}\int_L {}^{ijk}C_2\;{}^{j}\bar{V}_{,xx}\,{}^{i}\overset{+}{V}_{,xx}\,\delta^{k}\overset{+}{V}_{,xx}\,\mathrm{d}x \\
&+\sum_{j,i,k}\int_L {}^{kji}C_1\;{}^{j}\bar{V}_{,x}\,{}^{i}\overset{+}{V}_{,x}\,\delta^{k}\overset{+}{V}_{,xx}\,\mathrm{d}x+\sum_{j,i,k}\int_L {}^{kji}C_2\;{}^{j}\bar{V}_{,xx}\,{}^{i}\overset{+}{V}_{,xx}\,\delta^{k}\overset{+}{V}_{,xx}\,\mathrm{d}x
\end{aligned}\right\} K_{\mathrm{uL}} \\
& \left.\begin{aligned}
&+\sum_{j,l,i,k}\int_L {}^{jilk}C_1\;{}^{j}\bar{V}_{,x}\,{}^{l}\bar{V}_{,x}\,{}^{i}\overset{+}{V}_{,x}\,\delta^{k}\overset{+}{V}_{,x}\,\mathrm{d}x+\sum_{j,l,i,k}\int_L {}^{jilk}C_2\;{}^{j}\bar{V}_{,xx}\,{}^{l}\bar{V}_{,xx}\,{}^{i}\overset{+}{V}_{,xx}\,\delta^{k}\overset{+}{V}_{,xx}\,\mathrm{d}x \\
&+\sum_{j,l,i,k}\int_L {}^{lkji}C_{12}\;{}^{j}\bar{V}_{,x}\,{}^{l}\bar{V}_{,xx}\,{}^{i}\overset{+}{V}_{,x}\,\delta^{k}\overset{+}{V}_{,xx}\,\mathrm{d}x+\sum_{j,l,i,k}\int_L {}^{jilk}C_{12}\;{}^{j}\bar{V}_{,xx}\,{}^{l}\bar{V}_{,x}\,{}^{i}\overset{+}{V}_{,xx}\,\delta^{k}\overset{+}{V}_{,x}\,\mathrm{d}x
\end{aligned}\right\} K_{\mathrm{uN}} \\
& \left.\sum_{j,i,k}\int_L {}^{jik}C_1\;{}^{j}\bar{V}_{,xx}\,{}^{i}\overset{+}{V}_{,x}\,\delta^{k}\overset{+}{V}_{,x}\,\mathrm{d}x+\sum_{j,i,k}\int_L {}^{jik}C_2\;{}^{j}\bar{V}_{,xx}\,{}^{i}\overset{+}{V}_{,xx}\,\delta^{k}\overset{+}{V}_{,xx}\,\mathrm{d}x\;\right\} K_{\sigma\mathrm{L}} \\
& \left.\begin{aligned}
&+\sum_{j,l,i,k}\int_L \frac{{}^{jlik}C_1}{2}\;{}^{j}\bar{V}_{,x}\,{}^{l}\bar{V}_{,x}\,{}^{i}\overset{+}{V}_{,x}\,\delta^{k}\overset{+}{V}_{,x}\,\mathrm{d}x+\sum_{j,l,i,k}\int_L \frac{{}^{jlik}C_2}{2}\;{}^{j}\bar{V}_{,xx}\,{}^{l}\bar{V}_{,xx}\,{}^{i}\overset{+}{V}_{,xx}\,\delta^{k}\overset{+}{V}_{,xx}\,\mathrm{d}x \\
&+\sum_{j,l,i,k}\int_L \frac{{}^{jlik}C_{12}}{2}\;{}^{j}\bar{V}_{,xx}\,{}^{l}\bar{V}_{,xx}\,{}^{i}\overset{+}{V}_{,x}\,\delta^{k}\overset{+}{V}_{,x}\,\mathrm{d}x+\sum_{j,l,i,k}\int_L \frac{{}^{ikjl}C_{12}}{2}\;{}^{j}\bar{V}_{,x}\,{}^{l}\bar{V}_{,x}\,{}^{i}\overset{+}{V}_{,xx}\,\delta^{k}\overset{+}{V}_{,xx}\,\mathrm{d}x
\end{aligned}\right\} K_{\sigma\mathrm{N}} \\
& \left.\begin{aligned}
&+\sum_{i,k}\int_L {}^{ik}C\;{}^{i}\bar{V}_{,xx}\,\delta^{k}\overset{+}{V}_{,xx}\,\mathrm{d}x+\sum_{j,i,k}\int_L {}^{jik}C_1\;{}^{j}\bar{V}_{,xx}\,{}^{i}\bar{V}_{,x}\,\delta^{k}\overset{+}{V}_{,x}\,\mathrm{d}x \\
&+\sum_{j,i,k}\int_L {}^{jik}C_2\;{}^{j}\bar{V}_{,xx}\,{}^{i}\bar{V}_{,xx}\,\delta^{k}\overset{+}{V}_{,xx}\,\mathrm{d}x+\sum_{j,i,k}\int_L \frac{{}^{kji}C_1}{2}\;{}^{j}\bar{V}_{,x}\,{}^{i}\bar{V}_{,x}\,\delta^{k}\overset{+}{V}_{,xx}\,\mathrm{d}x \\
&+\sum_{j,i,k}\int_L \frac{{}^{kji}C_2}{2}\;{}^{j}\bar{V}_{,xx}\,{}^{i}\bar{V}_{,xx}\,\delta^{k}\overset{+}{V}_{,xx}\,\mathrm{d}x+\sum_{j,l,i,k}\int_L \frac{{}^{jlik}C_1}{2}\;{}^{j}\bar{V}_{,x}\,{}^{l}\bar{V}_{,x}\,{}^{i}\bar{V}_{,x}\,\delta^{k}\overset{+}{V}_{,x}\,\mathrm{d}x \\
&+\sum_{j,l,i,k}\int_L \frac{{}^{jlik}C_2}{2}\;{}^{j}\bar{V}_{,xx}\,{}^{l}\bar{V}_{,xx}\,{}^{i}\bar{V}_{,xx}\,\delta^{k}\overset{+}{V}_{,xx}\,\mathrm{d}x+\sum_{j,l,i,k}\int_L \frac{{}^{ikjl}C_{12}}{2}\;{}^{j}\bar{V}_{,x}\,{}^{l}\bar{V}_{,x}\,{}^{i}\bar{V}_{,xx}\,\delta^{k}\overset{+}{V}_{,xx}\,\mathrm{d}x \\
&+\sum_{j,l,i,k}\int_L \frac{{}^{jlik}C_{12}}{2}\;{}^{j}\bar{V}_{,xx}\,{}^{l}\bar{V}_{,xx}\,{}^{i}\bar{V}_{,x}\,\delta^{k}\overset{+}{V}_{,x}\,\mathrm{d}x
\end{aligned}\right\} F_{\mathrm{int}}
\end{aligned}
\tag{5.36}
$$

with the section properties

$${}^{ik}C = Q\oint {}^{i}u(\theta)\,{}^{k}u(\theta)\;r\,d\theta \tag{5.37}$$

$${}^{jik}C_1 = Q\oint {}^{j}u(\theta)\left({}^{i}v(\theta)\,{}^{k}v(\theta)+{}^{i}w(\theta)\,{}^{k}w(\theta)\right)\;r\,d\theta \tag{5.38}$$

$${}^{jik}C_2 = Q\oint {}^{j}u(\theta)\;{}^{i}u(\theta)\;{}^{k}u(\theta)\;r\,d\theta \tag{5.39}$$

$$^{jlik}C_1 = Q \oint \left({}^{j}v(\theta)^{l}v(\theta) + {}^{j}w(\theta)^{l}w(\theta)\right)\left({}^{i}v(\theta)^{k}v(\theta) + {}^{i}w(\theta)^{k}w(\theta)\right) r\, d\theta \tag{5.40}$$

$$^{jlik}C_2 = Q \oint {}^{j}u(\theta)^{l}u(\theta)^{i}u(\theta)^{k}u(\theta)\, r\, d\theta \tag{5.41}$$

$$^{jlik}C_{12} = Q \oint {}^{j}u(\theta)^{l}u(\theta)\left({}^{i}v(\theta)^{k}v(\theta) + {}^{i}w(\theta)^{k}w(\theta)\right) r\, d\theta \tag{5.42}$$

In equation (5.35)'s summation notation $\sum_{i,k,\cdots}$ is a compact representation of $\sum_i \sum_k \cdots$.
The coefficients in equations (5.37) to (5.42) are described as:

- ^{ik}C is a second-order tensor associated with the linear stiffness matrix $[K_{\mathrm{L}}]$ similar to equation (2.20),
- $^{ijk}C_1$ and $^{ijk}C_2$ are third-order tensors associated with the linear initial stress $[K_{\sigma\mathrm{L}}]$ and displacement stiffness matrix $[K_{\mathrm{uL}}]$,
- $^{ijkl}C_1$, $^{ijkl}C_2$, and $^{ijkl}C_{12}$ are fourth-order tensors associated with the quadratic initial stress $[K_{\sigma\mathrm{N}}]$ and displacement stiffness matrix $[K_{\sigma\mathrm{N}}]$.

In these coefficients, only the linear and nonlinear stiffness contributions of the membrane are shown. The plate contributions are kept linear and similar to the ones derived in Chapter 2.

5.3.2 Variation of the transverse internal energy

Similarly, the variation of the transverse internal energy can be formulated as:

$$\begin{aligned}\delta U_\theta &= \int_V \sigma_\theta \delta\varepsilon_\theta \mathrm{d}V = \int_V \frac{E}{1-\mu^2}\left(\bar{\varepsilon}_\theta + \overset{+}{\varepsilon}_\theta + \overset{++}{\varepsilon}_\theta + \mu(\bar{\varepsilon}_x + \overset{+}{\varepsilon}_x + \overset{++}{\varepsilon}_x)\right)\left(\overset{+}{\delta\varepsilon}_\theta + \overset{++}{\delta\varepsilon}_\theta\right)\mathrm{d}V \\ &= \frac{E}{1-\mu^2}\int_V \left(\bar{\varepsilon}_\theta\overset{+}{\delta\varepsilon}_\theta + \overset{+}{\varepsilon}_\theta\overset{+}{\delta\varepsilon}_\theta + \bar{\varepsilon}_\theta\overset{++}{\delta\varepsilon}_\theta + \mu\left(\bar{\varepsilon}_x\overset{+}{\delta\varepsilon}_\theta + \overset{+}{\varepsilon}_x\overset{+}{\delta\varepsilon}_\theta + \bar{\varepsilon}_x\overset{++}{\delta\varepsilon}_\theta\right)\right)\mathrm{d}V\end{aligned} \tag{5.43}$$

Substituting the strain-displacement kinematic relations in equations (5.16), (5.17), (5.24) and (5.25) into equation (5.43) and neglecting the terms related to Poisson effect for the reason of simplicity, the variation of the transverse internal energy can be expressed as:

$$\delta U_\theta = \frac{E}{1-\mu^2}\left(\int_V \bar{\varepsilon}_\theta\overset{+}{\delta\varepsilon}_\theta \mathrm{d}V + \int_V \overset{+}{\varepsilon}_\theta\overset{+}{\delta\varepsilon}_\theta \mathrm{d}V + \int_V \bar{\varepsilon}_\theta\overset{++}{\delta\varepsilon}_\theta \mathrm{d}V\right) = \delta U_{\theta(\mathrm{int})} + \delta U_{\theta(\mathrm{u})} + \delta U_{\theta(\sigma)} \tag{5.44}$$

where:

$$\begin{aligned}\delta U_{\theta(\mathrm{int})} = \frac{E}{1-\mu^2}\int_V &\left(\frac{\bar{v}_{,\theta} + \bar{w}}{r} + \frac{\bar{u}_{,\theta}\bar{u}_{,\theta}}{2r^2} + \frac{\bar{v}_{,\theta}\bar{v}_{,\theta} + 2\bar{v}_{,\theta}\bar{w} + \bar{w}\bar{w}}{2r^2} + \frac{\bar{w}_{,\theta}\bar{w}_{,\theta} - 2\bar{w}_{,\theta}\bar{v} + \bar{v}\bar{v}}{2r^2}\right) \\ \times &\left(\frac{\overset{+}{\delta v}_{,\theta} + \overset{+}{\delta w}}{r} + \frac{\bar{u}_{,\theta}\overset{+}{\delta u}_{,\theta}}{r^2} + \frac{\bar{v}_{,\theta}\overset{+}{\delta v}_{,\theta} + \bar{v}_{,\theta}\overset{+}{\delta w} + \bar{w}\overset{+}{\delta v}_{,\theta} + \overset{+}{\delta w}\bar{w}}{r^2} + \frac{\bar{w}_{,\theta}\overset{+}{\delta w}_{,\theta} - \bar{w}_{,\theta}\overset{+}{\delta v} - \bar{v}\overset{+}{\delta w}_{,\theta} + \bar{v}\overset{+}{\delta v}}{r^2}\right)\mathrm{d}V\end{aligned} \tag{5.45}$$

$$\delta U_{\theta(\mathrm{u})} = \frac{E}{1-\mu^2}\int_V \left(\frac{\overset{+}{v}_{,\theta}+\overset{+}{w}}{r}+\frac{\bar{u}_{,\theta}\overset{+}{u}_{,\theta}}{r^2}+\frac{\bar{v}_{,\theta}\overset{+}{v}_{,\theta}+\bar{v}_{,\theta}\overset{+}{w}+\bar{w}\overset{+}{v}_{,\theta}+\overset{+}{w}\bar{w}}{r^2}+\frac{\bar{w}_{,\theta}\overset{+}{w}_{,\theta}-\bar{w}_{,\theta}\overset{+}{v}-\bar{v}\overset{+}{w}_{,\theta}+\bar{v}\overset{+}{v}}{r^2}\right)$$
$$\times\left(\frac{\delta\overset{+}{v}_{,\theta}+\delta\overset{+}{w}}{r}+\frac{\bar{u}_{,\theta}\delta\overset{+}{u}_{,\theta}}{r^2}+\frac{\bar{v}_{,\theta}\delta\overset{+}{v}_{,\theta}+\bar{v}_{,\theta}\delta\overset{+}{w}+\bar{w}\delta\overset{+}{v}_{,\theta}+\delta\overset{+}{w}\bar{w}}{r^2}\right.$$
$$\left.+\frac{\bar{w}_{,\theta}\delta\overset{+}{w}_{,\theta}-\bar{w}_{,\theta}\delta\overset{+}{v}-\bar{v}\delta\overset{+}{w}_{,\theta}+\bar{v}\delta\overset{+}{v}}{r^2}\right)\mathrm{d}V \tag{5.46}$$

$$\delta U_{\theta(\sigma)} = \frac{E}{1-\mu^2}\int_V \left(\frac{\bar{v}_{,\theta}+\bar{w}}{r}+\frac{\bar{u}_{,\theta}\bar{u}_{,\theta}}{2r^2}+\frac{\bar{v}_{,\theta}\bar{v}_{,\theta}+2\bar{v}_{,\theta}\bar{w}+\bar{w}\bar{w}}{2r^2}+\frac{\bar{w}_{,\theta}\bar{w}_{,\theta}-2\bar{w}_{,\theta}\bar{v}+\bar{v}\bar{v}}{2r^2}\right)$$
$$\times\left(\frac{\overset{+}{u}_{,\theta}\delta\overset{+}{u}_{,\theta}}{r^2}+\frac{\overset{+}{v}_{,\theta}\delta\overset{+}{v}_{,\theta}+\overset{+}{v}_{,\theta}\delta\overset{+}{w}+\delta\overset{+}{v}_{,\theta}\overset{+}{w}+\overset{+}{w}\delta\overset{+}{w}}{r^2}+\frac{\overset{+}{w}_{,\theta}\delta\overset{+}{w}_{,\theta}-\overset{+}{w}_{,\theta}\delta\overset{+}{v}-\delta\overset{+}{w}_{,\theta}\overset{+}{v}+\overset{+}{v}\delta\overset{+}{v}}{r^2}\right)\mathrm{d}V \tag{5.47}$$

Introducing GBT's separation of variable assumptions and modes superposition concept, given in equations (2.2) to (2.4), the domain of integration in equations (5.45) to (5.47) can be split into longitudinal and transversal directions x and θ, respectively. This gives:

$$\begin{aligned}\delta U_{\theta(\mathrm{u})} &= \left.\sum_{i,k}\int_L {}^{ik}B\,{}^{i}\overset{+}{V}\,\delta^{k}\overset{+}{V}\,\mathrm{d}x\;\right\}K_{\mathrm{L}}\\
&\left.\begin{aligned}&+\sum_{j,i,k}\int_L {}^{ijk}B_1\,{}^{j}\bar{V}\,{}^{i}\overset{+}{V}\,\delta^{k}\overset{+}{V}\,\mathrm{d}x+\sum_{j,i,k}\int_L {}^{ijk}B_2\,{}^{j}\bar{V}_{,x}\,{}^{i}\overset{+}{V}\,\delta^{k}\overset{+}{V}_{,x}\,\mathrm{d}x\\
&+\sum_{j,i,k}\int_L {}^{kji}B_1\,{}^{j}\bar{V}\,{}^{i}\overset{+}{V}\,\delta^{k}\overset{+}{V}\,\mathrm{d}x+\sum_{j,i,k}\int_L {}^{kji}B_2\,{}^{j}\bar{V}_{,x}\,{}^{i}\overset{+}{V}_{,x}\,\delta^{k}\overset{+}{V}\,\mathrm{d}x\end{aligned}\right\}K_{\mathrm{uL}}\\
&\left.\begin{aligned}&+\sum_{j,l,i,k}\int_L {}^{jilk}B_1\,{}^{j}\bar{V}\,{}^{l}\bar{V}\,{}^{i}\overset{+}{V}\,\delta^{k}\overset{+}{V}\,\mathrm{d}x+\sum_{j,l,i,k}\int_L {}^{jilk}B_2\,{}^{j}\bar{V}_{,x}\,{}^{l}\bar{V}_{,x}\,{}^{i}\overset{+}{V}_{,x}\,\delta^{k}\overset{+}{V}_{,x}\,\mathrm{d}x\\
&+\sum_{j,l,i,k}\int_L {}^{lkji}B_{12}\,{}^{j}\bar{V}\,{}^{l}\bar{V}_{,x}\,{}^{i}\overset{+}{V}\,\delta^{k}\overset{+}{V}_{,x}\,\mathrm{d}x+\sum_{j,l,i,k}\int_L {}^{jilk}B_{12}\,{}^{j}\bar{V}_{,x}\,{}^{l}\bar{V}\,{}^{i}\overset{+}{V}_{,x}\,\delta^{k}\overset{+}{V}\,\mathrm{d}x\end{aligned}\right\}K_{\mathrm{uN}}\end{aligned} \tag{5.48}$$

$$\begin{aligned}\delta U_{\theta(\sigma)} &= \left.\sum_{j,i,k}\int_L {}^{jik}B_1\,{}^{j}\bar{V}\,{}^{i}\overset{+}{V}\,\delta^{k}\overset{+}{V}\,\mathrm{d}x+\sum_{j,i,k}\int_L {}^{jik}B_2\,{}^{j}\bar{V}\,{}^{i}\overset{+}{V}_{,x}\,\delta^{k}\overset{+}{V}_{,x}\,\mathrm{d}x\;\right\}K_{\sigma\mathrm{L}}\\
&\left.\begin{aligned}&+\sum_{j,l,i,k}\int_L \frac{{}^{jlik}B_1}{2}\,{}^{j}\bar{V}\,{}^{l}\bar{V}\,{}^{i}\overset{+}{V}\,\delta^{k}\overset{+}{V}\,\mathrm{d}x+\sum_{j,l,i,k}\int_L \frac{{}^{jlik}B_2}{2}\,{}^{j}\bar{V}_{,x}\,{}^{l}\bar{V}_{,x}\,{}^{i}\overset{+}{V}_{,x}\,\delta^{k}\overset{+}{V}_{,x}\,\mathrm{d}x\\
&+\sum_{j,l,i,k}\int_L \frac{{}^{jlik}B_{12}}{2}\,{}^{j}\bar{V}_{,x}\,{}^{l}\bar{V}_{,x}\,{}^{i}\overset{+}{V}\,\delta^{k}\overset{+}{V}\,\mathrm{d}x+\sum_{j,l,i,k}\int_L \frac{{}^{ikjl}B_{12}}{2}\,{}^{j}\bar{V}\,{}^{l}\bar{V}\,{}^{i}\overset{+}{V}_{,x}\,\delta^{k}\overset{+}{V}_{,x}\,\mathrm{d}x\end{aligned}\right\}K_{\sigma\mathrm{N}}\end{aligned} \tag{5.49}$$

$$\begin{aligned}
\delta U_{\theta(\mathrm{int})} = &\sum_{i,k} \int_L {}^{ik}B\, {}^{i}\bar{V}\, \delta^{k}\overset{+}{V}\, \mathrm{d}x + \sum_{j,i,k} \int_L {}^{jik}B_1\, {}^{j}\bar{V}\, {}^{i}\bar{V}\, \delta^{k}\overset{+}{V}\, \mathrm{d}x + \sum_{j,i,k} \int_L {}^{jik}B_2\, {}^{j}\bar{V}\, {}^{i}\bar{V}_{,x}\, \delta^{k}\overset{+}{V}_{,x}\, \mathrm{d}x \\
&+ \sum_{j,i,k} \int_L \frac{{}^{kji}B_1}{2}\, {}^{j}\bar{V}\, {}^{i}\bar{V}\, \delta^{k}\overset{+}{V}\, \mathrm{d}x + \sum_{j,i,k} \int_L \frac{{}^{kji}B_2}{2}\, {}^{j}\bar{V}_{,x}\, {}^{i}\bar{V}_{,x}\, \delta^{k}\overset{+}{V}\, \mathrm{d}x \\
&+ \sum_{j,l,i,k} \int_L \frac{{}^{jlik}B_1}{2}\, {}^{j}\bar{V}\, {}^{l}\bar{V}\, {}^{i}\bar{V}\, \delta^{k}\overset{+}{V}\, \mathrm{d}x + \sum_{j,l,i,k} \int_L \frac{{}^{jlik}B_2}{2}\, {}^{j}\bar{V}_{,x}\, {}^{l}\bar{V}_{,x}\, {}^{i}\bar{V}_{,x}\, \delta^{k}\overset{+}{V}_{,x}\, \mathrm{d}x \\
&+ \sum_{j,l,i,k} \int_L \frac{{}^{ikjl}B_{12}}{2}\, {}^{j}\bar{V}\, {}^{l}\bar{V}\, {}^{i}\bar{V}_{,x}\, \delta^{k}\overset{+}{V}_{,x}\, \mathrm{d}x + \sum_{j,l,i,k} \int_L \frac{{}^{jlik}B_{12}}{2}\, {}^{j}\bar{V}_{,x}\, {}^{l}\bar{V}_{,x}\, {}^{i}\bar{V}\, \delta^{k}\overset{+}{V}\, \mathrm{d}x
\end{aligned} \tag{5.50}$$

with the section properties

$${}^{ik}B = Q \oint \frac{{}^{i}v_{,\theta}(\theta) + {}^{i}w(\theta)}{r} \frac{{}^{k}v_{,\theta}(\theta) + {}^{k}w(\theta)}{r} r\, d\theta \tag{5.51}$$

$$\begin{aligned}
{}^{jik}B_1 = Q \oint &\frac{{}^{j}v_{,\theta}(\theta) + {}^{j}w(\theta)}{r} \Big(\frac{{}^{i}v_{,\theta}(\theta)^{k}v_{,\theta}(\theta) + {}^{i}v_{,\theta}(\theta)^{k}w(\theta) + {}^{i}w(\theta)^{k}v_{,\theta}(\theta) + {}^{i}w(\theta)^{k}w(\theta)}{r^2} \\
&+ \frac{{}^{i}w_{,\theta}(\theta)^{k}w_{,\theta}(\theta) - {}^{i}w_{,\theta}(\theta)^{k}v(\theta) - {}^{i}v(\theta)^{k}w_{,\theta}(\theta) + {}^{i}v(\theta)^{k}v(\theta)}{r^2} \Big) r\, d\theta
\end{aligned} \tag{5.52}$$

$${}^{jik}B_2 = Q \oint \frac{{}^{j}v_{,\theta}(\theta) + {}^{j}w(\theta)}{r} \frac{{}^{i}u_{,\theta}(\theta)^{k}u_{,\theta}(\theta)}{r^2} r\, d\theta \tag{5.53}$$

$$\begin{aligned}
{}^{jlik}B_1 = Q \oint &\Big(\frac{{}^{j}v_{,\theta}(\theta)^{l}v_{,\theta}(\theta) + {}^{j}v_{,\theta}(\theta)^{l}w(\theta) + {}^{j}w(\theta)^{l}v_{,\theta}(\theta) + {}^{j}w(\theta)^{l}w(\theta)}{r^2} \\
&+ \frac{{}^{j}w_{,\theta}(\theta)^{l}w_{,\theta}(\theta) - {}^{j}w_{,\theta}(\theta)^{l}v(\theta) - {}^{j}v(\theta)^{l}w_{,\theta}(\theta) + {}^{j}v(\theta)^{l}v(\theta)}{r^2} \Big) \\
&\times \Big(\frac{{}^{i}v_{,\theta}(\theta)^{k}v_{,\theta}(\theta) + {}^{i}v_{,\theta}(\theta)^{k}w(\theta) + {}^{i}w(\theta)^{k}v_{,\theta}(\theta) + {}^{i}w(\theta)^{k}w(\theta)}{r^2} \\
&+ \frac{{}^{i}w_{,\theta}(\theta)^{k}w_{,\theta}(\theta) - {}^{i}w_{,\theta}(\theta)^{k}v(\theta) - {}^{i}v(\theta)^{k}w_{,\theta}(\theta) + {}^{i}v(\theta)^{k}v(\theta)}{r^2} \Big) r\, d\theta
\end{aligned} \tag{5.54}$$

$${}^{jlik}B_2 = Q \oint \frac{{}^{j}u_{,\theta}(\theta)^{l}u_{,\theta}(\theta)}{r^2} \frac{{}^{i}u_{,\theta}(\theta)^{k}u_{,\theta}(\theta)}{r^2} r\, d\theta \tag{5.55}$$

$$\begin{aligned}
{}^{jlik}B_{12} = Q \oint &\frac{{}^{j}u_{,\theta}(\theta)^{l}u_{,\theta}(\theta)}{r^2} \Big(\frac{{}^{i}v_{,\theta}(\theta)^{k}v_{,\theta}(\theta) + {}^{i}v_{,\theta}(\theta)^{k}w(\theta) + {}^{i}w(\theta)^{k}v_{,\theta}(\theta) + {}^{i}w(\theta)^{k}w(\theta)}{r^2} \\
&+ \frac{{}^{i}w_{,\theta}(\theta)^{k}w_{,\theta}(\theta) - {}^{i}w_{,\theta}(\theta)^{k}v(\theta) - {}^{i}v(\theta)^{k}w_{,\theta}(\theta) + {}^{i}v(\theta)^{k}v(\theta)}{r^2} \Big) r\, d\theta
\end{aligned} \tag{5.56}$$

The coefficients in equations (5.51) to (5.56) are described as:

- ${}^{ik}B$ is a second-order tensor associated with the linear stiffness matrix $[K_{\mathrm{L}}]$ similar to equation (2.21),
- ${}^{ijk}B_1$ and ${}^{ijk}B_2$ are third-order tensors associated with the linear initial stress $[K_{\sigma\mathrm{L}}]$ and displacement stiffness matrix $[K_{\mathrm{uL}}]$,
- ${}^{ijkl}B_1$, ${}^{ijkl}B_2$, and ${}^{ijkl}B_{12}$ are fourth-order tensors associated with the quadratic initial stress $[K_{\sigma\mathrm{N}}]$ and displacement stiffness matrix $[K_{\sigma\mathrm{N}}]$.

5.3.3 Variation of the shear internal energy

Finally, the variation of the shear internal energy can be formulated as:

$$\begin{aligned}\delta U_{x\theta} &= \int_V \tau_{x\theta}\,\delta\gamma_{x\theta}\mathrm{d}V = \int_V G\left(\bar{\gamma}_{x\theta} + \overset{+}{\gamma}_{x\theta} + \overset{++}{\gamma}_{x\theta}\right)\left(\delta\overset{+}{\gamma}_{x\theta} + \delta\overset{++}{\gamma}_{x\theta}\right)\mathrm{d}V \\ &= G\int_V \left(\bar{\gamma}_{x\theta}\delta\overset{+}{\gamma}_{x\theta} + \overset{+}{\gamma}_{x\theta}\delta\overset{+}{\gamma}_{x\theta} + \bar{\gamma}_{x\theta}\delta\overset{++}{\gamma}_{x\theta}\right)\mathrm{d}V \end{aligned} \tag{5.57}$$

Substituting the strain-displacement kinematic relations in equations (5.19), (5.20), (5.26), and (5.27) into equation (5.57), the variation of the shear internal energy can be expressed as:

$$\begin{aligned}\delta U_{x\theta} &= G\int_V \bar{\gamma}_{x\theta}\delta\overset{+}{\gamma}_{x\theta}\mathrm{d}V + G\int_V \overset{+}{\gamma}_{x\theta}\delta\overset{+}{\gamma}_{x\theta}\mathrm{d}V + G\int_V \bar{\gamma}_{x\theta}\delta\overset{++}{\gamma}_{x\theta}\mathrm{d}V \\ &= \delta U_{x\theta(\mathrm{int})} + \delta U_{x\theta(\mathrm{u})} + \delta U_{x\theta(\sigma)} \end{aligned} \tag{5.58}$$

where:

$$\begin{aligned}\delta U_{x\theta(\mathrm{u})} = G\int_V &\left(\frac{\overset{+}{u}_{,\theta}}{r} + \overset{+}{v}_{,x} + \frac{\bar{u}_{,x}\overset{+}{u}_{,\theta} + \overset{+}{u}_{,x}\bar{u}_{,\theta}}{r} + \frac{\bar{v}_{,x}\overset{+}{v}_{,\theta} + \bar{v}_{,x}\overset{+}{w} + \bar{w}_{,x}\overset{+}{w}_{,\theta} - \bar{w}_{,x}\overset{+}{v}}{r}\right. \\ &\left. + \frac{\overset{+}{v}_{,x}\bar{v}_{,\theta} + \overset{+}{v}_{,x}\bar{w} + \overset{+}{w}_{,x}\bar{w}_{,\theta} - \overset{+}{w}_{,x}\bar{v}}{r}\right) \\ &\times\left(\frac{\delta\overset{+}{u}_{,\theta}}{r} + \delta\overset{+}{v}_{,x} + \frac{\bar{u}_{,x}\delta\overset{+}{u}_{,\theta} + \delta\overset{+}{u}_{,x}\bar{u}_{,\theta}}{r}\,\frac{\bar{v}_{,x}\delta\overset{+}{v}_{,\theta} + \bar{v}_{,x}\delta\overset{+}{w} + \bar{w}_{,x}\delta\overset{+}{w}_{,\theta} - \bar{w}_{,x}\delta\overset{+}{v}}{r}\right. \\ &\left. + \frac{\delta\overset{+}{v}_{,x}\bar{v}_{,\theta} + \delta\overset{+}{v}_{,x}\bar{w} + \delta\overset{+}{w}_{,x}\bar{w}_{,\theta} - \delta\overset{+}{w}_{,x}\bar{v}}{r}\right)\mathrm{d}V \end{aligned} \tag{5.59}$$

$$\begin{aligned}\delta U_{x\theta(\sigma)} = G\int_V &\left(\frac{\bar{u}_{,\theta}}{r} + \bar{v}_{,x} + \frac{\bar{u}_{,x}\bar{u}_{,\theta}}{r} + \frac{\bar{v}_{,x}\bar{v}_{,\theta} + \bar{v}_{,x}\bar{w} + \bar{w}_{,x}\bar{w}_{,\theta} - \bar{w}_{,x}\bar{v}}{r}\right) \\ &\times\left(\frac{\delta\overset{+}{u}_{,x}\overset{+}{u}_{,\theta} + \overset{+}{u}_{,x}\delta\overset{+}{u}_{,\theta}}{r} + \frac{\overset{+}{v}_{,x}\delta\overset{+}{v}_{,\theta} + \overset{+}{v}_{,x}\delta\overset{+}{w} + \overset{+}{w}_{,x}\delta\overset{+}{w}_{,\theta} - \overset{+}{w}_{,x}\delta\overset{+}{v}}{r}\right. \\ &\left. + \frac{\delta\overset{+}{v}_{,x}\overset{+}{v}_{,\theta} + \delta\overset{+}{v}_{,x}\overset{+}{w} + \delta\overset{+}{w}_{,x}\overset{+}{w}_{,\theta} - \delta\overset{+}{w}_{,x}\overset{+}{v}}{r}\right)\mathrm{d}V \end{aligned} \tag{5.60}$$

$$\begin{aligned}\delta U_{x\theta(\mathrm{int})} = G\int_V &\left(\frac{\bar{u}_{,\theta}}{r} + \bar{v}_{,x} + \frac{\bar{u}_{,x}\bar{u}_{,\theta}}{r} + \frac{\bar{v}_{,x}\bar{v}_{,\theta} + \bar{v}_{,x}\bar{w} + \bar{w}_{,x}\bar{w}_{,\theta} - \bar{w}_{,x}\bar{v}}{r}\right) \\ &\times\left(\frac{\delta\overset{+}{u}_{,\theta}}{r} + \delta\overset{+}{v}_{,x} + \frac{\bar{u}_{,x}\delta\overset{+}{u}_{,\theta} + \delta\overset{+}{u}_{,x}\bar{u}_{,\theta}}{r} + \frac{\bar{v}_{,x}\delta\overset{+}{v}_{,\theta} + \bar{v}_{,x}\delta\overset{+}{w} + \bar{w}_{,x}\delta\overset{+}{w}_{,\theta} - \bar{w}_{,x}\delta\overset{+}{v}}{r}\right. \\ &\left. + \frac{\delta\overset{+}{v}_{,x}\bar{v}_{,\theta} + \delta\overset{+}{v}_{,x}\bar{w} + \delta\overset{+}{w}_{,x}\bar{w}_{,\theta} - \delta\overset{+}{w}_{,x}\bar{v}}{r}\right)\mathrm{d}V \end{aligned} \tag{5.61}$$

Introducing GBT's separation of variable assumptions and modes superposition concept, given in equations (2.2) to (2.4), the domain of integration in equations (5.59) to (5.61) can be split into longitudinal and transversal directions x and θ, respectively. This gives:

$$
\begin{aligned}
\delta U_{x\theta(\mathrm{u})} \;=\; & \left.\sum_{i,k}\int_L {}^{ik}D\;{}^{i}\overset{+}{V}_{,x}\,\delta^{k}\overset{+}{V}_{,x}\,\mathrm{d}x\;\right\} K_{\mathrm{L}} \\
& \left.\begin{aligned}
& + \sum_{j,i,k}\int_L {}^{ijk}D_1\;{}^{j}\bar{V}_{,x}\;{}^{i}\overset{+}{V}_{,x}\,\delta^{k}\overset{+}{V}\,\mathrm{d}x + \sum_{j,i,k}\int_L {}^{ikj}D_1\;{}^{j}\bar{V}\;{}^{i}\overset{+}{V}_{,x}\,\delta^{k}\overset{+}{V}_{,x}\,\mathrm{d}x \\
& + \sum_{j,i,k}\int_L {}^{ijk}D_2\;{}^{j}\bar{V}_{,xx}\;{}^{i}\overset{+}{V}_{,x}\,\delta^{k}\overset{+}{V}_{,x}\,\mathrm{d}x + \sum_{j,i,k}\int_L {}^{ikj}D_2\;{}^{j}\bar{V}_{,x}\;{}^{i}\overset{+}{V}_{,x}\,\delta^{k}\overset{+}{V}_{,xx}\,\mathrm{d}x \\
& + \sum_{j,i,k}\int_L {}^{kji}D_1\;{}^{j}\bar{V}_{,x}\;{}^{i}\overset{+}{V}\,\delta^{k}\overset{+}{V}_{,x}\,\mathrm{d}x + \sum_{j,i,k}\int_L {}^{kij}D_1\;{}^{j}\bar{V}\;{}^{i}\overset{+}{V}_{,x}\,\delta^{k}\overset{+}{V}_{,x}\,\mathrm{d}x \\
& + \sum_{j,i,k}\int_L {}^{kji}D_2\;{}^{j}\bar{V}_{,xx}\;{}^{i}\overset{+}{V}_{,x}\,\delta^{k}\overset{+}{V}_{,x}\,\mathrm{d}x + \sum_{j,i,k}\int_L {}^{kij}D_2\;{}^{j}\bar{V}_{,x}\;{}^{i}\overset{+}{V}_{,xx}\,\delta^{k}\overset{+}{V}_{,x}\,\mathrm{d}x
\end{aligned}\right\} K_{\mathrm{uL}} \\
& \left.\begin{aligned}
& + \sum_{j,l,i,k}\int_L {}^{jilk}D_1\;{}^{j}\bar{V}_{,x}\;{}^{l}\bar{V}_{,x}\;{}^{i}\overset{+}{V}\,\delta^{k}\overset{+}{V}\,\mathrm{d}x + \sum_{j,l,i,k}\int_L {}^{jikl}D_1\;{}^{j}\bar{V}_{,x}\;{}^{l}\bar{V}\;{}^{i}\overset{+}{V}\,\delta^{k}\overset{+}{V}_{,x}\,\mathrm{d}x \\
& + \sum_{j,l,i,k}\int_L {}^{ijlk}D_1\;{}^{j}\bar{V}\;{}^{l}\bar{V}_{,x}\;{}^{i}\overset{+}{V}_{,x}\,\delta^{k}\overset{+}{V}\,\mathrm{d}x + \sum_{j,l,i,k}\int_L {}^{ijkl}D_1\;{}^{j}\bar{V}\;{}^{l}\bar{V}\;{}^{i}\overset{+}{V}_{,x}\,\delta^{k}\overset{+}{V}_{,x}\,\mathrm{d}x \\
& + \sum_{j,l,i,k}\int_L {}^{jilk}D_2\;{}^{j}\bar{V}_{,xx}\;{}^{l}\bar{V}_{,xx}\;{}^{i}\overset{+}{V}_{,x}\,\delta^{k}\overset{+}{V}_{,x}\,\mathrm{d}x + \sum_{j,l,i,k}\int_L {}^{jikl}D_2\;{}^{j}\bar{V}_{,xx}\;{}^{l}\bar{V}_{,x}\;{}^{i}\overset{+}{V}_{,x}\,\delta^{k}\overset{+}{V}_{,xx}\,\mathrm{d}x \\
& + \sum_{j,l,i,k}\int_L {}^{ijlk}D_2\;{}^{j}\bar{V}_{,x}\;{}^{l}\bar{V}_{,xx}\;{}^{i}\overset{+}{V}_{,xx}\,\delta^{k}\overset{+}{V}_{,x}\,\mathrm{d}x + \sum_{j,l,i,k}\int_L {}^{ijkl}D_2\;{}^{j}\bar{V}_{,x}\;{}^{l}\bar{V}_{,x}\;{}^{i}\overset{+}{V}_{,xx}\,\delta^{k}\overset{+}{V}_{,xx}\,\mathrm{d}x \\
& + \sum_{j,l,i,k}\int_L {}^{jkli}D_{12}\;{}^{j}\bar{V}_{,xx}\;{}^{l}\bar{V}_{,x}\;{}^{i}\overset{+}{V}\,\delta^{k}\overset{+}{V}\,\mathrm{d}x + \sum_{j,l,i,k}\int_L {}^{jkil}D_{12}\;{}^{j}\bar{V}_{,xx}\;{}^{l}\bar{V}\;{}^{i}\overset{+}{V}_{,x}\,\delta^{k}\overset{+}{V}\,\mathrm{d}x \\
& + \sum_{j,l,i,k}\int_L {}^{kjli}D_{12}\;{}^{j}\bar{V}\;{}^{l}\bar{V}_{,x}\;{}^{i}\overset{+}{V}\,\delta^{k}\overset{+}{V}_{,xx}\,\mathrm{d}x + \sum_{j,l,i,k}\int_L {}^{kjil}D_{12}\;{}^{j}\bar{V}\;{}^{l}\bar{V}\;{}^{i}\overset{+}{V}_{,x}\,\delta^{k}\overset{+}{V}_{,xx}\,\mathrm{d}x \\
& + \sum_{j,l,i,k}\int_L {}^{jilk}D_{12}\;{}^{j}\bar{V}_{,xx}\;{}^{l}\bar{V}_{,x}\;{}^{i}\overset{+}{V}\,\delta^{k}\overset{+}{V}\,\mathrm{d}x + \sum_{j,l,i,k}\int_L {}^{jikl}D_{12}\;{}^{j}\bar{V}_{,xx}\;{}^{l}\bar{V}\;{}^{i}\overset{+}{V}\,\delta^{k}\overset{+}{V}_{,x}\,\mathrm{d}x \\
& + \sum_{j,l,i,k}\int_L {}^{ijlk}D_{12}\;{}^{j}\bar{V}\;{}^{l}\bar{V}_{,x}\;{}^{i}\overset{+}{V}_{,xx}\,\delta^{k}\overset{+}{V}\,\mathrm{d}x + \sum_{j,l,i,k}\int_L {}^{ijkl}D_{12}\;{}^{j}\bar{V}\;{}^{l}\bar{V}\;{}^{i}\overset{+}{V}_{,xx}\,\delta^{k}\overset{+}{V}_{,x}\,\mathrm{d}x
\end{aligned}\right\} K_{\mathrm{uN}}
\end{aligned}
\tag{5.62}
$$

with the section properties

$${}^{ik}D = Gt\oint\left(\frac{{}^{i}u_{,\theta}(\theta)}{r} + {}^{i}v(\theta)\right)\left(\frac{{}^{k}u_{,\theta}(\theta)}{r} + {}^{k}v(\theta)\right)r\,d\theta \tag{5.63}$$

$$
\begin{aligned}
{}^{jik}D_1 &= Gt \oint \left(\frac{{}^{j}u_{,\theta}(\theta)}{r} + {}^{j}v(\theta)\right) \\
&\quad \times \left(\frac{{}^{i}v(\theta)^{k}v_{,\theta}(\theta) + {}^{i}v(\theta)^{k}w(\theta) + {}^{i}w(\theta)^{k}w_{,\theta}(\theta) - {}^{i}w(\theta)^{k}v(\theta)}{r}\right) r\, d\theta \qquad (5.64)\\
{}^{jik}D_2 &= Gt \oint \left(\frac{{}^{j}u_{,\theta}(\theta)}{r} + {}^{j}v(\theta)\right) \frac{{}^{i}u(\theta)^{k}u_{,\theta}(\theta)}{r} r\, d\theta \qquad (5.65)\\
{}^{jlik}D_1 &= Gt \oint \left(\frac{{}^{j}v(\theta)^{l}v_{,\theta}(\theta) + {}^{j}v(\theta)^{l}w(\theta) + {}^{j}w(\theta)^{l}w_{,\theta}(\theta) - {}^{j}w(\theta)^{l}v(\theta)}{r}\right) \\
&\quad \times \left(\frac{{}^{i}v(\theta)^{k}v_{,\theta}(\theta) + {}^{i}v(\theta)^{k}w(\theta) + {}^{i}w(\theta)^{k}w_{,\theta}(\theta) - {}^{i}w(\theta)^{k}v(\theta)}{r}\right) r\, d\theta \qquad (5.66)\\
{}^{jlik}D_2 &= Gt \oint \frac{{}^{j}u(\theta)^{l}u_{,\theta}(\theta)}{r} \frac{{}^{i}u(\theta)^{k}u_{,\theta}(\theta)}{r} r\, d\theta \qquad (5.67)\\
{}^{jlik}D_{12} &= Gt \oint \frac{{}^{j}u(\theta)^{l}u_{,\theta}(\theta)}{r} \\
&\quad \times \left(\frac{{}^{i}v(\theta)^{k}v_{,\theta}(\theta) + {}^{i}v(\theta)^{k}w(\theta) + {}^{i}w(\theta)^{k}w_{,\theta}(\theta) - {}^{i}w(\theta)^{k}v(\theta)}{r}\right) r\, d\theta \qquad (5.68)
\end{aligned}
$$

The coefficients in equations (5.63) to (5.68) are described as:

- ${}^{ik}D$ is a second-order tensor associated with the linear stiffness matrix $[K_{\mathrm{L}}]$ similar to equation (2.22),
- ${}^{ijk}D_1$ and ${}^{ijk}B_2$ are third-order tensors associated with the linear initial stress $[K_{\sigma\mathrm{L}}]$ and displacement stiffness matrix $[K_{\mathrm{uL}}]$,
- ${}^{ijkl}D_1$, ${}^{ijkl}D_2$, and ${}^{ijkl}D_{12}$ are fourth-order tensors associated with the quadratic initial stress $[K_{\sigma\mathrm{N}}]$ and displacement stiffness matrix $[K_{\sigma\mathrm{N}}]$.

The variation of the shear internal energy related with initial stress and internal force are shown in equations (5.69) and (5.70).

$$
\begin{aligned}
\delta U_{x\theta(\sigma)} = &\left.\begin{aligned}
&\sum_{j,i,k}\int_L {}^{jik}D_1\, {}^{j}\bar{V}_{,x}\, {}^{i}\overset{+}{V}_{,x}\, \delta^{k}\overset{+}{V}\, \mathrm{d}x + \sum_{j,i,k}\int_L {}^{jki}D_1\, {}^{j}\bar{V}_{,x}\, {}^{i}\overset{+}{V}\, \delta^{k}\overset{+}{V}_{,x}\, \mathrm{d}x \\
&+ \sum_{j,i,k}\int_L {}^{jik}D_2\, {}^{j}\bar{V}_{,x}\, {}^{i}\overset{+}{V}_{,xx}\, \delta^{k}\overset{+}{V}_{,x}\, \mathrm{d}x + \sum_{j,i,k}\int_L {}^{jki}D_2\, {}^{j}\bar{V}_{,x}\, {}^{i}\overset{+}{V}_{,x}\, \delta^{k}\overset{+}{V}_{,xx}\, \mathrm{d}x
\end{aligned}\right\} K_{\sigma\mathrm{L}} \\
&\left.\begin{aligned}
&+ \sum_{j,l,i,k}\int_L {}^{jlik}D_1\, {}^{j}\bar{V}_{,x}\, {}^{l}\bar{V}\, {}^{i}\overset{+}{V}_{,x}\, \delta^{k}\overset{+}{V}\, \mathrm{d}x + \sum_{j,l,i,k}\int_L {}^{jlki}D_1\, {}^{j}\bar{V}_{,x}\, {}^{l}\bar{V}\, {}^{i}\overset{+}{V}\, \delta^{k}\overset{+}{V}_{,x}\, \mathrm{d}x \\
&+ \sum_{j,l,i,k}\int_L {}^{jlik}D_2\, {}^{j}\bar{V}_{,xx}\, {}^{l}\bar{V}_{,x}\, {}^{i}\overset{+}{V}_{,xx}\, \delta^{k}\overset{+}{V}_{,x}\, \mathrm{d}x + \sum_{j,l,i,k}\int_L {}^{jlki}D_2\, {}^{j}\bar{V}_{,xx}\, {}^{l}\bar{V}_{,x}\, {}^{i}\overset{+}{V}_{,x}\, \delta^{k}\overset{+}{V}_{,xx}\, \mathrm{d}x \\
&+ \sum_{j,l,i,k}\int_L {}^{jlik}D_{12}\, {}^{j}\bar{V}_{,xx}\, {}^{l}\bar{V}_{,x}\, {}^{i}\overset{+}{V}_{,x}\, \delta^{k}\overset{+}{V}\, \mathrm{d}x + \sum_{j,l,i,k}\int_L {}^{jlki}D_{12}\, {}^{j}\bar{V}_{,xx}\, {}^{l}\bar{V}_{,x}\, {}^{i}\overset{+}{V}\, \delta^{k}\overset{+}{V}_{,x}\, \mathrm{d}x \\
&+ \sum_{j,l,i,k}\int_L {}^{kijl}D_{12}\, {}^{j}\bar{V}_{,x}\, {}^{l}\bar{V}\, {}^{i}\overset{+}{V}_{,x}\, \delta^{k}\overset{+}{V}_{,xx}\, \mathrm{d}x + \sum_{j,l,i,k}\int_L {}^{ikjl}D_{12}\, {}^{j}\bar{V}_{,x}\, {}^{l}\bar{V}\, {}^{i}\overset{+}{V}_{,xx}\, \delta^{k}\overset{+}{V}_{,x}\, \mathrm{d}x
\end{aligned}\right\} K_{\sigma\mathrm{N}}
\end{aligned}
\qquad (5.69)
$$

$$
\begin{aligned}
\delta U_{x\theta\,(\mathrm{int})} &= \sum_{i,k} \int_L {}^{ik}D\, {}^{i}\bar{V}_{,x}\, \delta^{k}\overset{+}{V}_{,x}\, \mathrm{d}x \\
&+ \sum_{j,i,k} \int_L {}^{jik}D_1\, {}^{j}\bar{V}_{,x}\, {}^{i}\bar{V}_{,x}\, \delta^{k}\overset{+}{V}\, \mathrm{d}x + \sum_{j,i,k} \int_L {}^{jki}D_1\, {}^{j}\bar{V}_{,x}\, {}^{i}\bar{V}\, \delta^{k}\overset{+}{V}_{,x}\, \mathrm{d}x \\
&+ \sum_{j,i,k} \int_L {}^{jik}D_2\, {}^{j}\bar{V}_{,x}\, {}^{i}\bar{V}_{,xx}\, \delta^{k}\overset{+}{V}_{,x}\, \mathrm{d}x + \sum_{j,i,k} \int_L {}^{jki}D_2\, {}^{j}\bar{V}_{,x}\, {}^{i}\bar{V}_{,x}\, \delta^{k}\overset{+}{V}_{,xx}\, \mathrm{d}x \\
&+ \sum_{j,i,k} \int_L {}^{kji}D_1\, {}^{j}\bar{V}_{,x}\, {}^{i}\bar{V}\, \delta^{k}\overset{+}{V}_{,x}\, \mathrm{d}x + \sum_{j,i,k} \int_L {}^{kji}D_2\, {}^{j}\bar{V}_{,xx}\, {}^{i}\bar{V}_{,x}\, \delta^{k}\overset{+}{V}_{,x}\, \mathrm{d}x \\
&+ \sum_{j,l,i,k} \int_L {}^{jlik}D_1\, {}^{j}\bar{V}_{,x}\, {}^{l}\bar{V}\, {}^{i}\bar{V}_{,x}\, \delta^{k}\overset{+}{V}\, \mathrm{d}x + \sum_{j,l,i,k} \int_L {}^{jlki}D_1\, {}^{j}\bar{V}_{,x}\, {}^{l}\bar{V}\, {}^{i}\bar{V}\, \delta^{k}\overset{+}{V}_{,x}\, \mathrm{d}x \\
&+ \sum_{j,l,i,k} \int_L {}^{jlik}D_2\, {}^{j}\bar{V}_{,xx}\, {}^{l}\bar{V}_{,x}\, {}^{i}\bar{V}_{,xx}\, \delta^{k}\overset{+}{V}_{,x}\, \mathrm{d}x + \sum_{j,l,i,k} \int_L {}^{jlki}D_2\, {}^{j}\bar{V}_{,xx}\, {}^{l}\bar{V}_{,x}\, {}^{i}\bar{V}_{,x}\, \delta^{k}\overset{+}{V}_{,xx}\, \mathrm{d}x \\
&+ \sum_{j,l,i,k} \int_L {}^{jlik}D_{12}\, {}^{j}\bar{V}_{,xx}\, {}^{l}\bar{V}_{,x}\, {}^{i}\bar{V}_{,x}\, \delta^{k}\overset{+}{V}\, \mathrm{d}x + \sum_{j,l,i,k} \int_L {}^{jlki}D_{12}\, {}^{j}\bar{V}_{,xx}\, {}^{l}\bar{V}_{,x}\, {}^{i}\bar{V}\, \delta^{k}\overset{+}{V}_{,x}\, \mathrm{d}x \\
&+ \sum_{j,l,i,k} \int_L {}^{kijl}D_{12}\, {}^{j}\bar{V}_{,x}\, {}^{l}\bar{V}\, {}^{i}\bar{V}_{,x}\, \delta^{k}\overset{+}{V}_{,xx}\, \mathrm{d}x + \sum_{j,l,i,k} \int_L {}^{ikjl}D_{12}\, {}^{j}\bar{V}_{,x}\, {}^{l}\bar{V}\, {}^{i}\bar{V}_{,xx}\, \delta^{k}\overset{+}{V}_{,x}\, \mathrm{d}x \\
&+ \sum_{j,l,i,k} \int_L {}^{jilk}D_1\, {}^{j}\bar{V}_{,x}\, {}^{l}\bar{V}_{,x}\, {}^{i}\bar{V}\, \delta^{k}\overset{+}{V}\, \mathrm{d}x + \sum_{j,l,i,k} \int_L {}^{ijlk}D_1\, {}^{j}\bar{V}\, {}^{l}\bar{V}_{,x}\, {}^{i}\bar{V}_{,x}\, \delta^{k}\overset{+}{V}\, \mathrm{d}x \\
&+ \sum_{j,l,i,k} \int_L {}^{jilk}D_2\, {}^{j}\bar{V}_{,xx}\, {}^{l}\bar{V}_{,xx}\, {}^{i}\bar{V}_{,x}\, \delta^{k}\overset{+}{V}_{,x}\, \mathrm{d}x + \sum_{j,l,i,k} \int_L {}^{ijlk}D_2\, {}^{j}\bar{V}_{,x}\, {}^{l}\bar{V}_{,xx}\, {}^{i}\bar{V}_{,xx}\, \delta^{k}\overset{+}{V}_{,x}\, \mathrm{d}x \\
&+ \sum_{j,l,i,k} \int_L {}^{jkli}D_{12}\, {}^{j}\bar{V}_{,xx}\, {}^{l}\bar{V}_{,x}\, {}^{i}\bar{V}\, \delta^{k}\overset{+}{V}\, \mathrm{d}x + \sum_{j,l,i,k} \int_L {}^{kjli}D_{12}\, {}^{j}\bar{V}\, {}^{l}\bar{V}_{,x}\, {}^{i}\bar{V}\, \delta^{k}\overset{+}{V}_{,xx}\, \mathrm{d}x \\
&+ \sum_{j,l,i,k} \int_L {}^{jilk}D_{12}\, {}^{j}\bar{V}_{,xx}\, {}^{l}\bar{V}_{,x}\, {}^{i}\bar{V}\, \delta^{k}\overset{+}{V}\, \mathrm{d}x + \sum_{j,l,i,k} \int_L {}^{ijlk}D_{12}\, {}^{j}\bar{V}\, {}^{l}\bar{V}_{,x}\, {}^{i}\bar{V}_{,xx}\, \delta^{k}\overset{+}{V}\, \mathrm{d}x
\end{aligned}
\tag{5.70}
$$

5.4 Deformation modes coupling

The nonlinear GBT coefficient tensors C, B, and D, which stem from the longitudinal extensions, transverse extensions, and shear strains, respectively, are important for the mapping of all possible coupling effects of the cross-section and in building the tangent stiffness matrix. The value of these coefficients can be computed from their respective equations by substituting the deformation mode functions described in Section 2.2.5 and computing the integrations analytically or numerically.

5.4.1 Third-order coupling tensor

The third-order coupling tensors ${}^{jik}C$, ${}^{jik}B$ and ${}^{jik}D$ define the relationship between the initial stress or displacement in mode j with the incremental displacements in mode i and forces in mode k. The C

and B third-order coupling tensors are symmetric in such a way that ${}^{jik}C_1 = {}^{jki}C_1$ and ${}^{jik}B_1 = {}^{jki}B_1$. Figures 5.3 to 5.5 show the nonlinear mode couplings between t, a, and the first five conventional and non-conventional GBT deformation modes as a sample in a table (matrix). These tables are the projections of the third-order tensors by reducing the dimension in j as shown in Figure 5.5b. In Figures 5.4 and 5.5, the row and column of the deformation mode indices with no coupling are removed from the table. The empty cells in the tables make evident that the coupling between modes j, i, and k is zero whereas cells with values show the list of all possible combinations of the deformation mode indices j, i, and k in separate rows within a cell.

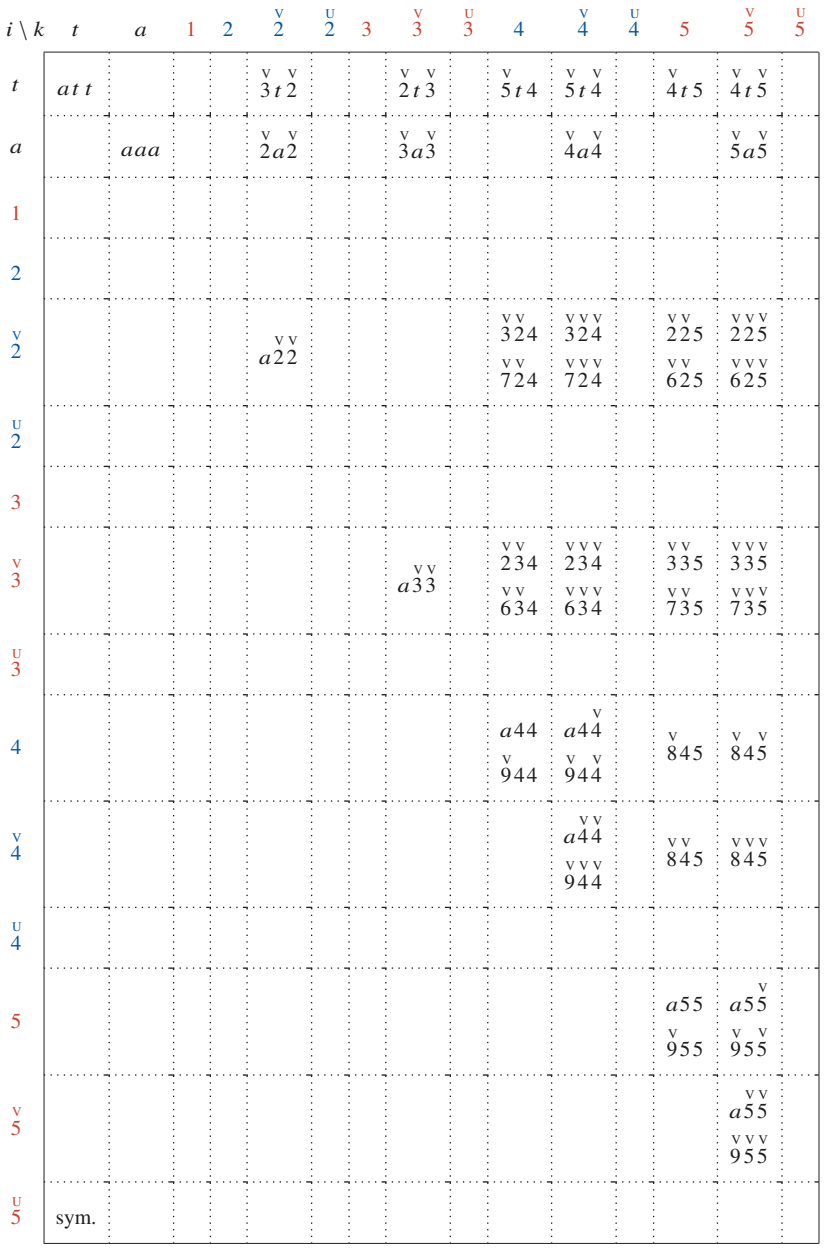

Figure 5.3: Third-order coupling tensor ${}^{jik}B_1$.

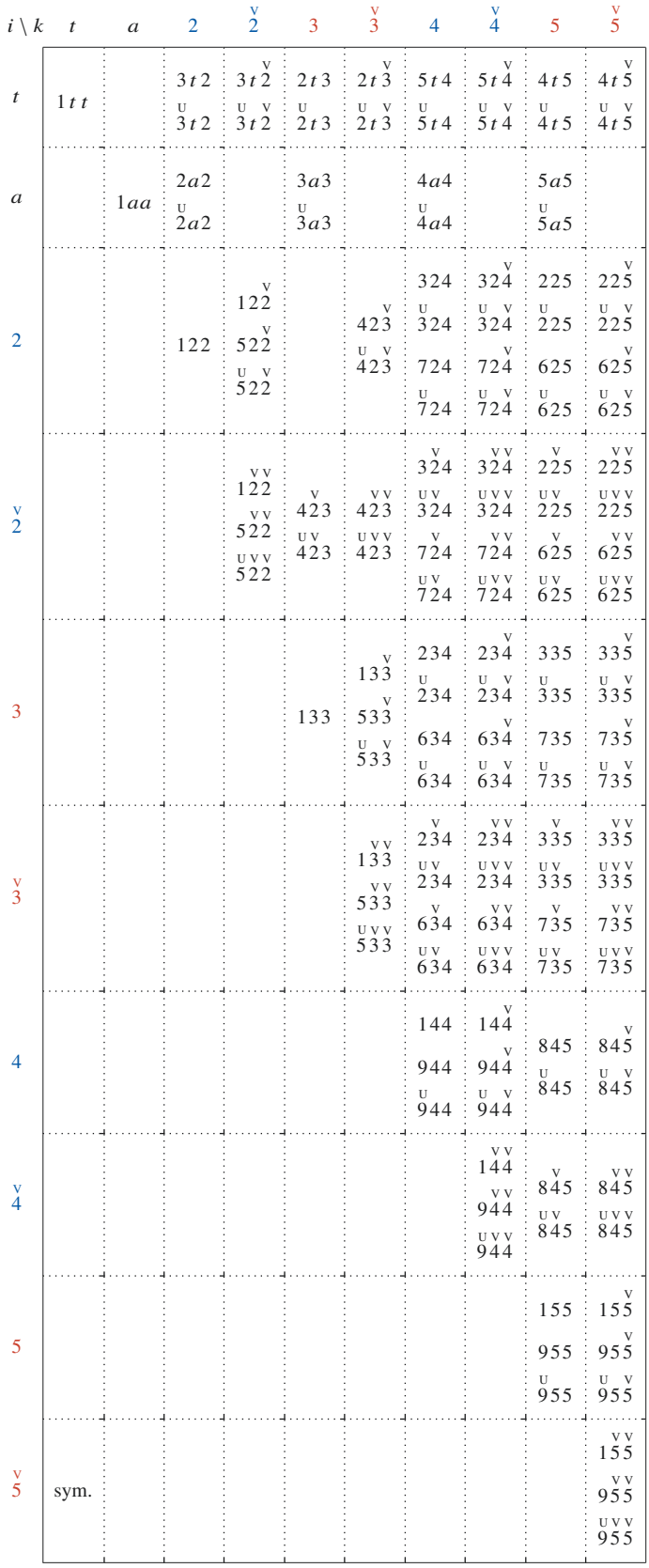

Figure 5.4: Third-order coupling tensor ${}^{jik}C_1$.

	t	a	2	v 2	3	v 3	4	v 4	5
t		$t\,t\,a$		v v 3 t 2 u v 3 t 2		v v 2 t 3 u v 2 t 3		v v 5 t 4 u v 5 t 4	
a	$t\,a\,t$			v v 2 a 2 u v 2 a 2		v v 3 a 3 u v 3 a 3	v 4 a 4 u 4 a 4	v v 4 a 4 u v 4 a 4	v 5 a 5 u 5 a 5
2	v 32 t u 32 t	v 22 a u 22 a		v v 522 u v 522		v v 423 u v 423	v 324 u 324 v 724 u 724	v v 324 u v 324 v v 724 u v 724	v 225 u 225 v 625 u 625
v 2		v v 22 a u v 22 a		u v v 522		v v t 23 v v v 423 u v v 423		v v v 324 u v v 324 v v v 724 u v v 724	
3	v 23 t u 23 t	v 33 a u 33 a		v v 432 u v 432		v v 533 u v 533	v 234 u 234 v 634 u 634	v v 234 u v 234 v v 634 u v 634	v 335 u 335 v 735 u 735
v 3		v v 33 a u v 33 a		v v t 32 v v v 432 u v v 432		u v v 533		v v v 234 u v v 234 v v v 634 u v v 634	
4	v 54 t u 54 t	v 44 a u 44 a		v v 342 u v 342 v v 742 u v 742		v v 243 u v 243 v v 643 u v 643	v 944 u 944	v v 944 u v 944	t 45 v 845 u 845
v 4		v v 44 a u v 44 a		v v v 342 u v v 342 v v v 742 u v v 742		v v v 243 u v v 243 v v v 643 u v v 643		v v v 944 u v v 944	
5	v 45 t u 45 t	v 55 a u 55 a		v v 252 u v 252 v v 652 u v 652		v v 353 u v 353 v v 753 u v 753	t 54 v 854 u 854	v v 854 u v 854	v 955 u 955

(a) Third-order coupling tensor ${}^{jik}D_1$.

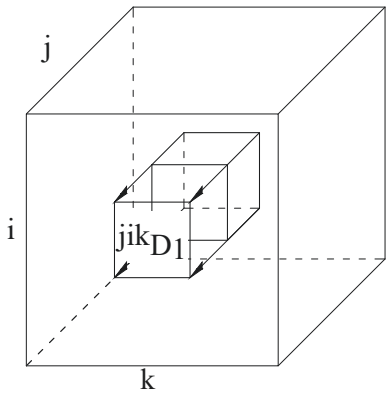

(b) Projection of a third-order tensor.

Figure 5.5: The projected view of the third-order coupling tensor ${}^{jik}D_1$.

5.4.2 Fourth-order coupling tensor

The fourth-order coupling tensors ${}^{jlik}C$, ${}^{jlik}B$ and ${}^{jlik}D$ define the relationship between the initial stress or displacement in modes j and l with the incremental displacements in mode i and forces in mode k. The C and B fourth-order coupling tensors are symmetric in such a way that ${}^{jlik}C_1 = {}^{jlki}C_1 = {}^{ljik}C_1 = {}^{ljki}C_1$ and ${}^{jlik}B_1 = {}^{jlki}B_1 = {}^{ljik}B_1 = {}^{ljki}B_1$. Figures 5.3 to 5.5 show the nonlinear mode couplings between t, a and the first five conventional and non-conventional GBT deformation modes as a sample in a table.

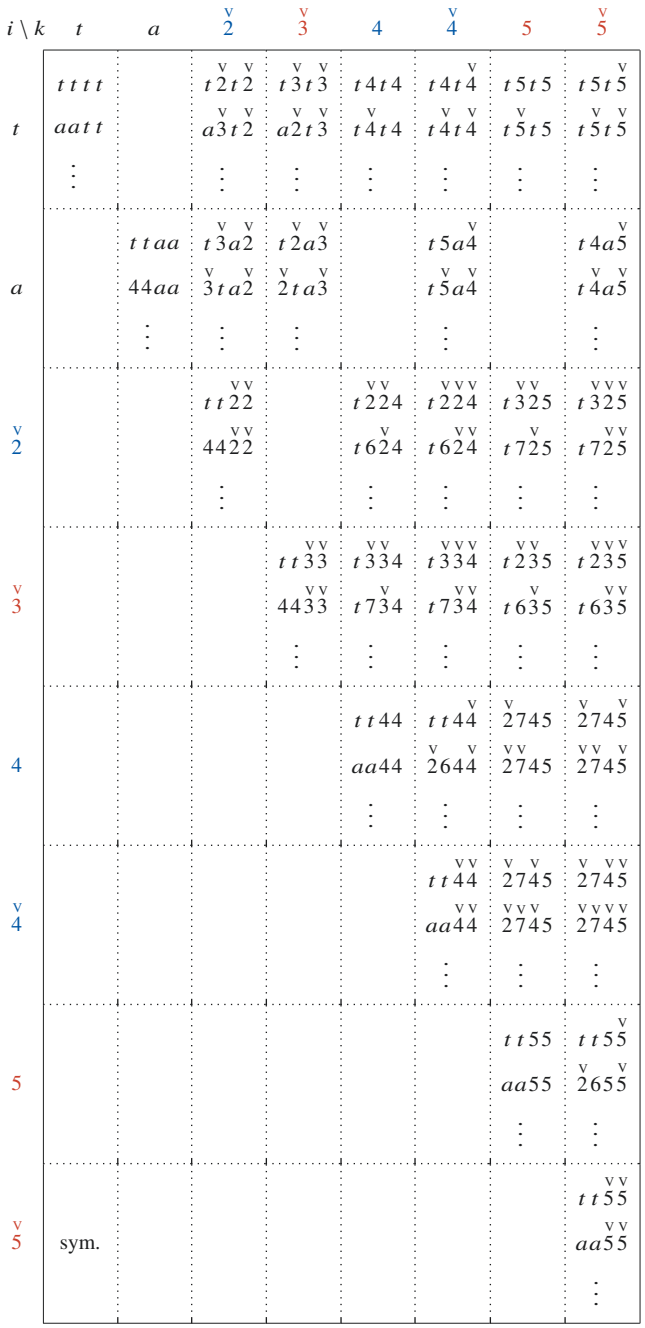

Figure 5.6: Fourth-order coupling tensor ${}^{jlik}B_1$.

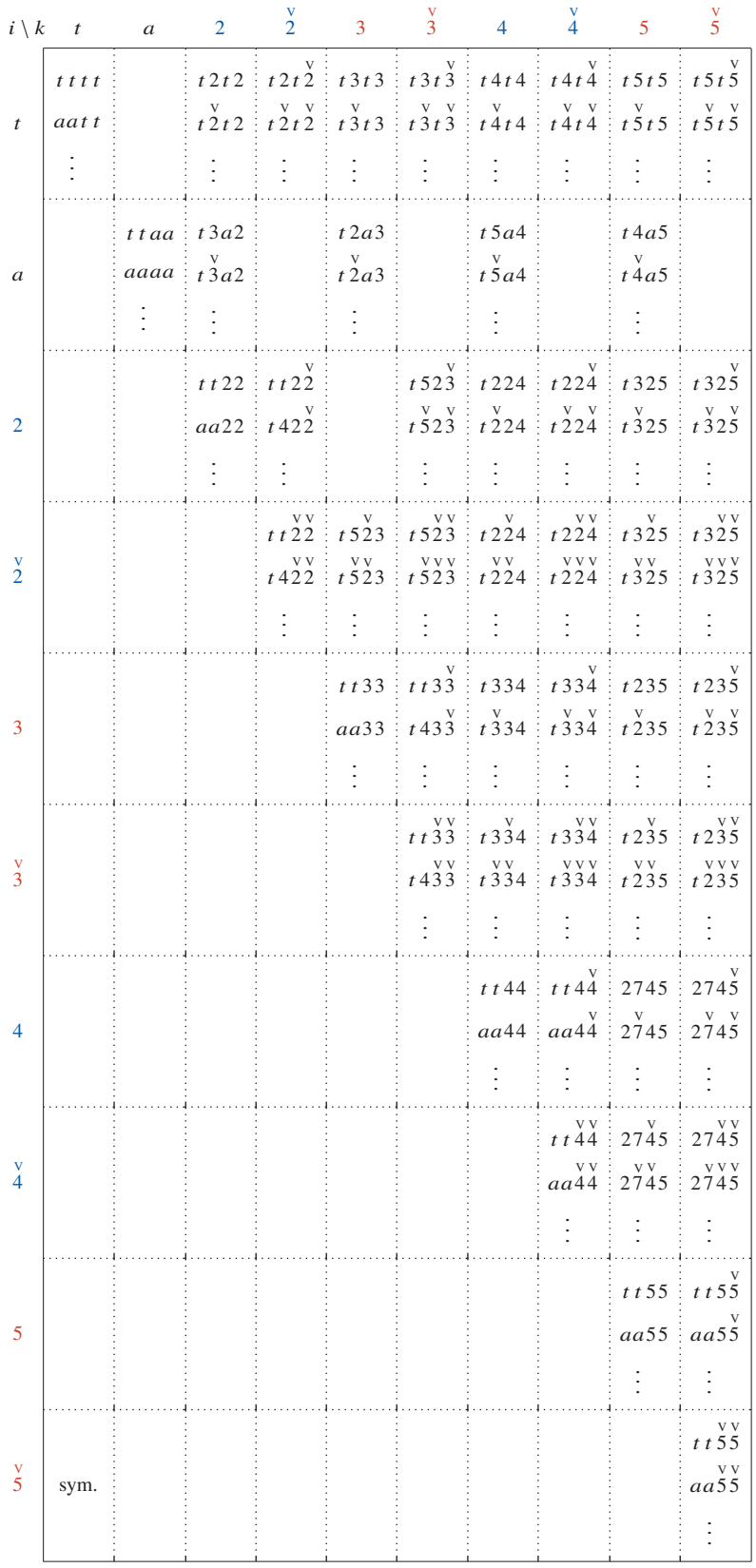

Figure 5.7: Fourth-order coupling tensor ${}^{jlik}C_1$.

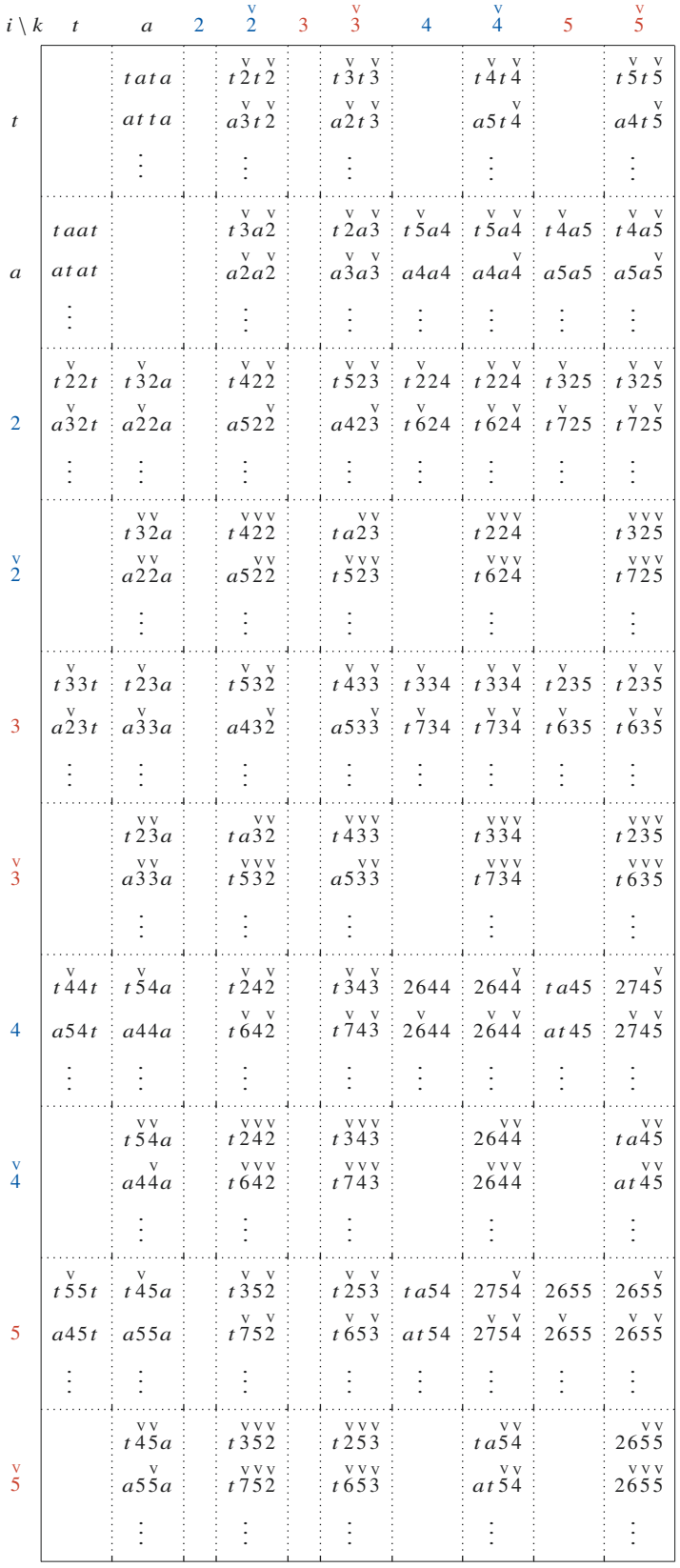

Figure 5.8: Fourth-order coupling tensor ${}^{jlik}D_1$.

In these tables, the projection of the fourth-order tensors is shown by reducing the dimension in j and l. In Figures 5.7 to 5.8, the row and column of deformation mode indices with no coupling are removed from the tables. The empty cells in the tables make evident that the coupling between modes j, l, i, and k is zero. The cells with values only show two of the possible combinations of deformation mode indices j, l, i, and k due to a large number of possibilities. The determination of the fourth-order tensors is computationally costly if large numbers of deformation modes are considered in the analysis. Here, the symmetric properties of these tensors can be used to reduce the computation effort.

5.5 Finite element formulation

Following the same procedure used to formulate the GBT linear element stiffness matrix in Section 2.2.6, the nonlinear GBT tangent element stiffness matrices and the element internal force vectors are derived by substituting equations (2.39) and (2.40) into the variation of the internal energy in equations (5.36), (5.48), (5.49), (5.50), (5.62), (5.69) and (5.70). As shown in equation (5.71), the formulation of the sub-matrix components ${}^{ik}[k_{\mathrm{T}}]$ of the tangent element stiffness matrices can be classified as the linear stiffness sub-matrix ${}^{ik}[k]$ which is independent of the displacements and is the same as equation (2.51) in Chapter 2, the initial linear displacement sub-matrix ${}^{jik}[k_{\mathrm{uL}}]$ which is linearly dependent on the initial displacements, the initial quadratic displacement sub-matrix ${}^{jlik}[k_{\mathrm{uN}}]$ which is quadratically dependent on the initial displacements, the initial linear stress stiffness sub-matrix ${}^{jik}[k_{\sigma\mathrm{L}}]$ and the initial quadratic stress stiffness sub-matrix ${}^{jlik}[k_{\sigma\mathrm{N}}]$.

$$ {}^{ik}[k_{\mathrm{T}}] = {}^{ik}[k] + {}^{jik}[k_{\mathrm{uL}}] + {}^{jlik}[k_{\mathrm{uN}}] + {}^{jik}[k_{\sigma\mathrm{L}}] + {}^{jlik}[k_{\sigma\mathrm{N}}] \tag{5.71} $$

Following, the derivation of each of the nonlinear terms in equation (5.71) is shown.

a) The initial linear displacement sub-matrix ${}^{jik}[k_{\mathrm{uL}}]$ can be extracted from the variation of the internal energy in equations (5.36), (5.48), and (5.62) by taking the summations related with K_{uL} and substituting equations (2.39) and (2.40).

$$ \begin{aligned} {}^{jik}[k_{\mathrm{uL}}] = {} & \left({}^{ijk}C_1 + {}^{kij}D_2\right) {}^{jik}[\mathbb{V}_9] + \left({}^{kji}C_1 + {}^{ikj}D_2\right) {}^{jik}[\mathbb{V}_{10}] + \left({}^{ijk}C_2 + {}^{kji}C_2\right) {}^{jik}[\mathbb{V}_{11}] \\ & + \left({}^{ijk}B_1 + {}^{kji}B_1\right) {}^{jik}[\mathbb{V}_{12}] + \left({}^{ijk}B_2 + {}^{kji}D_1\right) {}^{jik}[\mathbb{V}_{13}] + \left({}^{kji}B_2 + {}^{ijk}D_1\right) {}^{jik}[\mathbb{V}_{14}] \\ & + \left({}^{ikj}D_1 + {}^{kij}D_1\right) {}^{jik}[\mathbb{V}_{15}] + \left({}^{ijk}D_2 + {}^{kji}D_2\right) {}^{jik}[\mathbb{V}_{16}] \end{aligned} \tag{5.72} $$

b) The initial quadratic displacement sub-matrix ${}^{jlik}[k_{\mathrm{uN}}]$ can be extracted from the variation of the internal energy in equations (5.36), (5.48), and (5.62) by taking the summations related with K_{uN}

and substituting equations (2.39) and (2.40).

$$\begin{aligned}
{}^{jlik}[k_{\mathrm{uN}}] = &\left({}^{jilk}C_1 + {}^{jilk}B_2\right){}^{jlik}[\mathbb{V}_{17}] + {}^{jilk}C_2\,{}^{jlik}[\mathbb{V}_{18}] + {}^{ikjl}C_{12}\,{}^{jlik}[\mathbb{V}_{19}] \\
&+ {}^{jilk}C_{12}\,{}^{jlik}[\mathbb{V}_{20}] + {}^{jilk}B_1\,{}^{jlik}[\mathbb{V}_{21}] + {}^{lkji}B_{12}\,{}^{jlik}[\mathbb{V}_{22}] + {}^{jilk}B_{12}\,{}^{jlik}[\mathbb{V}_{23}] \\
&+ {}^{jilk}D_1\,{}^{jlik}[\mathbb{V}_{24}] + {}^{jikl}D_1\,{}^{jlik}[\mathbb{V}_{25}] + {}^{ijlk}D_1\,{}^{jlik}[\mathbb{V}_{26}] + {}^{ijkl}D_1\,{}^{jlik}[\mathbb{V}_{27}] \\
&+ {}^{jilk}D_2\,{}^{jlik}[\mathbb{V}_{28}] + {}^{jikl}D_2\,{}^{jlik}[\mathbb{V}_{29}] + {}^{ijlk}D_2\,{}^{jlik}[\mathbb{V}_{30}] + {}^{ijkl}D_2\,{}^{jlik}[\mathbb{V}_{31}] \\
&+ \left({}^{jkli}D_{12} + {}^{jilk}D_{12}\right){}^{jlik}[\mathbb{V}_{32}] + {}^{jkil}D_{12}\,{}^{jlik}[\mathbb{V}_{33}] + {}^{kjli}D_{12}\,{}^{jlik}[\mathbb{V}_{34}] \\
&+ {}^{kjil}D_{12}\,{}^{jlik}[\mathbb{V}_{35}] + {}^{jikl}D_{12}\,{}^{jlik}[\mathbb{V}_{36}] + {}^{ijlk}D_{12}\,{}^{jlik}[\mathbb{V}_{37}] + {}^{ijkl}D_{12}\,{}^{jlik}[\mathbb{V}_{38}]
\end{aligned} \tag{5.73}$$

c) The initial linear stress sub-matrix ${}^{jik}[k_{\sigma\mathrm{L}}]$ can be extracted from the variation of the internal energy in equations (5.36), (5.49) and (5.69) by taking the summations related with $K_{\sigma\mathrm{L}}$ and substituting equations (2.39) and (2.40).

$$\begin{aligned}
{}^{jik}[k_{\sigma\mathrm{L}}] = &\,{}^{jik}C_1\,{}^{jik}[\mathbb{V}_{16}] + {}^{jik}C_2\,{}^{jik}[\mathbb{V}_{11}] + {}^{jik}B_1\,{}^{jik}[\mathbb{V}_{12}] + {}^{jik}B_2\,{}^{jik}[\mathbb{V}_{15}] \\
&+ {}^{jik}D_1\,{}^{jik}[\mathbb{V}_{14}] + {}^{jki}D_1\,{}^{jik}[\mathbb{V}_{13}] + {}^{jik}D_2\,{}^{jik}[\mathbb{V}_{9}] + {}^{jki}D_2\,{}^{jik}[\mathbb{V}_{10}]
\end{aligned} \tag{5.74}$$

d) The initial quadratic stress sub-matrix ${}^{jlik}[k_{\sigma\mathrm{N}}]$ can be extracted from the variation of the internal energy in equations (5.36), (5.49) and (5.69) by taking the summations related with $K_{\sigma\mathrm{N}}$ and substituting equations (2.39) and (2.40).

$$\begin{aligned}
{}^{jlik}[k_{\sigma\mathrm{N}}] = &\left(\frac{{}^{jlik}C_1}{2} + \frac{{}^{jlik}B_2}{2}\right){}^{jlik}[\mathbb{V}_{17}] + \frac{{}^{jlik}C_2}{2}\,{}^{jlik}[\mathbb{V}_{18}] + \frac{{}^{jlik}C_{12}}{2}\,{}^{jlik}[\mathbb{V}_{28}] \\
&+ \frac{{}^{ikjl}C_{12}}{2}\,{}^{jlik}[\mathbb{V}_{31}] + \frac{{}^{jlik}B_1}{2}{}^{jlik}[\mathbb{V}_{21}] + \frac{{}^{jlik}B_{12}}{2}\,{}^{jlik}[\mathbb{V}_{24}] + \frac{{}^{ikjl}B_{12}}{2}\,{}^{jlik}[\mathbb{V}_{27}] \\
&+ {}^{jlik}D_1\,{}^{jlik}[\mathbb{V}_{23}] + {}^{jlki}D_1\,{}^{jlik}[\mathbb{V}_{25}] + {}^{jlik}D_2\,{}^{jlik}[\mathbb{V}_{20}] + {}^{jlki}D_2\,{}^{jlik}[\mathbb{V}_{29}] \\
&+ {}^{jlik}D_{12}\,{}^{jlik}[\mathbb{V}_{39}] + {}^{jlki}D_{12}\,{}^{jlik}[\mathbb{V}_{40}] + {}^{kijl}D_{12}\,{}^{jlik}[\mathbb{V}_{41}] + {}^{ikjl}D_{12}\,{}^{jlik}[\mathbb{V}_{42}]
\end{aligned} \tag{5.75}$$

In equations (5.72) and (5.74), the terms ${}^{jik}[\mathbb{V}_{...}]$ represent the corresponding longitudinal integrations in the variation of the internal energy equations. For illustration purposes, the derivation of ${}^{jik}[\mathbb{V}_9]$ is shown, assuming that j, i, and k are not equal to 1 and can be approximated using the Hermite cubic polynomials.

$$\begin{aligned}
{}^{jik}[\mathbb{V}_9] &= \int_L {}^{j}\bar{V}_{,x}(x)\,{}^{i}\overset{+}{V}_{,xx}(x)\,\delta^{k}\overset{+}{V}_{,x}(x)\,\mathrm{d}x \\
&= \int_{\frac{-L}{2}}^{\frac{+L}{2}} {}^{j}\{Tx\}_{,x}\,{}^{j}[Sh]\,{}^{j}\{\bar{\vartheta}\}\,{}^{k}[Sh]^{T}\,{}^{k}\{Tx\}_{,x}^{T}\,{}^{i}\{Tx\}_{,xx}\,{}^{i}[Sh]\,\mathrm{d}x
\end{aligned} \tag{5.76}$$

Here, the completeness coefficient matrix ${}^{j}[Sh_{\mathrm{H}}]$ can be expressed using row vectors ${}^{j}\{Sh_{\mathrm{r}}\}$.

$$
{}^{j}[Sh_{\mathrm{H}}] = \begin{bmatrix} \frac{2}{L^3} & \frac{1}{L^2} & -\frac{2}{L^3} & \frac{1}{L^2} \\ 0 & -\frac{1}{2L} & 0 & \frac{1}{2L} \\ -\frac{3}{2L} & -\frac{1}{4} & \frac{3}{2L} & -\frac{1}{4} \\ \frac{1}{2} & \frac{L}{8} & \frac{1}{2} & -\frac{L}{8} \end{bmatrix} = \begin{bmatrix} \{Sh_{\mathrm{r1}}\} \\ \{Sh_{\mathrm{r2}}\} \\ \{Sh_{\mathrm{r3}}\} \\ \{Sh_{\mathrm{r4}}\} \end{bmatrix} \tag{5.77}
$$

Substituting equation (5.77) into equation (5.76), the term ${}^{jik}[\mathbb{V}_9]$ can be written as:

$$
\begin{aligned}
{}^{jik}[\mathbb{V}_9] = {}& {}^{j}\{Sh_{\mathrm{r1}}\}\ {}^{j}\{\bar{\vartheta}\}\ {}^{k}[Sh]^T \int_{\frac{-L}{2}}^{\frac{+L}{2}} 3x^2\ {}^{k}\{Tx\}_{,x}^{T}\ {}^{i}\{Tx\}_{,xx}\,\mathrm{d}x\ {}^{i}[Sh] \\
& + {}^{j}\{Sh_{\mathrm{r2}}\}\ {}^{j}\{\bar{\vartheta}\}\ {}^{k}[Sh]^T \int_{\frac{-L}{2}}^{\frac{+L}{2}} 2x\ {}^{k}\{Tx\}_{,x}^{T}\ {}^{i}\{Tx\}_{,xx}\,\mathrm{d}x\ {}^{i}[Sh] \\
& + {}^{j}\{Sh_{\mathrm{r3}}\}\ {}^{j}\{\bar{\vartheta}\}\ {}^{k}[Sh]^T \int_{\frac{-L}{2}}^{\frac{+L}{2}} {}^{k}\{Tx\}_{,x}^{T}\ {}^{i}\{Tx\}_{,xx}\,\mathrm{d}x\ {}^{i}[Sh]
\end{aligned} \tag{5.78}
$$

Computing the integrals in equation (5.78), ${}^{jik}[\mathbb{V}_9]$ can be expressed as the following matrix:

$$
\begin{aligned}
{}^{jik}[\mathbb{V}_9] = {}& {}^{j}\{Sh_{\mathrm{r1}}\}\ {}^{j}\{\bar{\vartheta}\}\ \frac{L}{40} \begin{bmatrix} 0 & 6 & 0 & -6 \\ -18 & -11\,L & 18 & -7\,L \\ 0 & -6 & 0 & 6 \\ 18\,L & 7\,L & -18 & 11\,L \end{bmatrix} \\
& + {}^{j}\{Sh_{\mathrm{r2}}\}\ {}^{j}\{\bar{\vartheta}\}\ \frac{1}{30L} \begin{bmatrix} -36 & -18\,L & 36 & -18\,L \\ 12\,L & 11\,L^2 & -12\,L & L^2 \\ 36 & 18\,L & -36 & 18\,L \\ 12\,L & L^2 & -12\,L & 11\,L^2 \end{bmatrix} \\
& + {}^{j}\{Sh_{\mathrm{r3}}\}\ {}^{j}\{\bar{\vartheta}\}\ \frac{1}{2L} \begin{bmatrix} 0 & 2 & 0 & -2 \\ -2 & -L & 2 & -L \\ 0 & -2 & 0 & 2 \\ 2 & L & -2 & L \end{bmatrix}
\end{aligned} \tag{5.79}
$$

Similarly, in equations (5.73) and (5.75) the terms ${}^{jlik}[\mathbb{V}_{...}]$ represent the corresponding longitudinal integrations in the variation of the internal energy equations. For illustration purposes, the derivation of ${}^{jlik}[\mathbb{V}_{17}]$ is shown assuming that j, l, i, and k are not equal to 1 and can be approximated using the Hermite cubic polynomials.

$$
\begin{aligned}
{}^{jlik}[\mathbb{V}_{17}] &= \int_L {}^{j}\bar{V}_{,x}(x)\,{}^{l}\bar{V}_{,x}(x)\,{}^{i}\overset{+}{V}_{,x}(x)\,\delta^{k}\overset{+}{V}_{,x}(x)\,\mathrm{d}x \\
&= \int_{\frac{-L}{2}}^{\frac{+L}{2}} {}^{j}\{Tx\}_{,x}{}^{j}[Sh]\;{}^{j}\{\bar{\vartheta}\}\;{}^{l}\{Tx\}_{,x}{}^{l}[Sh]\;{}^{l}\{\bar{\vartheta}\}\;{}^{k}[Sh]^{T}\;{}^{k}\{Tx\}_{,x}^{T}\;{}^{i}\{Tx\}_{,x}{}^{i}[Sh]\,\mathrm{d}x \\
&= {}^{j}\{Sh_{\mathrm{r1}}\}\;{}^{j}\{\bar{\vartheta}\}\;{}^{l}\{Sh_{\mathrm{r1}}\}\;{}^{l}\{\bar{\vartheta}\}^{k}[Sh]^{T}\int_{\frac{-L}{2}}^{\frac{+L}{2}} 9x^{4}\;{}^{k}\{Tx\}_{,x}^{T}\;{}^{i}\{Tx\}_{,x}\,\mathrm{d}x\;{}^{i}[Sh] \\
&+ {}^{j}\{Sh_{\mathrm{r1}}\}\;{}^{j}\{\bar{\vartheta}\}\;{}^{l}\{Sh_{\mathrm{r2}}\}\;{}^{l}\{\bar{\vartheta}\}^{k}[Sh]^{T}\int_{\frac{-L}{2}}^{\frac{+L}{2}} 12x^{3}\;{}^{k}\{Tx\}_{,x}^{T}\;{}^{i}\{Tx\}_{,x}\,\mathrm{d}x\;{}^{i}[Sh] \\
&+ {}^{j}\{Sh_{\mathrm{r1}}\}\;{}^{j}\{\bar{\vartheta}\}\;{}^{l}\{Sh_{\mathrm{r3}}\}\;{}^{l}\{\bar{\vartheta}\}^{k}[Sh]^{T}\int_{\frac{-L}{2}}^{\frac{+L}{2}} 6x^{2}\;{}^{k}\{Tx\}_{,x}^{T}\;{}^{i}\{Tx\}_{,x}\,\mathrm{d}x\;{}^{i}[Sh] \\
&+ {}^{j}\{Sh_{\mathrm{r2}}\}\;{}^{j}\{\bar{\vartheta}\}\;{}^{l}\{Sh_{\mathrm{r2}}\}\;{}^{l}\{\bar{\vartheta}\}^{k}[Sh]^{T}\int_{\frac{-L}{2}}^{\frac{+L}{2}} 4x^{2}\;{}^{k}\{Tx\}_{,x}^{T}\;{}^{i}\{Tx\}_{,x}\,\mathrm{d}x\;{}^{i}[Sh] \\
&+ {}^{j}\{Sh_{\mathrm{r2}}\}\;{}^{j}\{\bar{\vartheta}\}\;{}^{l}\{Sh_{\mathrm{r3}}\}\;{}^{l}\{\bar{\vartheta}\}^{k}[Sh]^{T}\int_{\frac{-L}{2}}^{\frac{+L}{2}} 4x\;{}^{k}\{Tx\}_{,x}^{T}\;{}^{i}\{Tx\}_{,x}\,\mathrm{d}x\;{}^{i}[Sh] \\
&+ {}^{j}\{Sh_{\mathrm{r3}}\}\;{}^{j}\{\bar{\vartheta}\}\;{}^{l}\{Sh_{\mathrm{r3}}\}\;{}^{l}\{\bar{\vartheta}\}^{k}[Sh]^{T}\int_{\frac{-L}{2}}^{\frac{+L}{2}} {}^{k}\{Tx\}_{,x}^{T}\;{}^{i}\{Tx\}_{,x}\,\mathrm{d}x\;{}^{i}[Sh]
\end{aligned}
\tag{5.80}
$$

Computing the integrals in equation (5.80), ${}^{jlik}[\mathbb{V}_{17}]$ is expressed as matrix in equation (5.81).

$$
\begin{aligned}
{}^{jlik}[\mathbb{V}_{17}] = {}^{j}\{Sh_{\mathrm{r1}}\}\,{}^{j}\{\bar{\vartheta}\}\,{}^{l}\{Sh_{\mathrm{r1}}\}\,{}^{l}\{\bar{\vartheta}\}\,\frac{L^3}{1120}
&\begin{bmatrix}
36 & -9\,L & -36 & -9\,L \\
 & 36\,L^2 & 9\,L & -9\,L^2 \\
 & & 36 & 9\,L \\
\text{sym.} & & & 36\,L^2
\end{bmatrix} \\
+\,{}^{j}\{Sh_{\mathrm{r1}}\}\,{}^{j}\{\bar{\vartheta}\}\,{}^{l}\{Sh_{\mathrm{r2}}\}\,{}^{l}\{\bar{\vartheta}\}\,\frac{3L^3}{140}
&\begin{bmatrix}
0 & 3 & 0 & -3 \\
 & -4\,L & -3 & 0 \\
 & & 0 & 3 \\
\text{sym.} & & & 4\,L
\end{bmatrix} \\
+\,{}^{j}\{Sh_{\mathrm{r1}}\}\,{}^{j}\{\bar{\vartheta}\}\,{}^{l}\{Sh_{\mathrm{r3}}\}\,{}^{l}\{\bar{\vartheta}\}\,\frac{L}{140}
&\begin{bmatrix}
36 & -3\,L & -36 & -3\,L \\
 & 16\,L^2 & 3\,L & -5\,L^2 \\
 & & 36 & 3\,L \\
\text{sym.} & & & 16\,L^2
\end{bmatrix} \\
+\,{}^{j}\{Sh_{\mathrm{r2}}\}\,{}^{j}\{\bar{\vartheta}\}\,{}^{l}\{Sh_{\mathrm{r2}}\}\,{}^{l}\{\bar{\vartheta}\}\,\frac{L}{210}
&\begin{bmatrix}
36 & -3\,L & -36 & -3\,L \\
 & 16\,L^2 & 3\,L & -5\,L^2 \\
 & & 36 & 3\,L \\
\text{sym.} & & & 16\,L^2
\end{bmatrix} \\
+\,{}^{j}\{Sh_{\mathrm{r2}}\}\,{}^{j}\{\bar{\vartheta}\}\,{}^{l}\{Sh_{\mathrm{r3}}\}\,{}^{l}\{\bar{\vartheta}\}\,\frac{L}{15}
&\begin{bmatrix}
0 & 3 & 0 & -3 \\
 & -2\,L & -3 & 0 \\
 & & 0 & 3 \\
\text{sym.} & & & 2\,L
\end{bmatrix} \\
+\,{}^{j}\{Sh_{\mathrm{r3}}\}\,{}^{j}\{\bar{\vartheta}\}\,{}^{l}\{Sh_{\mathrm{r3}}\}\,{}^{l}\{\bar{\vartheta}\}\,\frac{1}{30L}
&\begin{bmatrix}
36 & 3\,L & -36 & 3\,L \\
 & 4\,L^2 & -3\,L & -L^2 \\
 & & 36 & -3\,L \\
\text{sym.} & & & 4\,L^2
\end{bmatrix}
\end{aligned}
\tag{5.81}
$$

Once all the sub-matrices are computed the tangent element stiffness matrix can be assembled as shown in equation (5.82). Here, if the initial conditions are assumed to be zero at the beginning of the nonlinear analysis, then the tangent element stiffness matrix will be reduced to the elastic stiffness matrix.

$$
[K_{\mathrm{T}}]^e = \begin{bmatrix}
{}^{tt}[k] & [0] & [0] & [0] & [0] & [0] & [0] & \dots \\
 & {}^{aa}[k] & [0] & [0] & [0] & [0] & [0] & \dots \\
 & & {}^{11}[k] & [0] & [0] & [0] & [0] & \dots \\
 & & & {}^{22}[k] & {}^{\mathrm{V}}_{22}[k] & {}^{\mathrm{U}}_{22}[k] & [0] & \dots \\
 & & & & {}^{\mathrm{V}\mathrm{V}}_{22}[k] & {}^{\mathrm{V}\mathrm{U}}_{22}[k] & [0] & \dots \\
 & & & & & {}^{\mathrm{U}\mathrm{U}}_{22}[k] & [0] & \dots \\
 & & & & & & {}^{33}[k] & \dots \\
\text{sym.} & & & & & & & \ddots
\end{bmatrix}
$$

$$
+\sum_j \begin{bmatrix}
{}^{jtt}[k] & {}^{jta}[k] & {}^{jt1}[k] & {}^{jt2}[k] & {}^{jt\mathrm{V}}_{2}[k] & {}^{jt\mathrm{U}}_{2}[k] & {}^{jt3}[k] & \dots \\
 & {}^{jaa}[k] & {}^{ja1}[k] & {}^{ja2}[k] & {}^{ja\mathrm{V}}_{2}[k] & {}^{ja\mathrm{U}}_{2}[k] & {}^{ja3}[k] & \dots \\
 & & {}^{j11}[k] & {}^{j12}[k] & {}^{j1\mathrm{V}}_{2}[k] & {}^{j1\mathrm{U}}_{2}[k] & {}^{j13}[k] & \dots \\
 & & & {}^{j22}[k] & {}^{j2\mathrm{V}}_{2}[k] & {}^{j2\mathrm{U}}_{2}[k] & {}^{j23}[k] & \dots \\
 & & & & {}^{j\mathrm{V}\mathrm{V}}_{22}[k] & {}^{j\mathrm{V}\mathrm{U}}_{22}[k] & {}^{j\mathrm{V}}_{23}[k] & \dots \\
 & & & & & {}^{j\mathrm{U}\mathrm{U}}_{22}[k] & {}^{j\mathrm{U}}_{23}[k] & \dots \\
 & & & & & & {}^{j33}[k] & \dots \\
sym. & & & & & & & \ddots
\end{bmatrix}
$$

$$
+\sum_{j,l} \begin{bmatrix}
{}^{jltt}[k] & {}^{jlta}[k] & {}^{jlt1}[k] & {}^{jlt2}[k] & {}^{jlt\mathrm{V}}_{2}[k] & {}^{jlt\mathrm{U}}_{2}[k] & {}^{jlt3}[k] & \dots \\
 & {}^{jlaa}[k] & {}^{jla1}[k] & {}^{jla2}[k] & {}^{jla\mathrm{V}}_{2}[k] & {}^{jla\mathrm{U}}_{2}[k] & {}^{jla3}[k] & \dots \\
 & & {}^{jl11}[k] & {}^{jl12}[k] & {}^{jl1\mathrm{V}}_{2}[k] & {}^{jl1\mathrm{U}}_{2}[k] & {}^{jl13}[k] & \dots \\
 & & & {}^{jl22}[k] & {}^{jl2\mathrm{V}}_{2}[k] & {}^{jl2\mathrm{U}}_{2}[k] & {}^{jl23}[k] & \dots \\
 & & & & {}^{jl\mathrm{V}\mathrm{V}}_{22}[k] & {}^{jl\mathrm{V}\mathrm{U}}_{22}[k] & {}^{jl\mathrm{V}}_{23}[k] & \dots \\
 & & & & & {}^{jl\mathrm{U}\mathrm{U}}_{22}[k] & {}^{jl\mathrm{U}}_{23}[k] & \dots \\
 & & & & & & {}^{jl33}[k] & \dots \\
sym. & & & & & & & \ddots
\end{bmatrix} \tag{5.82}
$$

The initial linear and quadratic tangent element stiffness matrices, which are the second and third terms in equation (5.82), respectively, are activated after the first step due to the change in displacements. The correct values of these matrices in each load increment step are determined using the Newton-Raphson iterative solver.

The other important parameter in a nonlinear analysis is the formulation of the element internal force vectors. As explained in equation (5.3), the relationship between the tangent stiffness matrix $\mathbf{K}_{\mathrm{T}}$, internal force $\mathbf{F}_{\mathrm{int}}$ and displacement $\mathbf{V}$ can be defined as:

$$\mathbf{K}_{\mathrm{T}} = \frac{\partial \mathbf{F}_{\mathrm{int}}}{\partial \mathbf{V}} \tag{5.83}$$

This relationship is important for checking the consistency of the formulation. Here, the element internal force vector is derived or extracted from the variation of the internal energy equations (5.36), (5.50), and (5.70). As shown in equation (5.84), the formulation of sub-vector components ${}^{k}\{f_{\mathrm{int}}\}$ of the element internal force vector can be classified as the linear internal force sub-vector ${}^{ik}\{f\}$ which is linearly dependent on the displacements, the initial linear internal force sub-vector ${}^{jik}\{f_{\mathrm{L}}\}$ which is quadratically dependent on the initial displacements and the initial quadratic internal force sub-vector ${}^{jlik}\{f_{\mathrm{N}}\}$ which is cubically dependent on the initial displacements.

$${}^{k}\{f_{\mathrm{int}}\} = {}^{ik}\{f\} + {}^{jik}\{f_{\mathrm{L}}\} + {}^{jlik}\{f_{\mathrm{N}}\} \tag{5.84}$$

Following, the derivation of each of these terms in equation (5.84) is shown.

a) The sub-vector ${}^{ik}\{f\}$ can be extracted from the variation of the internal energy in equations (5.36), (5.50) and (5.70) by taking the summations related with the second-order coupling tensors in the F_{int} and substituting equations (2.39) and (2.40).

$${}^{ik}\{f\} = {}^{ik}C\ {}^{ik}\{\mathbb{V}_1\} + {}^{ik}B\ {}^{ik}\{\mathbb{V}_2\} + {}^{ik}D\ {}^{ik}\{\mathbb{V}_3\} \tag{5.85}$$

b) The sub-vector ${}^{jik}\{f_{\mathrm{L}}\}$ can be extracted from the variation of the internal energy in equations (5.36), (5.50) and (5.70) by taking the summations related with the third-order coupling tensors in the F_{int} and substituting equations (2.39) and (2.40).

$$\begin{aligned}{}^{jik}\{f_{\mathrm{L}}\} = &\left({}^{ijk}C_1 + {}^{kji}D_2\right){}^{jik}\{\mathbb{V}_4\} + \left({}^{jik}C_2 + \frac{{}^{kji}C_2}{2}\right){}^{jik}\{\mathbb{V}_5\} + \left(\frac{{}^{kji}C_1}{2} + {}^{jki}D_2\right){}^{jik}\{\mathbb{V}_6\} \\ &+ \left({}^{jik}B_1 + \frac{{}^{kji}B_1}{2}\right){}^{jik}\{\mathbb{V}_7\} + {}^{jik}B_2\ {}^{jik}\{\mathbb{V}_8\} + \left(\frac{{}^{kji}B_2}{2} + {}^{jik}D_1\right){}^{jik}\{\mathbb{V}_9\} \\ &+ \left({}^{jki}D_1 + {}^{kji}D_1\right){}^{jik}\{\mathbb{V}_{10}\} + {}^{jik}D_2\ {}^{jik}\{\mathbb{V}_{11}\}\end{aligned} \tag{5.86}$$

c) The sub-vector ${}^{jlik}\{f_{\mathrm{N}}\}$ can be extracted from the variation of the internal energy in equations (5.36), (5.50) and (5.70) by taking the summations related with the fourth-order coupling tensors

in the F_{int} and substituting equations (2.39) and (2.40).

$$
\begin{aligned}
{}^{jlik}\{f_{\text{N}}\} = &\left(\frac{{}^{jlik}C_1}{2} + \frac{{}^{jlik}B_2}{2}\right) {}^{jlik}\{\mathbb{V}_{12}\} + \frac{{}^{jlik}C_2}{2}\ {}^{jlik}\{\mathbb{V}_{13}\} + \frac{{}^{ikjl}C_{12}}{2}\ {}^{jlik}\{\mathbb{V}_{14}\} \\
&+ \left(\frac{{}^{jlik}C_{12}}{2} + {}^{jilk}D_2\right) {}^{jlik}\{\mathbb{V}_{15}\} + \frac{{}^{jlik}B_1}{2}\ {}^{jlik}\{\mathbb{V}_{16}\} + \frac{{}^{ikjl}B_{12}}{2}\ {}^{jlik}\{\mathbb{V}_{17}\} \\
&+ \left(\frac{{}^{jlik}B_{12}}{2} + {}^{jilk}D_1\right) {}^{jlik}\{\mathbb{V}_{18}\} + {}^{jlik}D_1\ {}^{jlik}\{\mathbb{V}_{19}\} + {}^{jlki}D_1\ {}^{jlik}\{\mathbb{V}_{20}\} \\
&+ {}^{jlik}D_2\ {}^{jlik}\{\mathbb{V}_{21}\} + {}^{jlki}D_2\ {}^{jlik}\{\mathbb{V}_{22}\} + {}^{ijlk}D_1\ {}^{jlik}\{\mathbb{V}_{27}\} + {}^{ijlk}D_2\ {}^{jlik}\{\mathbb{V}_{28}\} \\
&+ \left({}^{jkli}D_{12} + {}^{jilk}D_{12}\right) {}^{jlik}\{\mathbb{V}_{29}\} + {}^{jlik}D_{12}\ {}^{jlik}\{\mathbb{V}_{23}\} + {}^{jlki}D_{12}\ {}^{jlik}\{\mathbb{V}_{24}\} \\
&+ {}^{kijl}D_{12}\ {}^{jlik}\{\mathbb{V}_{25}\} + {}^{ikjl}D_{12}\ {}^{jlik}\{\mathbb{V}_{26}\} + {}^{kjli}D_{12}\ {}^{jlik}\{\mathbb{V}_{30}\} + {}^{ijlk}D_{12}\ {}^{jlik}\{\mathbb{V}_{31}\}
\end{aligned} \tag{5.87}
$$

In equations (5.84) to (5.87) the terms ${}^{(\cdots)}\{\mathbb{V}_{(\cdot)}\}$ represent the corresponding longitudinal integration in the variation of the internal energy equations. For illustration purposes, the derivations of ${}^{ik}\{\mathbb{V}_1\}$, ${}^{jik}\{\mathbb{V}_4\}$, and ${}^{jlik}\{\mathbb{V}_{13}\}$ are shown, assuming that j, l, i, and k are not equal to 1 and can be approximated using the Hermite cubic polynomials.

$$
\begin{aligned}
{}^{ik}\{\mathbb{V}_1\} &= \int_L {}^{i}\bar{V}_{,xx}(x)\, \delta^{k}\overset{+}{V}_{,xx}(x)\, \mathrm{d}x \\
&= {}^{k}[Sh]^{T} \int_{\frac{-L}{2}}^{\frac{+L}{2}} {}^{k}\{Tx\}_{,xx}^{T}\, {}^{i}\{Tx\}_{,xx}\, \mathrm{d}x\ {}^{i}[Sh]^{i}\{\bar{\vartheta}\} \\
&= \frac{1}{L^3}\begin{bmatrix} 12 & 6L & -12 & 6L \\ & 4L^2 & -6L & 2L^2 \\ & & 12 & -6L \\ \text{sym.} & & & 4L^2 \end{bmatrix} {}^{i}\{\bar{\vartheta}\}
\end{aligned} \tag{5.88}
$$

Substituting the equations (2.39), (2.40), and (5.77), the term ${}^{jik}\{\mathbb{V}_4\}$ can be derived as:

$$
\begin{aligned}
{}^{jik}\{\mathbb{V}_4\} &= \int_L {}^{j}\bar{V}_{,xx}(x)\, {}^{i}\bar{V}_{,x}(x)\, \delta^{k}\overset{+}{V}_{,x}(x)\, \mathrm{d}x \\
&= \int_{\frac{-L}{2}}^{\frac{+L}{2}} {}^{j}\{Tx\}_{,xx}\, {}^{j}[Sh]^{j}\{\bar{\vartheta}\}^{k}[Sh]^{T}\, {}^{k}\{Tx\}_{,x}^{T}\, {}^{i}\{Tx\}_{,x}\, {}^{i}[Sh]^{i}\{\bar{\vartheta}\}\, \mathrm{d}x \\
&= {}^{j}\{Sh_{\text{r1}}\}\ {}^{j}\{\bar{\vartheta}\}^{k}[Sh]^{T} \int_{\frac{-L}{2}}^{\frac{+L}{2}} 6x\ {}^{k}\{Tx\}_{,x}^{T}\, {}^{i}\{Tx\}_{,x}\, \mathrm{d}x\ {}^{i}[Sh]\ {}^{i}\{\bar{\vartheta}\} \\
&+ {}^{j}\{Sh_{\text{r2}}\}\ {}^{j}\{\bar{\vartheta}\}^{k}[Sh]^{T} \int_{\frac{-L}{2}}^{\frac{+L}{2}} 2\ {}^{k}\{Tx\}_{,x}^{T}\, {}^{i}\{Tx\}_{,x}\, \mathrm{d}x\ {}^{i}[Sh]\ {}^{i}\{\bar{\vartheta}\}
\end{aligned} \tag{5.89}
$$

Computing the integrals in equation (5.89), ${}^{jik}\{\mathbb{V}_4\}$ is expressed as a vector in equation (5.90).

$$
\begin{aligned}
{}^{jik}\{\mathbb{V}_4\} = {}^{j}\{Sh_{\mathrm{r1}}\}\,{}^{j}\{\bar{\vartheta}\}\frac{1}{10}
&\begin{bmatrix}
0 & 3\,L & 0 & -3\,L \\
 & -2\,L^2 & -3\,L & 0 \\
 & & 0 & 3\,L \\
\text{sym.} & & & 2\,L^2
\end{bmatrix}
{}^{i}\{\bar{\vartheta}\} \\
+\,{}^{j}\{Sh_{\mathrm{r2}}\}\,{}^{j}\{\bar{\vartheta}\}\frac{1}{15L}
&\begin{bmatrix}
36 & 3\,L & -36 & 3\,L \\
 & 4\,L^2 & -3\,L & -L^2 \\
 & & 36 & -3\,L \\
\text{sym.} & & & 4\,L^2
\end{bmatrix}
{}^{i}\{\bar{\vartheta}\}
\end{aligned}
\tag{5.90}
$$

Substituting the equations (2.39), (2.40), and (5.77) the term ${}^{jlik}\{\mathbb{V}_{13}\}$ can be derived as:

$$
\begin{aligned}
{}^{jlik}\{\mathbb{V}_{13}\} &= \int_L {}^{j}\bar{V}_{,xx}(x)\,{}^{l}\bar{V}_{,xx}(x)\,{}^{i}\bar{V}_{,xx}(x)\,\delta^{k}\overset{+}{V}_{,xx}(x)\,\mathrm{d}x \\
&= \int_{\frac{-L}{2}}^{\frac{+L}{2}} {}^{j}\{Tx\}_{,xx}{}^{j}[Sh]\,{}^{j}\{\bar{\vartheta}\}\,{}^{l}\{Tx\}_{,xx}{}^{l}[Sh]\,{}^{l}\{\bar{\vartheta}\}\,{}^{k}[Sh]^{T}\,{}^{k}\{Tx\}^{T}_{,xx}{}^{i}\{Tx\}_{,xx}{}^{i}[Sh]\,{}^{i}\{\bar{\vartheta}\}\,\mathrm{d}x \\
&= {}^{j}\{Sh_{\mathrm{r1}}\}\,{}^{j}\{\bar{\vartheta}\}\,{}^{l}\{Sh_{\mathrm{r1}}\}\,{}^{l}\{\bar{\vartheta}\}\,{}^{k}[Sh]^{T}\int_{\frac{-L}{2}}^{\frac{+L}{2}} 36x^2\,{}^{k}\{Tx\}^{T}_{,xx}{}^{i}\{Tx\}_{,xx}\,\mathrm{d}x\,{}^{i}[Sh]\,{}^{i}\{\bar{\vartheta}\} \\
&+ {}^{j}\{Sh_{\mathrm{r1}}\}\,{}^{j}\{\bar{\vartheta}\}\,{}^{l}\{Sh_{\mathrm{r2}}\}\,{}^{l}\{\bar{\vartheta}\}\,{}^{k}[Sh]^{T}\int_{\frac{-L}{2}}^{\frac{+L}{2}} 24x\,{}^{k}\{Tx\}^{T}_{,xx}{}^{i}\{Tx\}_{,xx}\,\mathrm{d}x\,{}^{i}[Sh]\,{}^{i}\{\bar{\vartheta}\} \\
&+ {}^{j}\{Sh_{\mathrm{r2}}\}\,{}^{j}\{\bar{\vartheta}\}\,{}^{l}\{Sh_{\mathrm{r2}}\}\,{}^{l}\{\bar{\vartheta}\}\,{}^{k}[Sh]^{T}\int_{\frac{-L}{2}}^{\frac{+L}{2}} 4\,{}^{k}\{Tx\}^{T}_{,xx}{}^{i}\{Tx\}_{,xx}\,\mathrm{d}x\,{}^{i}[Sh]\,{}^{i}\{\bar{\vartheta}\}
\end{aligned}
\tag{5.91}
$$

Computing the integrals in equation (5.91), ${}^{jlik}\{\mathbb{V}_{13}\}$ is expressed as a vector in equation (5.92).

$$
\begin{aligned}
{}^{jlik}\{\mathbb{V}_{13}\} = {}^{j}\{Sh_{\mathrm{r1}}\}\,{}^{j}\{\bar{\vartheta}\}\,{}^{l}\{Sh_{\mathrm{r1}}\}\,{}^{l}\{\bar{\vartheta}\}\,\frac{6}{5L}
\begin{bmatrix}
54 & 27\,L & -54 & 27\,L \\
 & 16\,L^2 & -27\,L & 11\,L^2 \\
 & & 54 & -27\,L \\
\text{sym.} & & & 16\,L^2
\end{bmatrix}
{}^{i}\{\bar{\vartheta}\} \\
+ {}^{j}\{Sh_{\mathrm{r1}}\}\,{}^{j}\{\bar{\vartheta}\}\,{}^{l}\{Sh_{\mathrm{r2}}\}\,{}^{l}\{\bar{\vartheta}\}\,\frac{24}{L}
\begin{bmatrix}
0 & -1 & 0 & 1 \\
 & -L & 1 & 0 \\
 & & 0 & -1 \\
\text{sym.} & & & L
\end{bmatrix}
{}^{i}\{\bar{\vartheta}\} \\
+ {}^{j}\{Sh_{\mathrm{r2}}\}\,{}^{j}\{\bar{\vartheta}\}\,{}^{l}\{Sh_{\mathrm{r2}}\}\,{}^{l}\{\bar{\vartheta}\}\,\frac{4}{L^3}
\begin{bmatrix}
12 & 6\,L & -12 & 6\,L \\
 & 4\,L^2 & -6\,L & 2\,L^2 \\
 & & 12 & -6\,L \\
\text{sym.} & & & 4\,L^2
\end{bmatrix}
{}^{i}\{\bar{\vartheta}\}
\end{aligned}
\tag{5.92}
$$

Once all the sub-vectors are computed the element internal force vector can be assembled as shown in equation (5.93).

$$
\{F_{\mathrm{int}}\}^{e} = \sum_{i}
\begin{Bmatrix}
{}^{it}\{f\} \\
{}^{ia}\{f\} \\
{}^{i1}\{f\} \\
{}^{i2}\{f\} \\
{}^{i\overset{\mathrm{V}}{2}}\{f\} \\
{}^{i\overset{\mathrm{U}}{2}}\{f\} \\
{}^{i3}\{f\} \\
{}^{i\overset{\mathrm{V}}{3}}\{f\} \\
\vdots
\end{Bmatrix}
+ \sum_{j,i}
\begin{Bmatrix}
{}^{jit}\{f_{\mathrm{L}}\} \\
{}^{jia}\{f_{\mathrm{L}}\} \\
{}^{ji1}\{f_{\mathrm{L}}\} \\
{}^{ji2}\{f_{\mathrm{L}}\} \\
{}^{ji\overset{\mathrm{V}}{2}}\{f_{\mathrm{L}}\} \\
{}^{ji\overset{\mathrm{U}}{2}}\{f_{\mathrm{L}}\} \\
{}^{ji3}\{f_{\mathrm{L}}\} \\
{}^{ji\overset{\mathrm{V}}{3}}\{f_{\mathrm{L}}\} \\
\vdots
\end{Bmatrix}
+ \sum_{j,l,i}
\begin{Bmatrix}
{}^{jlit}\{f_{\mathrm{N}}\} \\
{}^{jlia}\{f_{\mathrm{N}}\} \\
{}^{jli1}\{f_{\mathrm{N}}\} \\
{}^{jli2}\{f_{\mathrm{N}}\} \\
{}^{jli\overset{\mathrm{V}}{2}}\{f_{\mathrm{N}}\} \\
{}^{jli\overset{\mathrm{U}}{2}}\{f_{\mathrm{N}}\} \\
{}^{jli3}\{f_{\mathrm{N}}\} \\
{}^{jli\overset{\mathrm{V}}{3}}\{f_{\mathrm{N}}\} \\
\vdots
\end{Bmatrix}
\tag{5.93}
$$

During the Python code implementation, the consistency of the derived tangent stiffness matrix in equation (5.82) and the internal force vector in equation (5.93) is checked based on the relationship defined in equation (5.83). In nonlinear analysis, the internal force vector is a parameter more crucial than the tangent stiffness matrix, since without the accurate calculation of the internal force the analysis cannot converge to the correct solution. In fact, in the explicit finite element method only the internal force vector is required for analysis.

5.6 Nonlinear stress resultants

In this section, the nonlinear stress resultants for the membrane forces are formulated for a CHS GBT element. Here, the stress resultants for the bending moment M_x, M_θ, $M_{x\theta}$, and shear stress Q_x and Q_θ are the same as the ones shown in equations (2.60) to (2.64) since the plate in bending strains are assumed to be linear. However, the membrane forces N_x, N_θ, and $N_{x\theta}$ in equations (5.97) to (5.101) are formulated based on the nonlinear initial membrane strains $\bar{\varepsilon}_x$, $\bar{\varepsilon}_\theta$, and $\bar{\gamma}_{x\theta}$ in equations (5.13), (5.16), and (5.19). For a linearly elastic material, the corresponding initial stresses can be defined as:

$$\bar{\sigma}_x = \frac{E}{1-\mu^2}\left(\bar{\varepsilon}_x + \mu\bar{\varepsilon}_\theta\right) \tag{5.94}$$

$$\bar{\sigma}_\theta = \frac{E}{1-\mu^2}\left(\bar{\varepsilon}_\theta + \mu\bar{\varepsilon}_x\right) \tag{5.95}$$

$$\bar{\tau}_{x\theta} = G\,\bar{\gamma}_{x\theta} \tag{5.96}$$

Substituting the initial stresses and strains in equations (5.94) to (5.96) and (5.13) to (5.19) and the GBT displacement functions in equations (2.2) to (2.4) into the membrane stress resultants which are based on the assumption (**A3)** in equations (5.97), (5.99) and (5.101), the GBT nonlinear membrane stress resultants can be derived as:

$$N_x = \int_{\frac{-t}{2}}^{\frac{+t}{2}} \bar{\sigma}_x \; dz \tag{5.97}$$

$$\begin{aligned}
&= Q\Bigg(\sum_{k=1}^{\infty} {}^{k}u(\theta)\,{}^{k}V_{,xx} + \sum_{i=1}^{\infty}\sum_{k=1}^{\infty}\Big(\frac{{}^{i}u(\theta)\,{}^{k}u(\theta)}{2}\,{}^{i}V_{,xx}\,{}^{k}V_{,xx} + \frac{{}^{i}v(\theta)\,{}^{k}v(\theta) + {}^{i}w(\theta)\,{}^{k}w(\theta)}{2}\,{}^{i}V_{,x}\,{}^{k}V_{,x}\Big)\\
&+ \mu\sum_{k=1}^{\infty}\frac{{}^{k}v_{,\theta}(\theta) + {}^{k}w(\theta)}{r}\,{}^{k}V + \mu\sum_{i=1}^{\infty}\sum_{k=1}^{\infty}\Big(\frac{{}^{i}u_{,\theta}(\theta)\,{}^{k}u_{,\theta}(\theta)}{2r^2}\,{}^{i}V_{,x}\,{}^{k}V_{,x}\\
&+ \frac{\left({}^{i}v_{,\theta}(\theta) + {}^{i}w(\theta)\right)\left({}^{k}v_{,\theta}(\theta) + {}^{k}w(\theta)\right) + \left({}^{i}w_{,\theta}(\theta) - {}^{i}v(\theta)\right)\left({}^{k}w_{,\theta}(\theta) - {}^{k}v(\theta)\right)}{2r^2}\,{}^{i}V\,{}^{k}V\Big)\Bigg)
\end{aligned} \tag{5.98}$$

$$N_\theta = \int_{\frac{-t}{2}}^{\frac{+t}{2}} \bar{\sigma}_\theta \; dz \tag{5.99}$$

$$\begin{aligned}
&= Q\Bigg(\sum_{k=1}^{\infty}\frac{{}^{k}v_{,\theta}(\theta) + {}^{k}w(\theta)}{r}\,{}^{k}V + \sum_{i=1}^{\infty}\sum_{k=1}^{\infty}\Big(\frac{{}^{i}u_{,\theta}(\theta)\,{}^{k}u_{,\theta}(\theta)}{2r^2}\,{}^{i}V_{,x}\,{}^{k}V_{,x}\\
&+ \frac{\left({}^{i}v_{,\theta}(\theta) + {}^{i}w(\theta)\right)\left({}^{k}v_{,\theta}(\theta) + {}^{k}w(\theta)\right) + \left({}^{i}w_{,\theta}(\theta) - {}^{i}v(\theta)\right)\left({}^{k}w_{,\theta}(\theta) - {}^{k}v(\theta)\right)}{2r^2}\,{}^{i}V\,{}^{k}V\Big)\\
&+ \mu\sum_{k=1}^{\infty}{}^{k}u(\theta)\,{}^{k}V_{,xx} + \mu\sum_{i=1}^{\infty}\sum_{k=1}^{\infty}\Big(\frac{{}^{i}u(\theta)\,{}^{k}u(\theta)}{2}\,{}^{i}V_{,xx}\,{}^{k}V_{,xx} + \frac{{}^{i}v(\theta)\,{}^{k}v(\theta) + {}^{i}w(\theta)\,{}^{k}w(\theta)}{2}\,{}^{i}V_{,x}\,{}^{k}V_{,x}\Big)\Bigg)
\end{aligned} \tag{5.100}$$

$$N_{x\theta} = \int_{\frac{-t}{2}}^{\frac{+t}{2}} \bar{\tau}_{x\theta}\ dz \tag{5.101}$$

$$= Gt\Bigg(\sum_{k=1}^{\infty} \Big(\frac{{}^{k}u_{,\theta}(\theta)}{r} + {}^{k}v(\theta) \Big) {}^{k}V_{,x} + \sum_{i=1}^{\infty}\sum_{k=1}^{\infty} \Big(\frac{{}^{i}u(\theta)\,{}^{k}u_{,\theta}(\theta)}{r} {}^{i}V_{,xx}\,{}^{k}V_{,x} + \frac{{}^{i}v(\theta)\big({}^{k}v_{,\theta}(\theta) + {}^{k}w(\theta)\big) + {}^{i}w(\theta)\big({}^{k}w_{,\theta}(\theta) - {}^{k}v(\theta)\big)}{r} {}^{i}V_{,x}\,{}^{k}V \Big) \Bigg) \tag{5.102}$$

5.7 Numerical examples

In this section, two examples are presented involving the transverse and longitudinal bending of short and long thin-walled circular pipes, respectively. The purpose of these examples is to validate and illustrate the application and capabilities of the formulated GBT element by analyzing the nonlinear relationship between transverse loading and cross-sectional deformations. Here, the GBT's generalized modal amplitude vector is determined within a single load step by solving equation (5.103) using the Newton-Raphson incremental iterative solver method.

$$[K_{\mathrm{T}}]\{\overset{+}{d}\} = \{F_{\mathrm{ext}}\} - \{F_{\mathrm{int}}\} \tag{5.103}$$

where $[K_{\mathrm{T}}]$ is the member tangent stiffness matrix, $\{F_{\mathrm{ext}}\}$ is the external load vector, $\{F_{\mathrm{int}}\}$ is the internal force vector, and $\{d\}$ is the incremental generalized modal amplitude vector. Both examples are compared with equivalent shell finite element models using ANSYS [10] software. These models have been developed using quadrilateral elements with 6 DoF per node which are based on Reissner-Mindlin's kinematic assumption with linear interpolation functions as implemented in the ANSYS software under the name SHELL 181.

5.7.1 Transverse bending

In this example, a short strip of a circular pipe is considered to be under a projected loading. As shown in Figure 5.9, the transverse loading q is applied at the top and bottom of the cross-section in such a way that the circular cross-section will undergo ovalization (or flattening if the contact is considered).

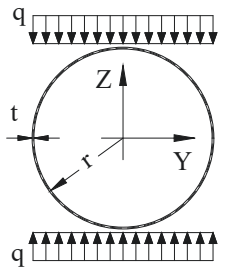

(a) Cross-section

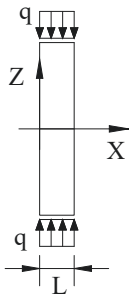

(b) Longitudinal section

$L = 200\,\mathrm{mm}$
$r = 500\,\mathrm{mm}$
$t = 10\,\mathrm{mm}$
$E = 205\,\mathrm{GPa}$
$\mu = 0.0$

Figure 5.9: Pipe section under projected loading.

Since this example has a free boundary condition, no axial loading, an elastic material behavior and no Poisson effect, the nonlinearity involved in this problem is effectively reduced to the nonlinear transverse membrane strain which can be simplified as:

$$\varepsilon_\theta^{\mathrm{M}} = \frac{v_{,\theta} + w}{r} + \frac{1}{2r^2}\Big((v_{,\theta} + w)^2 + (w_{,\theta} - v)^2\Big) \tag{5.104}$$

This means to build the tangent stiffness matrix and the internal force vector, the only third and fourth order tensors required will be ${}^{jik}B_1$ and ${}^{jlik}B_1$. Furthermore, the non-conventional shear-u modes can be neglected since there are no displacements in u.

As the first step in the GBT analysis, the projected load q is transformed into the local coordinates, x, θ, and z, whereas the longitudinal component in the x direction in this case is zero.

Table 5.1: External load modal decomposition.

Mode k	${}^{k}q_\theta\left[\frac{\mathrm{N}}{\mathrm{mm}}\right]$	${}^{k}q_z\left[\frac{\mathrm{N}}{\mathrm{mm}}\right]$
a	0	$-\pi\, qr$
5	$-\pi\, qr$	$-2\pi\, qr$
$\overset{\mathrm{v}}{5}$	$-\pi\, qr$	0

Substituting equations (2.66) and (2.67) into equations (2.33) and (2.34) the modal decomposition of the external load can be determined in $\left[\frac{\mathrm{N}}{\mathrm{mm}}\right]$ as:

$${}^{k}q_\theta = \int_0^{2\pi} q\sin(\theta)\cos(\theta)\ {}^{k}v(\theta)\, r d\theta \tag{5.105}$$

$${}^{k}q_z = \int_0^{2\pi} -q\cos(\theta)^2\ {}^{k}w(\theta)\, r d\theta \tag{5.106}$$

As shown in Table 5.1, the only modes which have an external load contribution are a, 5, and $\overset{\mathrm{v}}{5}$, since the respective integrals in equations (5.105) and (5.106) are zero for all other deformation modes. Here, the selection of deformation modes to be considered for the analysis depends on the external modal load participation, the third-order tensor ${}^{jik}B_1$, in Figure 5.3 and the fourth-order tensor ${}^{jlik}B_1$ in Figure 5.6. The two criteria for the selection of the deformation modes can be summarized as:

- First: all modes with external load participation should be considered.
- Second: since these modes with external load participation will produce deformations in the first step of the analysis, which is a linear elastic analysis, they being the cause of the initial stress and displacement, in the next step of the nonlinear analysis, they will activate other modes they are coupled to in the third ${}^{jik}B_1$ and fourth order tensor ${}^{jlik}B_1$ while building the tangent stiffness matrix. However, if these newly activated modes failed to create the corresponding internal force vector, they would have to be ignored. In other words, the modes without external load participation must be activated based on the coupling tensors in the tangent stiffness matrix and the internal force vector to be considered in the nonlinear GBT analysis. For example, due to the mode couplings ${}^{\mathrm{v}}_{559}B_1$ and ${}^{\mathrm{v}\ \mathrm{v}}_{559}B_1$, modes 9 and $\overset{\mathrm{v}}{9}$ will be activated in the tangent stiffness matrix and in the internal force vector. This can be generalized in such a way that if j and i in the third-order coupling tensor ${}^{jik}B_1$ have an initial displacement, then mode k will be activated, similarly, if j, l, and i in the fourth-order coupling tensor ${}^{jlik}B_1$ have an initial displacement, then mode k will be activated.

Based on these criteria, the types of deformation modes involved in a GBT nonlinear analysis can be decided at the beginning of the analysis. In this example, the type of modes involved in the analysis are (a, 5, $\overset{v}{5}$, 9, $\overset{v}{9}$, 13, $\overset{v}{13}$, 17, $\overset{v}{17}$, 21, $\overset{v}{21}$, ...). From this list, the number of modes to be considered can be decided based on a displacement convergence analysis. As shown in Figure 5.12, modes up to $\overset{v}{17}$ are sufficient to reach the displacement convergence in the GBT analysis. In the second step of the GBT analysis, the tangent element stiffness matrix $[K_T]^e$, the external force vector $\{F_{ext}\}^e$, and the internal force vector $\{F_{int}\}^e$ are built in order to calculate the incremental generalized modal amplitude vector $\{d\}^e$ in equation (5.103). To determine the tangent element stiffness matrix and the internal force vector, first all possible mode couplings must be identified in the third and fourth order coupling tensors. In this example for the selected seven modes, which are a, 5, $\overset{v}{5}$, 9, $\overset{v}{9}$, 13, and $\overset{v}{13}$, the possible nonzero number of third-order mode couplings ${}^{jik}B_1$ are only 55 out of $7^3 = 343$ total possibilities. Similarly, the possible nonzero number of fourth-order mode couplings ${}^{jlik}B_1$ are only 773 out of $7^4 = 2401$ total possibilities. This significant reduction in the possibilities of mode couplings is due to the brilliant modal nature of GBT. Furthermore, only half of these couplings need to be calculated due to the symmetric nature of the tensor ${}^{jik}B_1$ as shown in Figure (5.10).

$i \setminus k$	a	5	$\overset{v}{5}$	9	$\overset{v}{9}$	13	$\overset{v}{13}$
a	aaa		$\overset{v}{5}a\overset{v}{5}$		$\overset{v}{9}a\overset{v}{9}$		$\overset{v}{13}a\overset{v}{13}$
5		$a55$ $\overset{v}{9}55$	$a\overset{v}{5}5$ $\overset{v}{9}\overset{v}{5}5$	$\overset{v}{5}59$ $\overset{v}{1}359$	$\overset{v}{5}\overset{v}{9}9$ $\overset{v}{1}\overset{v}{3}59$	$\overset{v}{9}513$	$\overset{v}{9}\overset{v}{5}13$
$\overset{v}{5}$			$a\overset{v}{5}\overset{v}{5}$ $\overset{v}{9}\overset{v}{5}\overset{v}{5}$	$\overset{v}{5}\overset{v}{5}9$ $\overset{v}{1}\overset{v}{3}59$	$\overset{v}{5}\overset{v}{5}\overset{v}{9}$ $\overset{v}{1}\overset{v}{3}\overset{v}{5}9$	$\overset{v}{9}\overset{v}{5}13$	$\overset{v}{9}\overset{v}{5}\overset{v}{5}13$
9				$a99$	$a\overset{v}{9}9$	$\overset{v}{5}913$	$\overset{v}{5}\overset{v}{9}13$
$\overset{v}{9}$					$\overset{v}{9}\overset{v}{9}9$	$\overset{v}{5}\overset{v}{9}13$	$\overset{v}{5}\overset{v}{9}\overset{v}{9}13$
13						$a1313$	$a\overset{v}{1}313$
$\overset{v}{13}$	sym.						$a\overset{v}{1}\overset{v}{3}13$

Figure 5.10: The third-order coupling tensor ${}^{jik}B_1$ considering only the selected modes.

The tangent element stiffness matrix, which is given in equation (5.82), is built after determining the sub-matrices ${}^{jik}[k]$ and ${}^{jlik}[k]$ in equations (5.72) to (5.75) and considering the nonzero third and fourth order coupling tensor entities. Figure 5.11 shows the gradual development of the tangent stiffness matrix. The grid in this figure represents the selected deformation modes a, 5, $\overset{v}{5}$, 9, $\overset{v}{9}$, 13, and $\overset{v}{13}$. In this example,

since the initial stress and displacements are assumed to be zero at the beginning of the nonlinear analysis, the tangent stiffness matrix will be reduced to a linear stiffness matrix as shown in Figure 5.11a. However, once the iteration is started to achieve an equilibrium condition within the load step, the tangent element stiffness matrix will gradually become fully populated due to the coupling effect of the modes with initial displacement and stresses with the rest of the selected modes. In each iteration step, new modes and couplings between the modes will be activated. Here, for the selected type and number of deformation modes, all third and fourth order mode couplings will be activated in the second iteration step as shown in Figure 5.11c.

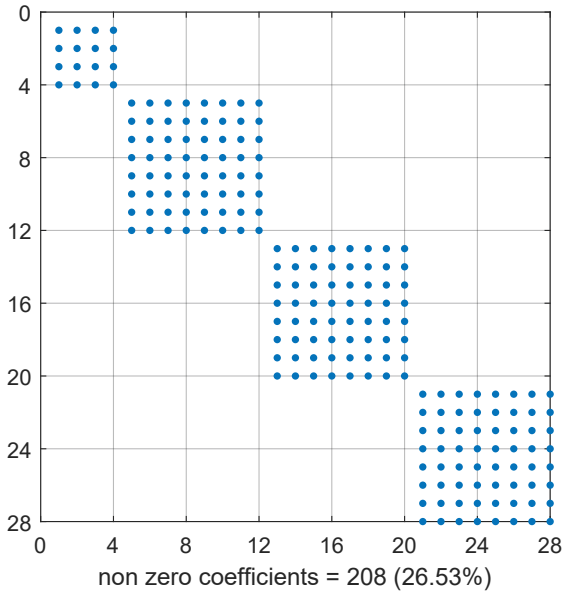

(a) Linear

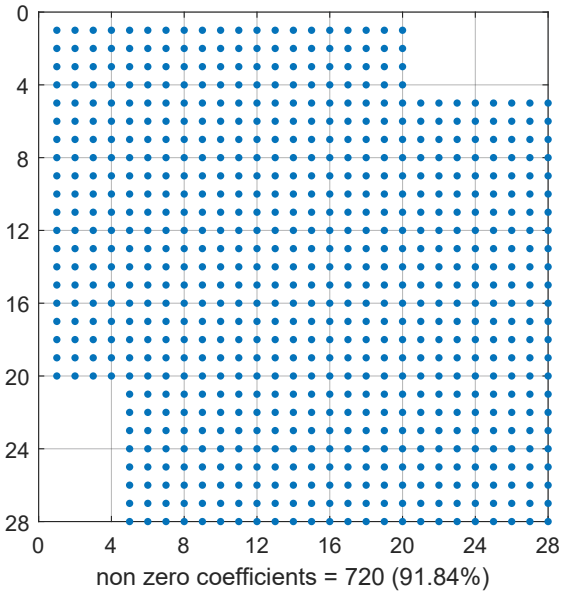

(b) 1^{st} iteration

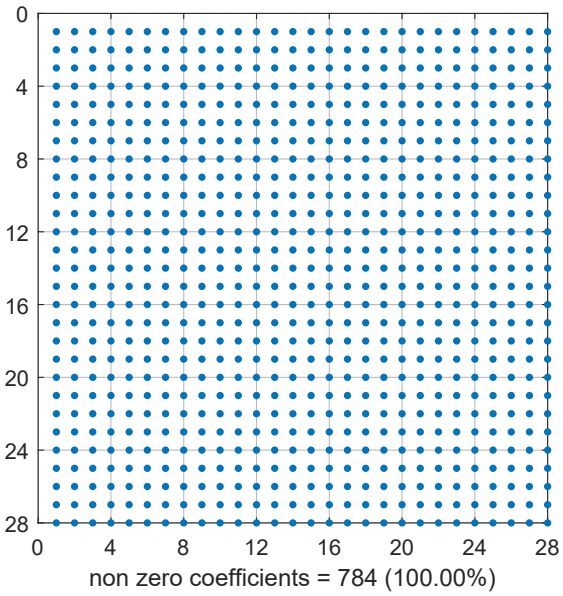

(c) 2^{nd} iteration

Figure 5.11: The sparsity patterns of the element linear and tangent stiffness matrices (the dots correspond to non-null entries).

In this example, only one GBT element is required to solve the problem since the displacements and stresses are constant longitudinally. Therefore, the total number DoF of the GBT model is 28. On the other hand, the equivalent shell element model for this example has 2,880 DoF, which means the GBT model's number of DoF is less than 1.0 % of the number of DoF in the shell model. The element sizes used for the shell element model are approximately 40×40 mm.

Even though the GBT model tangent stiffness matrix is fully populated as shown in Figure 5.11c, it will still be much more computationally efficient than the shell model due to its very small size which requires less number of operations and storage for computation. Furthermore, the computation of the GBT model can be optimized using algorithms specialized for solving dense matrices. However, the building processes of the GBT element nonlinear stiffness matrix and the internal forces vector can be time consuming for problems involving a higher number of deformation modes due to the cubic and quartic increase in the size of the third and fourth order modes coupling tensors, respectively.

In this example, using a load increment step of $q = 0.02 \, \frac{\mathrm{N}}{\mathrm{mm}^2}$, the nonlinear response path of the short circular pipe under projected loading is identified as shown in Figure 5.12. In this figure, the linear solution which is the same for the GBT and shell model, the nonlinear solution of the shell model, and the nonlinear solution of the GBT model considering different combinations of modes are shown. Here, the nonlinear GBT solution converges considering deformation modes a, 5, $\overset{\vee}{5}$, 9, $\overset{\vee}{9}$, 13, and $\overset{\vee}{13}$.

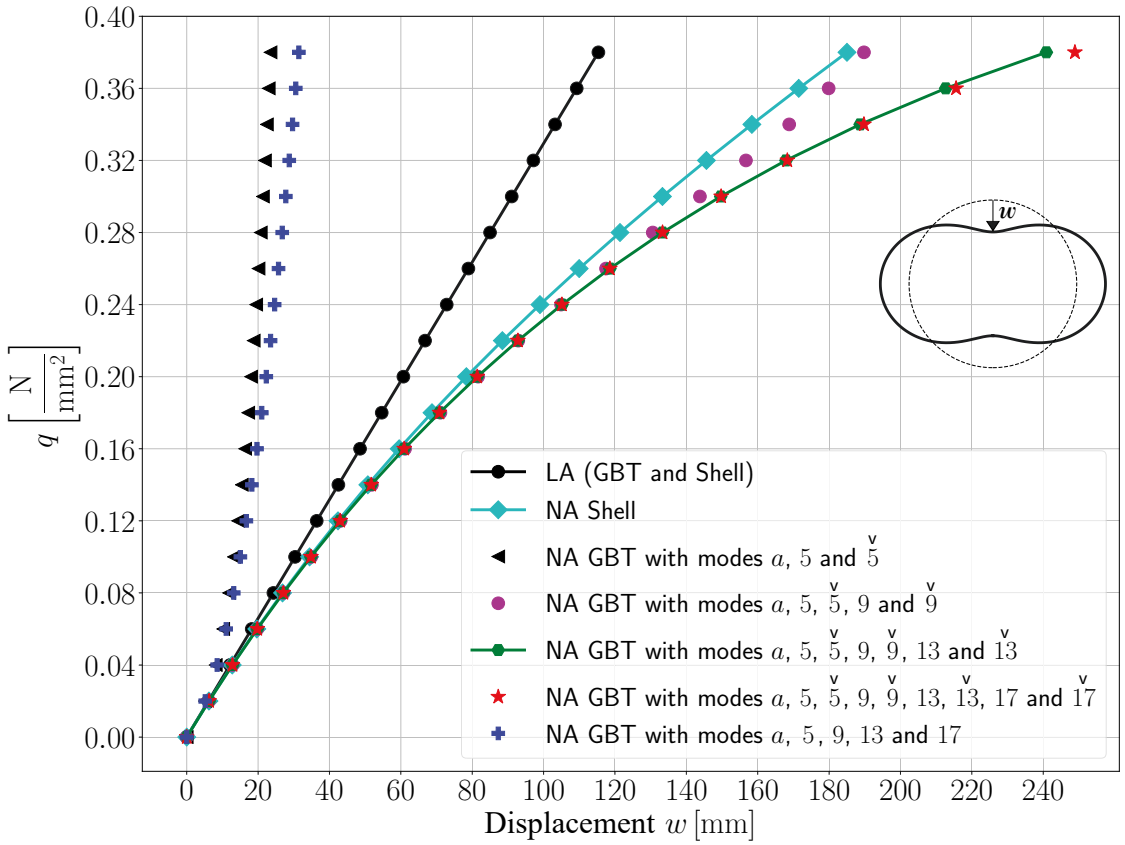

Figure 5.12: The linear analysis (LA) and nonlinear analyses (NA) displacement response of the pipe under gradually increasing load q.

The consideration of additional deformation modes does not improve the GBT result. Furthermore, considering the GBT deformation modes without the non-conventional shear-v modes or considering only modes a, 5, and $\overset{\text{v}}{5}$ will lead to a completely wrong result since the nonlinear membrane energy cannot be correctly approximated by the combination of these modes.

In Figures 5.13 and 5.14, the 3D and 2D deformed configuration of the pipe is shown at $q = 0.14\,\frac{\text{N}}{\text{mm}^2}$. Here, the mean relative difference between the GBT and shell model is below 2.0 % in the displacement field. At this load, the total deformation of the cross-section is around 10.0 % of the pipe radius r.

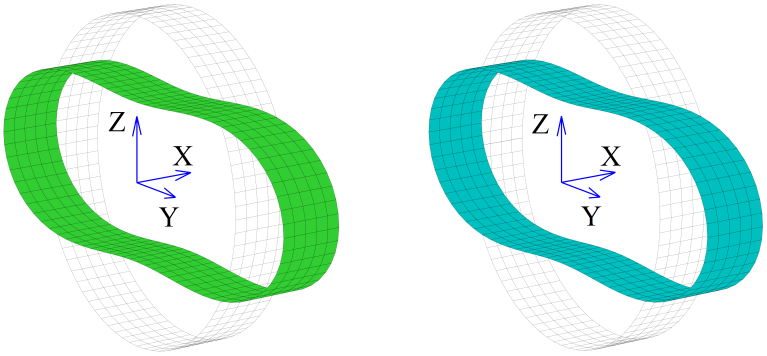

(a) GBT (b) Shell

Figure 5.13: The nonlinear deformation shape of the pipe (×5).

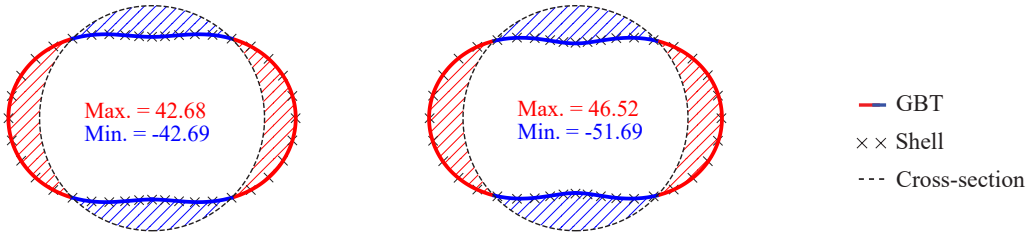

(a) Linear analysis w [mm] (×6) (b) Nonlinear analysis w [mm] (×6)

Figure 5.14: Comparison of displacements at $q = 0.14\,\frac{\text{N}}{\text{mm}^2}$.

In Figure 5.15, the cross-sectional displacement is shown after increasing the load to $q = 0.24\,\frac{\text{N}}{\text{mm}^2}$. At this load, the total deformation of the cross-section will become around 20.0 % of the pipe radius r and the difference between the displacement field of the GBT and shell model will increase to 7.0 %, since the approximation of the GBT model is limited by the total Lagrangian description. Here, it can be summarized that the developed nonlinear GBT formulation in this chapter is only applicable for deformations between 10.0 % to 20.0 %. To consider deformations higher than this, the current formulation must be updated using advanced kinematic description such as the corotational method or exact formulations not only in the longitudinal directions but also in the cross-sectional deformation modes.

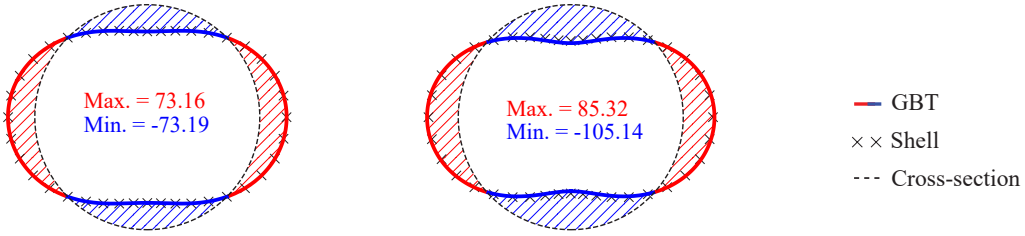

(a) Linear analysis w [mm] (×6) (b) Nonlinear analysis w [mm] (×6)

Figure 5.15: Comparison of displacements at $q = 0.24 \frac{\text{N}}{\text{mm}^2}$.

In Figure 5.16, the modal decomposition of GBT is presented for the longitudinal solution $V(x)$. Since the pipe has free boundary conditions and under a uniformly distributed load, the modal amplitudes are constant along the length of the pipe. In this figure, it can be observed that deformation mode 5 has the largest contribution among the conventional modes whereas mode $\overset{\text{v}}{9}$ has the largest contribution among the non-conventional modes.

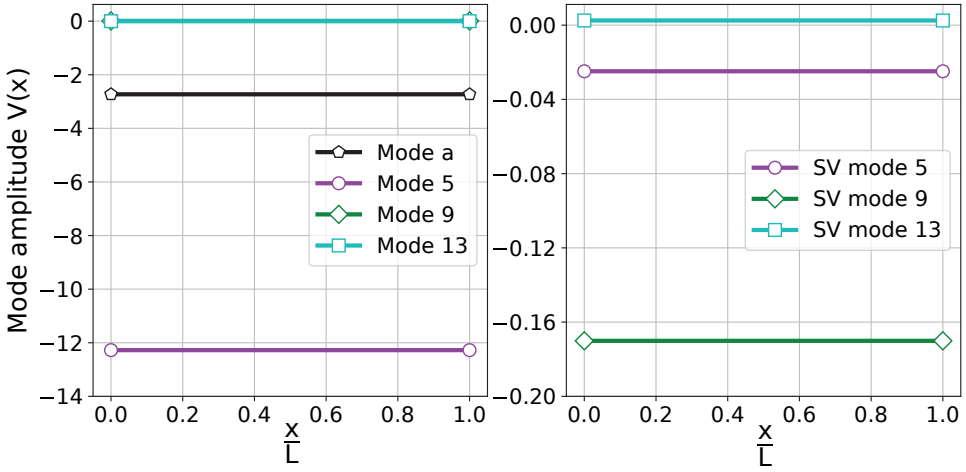

Figure 5.16: GBT deformation modes amplitude at $q = 0.14 \frac{\text{N}}{\text{mm}^2}$.

In the last step of the nonlinear GBT analysis, the stress resultants are determined based on equations (5.100), (2.61), and (2.64). In Figures 5.17 and 5.18, the linear and nonlinear analyses results of GBT and shell are presented at $q = 0.14 \frac{\text{N}}{\text{mm}^2}$. Similarly, in Figures 5.19 and 5.20, the linear and nonlinear analyses results of GBT and shell are presented at $q = 0.24 \frac{\text{N}}{\text{mm}^2}$.

Tables 5.2 and 5.3 summarize the quantitative deviations between the GBT and shell model analyses using the mean relative difference (Equation (2.89)) and the standard deviation of the relative differences. Here, the maximum difference of 21.10 % is observed between GBT and shell in the transversal normal force, which can be due to the nonlinear membrane behavior. However, the comparison between the GBT and shell model in the transverse bending moment and shear force show a good agreement which is generally below 5.0 %.

Table 5.2: Comparison of nonlinear analyses results of GBT and shell at $q = 0.14 \frac{\mathrm{N}}{\mathrm{mm}^2}$.

	M_θ	N_θ	Q_θ	w
MRD [%]	1.38	9.79	0.95	1.98
Standard deviation [%]	0.16	8.02	0.36	0.16

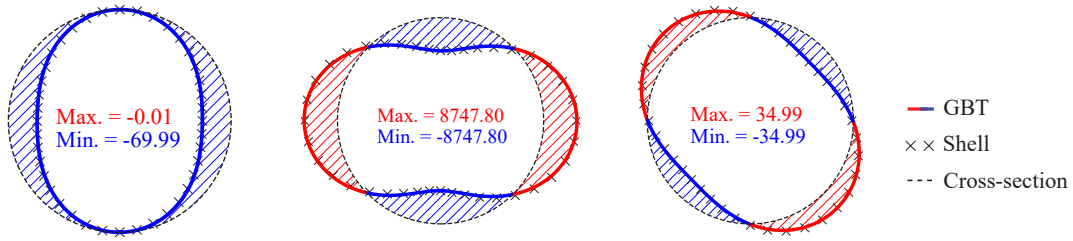

(a) N_θ (b) M_θ (c) Q_θ

Figure 5.17: Stress resultants of the linear analysis at $q = 0.14 \frac{\mathrm{N}}{\mathrm{mm}^2}$.

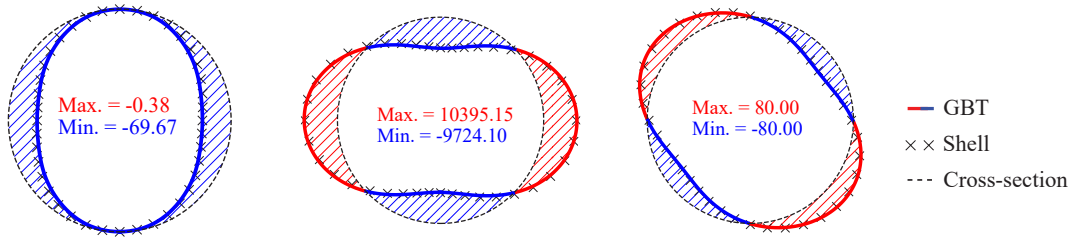

(a) N_θ (b) M_θ (c) Q_θ

Figure 5.18: Stress resultants of the nonlinear analysis at $q = 0.14 \frac{\mathrm{N}}{\mathrm{mm}^2}$.

Table 5.3: Comparison of nonlinear analyses results of GBT and shell at $q = 0.24 \frac{\mathrm{N}}{\mathrm{mm}^2}$.

	M_θ	N_θ	Q_θ	w
MRD [%]	4.70	21.10	3.88	6.67
Standard deviation [%]	0.64	17.92	1.36	0.44

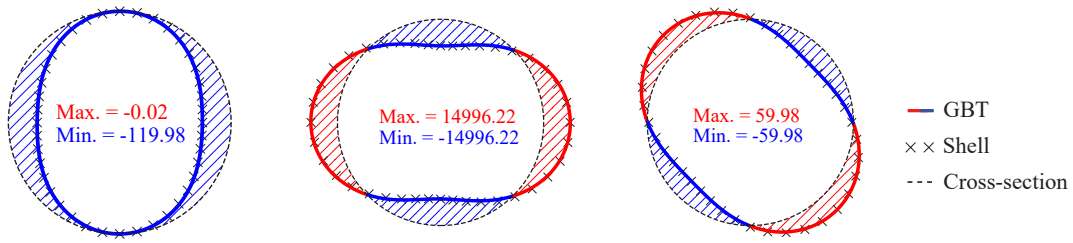

(a) N_θ (b) M_θ (c) Q_θ

Figure 5.19: Stress resultants of the linear analysis at $q = 0.24 \frac{\mathrm{N}}{\mathrm{mm}^2}$.

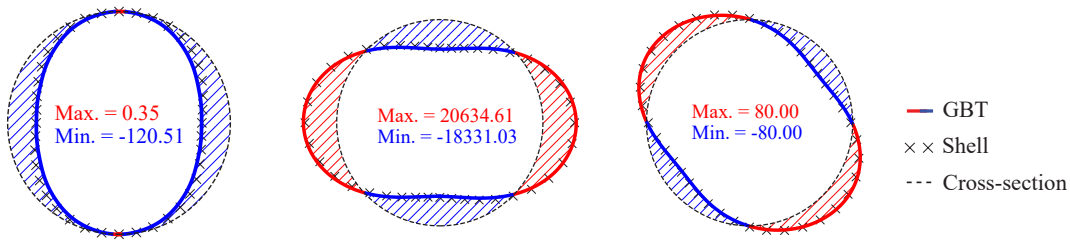

(a) N_θ (b) M_θ (c) Q_θ

Figure 5.20: Stress resultants of the nonlinear analysis at $q = 0.24 \dfrac{\text{N}}{\text{mm}^2}$.

5.7.2 Longitudinal bending

In this example, a cantilever thin-walled circular pipe is considered with a uniformly distributed line load q at the free end of the pipe as shown in Figure 5.21. Due to the loading condition, a linear analysis of this problem will not show any cross-sectional deformation in GBT or Shell based finite element analysis. In GBT this can easily be understood since in a linear analysis the deformation modes are decoupled and in this case the decomposition of the external load will only result in a rigid-body mode. However, in a nonlinear analysis, there will be a cross-sectional deformation throughout the pipe and a maximum ovalization will be expected near the support due to the strong coupling between rigid body and local shell-type GBT deformation modes which directly stem from the membrane nonlinearities in longitudinal, transverse, and shear directions.

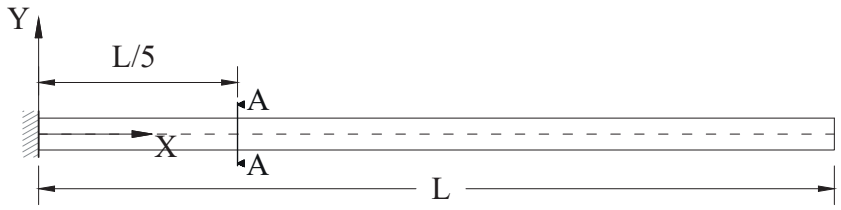

(a) Longitudinal section of the cantilever pipe

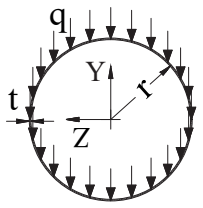

(b) Loading at the free end

$L = 10\,\text{m}$
$r = 200\,\text{mm}$
$t = 3\,\text{mm}$
$E = 205\,\text{GPa}$
$\mu = 0.0$

Figure 5.21: Geometry, material property, loading and boundary condition of a cantilever circular pipe section.

As the first step in the GBT analysis, the distributed load q is transformed into the local coordinates, x, θ, z, whereas the longitudinal component in the x direction in this case is zero. As shown in Table 5.4, only the modes 3 and $\overset{\text{V}}{3}$ have an external load contribution since the integrals in equations (5.107) and (5.108) are zero for all the other GBT deformation modes.

Table 5.4: External load modal decomposition.

Mode k	${}^{k}q_{\theta}$[N]	${}^{k}q_{z}$[N]
3	$-r\pi q$	$-r\pi q$
$\overset{\text{V}}{3}$	$-r\pi q$	0

Using equations (3.80) and (3.81), which are derived for a similar load case and substituting the GBT displacement functions in equations (2.3) and (2.4), the modal decomposition of the external load can be calculated as:

$${}^{k}q_{\theta} = \int_{0}^{2\pi} q\sin(\theta)\ {}^{k}v(\theta)\, r d\theta \tag{5.107}$$

$${}^{k}q_{z} = \int_{0}^{2\pi} -q\cos(\theta)\ {}^{k}w(\theta)\, r d\theta \tag{5.108}$$

Here, based on the two criteria discussed in the previous example, the types of deformation modes involved in this example can be decided as follows:

- First: modes 3 and $\overset{\text{V}}{3}$ should be considered since they have an external load participation.
- Second: the initial stresses and displacements produced by modes 3 and $\overset{\text{V}}{3}$ in the first step of the analysis will lead to a gradual activation of other modes. For example, considering the third-order coupling tensor ${}^{jik}C_1$ shown in Figure 5.22, it can be observed that modes 3 and $\overset{\text{V}}{3}$ will activate modes 5 and $\overset{\text{V}}{5}$ due to the coupling tensors ${}^{335}C_1$ and ${}^{33\overset{\text{V}}{5}}C_1$. Then modes 5 and $\overset{\text{V}}{5}$ will in turn activate modes 7 and $\overset{\text{V}}{7}$ in the next iteration step due to the coupling tensors ${}^{357}C_1$ and ${}^{35\overset{\text{V}}{7}}C_1$.

In this example, the types of modes involved in the analysis due to the external load and the third and fourth order coupling tensors related to C, B and D are a, 1, 3, $\overset{\text{V}}{3}$, $\overset{\text{U}}{3}$, 5, $\overset{\text{V}}{5}$, $\overset{\text{U}}{5}$, 7, $\overset{\text{V}}{7}$, $\overset{\text{U}}{7}$, 9, $\overset{\text{V}}{9}$, $\overset{\text{U}}{9}$, 11, $\overset{\text{V}}{11}$, $\overset{\text{U}}{11}$, 13, $\overset{\text{V}}{13}$, $\overset{\text{U}}{13}$, ... From this list, only modes up to $\overset{\text{U}}{11}$ are sufficient to reach the displacement convergence in the GBT analysis as shown in Figure 5.27. This makes the total number of modes considered in this example equal to seventeen.

In the second step of the GBT analysis, the element tangent stiffness matrix $[K_{\text{T}}]^{e}$, the external force vector $\{F_{\text{ext}}\}^{e}$, and the internal force vector $\{F_{\text{int}}\}^{e}$ are built in order to calculate the incremental generalized modal amplitude vector $\{d\}^{e}$ in equation (5.103). The assembly of the element tangent stiffness matrix and the internal force vector requires the identification and calculation of all possible third and fourth order mode couplings within the selected modes. In this example, for the selected seventeen modes the number of possible nonzero mode couplings are listed below in comparison to the total possibilities.

- 279 in ${}^{jik}C_1$ out of $17^3 = 4913$ (Figure 5.22)
- 116 in ${}^{jik}B_1$ out of $17^3 = 4913$
- 201 in ${}^{jik}D_1$ out of $17^3 = 4913$
- 5033 in ${}^{jlik}C_1$ out of $17^4 = 83521$
- 2648 in ${}^{jlik}B_1$ out of $17^4 = 83521$
- 2201 in ${}^{jlik}D_1$ out of $17^4 = 83521$

$i \setminus k$	a	3	v 3	5	v 5	7	v 7	9	v 9	11	v 11
a	$1aa$	$3a3$ U $3a3$		$5a5$ U $5a5$		$7a7$ U $7a7$		$9a9$ U $9a9$		$11a11$ U $11a11$	
3		133	v 133 v 533 U V 533	335 U 335 735 U 735	v 335 U V 335 v 735 U V 735	537 U 537 937 U 937	v 537 U V 537 v 937 U V 937	739 U 739 1139 U 1139	v 739 U V 739 v 1139 U V 1139	9311 U 9311	v 9311 U V 9311
v 3			v v 133 v v 533 U v v 533	v 335 U V 335 v 735 U V 735	v v 335 U v v 335 v v 735 U v v 735	v 537 U V 537 v 937 U V 937	v v 537 U v v 537 v v 937 U v v 937	v 739 U V 739 v 1139 U V 1139	v v 739 U v v 739 v v 1139 U v v 1139	v 9311 U V 9311	v v 9311 U v v 9311
5				155 955 U 955	v 155 v 955 U V 955	357 U 357 1157 U 1157	v 357 U V 357 v 1157 U V 1157	559 U 559	v 559 U V 559	7511 U 7511	v 7511 U V 7511
v 5					v v 155 v v 955 U v v 955	v 357 U V 357 v 1157 U V 1157	v v 357 U v v 357 v v 1157 U v v 1157	v 559 U V 559	v v 559 U v v 559	v 7511 U V 7511	v v 7511 U v v 7511
7						177	v 177	379 U 379	v 379 U V 379	5711 U 5711	v 5711 U V 5711
v 7							v v 177	v 379 U V 379	v v 379 U v v 379	v 5711 U V 5711	v v 5711 U v v 5711
9								199	v 199	3911 U 3911	v 3911 U V 3911
v 9									v v 199	v 3911 U V 3911	v v 3911 U v v 3911
11										11111	v 11111
v 11	sym.										v v 11111

Figure 5.22: The third-order coupling tensor ${}^{jik}C_1$ considering only the selected modes. Rows and columns related to shear-u modes are not shown since they have no coupling.

In Figures 5.23 and 5.24, the sparsity pattern of the element tangent stiffness matrices are shown as derived from the sub-matrices ${}^{jik}[k]$ and ${}^{jlik}[k]$, respectively. In these figures, each grid spacing represents the selected 17 modes with their 4 DoF. Here, the size of the element stiffness matrix will be $17 \times 4 = 68$.

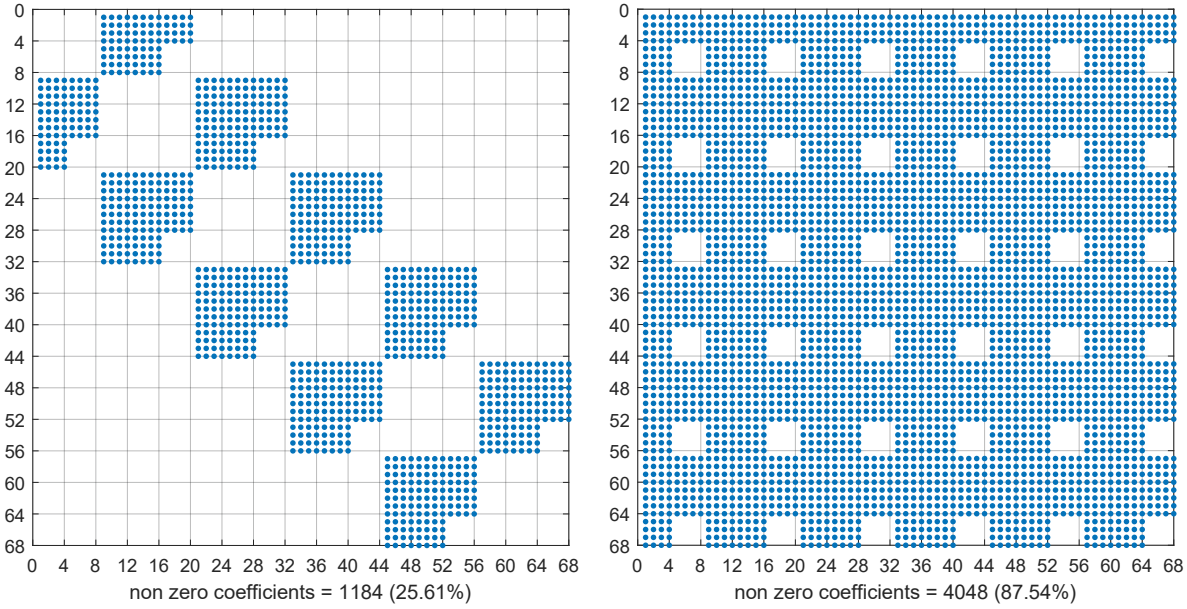

(a) 1^{st} iteration (b) 2^{nd} iteration

Figure 5.23: The sparsity patterns of the element initial linear stress and displacement stiffness matrices (the dots correspond to non-null entries).

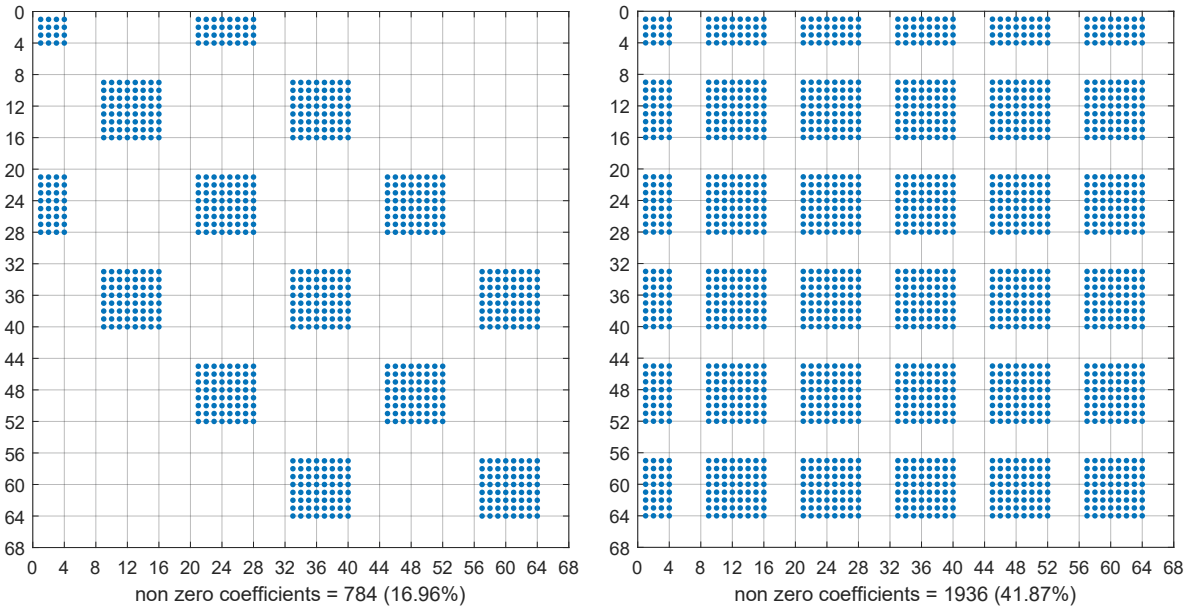

(a) 1^{st} iteration (b) 2^{nd} iteration

Figure 5.24: The sparsity patterns of the element initial quadratic stress and displacement stiffness matrices (the dots correspond to non-null entries).

The gradual development of the tangent stiffness matrix is shown in these figures for the first two iteration steps. In each iteration step, new deformation mode couplings are activated due to the initial stresses and

displacements induced by the deformation modes activated in the previous step. Similarly, the system tangent stiffness develops gradually starting from the linear stiffness matrix in Figure 5.25a, to a denser tangent stiffness matrix in the following iteration steps due to the newly activated deformation mode couplings. Here, the GBT model is discretized longitudinally by 20 elements, which is enough to reach a displacement convergence of above 99.00 % as shown in Figure 5.26.

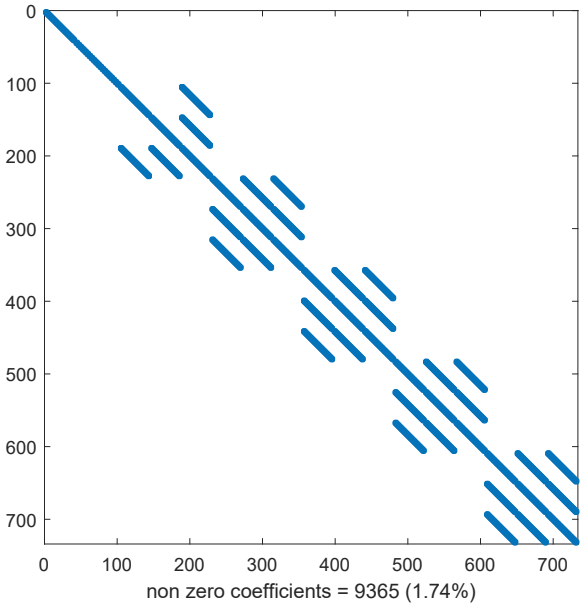

(a) Linear

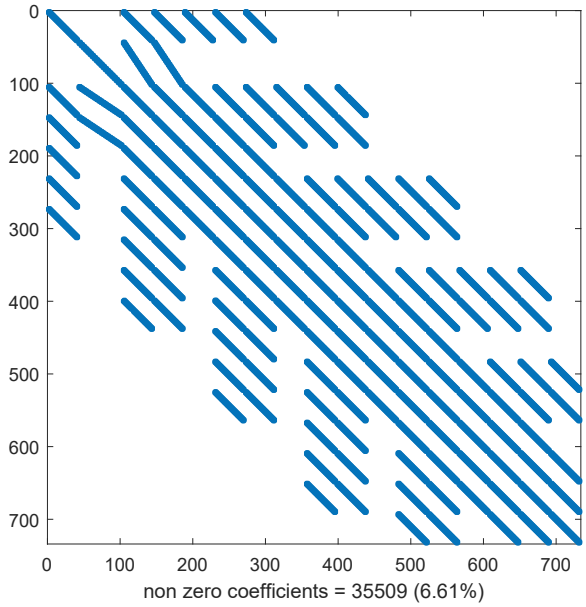

(b) 1^{st} iteration

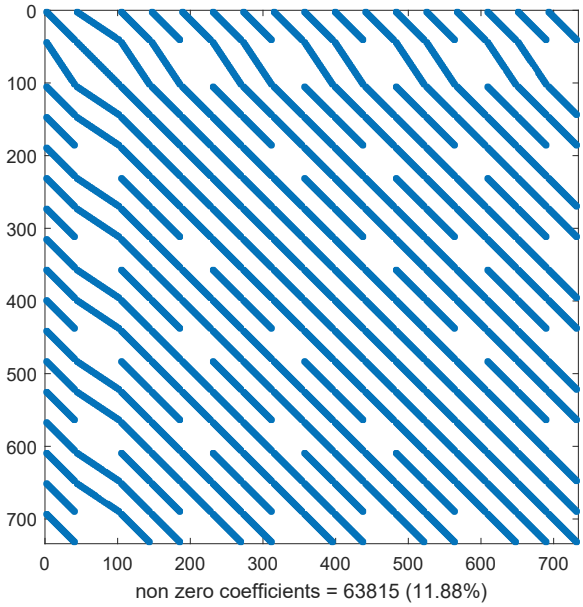

(c) 2^{nd} iteration

Figure 5.25: The sparsity patterns of the system tangent stiffness matrices.

Considering the numbers of modes and elements used, the total degrees of freedom for the GBT model is 733 which is below 0.40 % of the equivalent shell element model which has 192, 384 DoF. The element sizes used for the shell element model are approximately 20×20 mm.

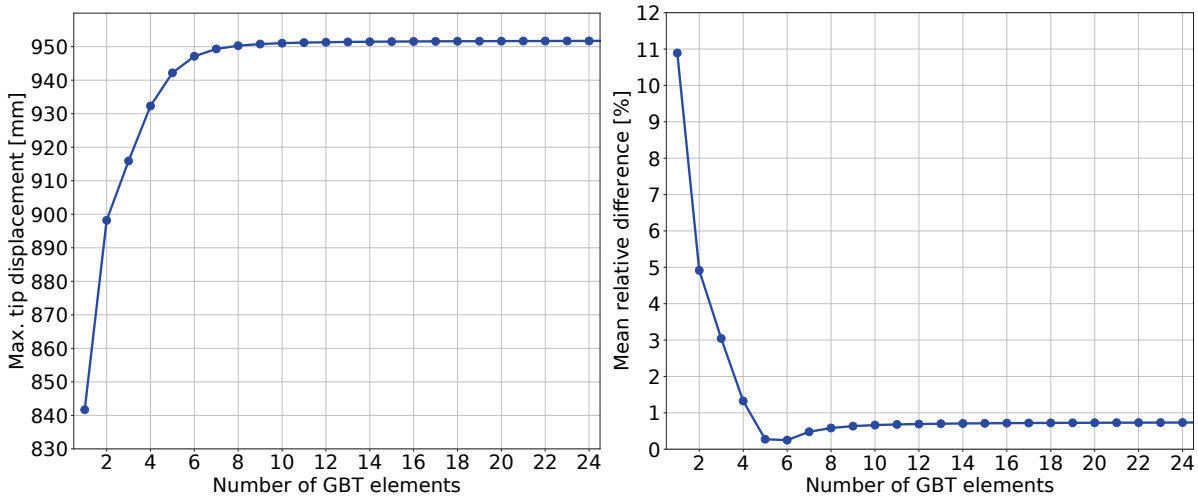

Figure 5.26: GBT solution convergence.

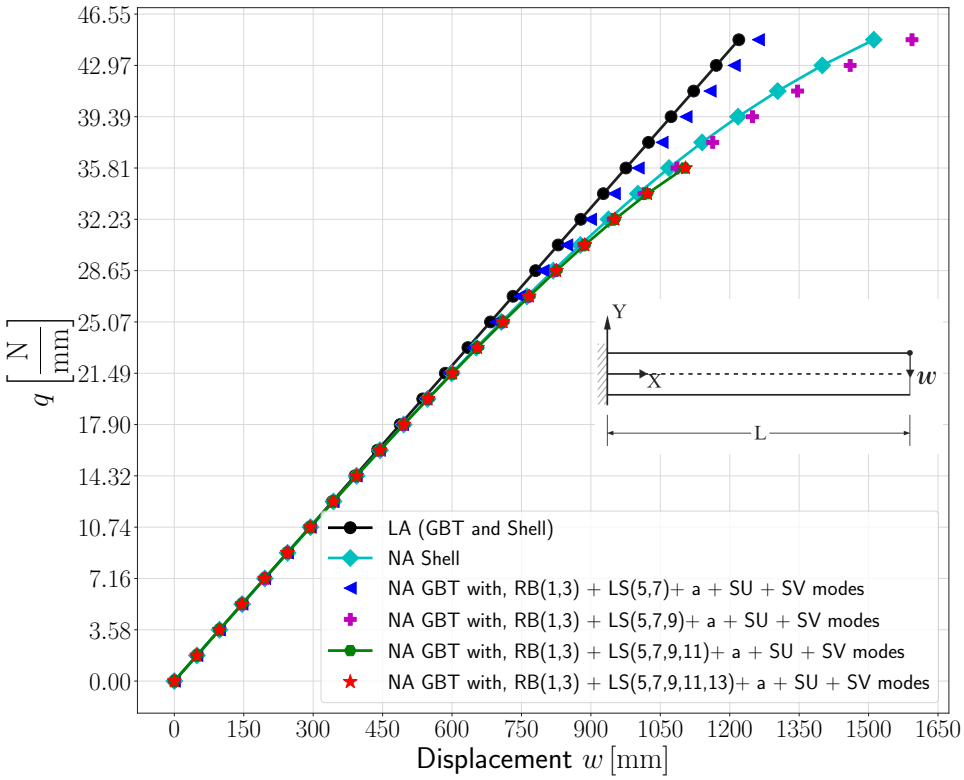

Figure 5.27: The linear analysis (LA) and nonlinear analysis (NA) transverse or radial displacement response of the cantilever pipe under gradually increasing load q.

In this example, using a load increment step of $q = \dfrac{2250}{2\pi r} = 1.79\,\dfrac{\mathrm{N}}{\mathrm{mm}}$, the nonlinear response path of the cantilever pipe is shown considering the radial displacement w in Figure 5.27. In this figure, the linear solution which is the same for the GBT and shell model, the nonlinear solution of the shell model, and the nonlinear solution of the GBT model considering different combinations of modes are shown. Here, the nonlinear GBT solution only converges up to the load level $q = 35.81\,\dfrac{\mathrm{N}}{\mathrm{mm}}$ considering deformation

modes a, 1, 3, $\overset{V}{3}$, $\overset{U}{3}$, 5, $\overset{V}{5}$, $\overset{U}{5}$, 7, $\overset{V}{7}$, $\overset{U}{7}$, 9, $\overset{V}{9}$, $\overset{U}{9}$, 11, $\overset{V}{11}$, and $\overset{U}{11}$. A consideration of additional deformation modes does not improve the GBT's result. Similarly, in Figure 5.28 the nonlinear response path of the cantilever pipe is shown considering the warping or longitudinal displacement u. In this figure, the nonlinear behavior of the problem is more visible and starts from the early stage of the nonlinear analysis since the deformation mode 3, which is the only cause of warping displacement in the linear analysis, will initiate a significant warping displacement of deformation mode 1 in the nonlinear analysis due to the third-order coupling tensor ${}^{331}C_1$ and ${}^{313}C_1$ in the initial displacement and ${}^{133}C_1$ in the initial stress stiffness matrices in equations (5.72) and (5.74), respectively.

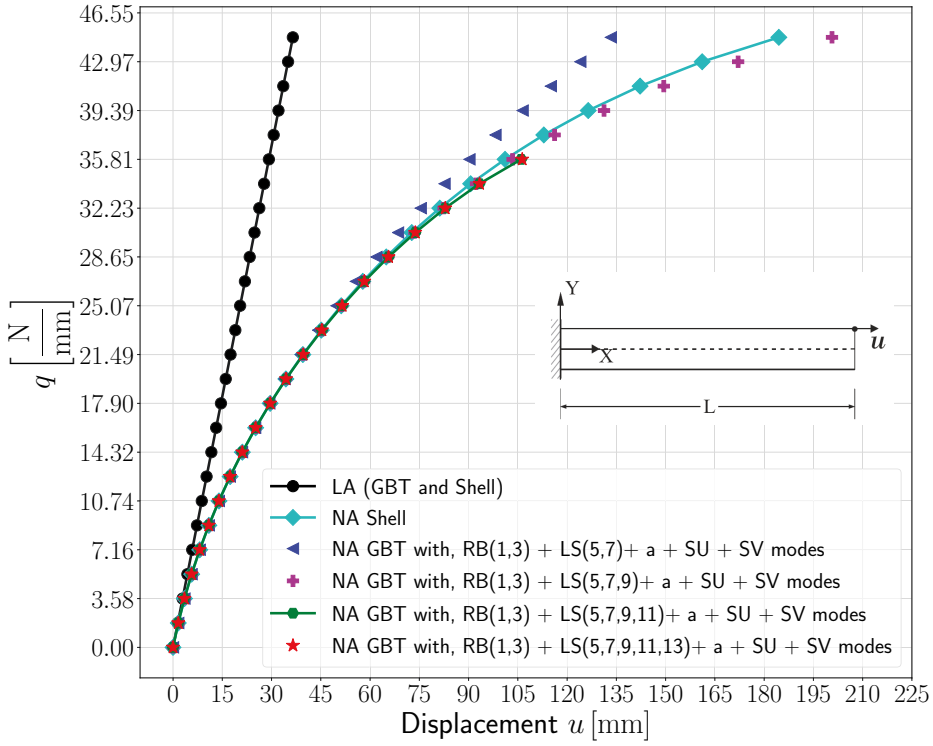

Figure 5.28: The linear analysis (LA) and nonlinear analysis (NA) longitudinal or warping displacement response of the cantilever pipe under gradually increasing load q.

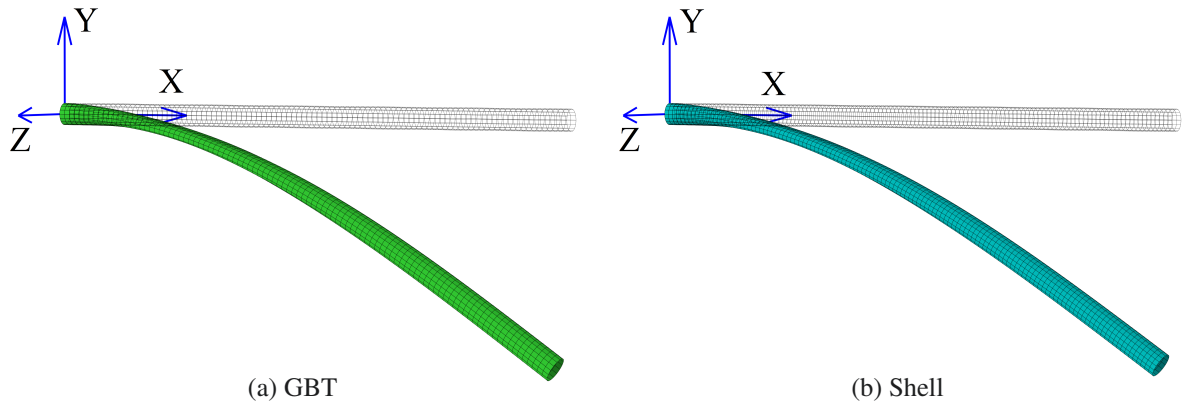

(a) GBT (b) Shell

Figure 5.29: The deformation shape of the cantilever pipe at $q = 35.81\ \frac{\mathrm{N}}{\mathrm{mm}}$ (×4).

In Figure 5.29, the deformed configuration of the cantilever pipe is shown at $q = 35.81 \frac{\text{N}}{\text{mm}}$ with a maximum ovalization at $0.25L$ from the support . Here, the mean relative difference between the GBT and the shell model is below 2.5 % in the displacement field. At this load, the total deformation of the cross-section is around 10.0 % of the pipe length L.

In Figure 5.30, the modal decomposition of the GBT's solution is presented for the longitudinal amplitude function $V(x)$. According to the results of modes 1 and 3, the maximum displacement occurs at the tip of the cantilever pipe. Due to this displacement, the maximum cross-sectional ovalization occurs at around $x = 0.25L$ in mode 5. In the case of a higher load or a large displacement, the pipe will gradually lose all bending stiffness at around $x = 0.25L$ and will form a hinge. Generally, the local shell-type conventional and the shear-v (SV) non-conventional modes have a higher amplitude near the support. In this figure, it can be observed that the shear-u (SU) modes in general have a higher contribution than the shear-v (SV) modes.

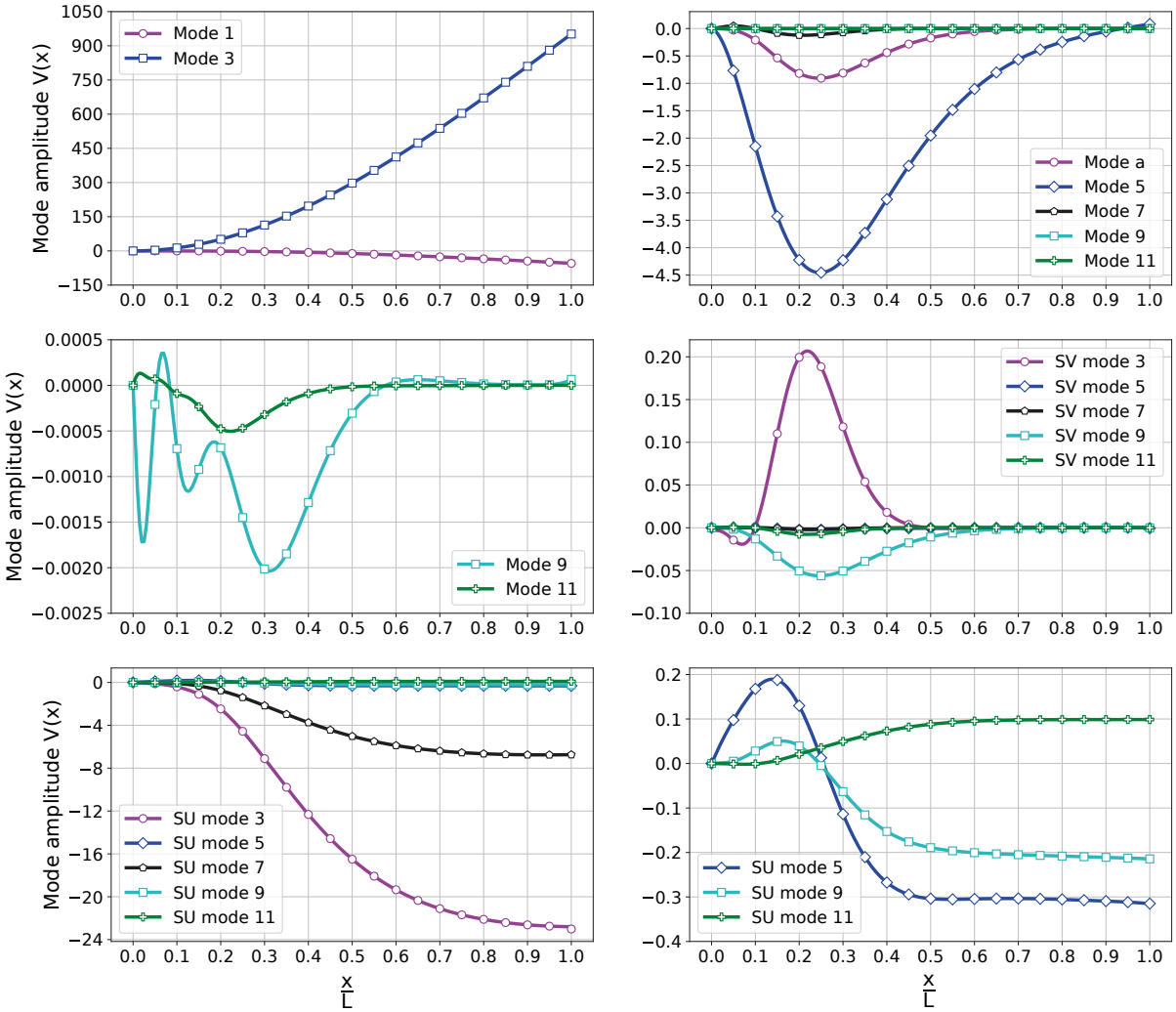

Figure 5.30: GBT deformation modes amplitude of the cantilever pipe at $q = 32.23 \frac{\text{N}}{\text{mm}}$.

In Figures 5.31 to 5.33, the cross-sectional displacement at the free end of the pipe (or tip) and at section A are shown for both GBT and shell models. Here, for the purpose of comparison, the results of the linear and nonlinear analyses are presented at the same load $q = 32.23 \frac{\text{N}}{\text{mm}}$. The nonlinear cross-sectional displacement at the tip shows almost no local deformations in comparison to the local deformation $w_{local} = 18.84\,\text{mm}$ at the section A. From the linear displacement results, it can be concluded that local cross-sectional deformations cannot be determined using a linear analysis in this example. At this load level, the mean relative difference of the nonlinear displacement between the GBT and shell model is below 0.5 %

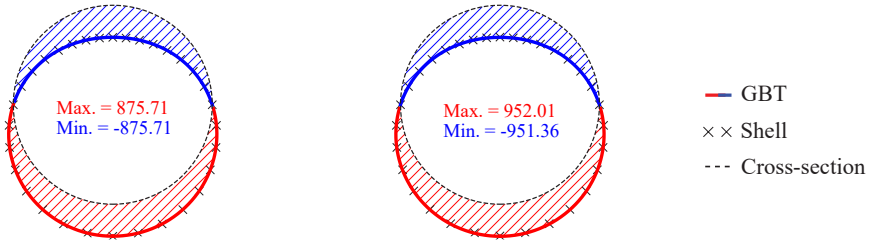

(a) linear w (×0.2) (b) nonlinear w (×0.2)

Figure 5.31: Comparison of displacements in [mm] at the tip of the cantilever pipe.

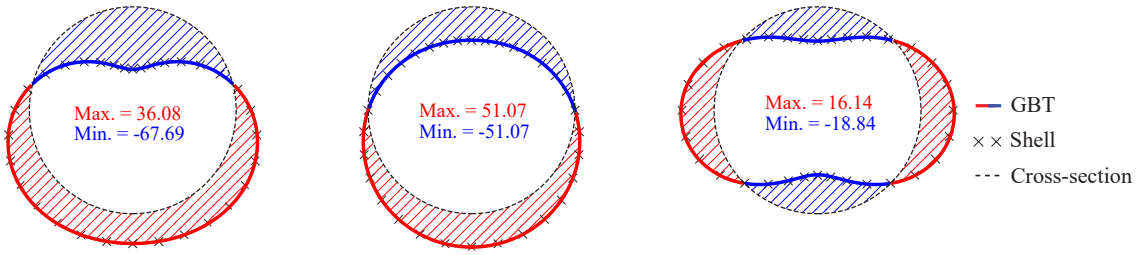

(a) w_{total} (×5) (b) w_{bending} (×5) (c) w_{local} (×12)

Figure 5.32: Comparison of nonlinear analysis displacements in [mm] at section A.

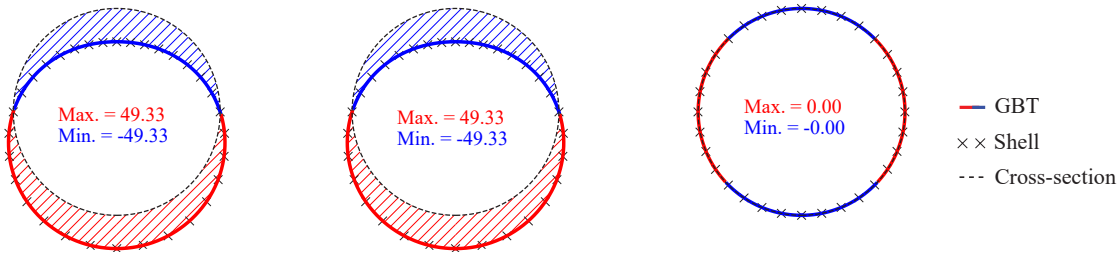

(a) w_{total} (×4) (b) w_{bending} (×4) (c) w_{local}

Figure 5.33: Comparison of linear analysis displacements in [mm] at section A.

In Figures 5.34 to 5.38, the linear and nonlinear analyses stress resultants of the GBT and shell model are presented at the load level $q = 32.23 \frac{\text{N}}{\text{mm}}$. Confirming with the large ovalization displacement at section A, the nonlinear transverse bending moment M_θ also has a large value at this section.

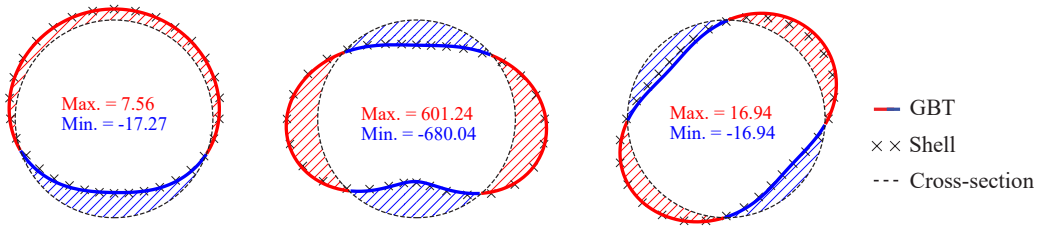

(a) M_x (b) M_θ (c) $M_{x\theta}$

Figure 5.34: Comparison of nonlinear analysis bending moments in $\left[\frac{\text{Nmm}}{\text{mm}}\right]$ at section A.

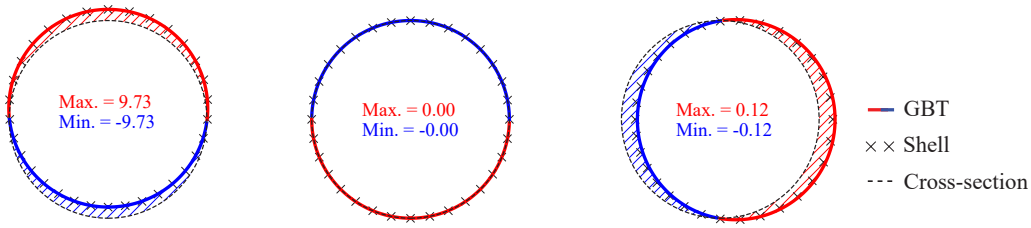

(a) M_x (b) M_θ (c) $M_{x\theta}$

Figure 5.35: Comparison of linear analysis bending moments in $\left[\frac{\text{Nmm}}{\text{mm}}\right]$ at section A.

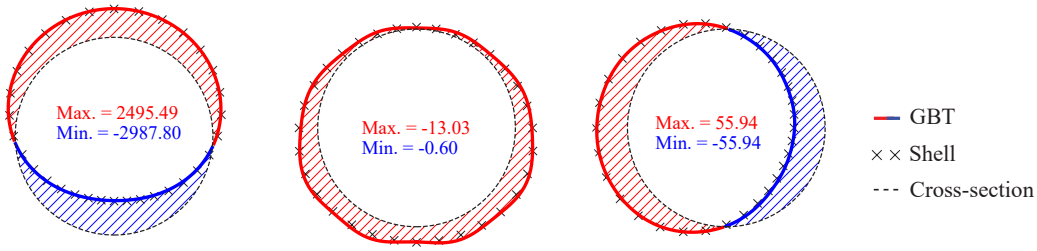

(a) N_x (b) N_θ (c) $N_{x\theta}$

Figure 5.36: Comparison of nonlinear analysis normal forces in $\left[\frac{\text{N}}{\text{mm}}\right]$ at section A.

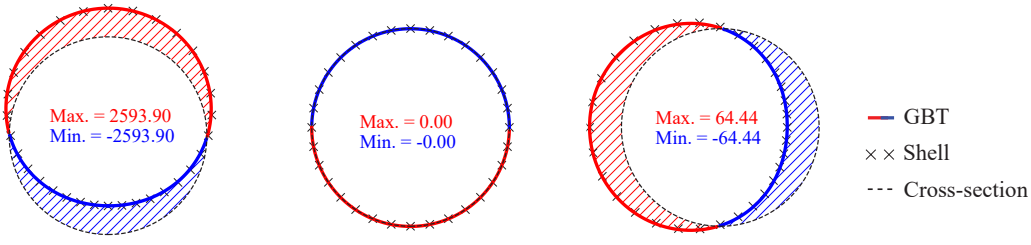

(a) N_x (b) N_θ (c) $N_{x\theta}$

Figure 5.37: Comparison of linear analysis normal forces in $\left[\frac{\text{N}}{\text{mm}}\right]$ at section A.

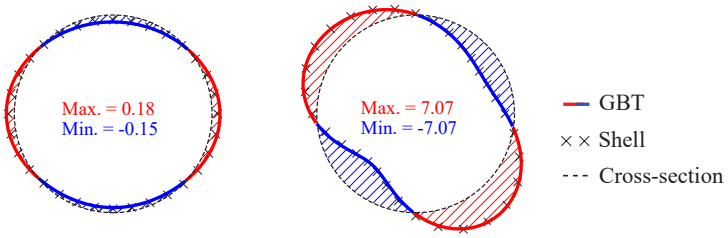

(a) Q_x (b) Q_θ

Figure 5.38: Comparison of nonlinear analysis shear forces in $\left[\frac{\text{N}}{\text{mm}}\right]$ at section A.

Table 5.5: Comparison of nonlinear analysis results of GBT and shell model at section A.

	M_x	M_θ	$M_{x\theta}$	N_x	N_θ	$N_{x\theta}$	Q_x	Q_θ	w_{local}	w_{bending}	w_{total}
MRD [%]	1.20	14.32	4.29	12.37	1.47	17.59	29.93	1.87	1.51	0.11	0.42
Standard deviation [%]	0.20	16.02	2.42	13.13	0.55	14.26	11.01	1.58	0.69	0.00	0.15

In Table 5.5, the quantitative deviations between the GBT and shell model analyses are summarized using the mean relative difference (Equation (2.89)) and the standard deviation of the relative differences. Here, the differences in the major stress resultants between the GBT and shell model are below 18.0 %.

5.8 Summary

In this chapter, the complete nonlinear membrane strain definition is considered in the formulation of the GBT tangent stiffness matrix and the internal forces. In comparison, the latest GBT study conducted by Basaglia [16] on the buckling analysis of CHS only considers the linear initial stress stiffness matrix $[K_{\sigma \text{L}}]$ associated with the longitudinal and shear membrane strains which limits the method to the analysis of members under axial compression and external pressure.

The geometrically nonlinear GBT analysis formulation developed in this chapter is applicable for thin-walled circular pipes under any arbitrary loading condition with small to moderate displacements (10 % to 20 % of the largest dimension of the member). This formulation can be extended to a large displacement and strain analysis by the modification of the kinematic assumptions made in this study towards more advanced or exact kinematic descriptions [119, 154].

In the numerical examples presented, the GBT solutions are shown to converge in terms of the displacement field components with an increasing number of modes taken into account. In all examples, the mean relative difference between GBT and shell models in the displacement fields is below 2.5 %, when the maximum displacement is about 10 % of the largest dimension of the member. Similarly, the mean relative difference in the stress fields is below 18.0 % for the two models. Furthermore, the numerical examples show that the GBT uses a much fewer number of DoF to achieve an accurate solution in both stress and displacement fields than the shell finite element analysis. Particularly in the second example,

the GBT model has only 0.40 % of the DoF needed in the shell model. However, the assembly processes of the GBT element nonlinear stiffness matrix and internal forces vector can be a time consuming procedure due to the need for identification and calculation of the third and fourth order mode coupling tensors.

Chapter 6

Conclusion and outlook

6.1 Conclusion

The main contribution of this dissertation is the development of a GBT formulation for linear static and dynamic analyses of thin-walled pipes with circular axis, and the geometrically nonlinear analysis of thin-walled straight pipes. Unlike the linear analysis of long straight pipes in classical GBT, these problems involve the coupling of the GBT deformation modes, and cannot be solved without eliminating the classical GBT assumption of null transverse and shear membrane energy through the consideration of non-conventional modes.

In GBT, the displacement fields of a thin-walled circular pipe member are described based on the separation of variables principle which leads to two analysis steps involving the cross-section and the longitudinal direction. In the cross-sectional analysis, a decomposition in the Fourier-Series is applied to the cross-sectional displacements to determine the GBT deformation modes. In the longitudinal direction, a standard beam finite element method is applied to determine the amplitude of these deformation modes.

The linear GBT formulation presented in Chapter 2 shows the fundamental concept of GBT starting from the classical GBT formulation to the state-of-the-art shear deformable GBT formulation. This chapter has a minor contribution in including the effect of the Poisson ratio in the shear deformable GBT formulation, which is otherwise ignored in the classical GBT formulation due to the lack of membrane transverse stresses. As a numerical example, the analysis of a short cantilever pipe under a projected loading is presented using the shear deformable GBT element which shows a very good agreement with the finely discretized equivalent shell finite element model in displacement and stress fields. Here, the difference between the two models is below 0.35 % in the displacement fields and is below 6 % in the stress fields. Due to the significantly lower discretization required by GBT, in this example, the GBT model needs less than 1.0 % of the computation time needed by the shell element model.

As an additional minor contribution in Chapter 2, the possibility of a locking problem in the shear deformable GBT element is investigated using specially formulated examples to test the shear and membrane locking problems. The GBT element passes both tests successfully without developing any

parasitic strains or stresses. However, it must be noted that the types of non-conventional modes introduced in the shear deformable GBT formulation leads to a strong coupling with conventional modes. Since this coupling reduces the computational efficiency of GBT, alternative types of non-conventional modes which have a reduced coupling effect needs to be investigated [28].

Chapter 3 has a major contribution in the formulation of GBT for the linear static analysis of naturally curved thin-walled circular pipes (pipe bends). In this formulation, the virtual work of internal and external forces is derived based on the linear kinematic description of the curved shell theory. In the cross-sectional analysis of GBT, the deformation modes of a straight pipe developed in Chapter 2 are reformulated to include the effect of the toroidal to cross-sectional radius ratio in pipe bends. The GBT element stiffness matrix formulated for pipe bends has coupling within even and odd modes while no coupling exists between even and odd modes. These couplings increase the density of the element stiffness matrix by about 50 %.

The curved pipe numerical examples presented in Chapter 3 show convergence in terms of the displacement field components with an increasing number of deformation modes and the longitudinal discretization. In these examples, the mean relative difference between GBT and shell models in the displacement fields is below 0.2 %. In some cases, it is observed that the number of GBT modes needed for the convergences of the stress field can be higher than that of the displacement field. In the examples studied, the stress field components of the GBT solutions in regions distant from the boundaries converge faster than those close to the boundaries. Here, depending on the location of the cross-section, the mean relative difference between GBT and shell models in the stress fields can be up to 6 %. Remarkably, the comparison of computation speed between the GBT and shell shows that the GBT models need less than 1.5 % of the time needed by the shell element models. However, the formulated displacement-based curved GBT element fails the membrane locking test, and therefore it should not be applied for the analysis of members with a higher slenderness ratio.

In Chapter 4 the major contribution is the formulation of GBT for the dynamic analyses of pipe bends which is an extension of the formulation presented in Chapter 3. In this formulation, the consistent element mass matrix is derived from the variation of the kinetic energy. Similar to the element stiffness matrix, the mass matrix is densely populated which can be a hindrance for the future implementation of the explicit finite element method without lumping the mass matrix. Here, two numerical examples have been presented involving the analysis of undamped free vibration of truncated and closed toroidal shells. The eigenvalues of the GBT modal solution converge with an increasing number of deformation modes. Based on the modal decomposition of GBT, the shear modes have a significant contribution to the vibration modes. In both examples, the relative difference between the GBT and shell models regarding the natural frequencies did not exceed 0.80%. In addition, the MAC values have demonstrated the full correlation of the mode shapes between the GBT and the shell models. Hence, the small number of GBT deformation modes and elements used in the GBT modal analysis provides a comprehensive insight into the structural behavior of curved members with significantly fewer DoF than the shell element models.

In Chapter 5 the geometrically nonlinear GBT is formulated for the analysis of straight pipes. The third and fourth order deformation mode couplings involved in this analysis are far more complicated than the second order mode couplings in Chapter 3. The major contribution of this chapter is the formulation of the linear and quadratic tangent stiffness matrix and the internal force vector based on the linearization of the nonlinear response curve and the high order deformation mode coupling tensors. This formulation is applicable to the nonlinear analysis of thin-walled circular pipes under any arbitrary loading condition which causes small to moderate displacement.

The two numerical examples presented in Chapter 5 show the detailed procedure involved in the nonlinear GBT analysis of pipe members. In the second example, the increase in the cross-sectional ovalization of the circular pipe section is shown due to longitudinal bending. In both examples, the difference between GBT and shell models in displacement fields is below 2.5 %, when the maximum displacement is about 10 % of the largest dimension of the member. Similarly, the mean relative difference in the stress fields is below 18.0 % for the two models. Furthermore, the numerical examples show that GBT uses a much smaller number of DoF than the shell finite element analysis to achieve an accurate solution in both stress and displacement fields. Particularly in the second example, the GBT model has only 0.40 % of the DoF needed in the shell model. However, the assembly processes of the GBT element nonlinear stiffness matrix and internal forces vector can be a time consuming procedure due to the need for identification and calculation of the third and fourth order mode coupling tensors.

Throughout this dissertation, GBT has shown a remarkable computational performance in the analysis of thin-walled circular pipe sections. Although the GBT stiffness matrix is relatively dense and has a low sparsity in comparison to the shell finite element method, the GBT stiffness matrix still requires significantly less storage (memory) due to its relatively small size. Furthermore, the computation of the GBT stiffness matrix can be optimized by applying algorithms specialized for dense matrices.

Based on the formulations and Python codes developed in this dissertation, and the recent studies which have developed a coupling scheme between the GBT and the shell finite element analysis [30, 95, 96], it is possible to incorporate GBT into standard commercial FEM software packages and utilize the exceptional computational efficiency of GBT in prismatic and circular thin-walled cross-sections. However, further studies are required which are stated in the next section.

6.2 Outlook

Related to the study areas presented in this dissertation, several topics can be suggested for further studies. These are:

- A systematic determination of the required GBT deformation modes at the beginning of the analysis. Currently, the only way to determine the number of deformation modes needed for the analysis is based on a convergence analysis. Since this procedure is time consuming and unpractical, more systematic and efficient ways need to be investigated such as by employing an error measurement to

estimate the number of Fourier series terms needed for the approximation with a certain accuracy.

- The geometrical nonlinear formulation of curved pipes: the formulation developed in Chapter 5 can be extended for analysis of pipe bends. Here, one can start by updating the nonlinear membrane strain equations (5.7), (5.8) and (5.9) for straight pipes to the following equations which represent the nonlinear membrane strain relationship for pipe bends:

$$\begin{aligned}\varepsilon_{\varphi}^{\mathrm{M}} =& \frac{1}{R\xi}\left(u_{,\varphi} - v\sin(\theta) + w\cos(\theta)\right) \\ &+ \frac{1}{2(R\xi)^2}\Big(\left(u_{,\varphi} - v\sin(\theta) + w\cos(\theta)\right)^2 + \left(v_{,\varphi} + u\sin(\theta)\right)^2 + \left(w_{,\varphi} + u\cos(\theta)\right)^2\Big)\end{aligned} \tag{6.1}$$

$$\varepsilon_{\theta}^{\mathrm{M}} = \frac{v_{,\theta} + w}{r} + \frac{1}{2r^2}\left(u_{,\theta}^2 + (v_{,\theta} + w)^2 + (w_{,\theta} - v)^2\right) \tag{6.2}$$

$$\begin{aligned}\gamma_{\varphi\theta}^{\mathrm{M}} =& \frac{u_{,\theta}}{r} + \frac{1}{\xi}\left(\frac{v_{,\varphi}}{R} + \frac{u\sin(\theta)}{R}\right) + \frac{1}{rR\xi}\Big(\left(u_{,\varphi} - v\sin(\theta) + w\cos(\theta)\right)u_{,\theta} \\ &+ \left(v_{,\varphi} + u\sin(\theta)\right)(v_{,\theta} + w) + \left(w_{,\varphi} + u\cos(\theta)\right)(w_{,\theta} - v)\Big)\end{aligned} \tag{6.3}$$

- The mixed GBT formulation of circular pipe bends: to overcome the membrane locking problem, which is observed in the displacement-based finite element formulation of the curved GBT element presented in Chapter 3, a mixed finite element formulation can be employed based on the Hellinger-Reissner variational principle [73, 118].
- The geometrically exact GBT formulation: the total Lagrangian formulation presented in Chapter 5 is limited to a small-to-moderate displacement range. This formulation can be extended for the analysis of large strains, deflections, and rotations based on Reissner-Simo's exact beam theory [119, 154].
- The lumping of the consistent GBT element mass matrix formulated in Chapter 4 : a diagonal or lumped mass matrix is an essential prerequisite for the explicit finite element based transient analysis of thin-walled pipes. Here, the applicability of methods such as the manifold-based mass lumping scheme [50] and the selective mass scaling technique [165] can be investigated.
- The formulation of GBT based on the explicit finite element method [175] for the analysis of complex dynamic problems involving large deformations and rotations, such as the demolition of guyed masts.

Bibliography

[1] Abambres, M., Camotim, D., and Silvestre, N. (2013). Physically non-linear GBT analysis of thin-walled members. *Computers & Structures*, 129:148–165.

[2] Abambres, M., Camotim, D., and Silvestre, N. (2014a). GBT-based elastic–plastic post-buckling analysis of stainless steel thin-walled members. *Thin-Walled Structures*, 83:85–102.

[3] Abambres, M., Camotim, D., Silvestre, N., and Rasmussen, K. J. (2014b). GBT-based structural analysis of elastic–plastic thin-walled members. *Computers & Structures*, 136:1–23.

[4] Adibi-Asl, R. and Seshadri, R. (2017). Decay length in pressure vessels. In *Pressure Vessels and Piping Conference Volume* 2: *Computer Technology and Bolted Joints*.

[5] Ahmad, S., Irons, B. M., and Zienkiewicz, O. (1970). Analysis of thick and thin shell structures by curved finite elements. *International Journal for Numerical Methods in Engineering*, 2(3):419–451.

[6] Allemang, R. J. and Brown, D. L. (1982). A correlation coefficient for modal vector analysis. In *Proceedings of the* 1*st international modal analysis conference*, volume 1, pages 110–116. SEM Orlando.

[7] Amabili, M. (2008). *Nonlinear vibrations and stability of shells and plates*. Cambridge University Press.

[8] Andreassen, M. J. and Jönsson, J. (2012). Distortional buckling modes of semi-discretized thin-walled columns. *Thin-Walled Structures*, 51:53–63.

[9] Andreassen, M. J. and Jönsson, J. (2013). A distortional semi-discretized thin-walled beam element. *Thin-Walled Structures*, 62:142–157.

[10] ANSYS Inc. (2015). ANSYS mechanical APDL: Version 15.0–User's guide.

[11] Basaglia, C., Camotim, D., and Silvestre, N. (2008). Global buckling analysis of plane and space thin-walled frames in the context of GBT. *Thin-Walles Structures*, 46:79–101.

[12] Basaglia, C., Camotim, D., and Silvestre, N. (2010). GBT-based buckling analysis of thin-walled steel frames with arbitrary loading and support conditions. *International Journal of Structural Stability and Dynamics*, 10(03):363–385.

[13] Basaglia, C., Camotim, D., and Silvestre, N. (2011). Non-linear GBT formulation for open-section thin-walled members with arbitrary support conditions. *Computers & structures*, 89(21-22):1906–1919.

[14] Basaglia, C., Camotim, D., and Silvestre, N. (2013). Post-buckling analysis of thin-walled steel frames using Generalized Beam Theory (GBT). *Thin-Walled Structures*, 62:229–242.

[15] Basaglia, C., Camotim, D., and Silvestre, N. (2015). Buckling and vibration analysis of cold-formed steel CHS members and frames using Generalized Beam Theory. *International Journal of Structural Stability and Dynamics*, 15(08):1540021.

[16] Basaglia, C., Camotim, D., and Silvestre, N. (2019). GBT-based buckling analysis of steel cylindrical shells under combinations of compression and external pressure. *Thin-Walled Structures*, 144:106274.

[17] Bathe, K. (1996). *Finite Element Procedures*. Prentice Hall.

[18] Bathe, K. J. and Almeida, C. A. (1980). A simple and effective pipe elbow element-linear analysis. *Journal of Applied Mechanics*, 47(1):93–100.

[19] Bebiano, R., Calçada, R., Camotim, D., and Silvestre, N. (2017a). Dynamic analysis of high-speed railway bridge decks using Generalized Beam Theory. *Thin-Walled Structures*, 114:22–31.

[20] Bebiano, R., Camotim, D., and Gonçalves, R. (2018a). GBTul 2.0- A second-generation code for the GBT-based buckling and vibration analysis of thin-walled members. *Thin-Walled Structures*, 124:235–257.

[21] Bebiano, R., Camotim, D., and Silvestre, N. (2013). Dynamic analysis of thin-walled members using Generalized Beam Theory (GBT). *Thin-Walled Structures*, 72:188–205.

[22] Bebiano, R., Eisenberger, M., Camotim, D., and Gonçalves, R. (2017b). GBT-based buckling analysis using the exact element method. *International Journal of Structural Stability and Dynamics*, 17(10):1750125.

[23] Bebiano, R., Eisenberger, M., Camotim, D., and Gonçalves, R. (2018b). GBT-based vibration analysis using the exact element method. *International Journal of Structural Stability and Dynamics*, 18(05):1850068.

[24] Bebiano, R., Gonçalves, R., and Camotim, D. (2015). A cross-section analysis procedure to rationalise and automate the performance of GBT-based structural analyses. *Thin-Walled Structures*, 92:29–47.

[25] Bebiano, R., Silvestre, N., and Camotim, D. (2007). GBT formulation to analyze the buckling behavior of thin-walled members subjected to non-uniform bending. *International Journal of Structural Stability and Dynamics*, 7(01):23–54.

[26] Bebiano, R., Silvestre, N., and Camotim, D. (2008). Local and global vibration of thin-walled members subjected to compression and non-uniform bending. *Journal of Sound and Vibration*, 315(3):509–535.

[27] Bianco, M. J. (2019). *Coupling between shell and Generalized Beam Theory* (*GBT*) *elements*. PhD thesis, Bauhaus-Universität Weimar, Weimar.

[28] Bianco, M. J., Habtemariam, A. K., Könke, C., Tartaglione, F., and Zabel, V. (2019a). Complementary shear and transversal elongation modes in Generalized Beam Theory (GBT) for thin-walled circular cross-sections. In *Advances in Engineering Materials, Structures and Systems*: *Innovations, Mechanics and Applications*, pages 825–830. CRC Press.

[29] Bianco, M. J., Habtemariam, A. K., Könke, C., Tartaglione, F., and Zabel, V. (2020). Analysis of support coupling GBT (Generalized Beam Theory) applied in pipeline systems. *Thin-Walled Structures*, 146:106439.

[30] Bianco, M. J., Habtemariam, A. K., Könke, C., and Zabel, V. (2019b). Analysis of warping and distortion transmission in mixed shell-GBT (Generalized Beam Theory) models. *International Journal of Advanced Structural Engineering*, 11(1):109–126.

[31] Bianco, M. J., Könke, C., Habtemariam, A. K., and Zabel, V. (2018a). Coupling between shell and Generalized Beam Theory (GBT) elements. In *Forschungskolloquium* 2018 *Grasellenbach*, pages 4–10. Springer.

[32] Bianco, M. J., Könke, C., Habtemariam, A. K., and Zabel, V. (2018b). Exact finite element formulation in Generalized Beam Theory. *International Journal of Advanced Structural Engineering*, 10(3):295–323.

[33] Bischoff, M. (2020). Finite elements for plates and shells. *Encyclopedia of Continuum Mechanics*, pages 898–920.

[34] Bischoff, M., Ramm, E., and Irslinger, J. (2018). Models and finite elements for thin-walled structures. *Encyclopedia of Computational Mechanics Second Edition*, pages 1–86.

[35] Camotim, D. and Basaglia, C. (2013). Buckling analysis of thin-walled steel structures using Generalized Beam Theory (GBT): state-of-the-art report. *Steel Construction*, 6(2):117–131.

[36] Camotim, D., Silvestre, N., Basaglia, C., and Bebiano, R. (2008). GBT-based buckling analysis of thin-walled members with non-standard support conditions. *Thin-Walled Structures*, 46(7-9):800–815.

[37] Cheung, Y. K. (1976). *Finite strip method in structural analysis*. Pergamon Press.

[38] Davies, J. (1986). An exact finite element for beam on elastic foundation problems. *Journal of structural mechanics*, 14(4):489–499.

[39] Davies, J. (1998). Generalized Beam Theory (GBT) for coupled instability problems. In *Coupled Instabilities in Metal Structures*, pages 151–223. Springer.

[40] Davies, J., Leach, P., and Heinz, D. (1994). Second-order Generalized Beam Theory. *Journal of Constructional Steel Research*, 31(2-3):221–241.

[41] de Miranda, S., Gutiérrez, A., Miletta, R., and Ubertini, F. (2013). A Generalized Beam Theory with shear deformation. *Thin-Walled Structures*, 67:88–100.

[42] Dinis, P. B., Camotim, D., and Silvestre, N. (2006). GBT formulation to analyse the buckling behaviour of thin-walled members with arbitrarily branched open cross-sections. *Thin-Walled Structures*, 44(1):20–38.

[43] Dinis, P. B., Camotim, D., and Silvestre, N. (2010). On the local and global buckling behaviour of angle, T-section and cruciform thin-walled members. *Thin-Walled Structures*, 48(10-11):786–797.

[44] Donnell, L. H. (1934). A new theory for the buckling of thin cylinders under axial compression and bending.

[45] Duan, L. and Zhao, J. (2018). A nonlinear explicit dynamic GBT formulationfor modeling impact response of thin-walled steel members. *Journal of Southeast University* (*English Edition*), 34 (2):237–250.

[46] Duan, L. and Zhao, J. (2019a). GBT deformation modes for thin-walled cross-sections with circular rounded corners. *Thin-Walled Structures*, 136:64–89.

[47] Duan, L. and Zhao, J. (2019b). A geometrically exact cross-section deformable thin-walled beam finite element based on Generalized Beam Theory. *Computers & Structures*, 218:32–59.

[48] Duan, L., Zhao, J., and Liu, S. (2016a). A B-splines based nonlinear GBT formulation for elasto-plastic analysis of prismatic thin-walled members. *Engineering Structures*, 110:325–346.

[49] Duan, L., Zhao, J., Liu, S., and Zhang, D. (2016b). A B-splines-based GBT formulation for modeling fire behavior of restrained steel beams. *Journal of Constructional Steel Research*, 116:65–78.

[50] Duczek, S. and Gravenkamp, H. (2019). Critical assessment of different mass lumping schemes for higher order serendipity finite elements. *Computer Methods in Applied Mechanics and Engineering*, 350:836–897.

[51] Echter, R. (2013). *Isogeometric analysis of shells*. PhD thesis, Universität Stuttgart.

[52] Ferrarotti, A. (2018). *New approaches for linear and nonlinear analyses of thin-walled members in the framework of Generalized Beam Theory*. PhD thesis, University of Sydney.

[53] Flügge, W. (1973). *Stresses in Shells*. Springer, Berlin, Heidelberg.

[54] Fonseca, E. and De Melo, F. (2010). Numerical solution of curved pipes submitted to in-plane loading conditions. *Thin-Walled Structures*, 48(2):103–109.

[55] Gonçalves, R., Bebiano, R., and Camotim, D. (2014). On the shear deformation modes in the framework of Generalized Beam Theory. *Thin-Walled Structures*, 84:325–334.

[56] Gonçalves, R. and Camotim, D. (2004). GBT local and global buckling analysis of aluminium and stainless steel columns. *Computers & Structures*, 82(17-19):1473–1484.

[57] Gonçalves, R. and Camotim, D. (2007). Thin-walled member plastic bifurcation analysis using Generalized Beam Theory. *Advances in Engineering Software*, 38(8-9):637–646.

[58] Gonçalves, R. and Camotim, D. (2012). Geometrically non-linear Generalized Beam Theory for elastoplastic thin-walled metal members. *Thin-Walled Structures*, 51:121–129.

[59] Gonçalves, R. and Camotim, D. (2014). The vibration behaviour of thin-walled regular polygonal tubes. *Thin-Walled Structures*, 84:177–188.

[60] Gonçalves, R. and Camotim, D. (2017). Improving the efficiency of GBT displacement-based finite elements. *Thin-Walled Structures*, 111:165–175.

[61] Gonçalves, R., Dinis, P., and Camotim, D. (2009). GBT formulation to analyse the first-order and buckling behaviour of thin-walled members with arbitrary cross-sections. *Thin-Walled Structures*, 47(5):583–600.

[62] Gonçalves, R., Peres, N., Bebiano, R., and Camotim, D. (2015). Global–local-distortional vibration of thin-walled rectangular multi-cell beams. *International Journal of Structural Stability and Dynamics*, 15(08):1540022.

[63] Gonçalves, R., Ritto-Corrêa, M., and Camotim, D. (2010a). A large displacement and finite rotation thin-walled beam formulation including cross-section deformation. *Computer Methods in Applied Mechanics and Engineering*, 199(23-24):1627–1643.

[64] Gonçalves, R., Ritto-Corrêa, M., and Camotim, D. (2010b). A new approach to the calculation of cross-section deformation modes in the framework of Generalized Beam Theory. *Computational Mechanics*, 46(5):759–781.

[65] Gonçalves, R., Ritto-Corrêa, M., and Camotim, D. (2011). Incorporation of wall finite relative rotations in a geometrically exact thin-walled beam element. *Computational Mechanics*, 48(2):229–244.

[66] Habtemariam, A. K., Bianco, M. J., Könke, C., and Zabel, V. (2019a). Nonlinear ovalization analysis of thin-walled circular pipes in Generalized Beam Theory. In 5*th ECCOMAS Young Investigators Conference* (*YIC*2019).

[67] Habtemariam, A. K., Könke, C., Zabel, V., and Bianco, M. J. (2021a). Generalized Beam Theory formulation for thin-walled pipes with circular axis. *Thin-Walled Structures*, 159:107243.

[68] Habtemariam, A. K., Tartaglione, F., Zabel, V., Könke, C., and Bianco, M. J. (2021b). Vibration analysis of thin-walled pipes with circular axis using the Generalized Beam Theory. *Thin-Walled Structures*, 163:107628.

[69] Habtemariam, A. K., Zabel, V., Bianco, M. J., and Könke, C. (2018). Blast demolition study of guyed masts. *Shock and Vibration*.

[70] Habtemariam, A. K., Zabel, V., Bianco, M. J., and Könke, C. (2019b). Simulation der Antwort von oberirdischen Rohrleitungen auf Erdbebeneinwirkung unter Verwendung der Verallgemeinerten Technischen Biegetheorie. In *D-A-CH-Tagung* 16: *Erdbebeningenieurwesen und Baudynamik*.

[71] Habtemariam, A. K., Zabel, V., Könke, C., Bianco, M. J., and Tartaglione, F. (2020). Study of seismic effects in pipelines using Generalized Beam Theory. In *Seismic design of industrial facilities*: *proceedings of the* 2*nd International Conference on Seismic Design of Industrial Facilities*.

[72] Hallquist, J. O. et al. (2006). LS-DYNA theory manual. *Livermore software Technology corporation*, 3:25–31.

[73] Hellinger, E. (1907). Die Allgemeinen Ansätze der Mechanik der Kontinua. In *Mechanik*, pages 601–694. Springer.

[74] Henriques, D., Gonçalves, R., and Camotim, D. (2015). A physically non-linear GBT-based finite element for steel and steel-concrete beams including shear lag effects. *Thin-Walled Structures*, 90:202–215.

[75] Honegger, D. G., Nyman, D. J., Johnson, E. R., Cluff, L. S., and Sorensen, S. P. (2004). Trans-Alaska pipeline system performance in the 2002 Denali fault, Alaska, earthquake. *Earthquake Spectra*, 20(3):707–738.

[76] Hughes, T. J. and Liu, W. K. (1981). Nonlinear finite element analysis of shells: Part I. Three-dimensional shells. *Computer methods in applied mechanics and engineering*, 26(3):331–362.

[77] Jönsson, J. and Andreassen, M. J. (2011). Distortional eigenmodes and homogeneous solutions for semi-discretized thin-walled beams. *Thin-Walled Structures*, 49(6):691–707.

[78] Jumikis, P. (1987). *Stability problems in steel silos*. PhD thesis, School of Civil and Mining Engineering, University of Sydney.

[79] Kang, J.-H. (2018). Vibration of toroidal shells with hollow circular cross-sections. *International Journal of Structural Stability and Dynamics*, 18(09):1850102.

[80] Karamanos, S. A. (2016). Mechanical behavior of steel pipe bends: an overview. *Journal of Pressure Vessel Technology*, 138(4).

[81] Koiter, W. (1960). A consistent first approximation in the general theory of thin elastic shells. *The theory of thin elastic shells*, pages 12–33.

[82] Koiter, W. T. (1966). On the nonlinear theory of thin elastic shells. *Proceedings Koninklijke Nederlandse Akademie van Wetenschappen, Series B*, 69:1–54.

[83] Könke, C. (2011). *Applied Finite Element Methods*. Professuren für Baustatik und Bauteilfestigkeit, Bauhaus-Universität Weimar.

[84] Kosawada, T., Suzuki, K., and Takahashi, S. (1985). Free vibrations of toroidal shells. *Bulletin of JSME*, 28(243):2041–2047.

[85] Krätzig, W. B. (1990). *Nichtlinearer Finite Elemente Methoden*. Lehrstuhl für Statik und Dynamik, Ruhr-Universität Bochum.

[86] Kreyszig, E. (2006). *Advanced Engineering Mathematics*, volume 9. John Wiley & Sons.

[87] Leach, P. and Davies, J. (1996). An experimental verification of the Generalized Beam Theory applied to interactive buckling problems. *Thin-Walled Structures*, 25(1):61–79.

[88] Leach, P. et al. (1989). *The Generalized Beam Theory with finite difference applications*. PhD thesis, University of Salford.

[89] Leissa, A. W. (1973). *Vibration of shells*, volume 288. Scientific and Technical Information Office, NASA.

[90] Leung, A. and Kwok, N. T. (1994). Free vibration analysis of a toroidal shell. *Thin-Walled Structures*, 18(4):317–332.

[91] Li, T. (2017). On the formulation of a 3-D smooth curved pipe finite element with arbitrary variable cross-section. *Thin-Walled Structures*, 117:314–331.

[92] Liepins, A. A. (1965a). Flexural vibrations of the prestressed toroidal shell. Technical report, Dynatech Corporation Cambridge MA.

[93] Liepins, A. A. (1965b). Free vibrations of prestressed toroidal membrane. *AIAA journal*, 3(10):1924–1933.

[94] Love, A. (1944). A treatise on the mathematical theory of elasticity. *Cambridge University Press*, 1:952.

[95] Manta, D., Gonçalves, R., and Camotim, D. (2020). Combining shell and GBT-based finite elements: Linear and bifurcation analysis. *Thin-Walled Structures*, 152:106665.

[96] Manta, D., Gonçalves, R., and Camotim, D. (2021). Combining shell and GBT-based finite elements: Plastic analysis with adaptive mesh refinement. *Thin-Walled Structures*, 158:107205.

[97] Martins, A. D., Camotim, D., Gonçalves, R., and Dinis, P. B. (2018). Enhanced geometrically non-linear Generalized Beam Theory formulation: Derivation, numerical implementation, and illustration. *Journal of Engineering Mechanics*, 144(6):04018036.

[98] Marwitz, S., Zabel, V., and Habtemariam, A. K. (2017). Betrachtung von Unsicherheiten in der

Modalanalyse mit der Stochastic Subspace Identification am Beispiel eines Seilabgespannten Masts. In *D-A-CH-Tagung* 15: *Erdbebeningenieurwesen und Baudynamik*.

[99] Mattern, S., Blankenhorn, G., and Schweizerhof, K. (2007). Computer-aided destruction of complex structures by blasting. In *High Performance Computing in Science and Engineering'*06, pages 449–457. Springer.

[100] Michaloudis, G., Mattern, S., and Schweizerhof, K. (2011). Computer simulation for building implosion using LS-DYNA. In *High Performance Computing in Science and Engineering'*10, pages 519–528. Springer.

[101] Ming, R., Pan, J., and Norton, M. (2002). Free vibrations of elastic circular toroidal shells. *Applied Acoustics*, 63(5):513–528.

[102] Miosga, G. (1976). *Vorwiegend längsbeanspruchte dünnwandige prismatische Stäbe und Platten mit endlichen elastischen Verformungen*. PhD thesis, Technischen Hochschule Darmstadt.

[103] Muresan, A.-A., Nedelcu, M., and Gonçalves, R. (2019). GBT-based FE formulation to analyse the buckling behaviour of isotropic conical shells with circular cross-section. *Thin-Walled Structures*, 134:84–101.

[104] Mushtari, K. M. (1938). On the stability of cylindrical shells subjected to torsion. *Trudy Kazanskego aviatsionnugo inatituta*, 2.

[105] Mynt-U, T. and Debnath, L. (2007). *Linear Partial Differential Equations for Scientists and Engineers*, volume 4. Birkhauser Boston.

[106] Nedelcu, M. (2010). GBT formulation to analyse the behaviour of thin-walled members with variable cross-section. *Thin-Walled Structures*, 48(8):629–638.

[107] Nedelcu, M. (2011). GBT formulation to analyse the buckling behaviour of isotropic conical shells. *Thin-Walled Structures*, 49(7):812–818.

[108] Novozhilov, V. V. (1964). *Thin shell theory*. P. Noordhoff.

[109] Orynyak, I. and Radchenko, S. (2007). Analytical and numerical solution for a elastic pipe bend at in-plane bending with consideration for the end effect. *International Journal of Solids and Structures*, 44(5):1488–1510.

[110] Palaninathan, R. and Chandrasekharan, P. (1985). Curved beam element stiffness matrix formulation. *Computers & structures*, 21(4):663–669.

[111] Peres, N., Gonçalves, R., and Camotim, D. (2016). First-order Generalized Beam Theory for curved thin-walled members with circular axis. *Thin-Walled Structures*, 107:345–361.

[112] Peres, N., Gonçalves, R., and Camotim, D. (2018). GBT-based cross-section deformation modes for curved thin-walled members with circular axis. *Thin-Walled Structures*, 127:769–780.

[113] Peres, N., Gonçalves, R., and Camotim, D. (2020). A GBT-based mixed finite element for curved thin-walled members with circular axis. *Thin-Walled Structures*, 146:106462.

[114] Piccardo, G., Ferrarotti, A., and Luongo, A. (2017). Nonlinear Generalized Beam Theory for open thin-walled members. *Mathematics and Mechanics of Solids*, 22(10):1907–1921.

[115] Piccardo, G., Ranzi, G., and Luongo, A. (2014). A complete dynamic approach to the Generalized Beam Theory cross-section analysis including extension and shear modes. *Mathematics and Mechanics of Solids*, 19(8):900–924.

[116] Ramberg, W. and Osgood, W. R. (1943). Description of stress-strain curves by three parameters.

[117] Ranzi, G. and Luongo, A. (2011). A new approach for thin-walled member analysis in the framework of GBT. *Thin-Walled Structures*, 49(11):1404–1414.

[118] Reissner, E. (1950). On a variational theorem in elasticity. *Journal of Mathematics and Physics*, 29(1-4):90–95.

[119] Reissner, E. (1972). On one-dimensional finite-strain beam theory: the plane problem. *Zeitschrift für angewandte Mathematik und Physik ZAMP*, 23(5):795–804.

[120] Rotter, J. M. and Jumikis, P. T. (1988). *Nonlinear strain-displacement relations for axisymmetric thin shells*. University of Sydney, School of Civil and Mining Engineering.

[121] Ruggerini, A., Madeo, A., Gonçalves, R., Camotim, D., Ubertini, F., and De Miranda, S. (2019). GBT post-buckling analysis based on the Implicit Corotational Method. *International Journal of Solids and Structures*, 163:40–60.

[122] Saal, G. (1974). *Ein Beitrag zur Schwingungsberechnung von dünnwandigen, prismatischen Schalentragwerken mit unverzweigtem Querschnitt*. PhD thesis, Technischen Hochschule Darmstadt.

[123] Saal, G. et al. (1980). Zur Berechnung offener Kreiszylinderschalen mit beliebigen Randbedingungen an den Längs-und Querrändern.

[124] Saleeb, A. and Chang, T. (1987). On the hybrid-mixed formulation of C0 curved beam elements. *Computer Methods in Applied Mechanics and Engineering*, 60(1):95–121.

[125] Sanders Jr, J. L. (1959). An improved first-approximation theory for thin shells. *NASA Rep.*, 24.

[126] Sanders Jr, J. L. (1963). Nonlinear theories for thin shells. *Quarterly of Applied Mathematics*, 21(1):21–36.

[127] Schardt, C. (1985). *Zur Berechnung des Kreiszylinders mit Ansätzen der verallgemeinerten technischen Biegetheorie*. PhD thesis, Diplomarbeit Institut für Mechanik, TU Darmstadt.

[128] Schardt, R. (1966). Eine Erweiterung der Technischen Biegelehre für die Berechnung biegesteifer prismatischer Faltwerke. *Der Stahlbau*, 6:164–171.

[129] Schardt, R. (1970). Anwendung der Erweiterten Technischen Biegetheorie auf die Berechnung prismatischer Faltwerke und Zylinderschalen nach Theorie I. und II. Ordnung. In *Proceedings of the IASS-Symposium on Folded Plates and Prismatic Structures, Wien*, volume 1.

[130] Schardt, R. (1983). The Generalized Beam Theory. instability and plastic collapse of steel structures.

[131] Schardt, R. (1989). *Verllgemeinerte Technische Biegetheorie*: *Lineare Probleme*. Springer-Vertrag.

[132] Schardt, R. (1994a). Generalized Beam Theory- an adequate method for coupled stability problems. *Thin-Walled Structures*, 19(2-4):161–180.

[133] Schardt, R. (1994b). Lateral torsional and distortional buckling of channel and hat sections. *Journal of Constructional Steel Research*, 31(2-3):243–265.

[134] Schardt, R. and Heinz, D. (1991). Vibrations of thin-walled prismatic structures simultaneous static load using Generalized Beam Theory. In *European conference on structural dynamics, EUDODYN'*90, pages 921–927.

[135] Schardt, R., Issmer, H., and Mörschardt, S. (1986). *Gesamtstabilität dünnwandiger Stäbe*. Inst. für Statik.

[136] Schardt, R. and Okur, H. (1971). Hilfswerte für die Lösung der Differentialgleichung. *Der Stahlbau*, 40:6–17.

[137] Schardt, R. and Steingaß, J. (1970). Eine Erweiterung der Technischen Biegelehre für die Berechnung dünnwandiger geschlossener Kreiszylinderschalen. *Der Stahlbau*, 39:65–73.

[138] Schardt, R. and Zhang, X. (1989). Die Anwendungen der Verallgemeinerten Technischen Biegetheorie im nichtlinearen Beulbereich. In *Nichtlineare Berechnungen im Konstruktiven Ingenieurbau*, pages 482–500. Springer.

[139] Senjanović, I., Alujević, N., Ćatipović, I., Čakmak, D., and Vladimir, N. (2018a). Vibration analysis of rotating toroidal shell by the Rayleigh-Ritz method and Fourier series. *Engineering Structures*, 173:870–891.

[140] Senjanović, I., Ćatipović, I., Alujević, N., Vladimir, N., and Čakmak, D. (2018b). A finite strip for the vibration analysis of rotating cylindrical shells. *Thin-Walled Structures*, 122:158–172.

[141] Silva, N., Silvestre, N., and Camotim, D. (2010). GBT formulation to analyse the buckling behaviour of FRP composite open-section thin-walled columns. *Composite Structures*, 93(1):79–92.

[142] Silva, N. F., Silvestre, N., and Camotim, D. (2006). GBT formulation to analyse the buckling behaviour of FRP composite branched thin-walled members. In *III European Conference on Computational Mechanics*, pages 705–705. Springer.

[143] Silvestre, N. (2007). Generalized Beam Theory to analyse the buckling behaviour of circular cylindrical shells and tubes. *Thin-Walled Structures*, 45(2):185–198.

[144] Silvestre, N. (2008). Buckling behaviour of elliptical cylindrical shells and tubes under compression. *International Journal of Solids and Structures*, 45(16):4427–4447.

[145] Silvestre, N. and Camotim, D. (2002). First-order Generalized Beam Theory for arbitrary orthotropic materials. *Thin-Walled Structures*, 40(9):755–789.

[146] Silvestre, N. and Camotim, D. (2003a). GBT buckling analysis of pultruded FRP lipped channel members. *Computers & structures*, 81(18-19):1889–1904.

[147] Silvestre, N. and Camotim, D. (2003b). Nonlinear Generalized Beam Theory for cold-formed steel members. *International Journal of Structural Stability and Dynamics*, 3(04):461–490.

[148] Silvestre, N. and Camotim, D. (2004). Influence of shear deformation on the local and global buckling behaviour of composite thin-walled members. *Thin walled structures*: *advances in research, design and manufacturing technology*, pages 659–668.

[149] Silvestre, N. and Camotim, D. (2006). Vibration behaviour of axially compressed cold-formed steel members. *Steel and Composite Structures*, 6(3):221.

[150] Silvestre, N. and Camotim, D. (2013). Shear deformable Generalized Beam Theory for the analysis of thin-walled composite members. *Journal of Engineering Mechanics*, 139(8):1010–1024.

[151] Simão, P. and da Silva, L. S. (2004). A unified energy formulation for the stability analysis of open and closed thin-walled members in the framework of the Generalized Beam Theory. *Thin-Walled Structures*, 42(10):1495–1517.

[152] Simão, P. D. (2007). *Post-buckling bifurcational analysis of thin-walled prismatic members in the context of the Generalized Beam Theory*. PhD thesis.

[153] Simão, P. D. (2017). Post-buckling analysis of nonlinear shear-deformable prismatic columns using a GBT consistent energy formulation. *Computers & Structures*, 190:186–204.

[154] Simo, J. C. (1985). A finite strain beam formulation. The three-dimensional dynamic problem. Part I. *Computer methods in applied mechanics and engineering*, 49(1):55–70.

[155] Simo, J. C., Fox, D. D., and Rifai, M. S. (1990). On a stress resultant geometrically exact shell model. Part III: Computational aspects of the nonlinear theory. *Computer Methods in Applied Mechanics and Engineering*, 79(1):21–70.

[156] Sobel, L. (1977). In-plane bending of elbows. *Computers & Structures*, 7(6):701–715.

[157] Sorensen, S. P. and Meyer, K. J. (2003). Effect of the Denali fault rupture on the Trans-Alaska pipeline. In *Advancing Mitigation Technologies and Disaster Response for Lifeline Systems*, pages 547–555.

[158] Stolarski, H. and Belytschko, T. (1982). Membrane locking and reduced integration for curved elements. *Journal of Applied Mechanics*, 49(1):172–176.

[159] Stolarski, H. and Belytschko, T. (1983). Shear and membrane locking in curved C0 elements. *Computer methods in applied mechanics and engineering*, 41(3):279–296.

[160] Taig, G., Ranzi, G., and D'Annibale, F. (2015). An unconstrained dynamic approach for the Generalized Beam Theory. *Continuum Mechanics and Thermodynamics*, 27(4):879–904.

[161] Teng, J. and Hong, T. (1998). Nonlinear thin shell theories for numerical buckling predictions. *Thin-Walled Structures*, 31(1-3):89–115.

[162] Teng, J.-G. and Rotter, J. M. (1989). Non-symmetric bifurcation of geometrically nonlinear elastic-plastic axisymmetric shells under combined loads including torsion. *Computers & structures*, 32(2):453–475.

[163] Timoshenko, S. (1970). Theory of elasticity. *New York McGraw-Hill*, 970(4):279–291.

[164] Timoshenko, S. (1983). *History of Strength of Materials*: *With a Brief Account of the History of Theory of Elasticity and Theory of Structures*. Dover Civil and Mechanical Engineering Series. Dover Publications.

[165] Tkachuk, A. and Bischoff, M. (2015). Direct and sparse construction of consistent inverse mass matrices: general variational formulation and application to selective mass scaling. *International Journal for Numerical Methods in Engineering*, 101(6):435–469.

[166] Uenishi, K., Takahashi, H., Yamachi, H., and Sakurai, S. (2010). PC-based simulations of blasting demolition of RC structures. *Construction and Building Materials*, 24(12):2401–2410.

[167] Uhlmann, W. (1970). Die Berechnung von im Grundriß gekrümmten biegesteifen Faltwerken mit offenem in Längsrichtung unveränderlichem Querschnitt. *Der Stahlbau*, 39:193–199.

[168] Van Rossum, G. and Drake Jr, F. L. (1995). *Python tutorial*, volume 620. Centrum voor Wiskunde en Informatica Amsterdam.

[169] Vlasov, V. (1961). *Thin-Walled Elastic Beams*. Israel Program for Scientific Translations.

[170] Vlasov, V. (1964). General theory of shells and its application in engineering. *NASA TT F*-99.

[171] von Kármán, T. (1911). Über die Formänderung dünnwandiger Rohre, insbesondere federnder Ausgleichrohre. *Z. VDI*, 55:1889–1895.

[172] von Kármán, T. and Tsien, H.-S. (1941). The buckling of thin cylindrical shells under axial compression. *Journal of the Aeronautical Sciences*, 8(8):303–312.

[173] Wang, X. and Redekop, D. (2005). Natural frequencies and mode shapes of an orthotropic thin shell of revolution. *Thin-Walled Structures*, 43(5):735–750.

[174] Wang, X., Xu, B., and Redekop, D. (2006). Theoretical natural frequencies and mode shapes for thin and thick curved pipes and toroidal shells. *Journal of sound and vibration*, 292(1-2):424–434.

[175] Wu, S. R. and Gu, L. (2012). *Introduction to the explicit finite element method for nonlinear transient dynamics*. Wiley Online Library.

[176] Yamaki, N. (1984). *Elastic stability of circular cylindrical shells*. Elsevier.

[177] Yoo, C. H. and Lee, S. (2011). *Stability of structures*: *principles and applications*. Elsevier.

[178] Zabel, V., Marwitz, S., and Habtemariam, A. K. (2020). Bestimmung von modalen Parametern seilabgespannter Rohrmasten. In *Baustatik–Baupraxis* 14, pages 519–527.

[179] Zhang, F. and Redekop, D. (1992). Surface loading of a thin-walled toroidal shell. *Computers & Structures*, 43(6):1019 – 1028.

[180] Zienkiewicz, O. C., Taylor, R. L., and Zhu, J. Z. (2005). *The finite element method*: *its basis and fundamentals*. Elsevier.

Publications of the author

International reviewed journals

Habtemariam, A. K., Könke, C., Zabel, V., and Bianco, M. J. (2021a). Generalized Beam Theory formulation for thin-walled pipes with circular axis. *Thin-Walled Structures*, 159:107243

Habtemariam, A. K., Tartaglione, F., Zabel, V., Könke, C., and Bianco, M. J. (2021b). Vibration analysis of thin-walled pipes with circular axis using the Generalized Beam Theory. *Thin-Walled Structures*, 163:107628

Habtemariam, A. K., Zabel, V., Bianco, M. J., and Könke, C. (2018). Blast demolition study of guyed masts. *Shock and Vibration*

Conference papers

Habtemariam, A. K., Zabel, V., Könke, C., Bianco, M. J., and Tartaglione, F. (2020). Study of seismic effects in pipelines using Generalized Beam Theory. In *Seismic design of industrial facilities*: *proceedings of the* 2*nd International Conference on Seismic Design of Industrial Facilities*

Habtemariam, A. K., Zabel, V., Bianco, M. J., and Könke, C. (2019b). Simulation der Antwort von oberirdischen Rohrleitungen auf Erdbebeneinwirkung unter Verwendung der Verallgemeinerten Technischen Biegetheorie. In *D-A-CH-Tagung* 16: *Erdbebeningenieurwesen und Baudynamik*

Journal paper co-authored

Bianco, M. J., Habtemariam, A. K., Könke, C., Tartaglione, F., and Zabel, V. (2020). Analysis of support coupling GBT (Generalized Beam Theory) applied in pipeline systems. *Thin-Walled Structures*, 146:106439

Bianco, M. J., Habtemariam, A. K., Könke, C., and Zabel, V. (2019b). Analysis of warping and distortion transmission in mixed shell-GBT (Generalized Beam Theory) models. *International Journal of Advanced Structural Engineering*, 11(1):109–126

Bianco, M. J., Könke, C., Habtemariam, A. K., and Zabel, V. (2018b). Exact finite element formulation in Generalized Beam Theory. *International Journal of Advanced Structural Engineering*, 10(3):295–323

Conference contributions

Zabel, V., Marwitz, S., and Habtemariam, A. K. (2020). Bestimmung von modalen Parametern seilabgespannter Rohrmasten. In *Baustatik–Baupraxis* 14, pages 519–527

Bianco, M. J., Habtemariam, A. K., Könke, C., Tartaglione, F., and Zabel, V. (2019a). Complementary shear and transversal elongation modes in Generalized Beam Theory (GBT) for thin-walled circular cross-sections. In *Advances in Engineering Materials, Structures and Systems*: *Innovations, Mechanics and Applications*, pages 825–830. CRC Press

Habtemariam, A. K., Bianco, M. J., Könke, C., and Zabel, V. (2019a). Nonlinear ovalization analysis of thin-walled circular pipes in Generalized Beam Theory. In 5*th ECCOMAS Young Investigators Conference* (*YIC*2019)

Bianco, M. J., Könke, C., Habtemariam, A. K., and Zabel, V. (2018a). Coupling between shell and Generalized Beam Theory (GBT) elements. In *Forschungskolloquium* 2018 *Grasellenbach*, pages 4–10. Springer

Marwitz, S., Zabel, V., and Habtemariam, A. K. (2017). Betrachtung von Unsicherheiten in der Modalanalyse mit der Stochastic Subspace Identification am Beispiel eines Seilabgespannten Masts. In *D-A-CH-Tagung* 15: *Erdbebeningenieurwesen und Baudynamik*